Department of Imaging and Applied Physics
Centre for Marine Science and Technology

A Smoothed Particle Hydrodynamics Study of Ship Bow Slamming in Ocean Waves

Daniel John Veen

This thesis is presented for the Degree of
Doctor of Philosophy
of
Curtin University of Technology

October 2010

Declaration

To the best of my knowledge and belief this thesis contains no material previously published by any other person except where due acknowledgment has been made.

This thesis contains no material which has been accepted for the award of any other degree or diploma in any university

Signature: …………………...

Date: …………………………

Abstract

Smoothed Particle Hydrodynamics (SPH) is a mesh-free Lagrangian computational method suited to modelling fluids with a freely deforming surface. This thesis describes the development, validation and application of a two-dimensional Smoothed Particle Hydrodynamics algorithm to the problem of ship bow slamming in regular ocean waves. Slam events often occur in rough seas and have the potential to cause significant structural and payload damage due to the loads and subsequent whipping experienced by the ship. SPH is well suited to modelling ship bow slamming because the interaction between the bow of the ship and the water surface is of a freely deforming transient nature.

The developed SPH algorithm was subjected to an extensive validation using both analytical and experimental data as a basis for comparison. The influence of each numerical correction – necessary for SPH stability – was evaluated using two theoretical problems free from the influence of external forces: the evolution of initially circular and square patches of fluid. Solid boundaries treated by the ghost particle technique were introduced and evaluated by way of the hydrostatic tank and the two-dimensional dam break.

Still water impacts of two-dimensional wedges and hull cross-sections were simulated using the SPH algorithm and the results were compared with the experimental data of Aarsnes (1996), Whelan (2004) and Breder (2005). The complexity of the slamming problem was then increased by imposing the relative vertical velocity profile (between the hull and the water surface) measured during the ocean wave basin experiments of Hermundstad and Moan (2005) on a hull cross-section. Reasonable agreement between the simulated and experimental slamming pressures confirmed that the two-dimensional SPH algorithm could be applied to a three-dimensional problem through the use of a relative vertical velocity profile.

Finally, the commercial ship motion prediction software SEAWAY and the validated SPH algorithm were combined in a 2D + t method to simulate bow slamming of a slender hull. The relative motion between the bow and the free water surface was extracted from the ship motion data and then imposed on a cross-section of a given hull form. Satisfactory agreement with the peak pressures measured on a model V-form hull in regular waves (Ochi, 1958) demonstrated that the developed two-dimensional SPH code is capable of modelling three-dimensional ship bow slamming.

Acknowledgements

While a PhD is ultimately awarded to the individual, the production of the thesis is by no means due to the efforts of a lone postgraduate student. This project would never have been possible without the support of the staff and students of the Centre of Marine Science and Technology (CMST) and the Department of Imaging and Applied Physics at Curtin University.

My future career will be indebted to my supervisor, Dr Tim Gourlay (CMST), who gave up so much of his valuable time to patiently wade through every one of my ideas, no matter how ridiculous they may have been. I must also thank my associate supervisor, Dr Kim Klaka (CMST), for imparting so much of his naval architecture knowledge through an unofficial open door policy and Dr Alec Duncan (CMST), whose wealth of Matlab knowledge has saved me on so many occasions. I would also like to thank Dr James Whelan (Intec Engineering) for providing the experimental wedge drop test data and Dr Csaba Pakozdi (Marintek) who graciously gave up his time to help me further the development and validation of the SPH algorithm.

I would especially like to thank the past and present members of the CMST postgraduate office including Miles Parsons, Grant Pusey, Daniel Wilkes, Nina Ribbat, Iain Parnum, Binghui Li and Cassandra Currie, and my moral supporters Renee Hinch and Lisa Swann for making the past four years that much more enjoyable.

Finally, my family and friends have noted my absence as I descended into a lifestyle akin to that of a hermit over the course of this PhD, and I wish to thank them all for their understanding. In particular, the completion of this thesis would not have been possible were it not for the enduring support of my parents, Glenn and Robyn. They have listened, smiled and nodded as I endlessly chattered on about all things SPH, all the while reminding me that it would be entirely worth the effort in the end. I think they were right. Thanks Mum and Dad.

Contents

List of figures

xiv

List of tables

Nomenclature

xviii

θ	Bearing from an intersection point to a fluid particle.	66
κ	Kernel compact support scale factor.	29
λ	Wavelength.	80
μ_{ab}	Artificial viscosity parameter.	49
π	Mathematical constant.	36
Π_{ab}	Artificial viscosity.	49
ρ	Fluid density.	23
ρ_0	Fluid reference density.	48
ρ_a	Density of the particle of interest.	39
ρ_b	Density of a neighbouring fluid particle.	31
$\bar{\rho}_{ab}$	Average density of a particle pair.	49
ρ_c	Corrected fluid particle density.	54
ρ_p	Predicted fluid particle density.	53
ρ_t	Fluid particle density at the current time step.	53
σ	Kernel normalising constant.	36
σ_a	Viscosity condition for the CFL stability condition.	54
ϕ	The angle swept by the overlapping ghost particle region.	66
ϕ_H	Phase of the heave motion.	156
ϕ_P	Phase of the pitch motion.	156
$\chi(x)$	Force component based on the boundary particle spacing.	60
φ	Initial pressure field (square patch) scale factor.	87
ω	Wave encounter frequency.	156
ω_0	Initial angular velocity (square fluid patch).	85
Ω	Problem space.	27

Mathematical	**Description**	**Page N^o**
∇	Gradient operator.	30
$\nabla_{\mathbf{r}}$ or ∇_a	Gradient at the particle of interest.	30
$\nabla_{\mathbf{r}'}$ or ∇_b	Gradient at a neighbouring particle's position.	30

Chapter 1

Introduction

1.1 Background and motivation

Numerical modelling of ships in rough seas has met with limited success using available techniques in Computational Fluid Dynamics (CFD), particularly when wave impacts are involved. An understanding of the sea loads on ships is essential to ensuring the structural design criteria are met and assessing the fatigue life of the structure. In this thesis, a two-dimensional Smoothed Particle Hydrodynamics (SPH) algorithm has been wholly developed and validated for use as a tool for predicting impact loads on a slender ship.

1.1.1 Slamming

The interaction between floating bodies and free surface waves is of great importance in the structural design of marine vessels. Of particular significance is the strongly nonlinear free surface problem of water impacting with large force on a ship's hull, commonly referred to as slamming. Often occurring in rough seas, slamming can potentially cause significant damage to a ship, typically near the bow where the relative velocity between the ship and the water surface is greatest. The subsequent whipping along hull girders - observed as a vibration on board the ship - can also cause antennae, masts and other appendages to be damaged or even dislodged (Faltinsen, 2005).

The slamming problem is not confined to the violent interaction between ships and ocean waves. An analysis of the impact of seaplane floats during landing was one of the first studies completed on slamming (von Karman, 1929). Another example is the

sloshing of fluid contained in ship tanks, which can cause significant loads on the tank structure when the ship is experiencing large motions. This problem is of particular importance to operators of liquefied natural gas carriers. Offshore platforms often experience high slamming pressures when breaking waves strike the support columns (Faltinsen, 1990). In extreme weather conditions, offshore platforms can also experience wave impacts on the underside of the platform and green water on the platform deck.

Figure 1.1 – A 56.8 m Armidale class patrol boat is known to have excellent seakeeping qualities despite experiencing hull bottom slamming in rough seas (photographs courtesy of Austal, Australia, 2010).

Many factors contribute to the strongly nonlinear fluid-body slamming problem. The fluid compressibility, air entrainment, bubble formation and the form and hydroelasticity of the structure all play a part in the complex interaction (Whelan, 2004). Furthermore, the formation and separation of the fluid jets produced during impact is particularly dependent upon impact velocity and the acceleration of the moving body.

Ship hull slamming can be categorised into four major types; bottom (see Figure 1.1), bow flare, bow stem or breaking wave, and wet-deck slamming (Korobkin, 1996). Bottom slamming occurs when the keel of the ship rises out of the water surface and impacts heavily upon re-entry. Bow flare slamming does not necessarily require the keel to emerge from the water surface as the high loads are experienced nearer the chine. Bow stem or breaking wave slamming occurs when a wave breaks on the fore part of the ship's structure and lastly, wet-deck slamming refers to the impact between the water surface and the cross deck structure of a multi-hulled vessel.

Slamming is a greater problem for ships with large block coefficients than for fine ships and often occurs more on ships in ballast compared to those that are fully loaded (Faltinsen, 1990). There is no threshold for the occurrence of slamming on a given hull form at a certain forward speed, so as a guide most ship masters will reduce a ship's speed if slams occur in three out of every hundred waves encountered (Faltinsen, 1990).

1.1.2 Experimental methods

Ship slamming has previously been studied experimentally using a variety of techniques. Yamamoto et al. (1985) examined the damage suffered by mono-hulled vessels caused by slam events in high sea states, while a number of other authors have instrumented ships with strain gauges and pressure sensors and actively pursued weather conditions conducive to slamming (Andrew and Lloyd, 1981; Vulovich et al., 1989). This approach is not easily repeatable as ocean waves have a range of periods, heights and directions and the exact wave conditions at the ship are not easily measured. Furthermore this type of study carries with it inherent dangers that

have the potential to cause irreversible damage to the subject vessel (see Section 2.1 for a review of previous full-scale slamming trials).

To simplify the problem, models of ship's hulls are often tested in towing tanks and ocean wave basins (see Section 2.2.4). These models are instrumented with a number of pressure sensors and accelerometers and are either towed or driven under their own power. In typical towing tanks the models are exposed to regular head or following seas with wave periods and heights that produce conditions likely to cause slamming. In an ocean wave basin the model is propelled through regular waves at a number of headings, allowing the contributions of yaw and roll to the slam event to be measured.

The maximum slamming pressure and load on individual sections of a three-dimensional hull can be difficult to determine in tow tank and ocean wave basin tests due to the number of sensors required. Furthermore, theoretical calculations of slamming loads on a three-dimensional model are still in their infancy. To simplify the problem, measurements of slamming loads on a body have been obtained by dropping a given hull section into still water from varying heights. Most of these drop tests approximate two-dimensional flow by taking a cross-section of the examined hull. This is particularly useful for measurements of bow flare slamming and hull bottom slamming. A two-dimensional wedge or a circular cylinder can approximate the shape of a hull bottom, which is advantageous because theoretical methods can be used to calculate the load, pressure and free surface position during the water entry.

1.1.3   Numerical methods

Computational fluid dynamics methods are classified into two major groups; mesh-based and mesh-free. The following is a summary of the numerical methods that have previously been employed to study ship slam events.

Mesh based methods

The most widely used numerical methods for fluid flows rely on solving the mass, momentum and energy conservation equations using a grid spread over the

computational domain. These CFD methods can be categorized into two types: Eulerian or fixed mesh methods and Lagrangian or moving mesh methods. Eulerian methods, for example the Finite Difference Method (FDM) and the Finite Volume Method (FVM), overlay the computational domain with a grid that is fixed in space and time. The fluid properties of each cell are evaluated from the flux equations for mass, momentum and energy. While proven to be effective for most problems, the Eulerian methods struggle to model deformable boundaries such as a free surface and require a very large grid, which is not computationally efficient.

Lagrangian mesh based methods such as the Finite Element Method (FEM) fix the grid to the material, so the grid moves and deforms as the material does. For any given part of the material, mass, energy and momentum are transported with the movement of the grid cells. While the time history of a given cell can be tracked and boundary conditions easily applied, the method cannot deal with severe distortion and material fracturing without re-meshing the computational domain. For this reason FEM is rarely used for fluid dynamics problems. However, as there is no need to mesh areas surrounding the material, FEM is computationally efficient and is widely used for studying the behaviour of solid structures.

The Boundary Element Method (BEM) uses potential flow theory to solve for the fluid flow. Unlike the FEM, FVM and FDM, only the fluid boundary is meshed into discrete nodes or elements. Each element consists of a source and a sink, and their strength is solved using the imposed boundary conditions. The properties of a given fluid particle located anywhere in the fluid are easily inferred by combining the strengths of each source and sink doublet. As only the boundary is meshed into discrete elements, the BEM is computationally very efficient.

Mesh based methods are not particularly suited to modelling ship slam events, although Sun (2007) has used the BEM for two-dimensional simulations. Mesh generation is time consuming and can be difficult for Eulerian models with complex moving boundaries such as a hull section. Furthermore, resolving the free surface position during impact is difficult with an Eulerian grid. Lagrangian models struggle to resolve the formation and subsequent fragmentation of a fluid jet without constant

re-meshing. For these reasons, this thesis is focused on using a mesh-free method to accurately simulate hull bottom and bow flare slamming.

Mesh-free methods

The major distinction between mesh based and mesh-free methods is the treatment of the individual computational nodes. Mesh-free methods calculate the solution to a set of integral or partial differential equations at arbitrarily distributed points that are free to move through time and space. Implementing a mesh-free method reduces preprocessing time as there is no longer the need to develop a potentially complex grid. Without a mesh, the nodes - in most methods generally referred to as particles - are free to move through space and time. If large deformations in the fluid occur, re-meshing is not required, which also improves computational efficiency.

Early mesh-free methods still employed a grid, but it was not used in the same way as the traditional mesh based methods. Particle in Cell (PIC) and Marker and Cell (MAC) methods use a fixed Eulerian grid to solve the Navier-Stokes equations and then move evenly distributed marker particles by the local fluid velocity. Key elements of the fluid flow such as a free surface are then easily identifiable. Both methods suffered from dissipation in their early forms, however the introduction of a number of corrections have allowed these methods to be applied to solid and fluid mechanics problems.

The Volume of Fluid (VOF) method also uses a fixed Eulerian grid, but focuses on tracking the position of the free surface with time while conserving mass. This method introduces a function that has the value of one for any point in the fluid domain that is occupied by a fluid particle and zero otherwise. The average value of this function at any given cell determines the volume of the cell occupied by fluid. Despite the dependence on a fixed grid, VOF has successfully been used to model free surface flows.

Smoothed Particle Hydrodynamics (SPH) – developed independently by Lucy (1977) and Gingold and Monaghan (1977) as a tool for simulating gas dynamics in stellar objects – was one of the first methods to use a set of arbitrarily defined particles without the assistance of a grid (see Chapter 3). Each SPH particle has constant

mass and is free to move about the problem domain. The pressure, density and momentum of each particle are interpolated from the properties of the other particles in its immediate neighbourhood through the use of a smoothing function. Boundary conditions are easily enforced in the SPH method, particularly at a free surface as the kinematic and dynamic conditions are implicitly satisfied (see Section 3.6.1). SPH is therefore particularly suited to modelling free surface flows (see Section 4.4).

Since the SPH method was introduced in 1977, it has been used to model a variety of different problems. Some recent applications include;

- Chemo-dynamical formation of stars in disk galaxies (Berczik, 1999),
- High pressure die casting of automotive parts (Cleary et al., 2006),
- Fluid-structure interaction (Anghileri et al., 2005; Antoci et al., 2007),
- Green water overtopping on a marine platform (Gomez-Gesteira et al., 2005) and waves breaking on a beach (Dalrymple and Rogers, 2006),
- Underwater explosions (Liu et al., 2003),
- Sloshing of fluid contained in ship tanks (Pakozdi, 2008; Delorme et al., 2009; Landrini et al., 2003) and,
- The overflow of a dam caused by a landslide (Roubtsova and Kahawita, 2005).

Every one of the previous SPH studies mentioned has involved a free surface that constantly deforms throughout the simulation. SPH has been implemented to model ship slam events in this thesis because the water surface deforms significantly during the water entry process.

2D + t theory

Solving the three-dimensional problem of a ship moving in waves with available CFD methods requires considerable computing time to obtain a solution even at relatively low resolution. For this reason the problem is often approximated by a set of time-dependent two-dimensional hull cross-section simulations lying in earth-fixed coordinates, commonly referred to as the 2D + t or 2.5D method. It is assumed that the fluid flow at any cross-section is influenced only by that upstream beginning at the bow, and the variation in fluid flow along the length of the hull is small when

compared to changes in the cross-sectional fluid flow (Faltinsen, 2005). This enables the model to partly consider three-dimensional effects using an essentially two-dimensional approach.

Strip theory, originally developed by Korvin-Kroukovsky and Jacobs (1957), is a commonly used 2D + t method for determining the global motions of a ship. The method breaks the ship's hull into a series of two-dimensional cross-sections, known as slices or strips (Lloyd, 1989). The global hull motions are obtained by evaluating the local hydrodynamic properties at each strip only, ignoring the contribution of neighbouring hull cross-sections. Therefore the method is limited to calculating global motions as it ignores three-dimensional effects such as flow leaking around the ends of the ship.

SEAWAY is one such example of commercial rigid-ship strip theory code used for seakeeping calculations. Originally developed at Delft University of Technology in the Netherlands, SEAWAY is now marketed by Amarcon as part of the OCTOPUS suite of software. In SEAWAY the wave excitation forces are calculated using the diffraction method, taking into account the modification of the wave field as it diffracts around the hull (Journée and Adegeest 2003).

Tulin and Landrini (2001) and Colagrossi (2004) utilised a simple 2D + t method in conjunction with a SPH algorithm to model breaking bow waves on slender ships. In this thesis SEAWAY has been used in conjunction with SPH to approximate the slamming loads on a typical merchant vessel (see Chapter 6).

1.2   Scope of the thesis

The present work describes the development of the SPH model including a review of the current state-of-the-art, the comprehensive validation process and the application of the validated algorithm to ship slam events. Chapter 2 reviews a number of published experimental slamming studies at full-scale, including an analysis of the damage suffered by ships in rough seas and sea trials that specifically targeted slamming. Also included is a review of a range of published model scale experiments, from simple vertical drop tests of wedges, cylinders and generic hull

forms, through to complicated ocean wave basin trials. The experimental studies are supported by various numerical investigations such as the simple added mass theories of von Karman (1929) and Wagner (1932), boundary element methods and smoothed particle hydrodynamics.

The history of the weakly compressible SPH method is discussed in Chapter 3. Particular attention has been paid to the wide range of interpolation kernels implemented by many authors as well as the variational consistency of the different density evolution and momentum conservation equations. A detailed review of the available solid boundary treatments is also provided, including an extension to the boundary intersection method proposed by Colagrossi et al. (2007). An outline of the SPH code - wholly developed by the author - is provided in Section 3.7.

An extensive validation of the developed SPH code was completed and the results are outlined in Chapter 4. Free surface problems in the absence of external forces were studied in detail along with gravity driven flows such as the classical dam break. In Chapter 5, the validated SPH code has been applied to constant velocity and variable velocity water entries of wedge shaped sections. The results have been compared against the experimental results of Breder (2005) and Whelan (2004) as well as the theoretical approximation of Wagner (1932). A more complex geometry that represents a typical flared bow section was also introduced in Chapter 5 and the results compared with the experimental data of Aarsnes (1996) and the BEM approximation of Sun (2007).

In Chapter 6 the typical merchant V-form hull studied by Ochi (1958) was modelled using an approach inspired by 2D + t theory. The ship motions were determined using the seakeeping software SEAWAY (Journée and Adegeest, 2003) and the relative vertical motions at three forward stations calculated. The loads at the stations were then calculated by simulating the local fluid flow with the SPH algorithm. Finally, the conclusions and recommendations for future work are outlined in chapter 7.

Chapter 2

Literature Review

The slamming behaviour of ships in rough seas has previously been investigated by a variety of different methods. At full-scale, a number of authors have performed sea trials on ships of varying size and shape. In the pursuit of a full analytical solution, the problem has been simplified by considering the constant and variable velocity water entry of wedges and circular cylinders. Two-dimensional approximations of the water entry of a typical hull section have also been studied numerically and experimentally. This chapter aims to review many of the previously published works, both numerical and experimental, on ship slam events with particular emphasis on SPH techniques.

2.1 Slamming studies of full-scale ships

The effect ocean wave slamming can have on a ship's structure was studied by Yamamoto et al. (1985). In January 1978, a 175 m high-speed containership was caught in heavy seas due to the presence of cyclones in the North Pacific Ocean. After suffering a number of severe slams near the bow, the ship developed corrugations in the hull plating on both sides and a long crack on the starboard side. Further plastic deformation was noticed on the deck and in the fore bulkheads. Upon analysis of the damage Yamamoto et al. (1985) recommended reducing the bow flare angle in future designs to prevent further incidents occurring. This study focused on the damage caused, but did not give any indication of the loads and pressures experienced by the hull during a large slam event. For this reason a number of authors have instrumented a variety of ships with strain gauges to determine the loads experienced by the hull during slamming.

Vulovich et al. (1989) measured the characteristics of hull stresses due to rough seas on the large containership *Sea-Land Independence* in the North Pacific Ocean from December 1985 through to March 1986. The bow of the *Sea-Land Independence* had a considerable flare leaving it vulnerable to significant slam loads. A number of strain and ship motion gauges were placed around the ship, with many concentrated near the bow. The impact pressures were derived from the strain sensors that were placed on the bow flare hull plating. Vulovich et al. (1989) found that the longitudinal stress at the fore deck was generally far greater than that experienced in the mid section. The mid section of the ship was only experiencing stress due to whipping through the hull structure, while the bow was suffering from large, short duration forces due to the localised water impact.

The slamming loads experienced at sea by military vessels have also been studied by several authors. Sea trials of an aluminium torpedo boat were used by Heller and Jasper (1961) as the basis for developing simple design procedures for planing craft. The trial was conducted at 35 knots in waves between 1 m and 2 m in height and the data recorded by a number of pressure gauges, strain gauges and accelerometers was used to develop design rules for planing hulls. Andrew & Lloyd (1981) reported on the sea trials of two larger ships: a 110 m Leander class frigate and a 107 m Tribal class frigate. The study was conducted in the North Atlantic Ocean south-west of Ireland in June 1977. The ships were selected because of their similar size yet different seakeeping qualities. Each ship was fitted with twelve strain gauges mounted to the longitudinal girders at various locations. It was assumed that the occurrence of a slam was associated with high frequency whipping recorded at the bridge as this is how a typical observer would recognise a slam event. The number of slams recorded in head seas with a characteristic period of 10 s and an average significant wave height of 8 m was found to increase with ship speed up to a maximum of 20 kts. At this speed the Tribal class frigate abandoned the trials because severe slams had damaged pipework and machinery mounts. By analysing the data recorded during the Leander and Tribal sea trials, Clarke (1982) noted that the probability of a slam event occurring rose rapidly above a ship speed of 10 kts, but the distribution of induced whipping stress did not change. It became more and more difficult to determine the difference between a small slam and continuing

structural whipping from a previous slam as the ship speed was increased (Clarke, 1982). Hay et al. (1994) performed a similar study on a 173 m CG-47 class guided missile cruiser in sea state 6 in the North Atlantic in January 1991. The authors believed most of the recorded slams to be the result of bow flare slamming as opposed to hull bottom slamming. The resultant whipping through the structure for the most severe slams was found to exceed the design limits of the ship.

The incidence of slamming on passenger ships has also been reported. Sebastiani et al. (2001) monitored the motions experienced by the 146 m *Aries* from June 1998 through to December 1999 on its regular services from mainland Italy to the island of Sardinia. Long base strain gauges accompanied by pressure sensors were placed at twelve locations on the forward part of the hull. The authors attempted to replicate the sea trials with a 1:28 scale model and also developed a correlation formula for the prediction of peak impact pressure at differing forward speeds and wave conditions. The correlation formula used two-dimensional wedge theory (see Section 2.1.2) with a three dimensional forward speed correction and found reasonable agreement with both the full scale and model scale peak pressures.

Ship slamming studies have not just been confined to single hulled vessels. In fact the slamming problem is potentially of greater importance in the design of multi-hulled ships due to the possibility of the cross deck structure enclosing water between the hulls. To study the slamming loads experienced by a catamaran, Steinmann et al. (1999) monitored the June 1997 delivery voyage of the 86 m Austal aluminium vehicle and passenger ferry *Adan Menderes* from Fremantle, Western Australia to Istanbul, Turkey. A combination of strain gauges, accelerometers, pitch and roll gyros and on-board wave meters were fitted at various locations around the vessel. The authors noted that the structure located nearest the slam event experienced a high forced response to the slam, yet sections of the hull structure located further from the point of impact responded only at the hull's modal frequencies. Thomas et al. (2003) performed a similar study on an 86 m Incat aluminium ferry during a segment of its delivery voyage from Sydney, New South Wales to Fremantle, Western Australia. To identify a slam event, the raw data recorded at a number of strain gauges was high pass filtered at 0.6 Hz in order to

remove the global wave load signal. For this particular vessel, slams occurred when the significant wave height reached 0.9 m and were most commonly wet deck slams rather than bottom or bow flare. Slams also occurred in series, with the first event predominantly more severe than the second (Thomas et al, 2003). A similar study undertaken during the delivery voyages of two Incat catamarans (81 m and 86 m) was presented by Roberts et al. (1997).

The full-scale slamming sea trials reviewed in this section have provided detailed information about the behaviour of a variety of vessels in rough seas, however there are some limitations. The loads and pressures measured on a hull at sea are often difficult to repeat due to the large number of variables affecting the motion of the ship and an indication of the wave motion causing the slam event is not easy to ascertain. Furthermore, the trials are performed after a ship has been built, making it difficult to decrease the ship's susceptibility to slamming due to the hull design in a given sea state. For this reason, slamming studies of many hull sections have been completed experimentally in drop or tow tanks and numerically using a variety of computational fluid dynamics techniques.

2.2 Model-scale slamming studies

Predicting slamming loads based on full-scale studies is a difficult and complex task, therefore the problem has been simplified by some researchers to simpler two-dimensional water entries of vee wedges and circular cylinders. This is particularly useful as ships often have elements of both shapes in their design. A brief review of previously published model scale tests is presented here; for a more detailed outline of early experimental and numerical wedge water entry studies see Korobkin and Pukhnachov (1988).

2.2.1 Water entry of two-dimensional wedges

The water entry of two-dimensional ship hull models has long been the principal technique used to investigate the slamming problem. However, it was the impact of sea plane floats during landing that originally inspired the first theoretical study by von Karman (1929). The process was simplified by von Karman (1929) to the

incompressible water entry of a two dimensional wedge section of any given deadrise angle (the angle between the horizontal and the underside of the wedge). The total force on the wedge was derived from the momentum theorem, assuming that during impact some of the momentum of the wedge would be imparted onto a mass of water (commonly termed the added mass method). Despite assuming that the pressure along the surface of the wedge was uniform during impact, the model showed reasonable agreement with the experimental force on a 20° deadrise wedge.

Wagner (1932) extended the study of von Karman (1929), reasoning that the formation of a jet and spray was caused by the pile-up of water near the surface of the wedge. This effectively increased the wetted area and therefore the net force during water entry. Wagner (1932) was able to predict the coefficient of maximum pressure $C_{p\,max}$ experienced by a wedge of deadrise angle β_D by,

$$C_{p\,max} = \frac{\pi^2}{4}\cotan^2\beta_D \qquad (2.1)$$

Garabedian (1953) developed a self-similar theory extension of Wagner's (1932) work using conformal mapping. An object is said to be self-similar if its properties can be written in terms of dimensionless time and space parameters. In the context of the impact of a wedge, the water surface constantly expands away from the vertex in time. Assuming that the free surface shape is self-similar through time allows the local fluid properties to be determined easily. Borg (1957) implemented an exact relaxation solution (an iterative method for solving partial differential equations) to Laplace's equation for the unsymmetrical water entry of a wedge. Borg (1957) compared the results with experimental water entries of an 80° deadrise wedge and a 45° deadrise wedge with reasonable results. The self-similar approach of Garabedian was developed further by Dobrovol'skaya (1969) to produce the first analytical solution for the water entry of a two-dimensional wedge. While all of these authors were able to predict the water pile up immediately adjacent to the wedge, the separation of the water jet and formation of spray was not able to be modelled.

Bisplinghoff and Doherty (1952) filmed vertical drop tests of a number of vee wedges, ranging in deadrise angle from 10° through to 50°, using a 1500 fps high-speed camera. The peak accelerations and added mass were found to agree well with the values expected by Wagner (1932) for all models except the 10° deadrise wedge. At the lower deadrise angles significant air compression effects resulted in the experiment recording much lower peak pressures and accelerations than those expected from the theoretical approach. Further experimental studies were required to study the influence of air during the impact of wedges at deadrise angles less than 10°.

Chuang (1966, 1967) dropped a flat plate into still water and found that the fluid pressures measured were considerably less than those expected by von Karman (1929) due to the air beneath the plate compressing and forming a cushion. Chuang (1967) investigated the air cushion effect further by dropping a range of wedges (1° through to 15° deadrise) and measuring the impact pressure and acceleration. The maximum fluid pressure was recorded when testing the 3° deadrise wedge. At this deadrise angle the trapped air was allowed to vent more easily than wedges with a lower deadrise angle. However, a reduction in fluid pressure when compared with the theoretical values of von Karman (1929) was still noted up to and including the 15° deadrise wedge. This implies that a CFD algorithm will only be able to accurately model wedges with a deadrise angle greater than 15° when using a single fluid model. Lower deadrise wedges require a complicated coupled algorithm including both air and water. Chuang (1969) also investigated theoretical slamming of three-dimensional high deadrise angle cone shaped objects without including a correction for trapped air. A solution similar to the Wagner (1932) approximation of the pressure distribution was obtained by approximating the cone with an equivalent flat plate using conformal mapping.

In 1981, Payne reviewed the developments of various added mass theories and compared the more advanced corrected versions of the von Karman (1929) and Wagner (1932) approximations with their original formulations. Using the experimental data of Bisplinghoff and Doherty (1952) as a reference, Payne (1981)

found that the simple von Karman (1929) and Wagner (1932) methods produced more accurate results than the newer corrected versions. An estimation of the spray volume in the Bisplinghoff and Doherty (1952) experiments was made and a force component was added into the numerical approximation. A reasonable improvement on the existing numerical model (Wagner, 1932) was achieved, however this method was not able to predict the separation of the water jet and the formation of the spray.

Cauchy's theorem for the integral of an analytic function around a closed loop was applied to two-dimensional wedge water entries by Vinje and Brevig (1980) and Greenhow (1987). In this case the analytic function was the complex potential; a combination of the fluid velocity potential and the stream function. Good agreement was found between drop tests of wedges at deadrise angles of 45°, 60° and 81° and the Cauchy method. Arai and Tasaki (1987) departed from the Wagner (1932) added mass approach and used a finite difference method on a regular grid to determine the loads on a free falling wedge. It was noted that the method could be easily applied to generic bow shapes, which is not easily done with evolutions of the Wagner (1932) method. While able to determine the pressure and loads on the bow section, the FDM cannot resolve large free surface deformation and fracture (see Section 1.1.3) because it is grid based.

Arai et al. (1994) used a fractional volume of fluid method over a body fitted coordinate system to solve for the transient deformation of the free surface. A circular cylinder, a 30° deadrise wedge, a 45° deadrise wedge and a ship bow section were simulated. Comparisons against the Wagner (1932) method showed reasonable agreement for all sections except the bow, as its motions could not be calculated via the added mass method. The same VOF method was applied by Arai et al. (1995a) to minimise slamming loads on the horizontal members of offshore structures. The investigation found that parabolic members had the potential to reduce impact loads to approximately half that of a cylinder. Arai et al. (1995b) then focused the method on studies of U-form, V-form and flared bow sections. The flared section was found to experience more violent slam events, while the V form was least susceptible to damage from an impact.

Zhao et al. (1997) presented two numerical methods for predicting slam events. The first was a fully nonlinear potential flow theory solver that allowed for fluid separation at the knuckles of a wedge or at predefined points along a curved surface. The second method was an extension of Wagner's (1932) solution that did not account for separation of the water jet. Both models were compared against an experimental drop test of a 30° deadrise wedge with reasonable agreement. The simple von Karman (1929) method was shown to give a low maximum and poor time history of the force.

In recent years a number of new experimental studies into the still water impact of a two-dimensional wedge have been reported. The advent of more sensitive instruments able to sample at higher rates has allowed for detailed time histories of the force and pressure on a wedge to be measured. Whelan (2004) dropped two wedges of equal beam but differing deadrise angle (15° and 25°) vertically (constrained in roll) into still water from varying drop heights. The time histories of pressure and force have been used as a validation case in this thesis (see Section 5.3). The water entry process was simplified further by Breder (2005) and Tveitnes et al. (2008) by imposing a constant velocity on the wedge during impact. Breder (2005) produced time histories of the still water impact of a marine panel at a number of angles and velocities which have also been used to validate the present SPH algorithm (see Section 5.2). Tveitnes et al. (2008) conducted an experimental program for validating CFD and momentum theory wedge results, ultimately to predict the behaviour of planing hulls in waves. The program consisted of water entry, exit and wet chine oscillation tests and found that the wetting factor (the ratio of the wetted width of the wedge surface to its wetted width from the initial still water level) was strongly dependent on the deadrise angle. However, the testing rig was subject to significant dynamic noise, limiting the accuracy of the results.

2.2.2 Water entry of two-dimensional circular cylinders

Wave impact loads on circular cylinders were studied experimentally by Sarpkaya (1978). The test cylinders were initially placed so that the bottom was just touching the free surface. The cylinder was then subjected to vertical oscillatory motion and the forces were recorded. The total force consisted of a slamming load and a drag

load and the calculated slamming coefficient was found to match that predicted by Wagner (1932). One of the test cylinders had a rough surface, which had no effect on the slam coefficient but did affect the rise time of the jet and resultant drag force.

A numerical study of the incompressible water entry of a rigid cylinder was completed by Armand and Cointe (1987). The method used matched asymptotic expansions, where the flow in an inner domain (immediately surrounding the cylinder) is matched to that of an outer domain in order to determine the thickness of the water jet. The results have justified the wetting, or pile-up, correction implemented by Wagner (1932). Previously, the method was used for planing craft and flow past blunt ships, but Faltinsen (2002) has since used it for modelling the impact of a two-dimensional wedge. The results were shown to be in agreement with the calculations made by Wagner (1932).

The water entry of a circular cylinder is an attractive SPH validation case, particularly for curved boundaries. Some of the hull sections considered in Chapter 6 of this thesis are similar in shape to a circular cylinder, however experimental force and pressure time series required to complete a validation of the water entry of a circular cylinder were not readily available.

2.2.3   Water entry of two-dimensional hull sections

The previous studies of two-dimensional wedges and circular cylinders are particularly relevant to this thesis as many bow sections are similar in form to both shapes. One early experimental study used a cylindrical form, but did not examine the hull of a ship. Baker and Westine (1967) measured the structural response due to still water impact of the Apollo space vehicle command module. The models, shaped like a spherical segment, were constructed from aluminium, which was less rigid (dimensionless) than the full-scale stainless steel prototype. The load data was compared with full-scale measurements and found to be in agreement, even with the use of dissimilar, less rigid materials.

Cross-sections representing the form of a generic flared bow section have been tested experimentally by a number of authors. One section studied by Aarsnes (1996) and

reported by Zhao et al. (1997) has been used as a case for comparison in this thesis. Aarsnes (1996) instrumented the test section with four pressure sensors and two force transducers producing a series of pressure, load and velocity traces for varying drop heights (see Section 5.4). Manganelli et al. (2003) performed rotating drop tests on a model of an Open 60' class yacht instrumented with slam patches (large area pressure transducers) on the hull plating. Large patches were used instead of small piezoelectric sensors because the patches gave an average pressure that correlates well with the measured load. The 1:7 scale hull model was fixed at the transom and allowed to rotate towards the water surface through differing angles above the horizontal. The rotating drop tests in calm water confirmed the relationship between impact pressure and structural response. As the hull section rotated into the water three-dimensional effects were significant, so the data recorded was not suitable for validating SPH drop test models.

Davis and Whelan (2007) examined the water entry of two-dimensional catamaran hull sections experimentally. Real slam events depend on the way in which the hull strikes the water surface, particularly for catamarans as the effects of air venting and entrainment must be considered. The loads measured during the two-dimensional drop tests were found to be three times that of full-scale measurements made on an 86 m Incat catamaran. The drop tests allowed some air to vent through the ends of the model, whereas at full scale residual air mixed with the water near the free surface causes a decrease in the measured load. This occurs over the whole period of the slam and is characterised by the compressibility of the entrained air (Davis and Whelan, 2007). As the SPH algorithm presented in this thesis can only model a single fluid, the data recorded by Davis and Whelan (2007) were not suitable for use in the validation process. However, the experimental drop test data would be very useful in validating future two fluid extensions to the SPH algorithm.

To calculate the pressures and loads on a given monohull section, Wraith (1998) modified von Karman's (1929) added mass method. The new method allowed curved hulls to be studied numerically and the results were shown to relate well to the damage suffered by sailing yachts after a slam event. Wraith (1998) found that the effect of hull curvature was insignificant but the relative angle between the hull and

the water surface was significant. Furthermore, the model mass was found to have a small effect on peak pressures.

An arbitrary hull section was studied numerically by Zhao and Faltinsen (1993) using a nonlinear boundary element method with a jet flow approximation. The BEM was verified by comparing the results with the self-similarity solution for constant velocity entry developed by Dobrovol'skaya (1969). Lu et al. (2000) extended the work of Zhao and Faltinsen (1993) by adding hydroelasticity to the analysis of the impact of a two-dimensional wedge. The model was said to be in development but the initial results presented were promising.

The boundary element method was also used by Chihua and Yousheng (1997) to model the constant velocity entry of the flared bow section studied by Zhao and Faltinsen (1993). It was concluded that a ship with a flared bow section would suffer more damage due to slamming in rough seas than a ship with a U-form section. Sun (2007) modelled the Aarsnes (1996) hull section using a combination of BEM and Wagner's (1932) formulation. The initial stages of the water entry were resolved using the Wagner (1932) method, then after a short time (less than 0.01s after initial impact) the model switched to the BEM to complete the solution (see Section 5.4.1). Wedges and circular cylinders were also included for validation purposes with a correction for hydroelasticity. The effect of heel angle for the same hull section was reported by Sun and Faltinsen (2008) and the model was found to be in reasonable agreement with experimental results. While the BEM is able to resolve the loads and pressures to within reasonable agreement of published experimental work, it does lack the ability to accurately model large deformation and fragmentation of the free surface.

2.2.4 Slamming of hull models in tow tanks

The water entry of a two-dimensional body does not always give an accurate indication of the slamming pressures and loads experienced by a ship at full scale. The two-dimensional experiments miss three-dimensional effects such as forward speed, longitudinal hull slope, dynamic swell up and free surface slope. For this

reason, many hull forms have been tested in tow tanks or ocean wave basins at a variety of different wave heights, wave headings and ship speeds.

Ochi (1958) was one of the first to publish the results of slamming investigations on slender hulls in a tow tank environment. A number of tests on two hulls were performed at various ship speeds, drafts, wavelengths and wave heights. Each hull, similar to a typical merchant ship, was identical aft of midships but differed in the bow with either a V-form or U-form section. Ochi (1958) fitted the 6.0 m long models with a number of brass diaphragm pressure sensors and towed the models through regular waves in a 200 m towing tank. The maximum slamming pressure was found to occur near the keel indicating that the ship was predominantly experiencing hull bottom slamming. An increase in forward speed pushed the location of maximum pressure aft. While the maximum pressures were published by Ochi (1958), the time series of the fluid pressure at each sensor was not. Numerical validation work using this study is therefore limited.

More recently Hermundstad and Moan (2005) conducted model tests of the 120m car carrier *Autoprestige* in the 80 m by 50 m ocean wave tank at MARINTEK, Norway. The 5.8 m self propelled model was fitted with slamming panels to determine the mean pressure on the bow flare 5% of the ship length aft of the forward perpendicular. Slamming was observed on the panels when the ship was in head to bow quartering regular waves at a period of 9.0 s and a wave height of 2.5 m (full scale). This study is particularly useful because the relative wave elevation was measured using an optical system, allowing the experiments to be reproduced numerically (see Chapter 6).

Dessi and Mariani (2008) carried out a similar study on a fast Ro-Ro ferry built by Fincantieri at the 220 m INSEAN towing tank basin in Italy. The work was focused on measuring the slamming loads and bending moments of the ship, so the model was divided into six segments all attached to a strain gauged elastic beam. The 4.3 m model was free to heave and pitch in regular waves of differing wave lengths at a variety of ship speeds. The model tests were used as a benchmark to test a numerical simulation using a joint analytical added mass and BEM approach. The numerical

model included an estimation of the effective wetted length and calculated loads that were found to be in reasonable agreement with the towing tank tests.

2.2.5 Use of model tests in slamming prediction software

Seakeeping software packages such as SEAWAY (Journée and Adegeest, 2003) often use one of two methods for the prediction of bow slamming. Ochi (1964) proposed a critical vertical velocity condition to define bow slamming by analysing experimental tow tank studies. The method calculates the emergence of the hull from the water surface 10% of the ship length aft of the forward perpendicular and then determines the relative vertical velocity between the hull and the water surface. If the bottom of the hull emerges from the water surface and the relative vertical velocity at impact is higher than the critical value $v_{slam} = 0.093\sqrt{gL_{pp}}$ – where g is the acceleration due to gravity and L_{pp} is the length between the ship's perpendiculars – a slam event is deemed to have occurred. The second method proposed by Conolly (1974) defined the emergence in the same way as Ochi (1964) but used a critical pressure as opposed to velocity. If the local fluid pressure exceeds $P_{slam} = 0.5C_P\rho v_{entry}^2$ – where C_P is a pressure coefficient determined from experimental drop tests of model hull forms and v_{entry} is the vertical water entry velocity – Conolly (1974) categorises the water entry as a slam event.

2.3 SPH slamming studies

A weakly compressible smoothed particle hydrodynamics algorithm has previously been used in the prediction of slamming loads on wedge shaped bodies by Oger et al. (2005). The computational domain was filled with 200 000 particles concentrated in the region surrounding the wedge and more sparsely separated in the far field. The model sampled the pressure of particles immediately adjacent to the surface of the wedge in order to determine the vertical load and subsequent change in velocity. The load on a 30° deadrise wedge was compared with the experimental and numerical results quoted in Zhao et al. (1997). The SPH model was also extended to allow the wedge to move in all degrees of freedom.

Shao (2009) developed an incompressible SPH method for modelling the slamming of two-dimensional wedges. The particle resolution was coarse, only 20 000 particles in the computational domain, but the load on a 30° wedge was comparable to that published by Zhao et al. (1997). Shao (2009) noted that a finer particle resolution was required to correctly resolve the pressure at discrete points on the wedge surface and the form of smaller flow features such as jets.

The experimental hull drop tests of Aarsnes (1996) and Zhao et al. (2007) were used as a validation case for the SPH and VOF models published by Viviani et al. (2009). At the time of publication, the SPH model was in the early stages of development. The initial results of the free drop tests of a 30° deadrise wedge were in satisfactory agreement with the experimental results. However, the SPH algorithm employed the simple repulsive particle technique to model the solid boundaries (see Section 3.6.2), which has the potential to corrupt the pressure field of the entire fluid domain over time (see Section 3.3.3).

Kalis (2007) used a coupled SPH/FEM algorithm to study the water entry of two-dimensional circular cylinders and found that the displacement of the cylinder with time matched theoretical and experimental data sets. However, pressure contours of the fluid domain showed considerable pressure waves propagating away from the surface of the cylinder during impact, gradually degrading the pressure field. Kalis' (2007) study was extended to model the three-dimensional free fall water entry of a lifeboat. By comparing against experimental studies, the simulation was found to overpredict the pressure and loads on the hull of the lifeboat, significantly affecting its trajectory after impact with the water surface. Cartwright et al. (2004 and 2006) used the same method for seakeeping calculations on a variety of single and multi-hulled vessels with limited success. The coarse fluid particle resolution required for three-dimensional calculations caused significant wave energy dissipation and only allowed for global load predictions. The authors recommended that further validation work be undertaken in order to prevent the wave energy from dissipating and allow for the calculation of local fluid loads on the ship. To date, no other SPH studies of three-dimensional ship motions or slamming have been found by the author of this thesis.

2.4 Summary

This chapter has reviewed a wide variety of experimental and numerical methods previously used to study ship slam events. Full-scale sea trials provide valuable information on the behaviour of a ship's hull during a slam event, however this is not easily repeatable due to the variable nature and difficulty in measuring the properties of ocean waves. For this reason, many ship models have been towed through regular waves or simply dropped from a height into still water to gain an understanding of the loads and pressures experienced during a slam. Two-dimensional drop tests of simpler shapes such as wedges and circular cylinders have allowed for the validation of a number of numerical models.

Numerical and analytical methods for modelling ship slamming have been developed in order to enable a wide variety of hull shapes to be studied prior to construction. Many of the analytical methods, such as that proposed by Wagner (1932), are able to predict the global loads and the local fluid pressure but lack the ability to model the evolution and fragmentation of the free surface. Eulerian methods such as FDM (Arai and Tasaki, 1987) and BEM (Zhao and Faltinsen, 1993) can predict the local fluid properties but also lack the ability to resolve the large deformation and fragmentation of the free surface.

SPH has already been successfully used to model free surface deformation and local fluid pressures due to the water entry of a two-dimensional wedge (Oger et al., 2005). Current three-dimensional SPH simulations of ship slamming are of low resolution and have not accurately modelled the local fluid pressure distribution or the loads on the vessel (Kalis, 2007). Therefore in order to predict slamming loads on three-dimensional hulls, this thesis employs a 2D + t method. Individual two-dimensional cross-sections are modelled at good resolution and then combined to give an indication of the loads experienced by the bow during a slam event.

Chapter 3

Smoothed Particle Hydrodynamics

The following is a detailed introduction to the mesh-free lagrangian method Smoothed Particle Hydrodynamics (SPH). Originally developed independently by Lucy (1977) and Gingold and Monaghan (1977), the heart of the method is a numerical interpolation governed by a smoothing function known as the kernel (Section 3.1). The interpolation is a key element of the SPH governing equations which are defined in Section 3.2 and corrected for numerical stability in Section 3.3.

Section 3.4 summarises a number of time stepping techniques for evolving the properties of the fluid particles, with particular emphasis placed on the modified Euler predictor-corrector scheme. An overview of the nearest neighbouring particle searching techniques (essential to the interpolation) is included in Section 3.5, followed by a discussion on the treatment of both the free surface and solid wall boundaries encountered in the latter chapters of the thesis (Section 3.6).

The SPH code utilised in this thesis is a blend of all of the elements described in this chapter. A guide to the implementation of the SPH code can be found in Section 3.7.

3.1 SPH integral interpolation

3.1.1 SPH interpolation in the continuum

Smoothed Particle Hydrodynamics is an integral interpolation method which uses the values of a function at a set of disordered points represented by particles to determine its value at any arbitrary point $\mathbf{r}$ in the space Ω.

The interpolation of any given function f is based on the expression,

$$f(\mathbf{r}) = \int_{\Omega} f(\mathbf{r}')\delta(\mathbf{r} - \mathbf{r}')d\mathbf{r}' \tag{3.1}$$

where $\delta(\mathbf{r} - \mathbf{r}')$ is the Dirac delta function which has the following properties:

$$\delta(\mathbf{r} - \mathbf{r}') = \begin{cases} \infty, & \mathbf{r} = \mathbf{r}' \\ 0, & \mathbf{r} \neq \mathbf{r}' \end{cases} \tag{3.2}$$

$$\int \delta(\mathbf{r} - \mathbf{r}')d\mathbf{r}' = 1 \tag{3.3}$$

The approximation of a given function $\langle f(\mathbf{r}) \rangle$ at the point of interest $\mathbf{r}$ is exact when utilising the Dirac delta function. In order to encompass a number of particles in the region surrounding the point of interest a slightly broader smoothing function or kernel $W(\mathbf{r} - \mathbf{r}'; h)$ is implemented.

$$\langle f(\mathbf{r}) \rangle = \int_{\Omega} f(\mathbf{r}')W(\mathbf{r} - \mathbf{r}'; h)d\mathbf{r}' \tag{3.4}$$
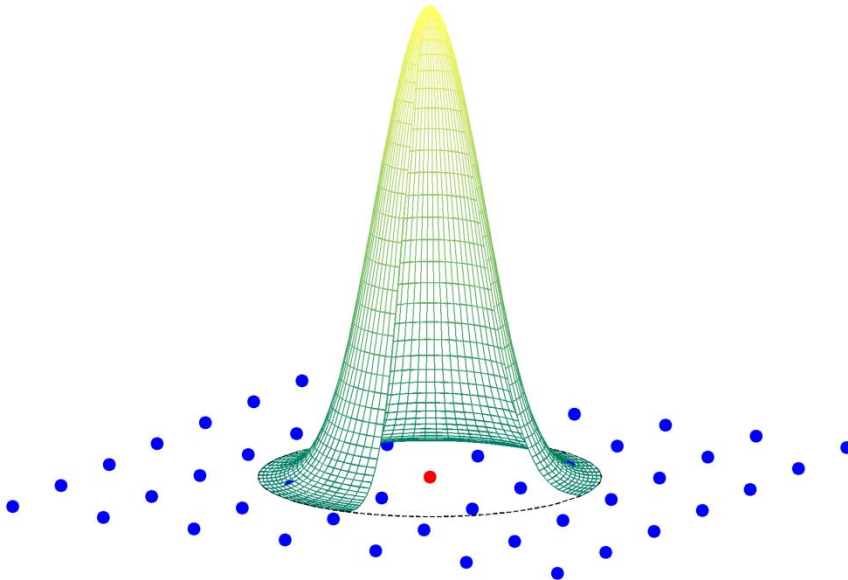
Figure 3.1 – The properties of a particle of interest (red) are determined
from the properties of its nearest neighbours (blue). The kernel, or
smoothing function, determines the level of influence that each
neighbouring particle has on the particle of interest.

The kernel is chosen such that as h - a measure of the support of $W(\mathbf{r} - \mathbf{r}'; h)$, commonly termed the *smoothing length* - approaches zero, the kernel function tends towards a Dirac delta function. There are no formal restrictions on the choice of kernel, however in practice a number of requirements are necessary in order to correctly reproduce a function at any given point. For mathematical simplicity and computational efficiency, SPH kernels are characterised by a compact support defined by equation (3.5),

$$W(\mathbf{r} - \mathbf{r}'; h) = 0 \quad if \;\; |\mathbf{r} - \mathbf{r}'| \geq \kappa h \tag{3.5}$$

where κ is typically set to 2 or 3 depending on the type of kernel in use (see Section 3.1.4). Within the compact support the kernel must be positive and normalised to 1 (3.6) in order to ensure the reproduced function is formed with a physically meaningful result.

$$\int W(\mathbf{r} - \mathbf{r}'; h) d\mathbf{r}' = 1 \tag{3.6}$$

The kernel must also monotonically decrease away from $\mathbf{r}$, guaranteeing the level of influence of a neighbouring particle reduces as the separation between the pair increases. It is equally important to make certain the kernel is an even function so equally spaced particle pairs will interact symmetrically. This also enables the discrete integral approximations to be simplified when using a smoothing length of constant size.

The gradient in one dimension of any function can also be reproduced via a valid kernel and the integral interpolant, similar to equation (3.4). In the approximation of the gradient, the differential acts only on the kernel,

$$\langle \frac{\partial f}{\partial x} \rangle = \int_{\Omega} f(\mathbf{r}') \frac{\partial W}{\partial x} (\mathbf{r} - \mathbf{r}'; h) d\mathbf{r}' \tag{3.7}$$

Rewriting (3.7) with the partial differential of $(\mathbf{r} - \mathbf{r}'; h)$ over x' instead of x gives,

$$\langle \frac{\partial f}{\partial x} \rangle = - \int_{\Omega} f(\mathbf{r}') \frac{\partial W}{\partial x'} (\mathbf{r} - \mathbf{r}'; h) d\mathbf{r}' \tag{3.8}$$

In multiple dimensions, the approximation of the gradient of the given function $f(\mathbf{r})$ can be written,

$$\langle \nabla f(\mathbf{r}) \rangle = \nabla_{\mathbf{r}} \int_{\Omega} f(\mathbf{r}') W(\mathbf{r} - \mathbf{r}'; h) d\mathbf{r}' \qquad (3.9)$$

Applying Gauss' theorem to the integral interpolant in equation (3.9) gives,

$$\langle \nabla f(\mathbf{r}) \rangle = \int_{\partial\Omega} f(\mathbf{r}') W(\mathbf{r} - \mathbf{r}'; h) \mathbf{n} dS - \int_{\Omega} f(\mathbf{r}') \nabla_{\mathbf{r}'} W(\mathbf{r} - \mathbf{r}'; h) d\mathbf{r}' \qquad (3.10)$$

where $\partial\Omega$ represents the surface of the problem domain. This approximation is simplified by ignoring the surface integral, assuming the kernel with compact support does not overlap any boundaries of the space Ω,

$$\langle \nabla f(\mathbf{r}) \rangle = - \int_{\Omega} f(\mathbf{r}') \nabla_{\mathbf{r}'} W(\mathbf{r} - \mathbf{r}'; h) d\mathbf{r}' \qquad (3.11)$$

Here, the gradient operator has been transferred from the function and now acts only on the kernel. Furthermore, the kernel is an even function which leads to,

$$\langle \nabla f(\mathbf{r}) \rangle = \nabla_{\mathbf{r}} \int_{\Omega} f(\mathbf{r}') W(\mathbf{r} - \mathbf{r}'; h) d\mathbf{r}' = \nabla \langle f(\mathbf{r}) \rangle \qquad (3.12)$$

Likewise the divergence of a vector function $\mathbf{F}$ can also be expressed as a product of the original function and the gradient of the kernel. Starting with the simple interpolation for the divergence of $\mathbf{F}$,

$$\langle \nabla \cdot \mathbf{F}(\mathbf{r}) \rangle = \nabla_{\mathbf{r}} \cdot \int_{\Omega} \mathbf{F}(\mathbf{r}') W(\mathbf{r} - \mathbf{r}'; h) d\mathbf{r}' \qquad (3.13)$$

and then applying the divergence theorem gives,

$$\langle \nabla \cdot \mathbf{F}(\mathbf{r}) \rangle = \int_{\partial\Omega} \mathbf{F}(\mathbf{r}') W(\mathbf{r} - \mathbf{r}'; h) \cdot \mathbf{n} dS - \int_{\Omega} \mathbf{F}(\mathbf{r}') \cdot [\nabla_{\mathbf{r}'} W(\mathbf{r} - \mathbf{r}'; h)] d\mathbf{r}'$$

Once again the surface integral is eliminated assuming the compact support does not overlap any boundaries,

$$\langle \nabla \cdot \mathbf{F}(\mathbf{r}) \rangle = - \int_{\Omega} \mathbf{F}(\mathbf{r}') \cdot [\nabla_{\mathbf{r}'} W(\mathbf{r} - \mathbf{r}'; h)] d\mathbf{r}' \qquad (3.14)$$

Similar to equation (3.11) for the gradient of any function, the gradient operator for the divergence of a vector field now acts only on the kernel, considerably simplifying the approximation.

3.1.2 Discrete SPH interpolation

In practice, the continuum approach to the SPH interpolation is not appropriate as the fluid domain is divided into a set of discrete particles. Replacing the integrand in equation (3.4) with a summation allows for the approximation of the function f over a set of disordered particles in the space Ω,

$$\langle f(\mathbf{r}) \rangle = \sum_{\Omega} f(\mathbf{r}')W(\mathbf{r} - \mathbf{r}'; h)d\mathbf{r}' \tag{3.15}$$

By implementing a kernel with compact support the approximation becomes,

$$\langle f(\mathbf{r}_a) \rangle = \sum_{b=1}^{N_b} f(\mathbf{r}_b)W(\mathbf{r}_a - \mathbf{r}_b; h)dV_b \tag{3.16}$$

where N_b is the total number of neighbouring particles. Equation (3.16) can also be written,

$$\langle f(\mathbf{r}_a) \rangle = \sum_{b=1}^{N_b} f(\mathbf{r}_b)\frac{m_b}{\rho_b}W_{ab} \tag{3.17}$$

where a is the particle of interest for which the function f is unknown, b is a neighbouring particle with mass m_b and density ρ_b, and W_{ab} is equivalent to $W(\mathbf{r}_a - \mathbf{r}_b; h)$. Despite the transformation to a discrete approximation, the kernel is still bound by the same rules as it was in the continuum, for example for regularly spaced data points,

$$\sum_{b=1}^{N_b} W_{ab}dV_b = 1 \tag{3.18}$$

Therefore the discrete derivative of the function $f(\mathbf{r}_a)$ is similar to the continuum

formulation (3.11),

$$\langle \nabla f(\mathbf{r}_a) \rangle = -\sum_{b=1}^{N_b} f(\mathbf{r}_b) \frac{m_b}{\rho_b} \nabla_a W_{ab} \qquad (3.19)$$

and for regularly spaced data points, the sum of the kernels gradient over all points within the compact support is zero.

$$\sum_{b=1}^{N_b} \nabla_a W_{ab} dV_b = \mathbf{0} \qquad (3.20)$$

Likewise the discrete divergence of $f(\mathbf{r}_a)$ from equation (3.14) becomes,

$$\langle \nabla \cdot \mathbf{F}(\mathbf{r}_a) \rangle = -\sum_{b=1}^{N_b} \frac{m_b}{\rho_b} \mathbf{F}(\mathbf{r}_b) \cdot [\nabla_a W_{ab}] \qquad (3.21)$$

3.1.3 Kernel corrections

Solving the discrete SPH equations for particles distributed evenly along a lattice results in a good approximation of the function $f(\mathbf{r}_a)$ or its derivatives at a given point. As most problems suited to SPH are of a transient, freely deforming nature, the particle nodes can easily become disordered, failing conditions such as (3.18). Spurious gradients and other numerical errors can propagate throughout the solution (Colagrossi, 2004) as the SPH equations become less consistent. This inconsistency arises because the derivative approximations do not necessarily converge to the continuum values as the separation of particle nodes approaches zero.

Establishing if the method is consistent requires an examination of the reproducing properties of the discrete interpolation. Belytschko et al. (1998) relates the convergence of the SPH method directly to its ability to reproduce a given polynomial of order k. As the original form of SPH suffers from a lack of zero order consistency when the particles are disordered, a number of techniques have been developed to ensure that it satisfies the required reproducing conditions.

Shepard (1968) introduced a two-dimensional approximation function for general use on disordered data. An SPH variant widely used in the filtering process is the following,

$$\langle f(\mathbf{r}_a) \rangle = \sum_{b=1}^{N_b} f(\mathbf{r}_b) \frac{m_b}{\rho_b} W^S(\mathbf{r}_a - \mathbf{r}_b; h) \tag{3.22}$$

where $W^S(\mathbf{r}_a - \mathbf{r}_b; h)$ is the Shepard filtered kernel, which attempts to renormalise the kernel through all the neighbouring data points c and is given by,

$$W^S(\mathbf{r}_a - \mathbf{r}_b; h) = \frac{W(\mathbf{r}_a - \mathbf{r}_b; h)}{\sum_{c=1}^{N_c} W(\mathbf{r}_a - \mathbf{r}_c; h) dV_c} \tag{3.23}$$

This allows functions such as $f(\mathbf{r}_a)$ to be reproduced exactly, as for disordered data points both (3.18) and (3.20) are satisfied,

$$\sum_{b=1}^{N_b} W^S_{ab} dV_b = 1 \tag{3.24}$$

$$\sum_{b=1}^{N_b} \nabla_a W^S_{ab} dV_b = 0 \tag{3.25}$$

Dilts (1999) proposed a moving least squares (MLS) interpolation to restore consistency of any order to the SPH equations. At randomly distributed points in two dimensions, MLS interpolants exactly reproduce a set of polynomials given by,

$$\mathbf{p}(\mathbf{r})^T = [1, x, y, x^2, xy, \dots] \tag{3.26}$$

A linear approximation of the MLS interpolant can be obtained by introducing the operator $\beta(\mathbf{r}_a)$ such that,

$$W^{MLS}_{ab} = \beta(\mathbf{r}_a) \cdot \mathbf{p}(\mathbf{r}_b) W_{ab}$$

$$W^{MLS}_{ab} = [\beta_0(\mathbf{r}_a) + \beta_1(\mathbf{r}_a)(x_a - x_b) + \beta_2(\mathbf{r}_a)(y_a - y_b)] W_{ab} \tag{3.27}$$

where Belytschko (1998) has defined the two dimensional first order operator $\beta(\mathbf{r}_a)$,

$$\beta(\mathbf{r}_a) = \begin{bmatrix} \beta_0(\mathbf{r}_a) \\ \beta_1(\mathbf{r}_a) \\ \beta_2(\mathbf{r}_a) \end{bmatrix} \tag{3.28}$$

Designed to correctly reproduce linear functions while satisfying (3.18) and (3.20), the actual values of the operator $\beta(\mathbf{r}_a)$ are established from the solution of the following expression for each data point,

$$\beta(\mathbf{r}_a) = \mathbf{A}^{-1}(\mathbf{r}_a) \begin{bmatrix} 1 \\ 0 \\ 0 \end{bmatrix} \tag{3.29}$$

where for a first order approximation, $\mathbf{A}(\mathbf{r}_a)$ is given by,

$$\mathbf{A}(\mathbf{r}_a) = \sum_{b=1}^{N_b} \mathbf{p}(\mathbf{r}_b)\mathbf{p}(\mathbf{r}_b)^{\mathrm{T}} W_{ab} dV_b \tag{3.30}$$

$$\mathbf{A}(\mathbf{r}_a) = \sum_{b=1}^{N_b} \begin{bmatrix} 1 & x_a - x_b & y_a - y_b \\ x_a - x_b & (x_a - x_b)^2 & (x_a - x_b)(y_a - y_b) \\ y_a - y_b & (x_a - x_b)(y_a - y_b) & (y_a - y_b)^2 \end{bmatrix} W_{ab} dV_b$$

Implementing the improved MLS kernel produces consistent approximations of any given field and its spatial derivatives (Dilts, 1999). From (3.19), the consistency of the gradient of any function can be improved by exchanging the original kernel with the MLS kernel,

$$\langle \nabla f(\mathbf{r}_a) \rangle = \sum_{b=1}^{N_b} f(\mathbf{r}_b) \nabla_a W_{ab}^{MLS} dV_b \tag{3.31}$$

To calculate the gradient of the MLS kernel, it is split into a vector consisting of both partial derivatives in two dimensions.

$$\nabla_a W_{ab}^{MLS} = \begin{bmatrix} \dfrac{\partial}{\partial x} W_{ab}^{MLS} \\ \dfrac{\partial}{\partial y} W_{ab}^{MLS} \end{bmatrix} \tag{3.32}$$

Colagrossi (2004) demonstrated that if the kernel is assumed to be Gaussian, the vector can be rewritten,

$$\nabla_a W_{ab}^{MLS} = \begin{bmatrix} \beta_x(\mathbf{r}_a) \cdot \mathbf{p}(\mathbf{r}_b) W_{ab} \\ \beta_y(\mathbf{r}_a) \cdot \mathbf{p}(\mathbf{r}_b) W_{ab} \end{bmatrix} \tag{3.33}$$

where,

$$\begin{aligned} \beta_x(\mathbf{r}_a) &= \begin{bmatrix} \beta_3(\mathbf{r}_a) \\ \beta_4(\mathbf{r}_a) \\ \beta_5(\mathbf{r}_a) \end{bmatrix} \\ \beta_y(\mathbf{r}_a) &= \begin{bmatrix} \beta_6(\mathbf{r}_a) \\ \beta_7(\mathbf{r}_a) \\ \beta_8(\mathbf{r}_a) \end{bmatrix} \end{aligned} \tag{3.34}$$

By performing the dot product on each component of (3.33), the partial derivatives of the MLS corrected kernel can be expressed as,

$$\frac{\partial}{\partial x} W_{ab}^{MLS} = [\beta_3(\mathbf{r}_a) + \beta_4(\mathbf{r}_a)(x_a - x_b) + \beta_5(\mathbf{r}_a)(y_a - y_b)]W_{ab}$$

$$\tag{3.35}$$

$$\frac{\partial}{\partial y} W_{ab}^{MLS} = [\beta_6(\mathbf{r}_a) + \beta_7(\mathbf{r}_a)(x_a - x_b) + \beta_8(\mathbf{r}_a)(y_a - y_b)]W_{ab}$$

The elements of $\beta_x(\mathbf{r}_a)$ and $\beta_y(\mathbf{r}_a)$ are then solved using the same matrix operation as described in (3.29) and (3.30), but with one minor change to the right hand side. This operation ultimately ensures that equation (3.20) is satisfied for disordered data points when the MLS correction is put into practice.

$$\beta_x(\mathbf{r}_a) = \mathbf{A}^{-1}(\mathbf{r}_a)\begin{bmatrix} 0 \\ 1 \\ 0 \end{bmatrix}; \qquad \beta_y(\mathbf{r}_a) = \mathbf{A}^{-1}(\mathbf{r}_a)\begin{bmatrix} 0 \\ 0 \\ 1 \end{bmatrix} \tag{3.36}$$

Higher orders of completeness can be achieved using a similar technique for both the field and its spatial derivatives. Second order and higher MLS kernel corrections have not been implemented in this thesis, but detailed derivations can be found in Pakozdi (2008) and Belytschko et al. (1998).

3.1.4 Kernel functions

Historically, SPH authors have used a variety of kernel functions ranging from the simple Gaussian kernel through to complex 3rd and 5th order spline functions. In the original publication by Gingold and Monaghan (1977), a number of typical kernel functions were proposed for use including the Gaussian kernel,

$$W(\mathbf{r} - \mathbf{r}', h) = \frac{\sigma}{h^n} e^{-q^2} \tag{3.37}$$

where n denotes the number of dimensions, the normalisation constant $\sigma = 1/\left(\sqrt{\pi}\right)^n$ and $q = |\mathbf{r} - \mathbf{r}'|/h$. The interpolation kernel must be accurate, smooth and computationally efficient for it to be viable in SPH (Monaghan and Lattanzio, 1985). The Gaussian kernel while accurate and smooth, is not computationally efficient as it suffers from a lack of compact support.

Early in the development of SPH considerable effort was focused on determining a suitable replacement for the Gaussian kernel that naturally had compact support while closely resembling its predecessor. By far one of the most commonly used kernels is the piecewise cubic spline (see Figure 3.2), with continuous first and second derivatives (Monaghan, 2005).
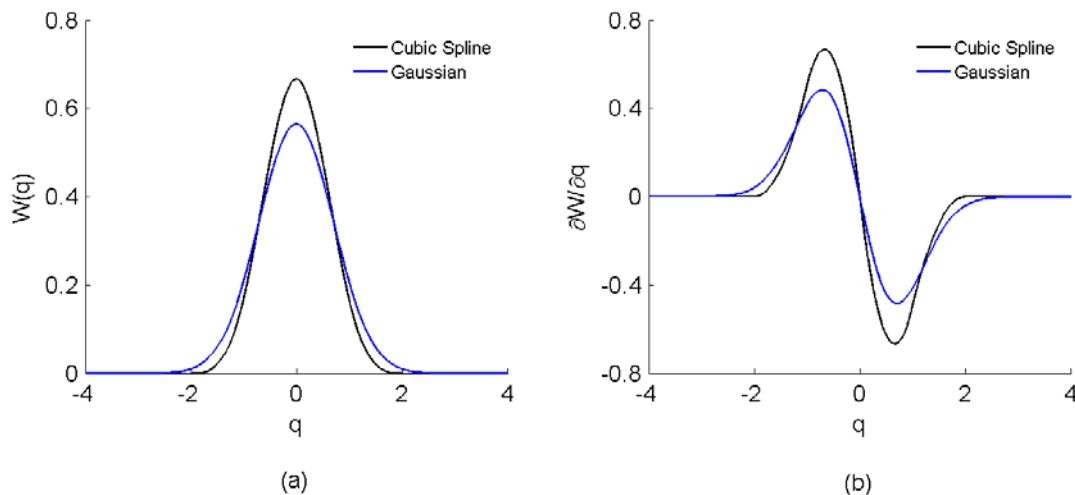
Figure 3.2 – Comparison between the cubic spline and Gaussian kernels (a) and their derivatives (b).

Equation (3.38) is an example of a third order spline function.

$$W(\mathbf{r} - \mathbf{r}', h) = \frac{\sigma}{h^n} \begin{cases} (2 - q)^3 - 4(1 - q)^3; & 0 \leq q \leq 1 \\ (2 - q)^3; & 1 < q \leq 2 \\ 0; & q > 2 \end{cases} \quad (3.38)$$

The normalisation constant σ varies with the number of dimensions n and has the value $1/6$ in one dimension, $15/14\pi$ in two dimensions and $1/4\pi$ in three dimensions. Morris et al. (1997) noted that the stability of SPH was strongly dependent on the derivative of the kernel, which for common applications of the cubic spline results in density variations of approximately 1%.

Employing higher-order spline functions that more closely approximate a Gaussian function reduces the instabilities related to the kernel. Fifth and seventh order spline functions have superior stability to the cubic spline but also have a larger compact support, therefore slightly increasing the computational cost.

The fifth order spline function is given by,

$$W(\mathbf{r} - \mathbf{r}', h) = \frac{\sigma}{h^n} \begin{cases} (3 - q)^5 - 6(2 - q)^5 + 15(2 - q)^5; & 0 \leq q \leq 1 \\ (3 - q)^5 - 6(2 - q)^5; & 1 < q \leq 2 \\ (3 - q)^5; & 2 < q \leq 3 \\ 0; & q > 3 \end{cases} \quad (3.39)$$

To produce a more stable kernel Landrini et al. (2003) introduced a cut-off limit to the Gaussian at some q value δ. The kernel is set to zero at this point by subtracting the value $W(\delta)$ from the regular Gaussian function (3.37), in effect not allowing any operations between particle pairs if their separation is greater than δ or less than $-\delta$ (see Figure 3.3a). Finally, the new cut-off Gaussian kernel is renormalised to 1 (see Figure 3.3b) in order to satisfy the kernel conditions described in Section 3.1.1.

$$W(\mathbf{r} - \mathbf{r}', h) = \frac{\sigma}{h^n} e^{-q^2} - W(\delta) \quad (3.40)$$
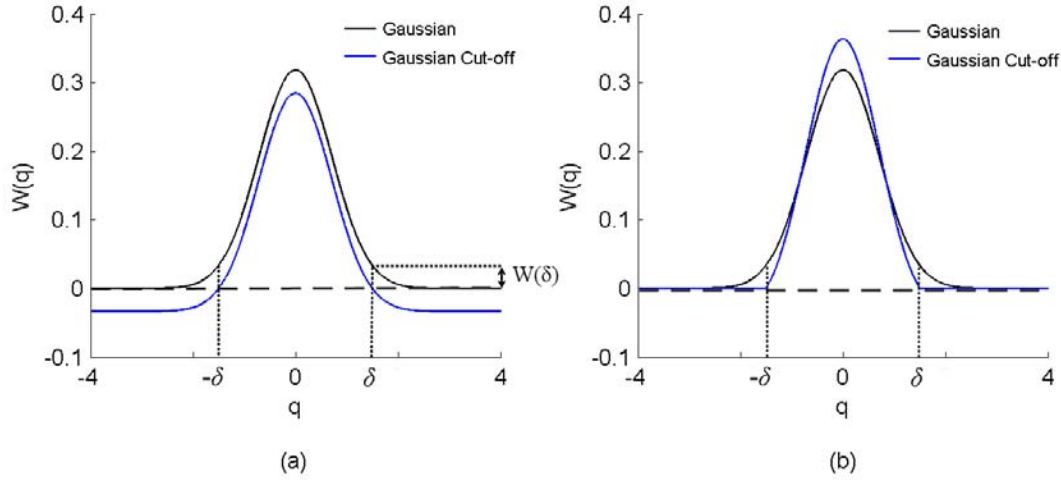
Figure 3.3 – The Gaussian cut-off kernel prior to (a) and post renormalisation (b). To demonstrate the vertical shift of the Gaussian function, the value of δ has been set at 1.5.

Landrini et al. (2003) noted that the Gaussian kernel and its first derivative reduce to less than 0.05% of their maxima near $q = 3$. The relative influence of any particle beyond this separation on the particle of interest is minimal and so the cut-off limit δ was set to 3.

Following (3.40), the value of the kernel at $\delta = 3$ is subtracted from the original to give,

$$W(\mathbf{r} - \mathbf{r}', h) = \frac{\sigma}{h^n}\left(e^{-q^2} - e^{-\delta^2}\right) \tag{3.41}$$

$$W(\mathbf{r} - \mathbf{r}', h) = \frac{\sigma}{h^n}\left(e^{-q^2} - e^{-9}\right) \tag{3.42}$$

Renormalising to find the constant σ in two dimensions yields,

$$\sigma = \frac{1}{2\pi \int_0^\delta q\left(e^{-q^2} - e^{-\delta^2}\right)dq} \tag{3.43}$$

which reduces to:

$$\sigma = \frac{1}{\pi\left(1 - (1 + \delta^2)e^{-\delta^2}\right)}$$

$$\sigma = \frac{1}{\pi(1 - 10e^{-9})} \tag{3.44}$$

Pakozdi (2008) performed a detailed error analysis of the modified Gaussian cut-off kernel in one, two and three dimensions verifying the validity of the approach.

3.2 SPH governing equations

The discrete SPH governing equations are derived using a variety of approaches, yet they all stem from the Euler equations for the rates of change of velocity, density and position. The discrete forms of the equations are dependent on the assumptions and simplifications made.

The motion of each particle is prescribed by the acceleration vector $\mathbf{a}_a$ which is governed by Newton's second law of motion,

$$\mathbf{a}_a = \frac{\mathbf{F}_a}{m_a} + \frac{\mathbf{T}_a}{m_a} \tag{3.45}$$

where $\mathbf{F}_a$ is the sum of the external forces acting on particle a and $\mathbf{T}_a$ represents the total internal force, typically due to the stress in the fluid.

3.2.1 Continuity equation

Early in the development of SPH, the equation for mass conservation was a simple summation of the density field surrounding the particle or point of interest,

$$\rho_a = \sum_{b=1}^{N_b} \rho_b W_{ab} dV_b \tag{3.46}$$

where W_{ab} is equivalent to $W(\mathbf{r} - \mathbf{r}_b, h)$ with units of inverse volume and $dV_b = m_b/\rho_b$. This approach was widely used for astrophysical problems where physical external boundaries were not of great importance. Despite the intrinsic conservation

of mass, the interpolation is poor near fluid boundaries due to a loss of mass density. Rewriting (3.46) yields the pure conservation of mass equation,

$$\rho_a = \sum_{b=1}^{N_b} m_b W_{ab} \tag{3.47}$$

The continuity equation can also be used to conserve mass through the rate of change of density. The Euler equation for the rate of change of density with time is given by,

$$\frac{d\rho}{dt} = -\rho \nabla \cdot \mathbf{u} \tag{3.48}$$

Noting the discrete SPH formulation for the velocity of a particle,

$$\mathbf{u}_a = \sum_{b=1}^{N_b} \mathbf{u}_b W_{ab} dV_b \tag{3.49}$$

The variation in density with respect to time can be found by substituting the discrete velocity formulation into the continuity equation,

$$\frac{d\rho_a}{dt} = -\rho_a \boldsymbol{\nabla}_a \cdot \sum_{b=1}^{N_b} \mathbf{u}_b W_{ab} dV_b \tag{3.50}$$

Applying the gradient operator to the summation yields,

$$\frac{d\rho_a}{dt} = -\rho_a \sum_{b=1}^{N_b} dV_b \mathbf{u}_b \cdot \boldsymbol{\nabla}_a W_{ab} \tag{3.51}$$

Alternatively, the right hand side of the continuity equation (3.48) can be expressed by use of the divergence theorem as,

$$\begin{aligned}
-\rho \nabla \cdot \mathbf{u} &= -(\mathbf{u} \cdot \nabla \rho + \rho \nabla \cdot \mathbf{u} - \mathbf{u} \cdot \nabla \rho) \\
-\rho \nabla \cdot \mathbf{u} &= -(\nabla \cdot (\rho \mathbf{u}) - \mathbf{u} \cdot \nabla \rho)
\end{aligned} \tag{3.52}$$

Using the above identity the discrete integral interpolant becomes:

$$-\rho \nabla \cdot \mathbf{u} = -\sum_{b=1}^{N_b} \frac{m_\mathbf{b}}{\rho_\mathbf{b}} \rho_b \mathbf{u}_b \cdot \nabla_a W_{ab} + \mathbf{u}_a \sum_{b=1}^{N_b} \frac{m_\mathbf{b}}{\rho_\mathbf{b}} \rho_b \nabla_a W_{ab} \tag{3.53}$$

which can be written,

$$\frac{d\rho_a}{dt} = -\sum_{b=1}^{N_b} m_b (\mathbf{u}_a - \mathbf{u}_b) \cdot \nabla_a W_{ab} \tag{3.54}$$

Therefore the rate of change of density with time can be expressed as a summation of the product of the neighbouring particles change in volume and velocity in (3.51) or as a summation of the mass and relative difference in velocity (3.54). Despite the difference, both equations ensure that the divergence of the velocity field is zero if the fluid velocity is constant.

3.2.2 Momentum equation

Like the discrete density formulation, the change in momentum of an individual particle can be expressed in multiple ways. The Euler equation for the rate of change of velocity is given by,

$$\frac{d\mathbf{u}}{dt} = -\frac{1}{\rho}\nabla P + \mathbf{g} \tag{3.55}$$

The original formulation of the SPH momentum equation is discretised (3.55) directly by writing,

$$\frac{d\mathbf{u}_a}{dt} = -\frac{1}{\rho_a}\sum_{b=1}^{N_b} P_b \nabla_a W_{ab} dV_b \tag{3.56}$$

Monaghan (2005) demonstrated that the acceleration in (3.56) does not conserve linear or angular momentum. Performing the calculation above on a system of two particles, it can be shown that the force on particle *a* is not equal and opposite to the force on particle *b*, thereby contradicting a fundamental law of motion. This problem can be alleviated by symmetrising (3.56) using the following vanishing summation,

$$\nabla 1 = \int_{\Omega} 1 \nabla W(\mathbf{r} - \mathbf{r}', h) d\mathbf{r}' \approx \sum_{b=1}^{N_b} V_b \nabla_a W_{ab} \approx 0 \tag{3.57}$$

41

Adding the product of the zero term and P_a/ρ_a to the right hand side of (3.57) yields the symmetric expression for the acceleration of particle a.

$$\frac{d\mathbf{u}_a}{dt} = -\frac{1}{\rho_a}\sum_{b=1}^{N_b} P_b\nabla_a W_{ab}dV_b + \frac{1}{\rho_a}\sum_{b=1}^{N_b} P_a\nabla_a W_{ab}dV_b \tag{3.58}$$

$$\frac{d\mathbf{u}_a}{dt} = -\frac{1}{\rho_a}\sum_{b=1}^{N_b}(P_a + P_b)\nabla_a W_{ab}dV_b \tag{3.59}$$

Therefore the total internal force on particle a can be expressed as,

$$\mathbf{T}_a = -\sum_{b=1}^{N_b}\frac{m_a}{\rho_a}(P_a + P_b)\nabla_a W_{ab}dV_b \tag{3.60}$$

Another approach described by Gingold and Monaghan (1982) obtained a slightly different symmetric expression for the acceleration of particle a. From the Euler equation for acceleration (3.55),

$$\frac{1}{\rho}\nabla P = \frac{\rho\nabla P}{\rho^2} \tag{3.61}$$

$$\frac{P\nabla\rho}{\rho^2} + \frac{1}{\rho}\nabla P = \frac{\rho\nabla P}{\rho^2} + \frac{P\nabla\rho}{\rho^2} \tag{3.62}$$

$$\frac{1}{\rho}\nabla P - \frac{P\nabla\rho}{\rho^2} = \frac{\rho\nabla P - P\nabla\rho}{\rho^2} \tag{3.63}$$

Rearranging (3.63) and applying the quotient rule in reverse gives,

$$\frac{1}{\rho}\nabla P = \nabla\frac{P}{\rho} + \frac{P}{\rho^2}\nabla\rho \tag{3.64}$$

Applying the discrete SPH interpolant to (3.64),

$$\frac{1}{\rho_a}\nabla P_a = \sum_{b=1}^{N_b}\frac{m_b}{\rho_b}\frac{P_b}{\rho_b}\nabla_a W_{ab} + \frac{P_a}{\rho_a^2}\sum_{b=1}^{N_b}\frac{m_b}{\rho_b}\rho_b\nabla_a W_{ab} \tag{3.65}$$

yields the final formulation of the Euler equation for acceleration in the discrete SPH

form,

$$\frac{d\mathbf{u}_a}{dt} = -\sum_{b=1}^{N_b} m_b \left(\frac{P_a}{\rho_a^2} + \frac{P_b}{\rho_b^2}\right) \nabla_a W_{ab} \qquad (3.66)$$

Performing the calculation on a system of two particles, the force on particle b is equal and opposite of that on a. Consequently, linear and angular momentum are conserved. Therefore, the total internal force using the Euler equation can be expressed as,

$$\mathbf{T}_a = -\sum_{b=1}^{N_b} m_a m_b \left(\frac{P_a}{\rho_a^2} + \frac{P_b}{\rho_b^2}\right) \nabla_a W_{ab} \qquad (3.67)$$

3.2.3 Discrete SPH variational consistency

The discrete SPH equations for density and momentum described in the previous section may only be used in certain combinations. Bonet and Lok (1999) performed a variational analysis on a range of combinations of governing equations and found that if they were applied in an inconsistent manner, the form of the simulation produced was quite poor. It is therefore important to verify that the arrangement of momentum and density equations used in the present SPH algorithm is consistent.

The variation, or directional derivative, describing the gradient of any function $f(\mathbf{r})$ at $\mathbf{r}$ is given by,

$$\boldsymbol{D}f(\mathbf{r})[\delta\mathbf{u}] = \frac{d}{d\varepsilon} f(\mathbf{r} - \varepsilon\delta\mathbf{u}) \Big|_{\varepsilon = 0} \qquad (3.68)$$

where $\delta\mathbf{u}$ is the virtual velocity field that describes the possible movement of a set of fluid particles in the small virtual time period ε. When the virtual velocity field matches that of the actual velocity field, the time derivative of the function f can be obtained.

$$\frac{df(\mathbf{r})}{dt} = \boldsymbol{D}f(\mathbf{r})[\delta\mathbf{u}] \qquad (3.69)$$

To ensure the SPH equations of motion are consistent with variation, the internal energy of the system is evaluated following Bonet and Lok (1999). Let R_V be the volume ratio between the current and initial state of the fluid,

$$R_V = \frac{V}{V_0} = \frac{\rho_0}{\rho} \tag{3.70}$$

For adiabatic processes, the pressure can be evaluated by differentiating the energy per unit volume stored in the system $U(R_V)$ with respect to the volume ratio such that,

$$P = \frac{dU}{dR_V} \tag{3.71}$$

Following the chain rule equation (3.71) becomes,

$$P = \frac{dU}{d\rho} \frac{d\rho}{dR_V}$$

$$\frac{dU}{d\rho} = P \frac{dR_V}{d\rho}$$

$$\frac{dU}{d\rho} = -P \frac{\rho_o}{\rho^2} \tag{3.72}$$

The total internal energy of the system can now be expressed as a summation of the stored energy per unit volume multiplied by the volume of each individual fluid particle,

$$Q_{int}(\mathbf{r}) = \sum_{a=1}^{N} V_{0a} U(R_{va}) \tag{3.73}$$

The variation of the internal energy is then calculated by replacing $f(\mathbf{r})$ in equation (3.68) with Q_{int},

$$\boldsymbol{D}Q_{int}[\delta \mathbf{u}] = \boldsymbol{D} \sum_{a=1}^{N} V_{0a} U(R_{va}) [\delta \mathbf{u}] \tag{3.74}$$

Applying the directional derivative along **r** enables (3.74) to be expressed as,

$$\boldsymbol{D}Q_{int}[\delta\mathbf{u}] = \sum_{a=1}^{N} V_{0a} \frac{dU(R_{va})}{d\mathbf{r}}[\delta\mathbf{u}]$$

$$\boldsymbol{D}Q_{int}[\delta\mathbf{u}] = \sum_{a=1}^{N} V_{0a} \frac{dU(R_{va})}{d\rho_a}\frac{d\rho_a}{d\mathbf{r}}[\delta\mathbf{u}]$$

$$\boldsymbol{D}Q_{int}[\delta\mathbf{u}] = -\sum_{a=1}^{N} V_{0a}P_a \frac{\rho_{0a}}{\rho_a^2}\frac{d\rho_a}{d\mathbf{r}}[\delta\mathbf{u}]$$

$$\boldsymbol{D}Q_{int}[\delta\mathbf{u}] = -\sum_{a=1}^{N} m_a \frac{P_a}{\rho_a^2}\boldsymbol{D}\rho_a\,[\delta\mathbf{u}] \tag{3.75}$$

The directional derivative on the right hand side of (3.75) now acts only upon the density of a given fluid particle a. In order to find a momentum equation that is consistent with the traditional summation approach for determining the density, ρ_a is replaced with (3.47) and the directional derivate of the density, $\boldsymbol{D}\rho_a[\delta\mathbf{u}]$, can be written,

$$\boldsymbol{D}\rho_a[\delta\mathbf{u}] = \sum_{b=1}^{N} m_b \frac{1}{r_{ab}}\frac{dW}{dr}(\mathbf{r}_a - \mathbf{r}_b)[\delta\mathbf{u}]$$

$$\boldsymbol{D}\rho_a[\delta\mathbf{u}] = \sum_{b=1}^{N} m_b \boldsymbol{\nabla}_a W_{ab}\,[\delta\mathbf{u}] \tag{3.76}$$

Substituting the above equation in to (3.75) gives,

$$\boldsymbol{D}Q_{int}[\delta\mathbf{u}] = -\sum_{a=1}^{N} m_a \frac{P_a}{\rho_a^2}\sum_{b=1}^{N} m_b \boldsymbol{\nabla}_a W_{ab}\,[\delta\mathbf{u}]$$

$$\boldsymbol{D}Q_{int}[\delta\mathbf{u}] = -\sum_{a=1}^{N}\sum_{b=1}^{N} m_a m_b \frac{P_a}{\rho_a^2}\boldsymbol{\nabla}_a W_{ab}\,(\delta\mathbf{u}_a - \delta\mathbf{u}_b)$$

which equates to,

$$\boldsymbol{D}Q_{int}[\delta\mathbf{u}] = -\sum_{a,b}^{N} m_a m_b \frac{P_a}{\rho_a^2}\boldsymbol{\nabla}_a W_{ab}\delta\mathbf{u}_a + \sum_{a,b}^{N} m_a m_b \frac{P_a}{\rho_a^2}\boldsymbol{\nabla}_a W_{ab}\delta\mathbf{u}_b \tag{3.77}$$

The gradient of the kernel $\nabla_a W_{ab}$ is equal and opposite to $\nabla_b W_{ba}$, which results in the following,

$$DQ_{int}[\delta\mathbf{u}] = -\sum_{a=1}^{N}\sum_{b=1}^{N} m_a m_b \frac{P_a}{\rho_a^2} \nabla_a W_{ab}\,\delta\mathbf{u}_a$$
$$-\sum_{b=1}^{N}\sum_{a=1}^{N} m_b m_a \frac{P_b}{\rho_b^2} \nabla_b W_{ba}\,\delta\mathbf{u}_a \qquad (3.78)$$

Rearranging (3.78) yields the final expression for the directional derivative of the internal energy,

$$DQ_{int}[\delta\mathbf{u}] = \sum_{a=1}^{N}\left[-\sum_{b=1}^{N} m_a m_b \left(\frac{P_a}{\rho_a^2}+\frac{P_b}{\rho_b^2}\right)\nabla_a W_{ab}\right]\delta\mathbf{u}_a \qquad (3.79)$$

Including equation (3.67), the final expression for the directional derivative of the internal energy is,

$$DQ_{int}[\delta\mathbf{u}] = \sum_{a=1}^{N} \mathbf{T}_a\,\delta\mathbf{u}_a \qquad (3.80)$$

Therefore by taking the directional derivative of Q_{int} with respect to $\mathbf{r}$, an expression containing the internal force described by Gingold and Monaghan (1982), $\mathbf{T}_a$, is obtained. As a result the traditional SPH approach for calculating the density directly from the particle mass (equation 3.47) is said to be variationally consistent with the symmetric approach for determining the acceleration on a particle, equation (3.66).

Similarly, the variational approach can be used to determine which momentum equation should be implemented alongside the continuity equation. The continuum form of the continuity equation (3.48) can be rewritten in terms of the directional time derivative (3.69) by replacing the actual velocity of the SPH particle with the virtual velocity described in (3.68),

$$D\rho[\delta\mathbf{u}] = -\rho\nabla\cdot\delta\mathbf{u} \qquad (3.81)$$

Substituting this in to the variational derivative of the internal energy equation (3.75) gives,

$$DQ_{int}[\delta\mathbf{u}] = -\sum_{a=1}^{N} m_a \frac{P_a}{\rho_a^2} D\rho_a[\delta\mathbf{u}]$$

$$DQ_{int}[\delta\mathbf{u}] = -\sum_{a=1}^{N} m_a \frac{P_a}{\rho_a^2}(-\rho_a)\nabla_a[\delta\mathbf{u}] \tag{3.82}$$

Introducing the SPH equation for the divergence of the velocity field – a derivation of (3.54) - yields,

$$Q_{int}[\delta\mathbf{u}] = \sum_{a=1}^{N} m_a \frac{P_a}{\rho_a^2}(-\rho_a)\frac{1}{\rho_a}\sum_{b}^{N} m_b(\delta\mathbf{u}_a - \delta\mathbf{u}_b) \cdot \nabla_a W_{ab}$$

$$Q_{int}[\delta\mathbf{u}] = -\sum_{a=1}^{N} m_a \frac{P_a}{\rho_a^2}\sum_{b=1}^{N} m_b(\delta\mathbf{u}_a - \delta\mathbf{u}_b) \cdot \nabla_a W_{ab}$$

$$Q_{int}[\delta\mathbf{u}] = -\sum_{a,b}^{N} m_a m_b \frac{P_a}{\rho_a^2}\nabla_a W_{ab}\delta\mathbf{u}_a + \sum_{a,b}^{N} m_a m_b \frac{P_a}{\rho_a^2}\nabla_a W_{ab}\delta\mathbf{u}_b \tag{3.83}$$

which is identical to the previous variational analysis using the traditional direct density SPH approach (3.79). Therefore the final directional derivative of the internal energy equation is,

$$DQ_{int}[\delta\mathbf{u}] = \sum_{a=1}^{N}\left[-\sum_{b=1}^{N} m_a m_b \left(\frac{P_a}{\rho_a^2} + \frac{P_b}{\rho_b^2}\right)\nabla_a W_{ab}\right]\delta\mathbf{u}_a \tag{3.84}$$

This proves that the continuity equation is variationally consistent with the symmetrical momentum equation (3.64) described by Gingold and Monaghan (1982), as the term in the square parentheses is identical to the internal force (3.65). Pakozdi (2008) describes how the continuity equation approach for calculating the density of a fluid particle is also consistent with the direct discretisation of the Euler equation (3.57), however this form of the SPH momentum equation has not been implemented in this thesis and as such the variational analysis is not described here.

3.2.4 Equation of state

The speed of sound in seawater (a near incompressible fluid) is in most cases much greater than the maximum fluid flow velocity. This high sound speed demands a very small time step by the Courant–Friedrichs–Lewy condition (3.104), which in turn forces a long inefficient computation time (see Appendix A). To decrease the computation time the sound speed is reduced, in effect approximating the real fluid with one that is artificially more compressible. The approximation of the incompressible fluid is valid if the maximum fluid flow velocity is less than Mach 0.1 to prevent compression effects and it is implemented through a modified state equation.

Equation (3.85) is the equation of state used in most single phase SPH algorithms,

$$P_a = P_S \left(\left(\frac{\rho_a}{\rho_0} \right)^\gamma - 1 \right) \tag{3.85}$$

where the values of γ (typically 7, the same value as in the sea water equation of state) and the scale factor P_S are chosen so that the fluctuations in density are no more than 1% of the reference value ρ_0. The scale factor P_S is directly related to the sound speed, so in order to reduce the computation time P_S is then defined using the modified sound speed through (3.86).

$$P_S = \frac{c_s^2 \rho_0}{\gamma} \tag{3.86}$$

3.3 Numerical corrections essential for stability

Applying the pure SPH equations of motion to a system of disordered particles will in most cases lead to numerical drift and an inherent lack of stability. Consequently since the inception of SPH considerable effort has been placed on correcting the method in order to obtain physically accurate results. A number of the SPH corrections are discussed here.

3.3.1 Artificial viscosity

This expression introduces a small shear and bulk viscosity to the momentum equation (3.66) in order to simulate shock problems, but for small values of the

coefficients α and β, the artificial viscosity Π_{ab} (equation 3.88) simply stabilises the algorithm, particularly the global fluid motion. The momentum equation can now be expressed as,

$$\frac{d\mathbf{u}_a}{dt} = -\sum_{b=1}^{N_b} m_b \left(\frac{P_a}{\rho_a^2} + \frac{P_b}{\rho_b^2} + \Pi_{ab} \right) \nabla_a W_{ab} \qquad (3.87)$$

Where Π_{ab} is given by,

$$\Pi_{ab} = \begin{cases} \dfrac{-\alpha \bar{c}_{ab} \mu_{ab} + \beta \mu_{ab}^2}{\bar{\rho}_{ab}}, & \mathbf{u}_{ab} \cdot \mathbf{r}_{ab} < 0 \\ 0 & , & \mathbf{u}_{ab} \cdot \mathbf{r}_{ab} > 0 \end{cases} \qquad (3.88)$$

$$\mu_{ab} = \frac{h\mathbf{u}_{ab} \cdot \mathbf{r}_{ab}}{\mathbf{r}_{ab}^2 + \varepsilon_a h^2} \qquad (3.89)$$

The double subscripts ab in (3.88) and (3.89) represent the interaction between the particle of interest a and a neighbour b (e.g. the relative velocity $\mathbf{u}_{ab}$ and the average density $\bar{\rho}_{ab}$).

Typical values for α and β in problems not involving shocks are 0.01-0.10 and 0 respectively, but can be as high as 1.0 or 2.0 for complex shock simulations (Monaghan, 2005). Colagrossi and Landrini (2003) compared values of α in a range from 0.005 to 0.1 using a two-dimensional dam break and found 0.03 to be the most appropriate value, maintaining stability without introducing a considerable bulk fluid viscosity. The value of ε_a in (3.89) is small, typically 0.01, and is placed here to avoid a singularity in the unlikely event of the particle separation $\mathbf{r}_{ab}$ approaching zero. Landrini et al. (2003) modified the artificial viscous term by introducing a rate of strain tensor designed to reduce the generation of spurious entropy due to a disordered particle distribution and rotation in the velocity field. Colagrossi (2004) reported improved results with the new form however it has not been included in this thesis.

It should be noted that the magnitude of the artificial viscosity is dependent upon the fluid sound speed, which can potentially cause large fluid motion damping when using the aforementioned values of α and β (see Appendix A).

3.3.2 Tensile stability

Smoothed particle hydrodynamics carries with it an inherent tensile instability, which in certain situations can result in artificial clustering of fluid particles. Under normal positive pressure conditions, a repelling force is applied between fluid particles via the momentum equation. However, if the local fluid pressure drops below zero (where the zero datum pressure is typically atmospheric pressure) the particles can attract. This results in an instability which becomes evident when small groups of particles cluster together in a higher particle number density not reflected in the fluid density.

A number of attempts to counter this tensile instability have been published, including an introduction of dissipative terms by Randles and Libersky (1996). Monaghan (2000) described a repulsive term inspired by physical forces between the molecules of a fluid or solid in order to eliminate the possibility of artificial particle clustering. This repulsive force term $R_{ab}f_{ab}^k$ is included in the extended SPH momentum equation (3.87),

$$\frac{d\mathbf{u}_a}{dt} = -\sum_{b=1}^{N_b} m_b \left(\frac{P_a}{\rho_a^2} + \frac{P_b}{\rho_b^2} + \Pi_{ab} + R_{ab}f_{ab}^k \right) \nabla_a W_{ab} \tag{3.90}$$

The R_{ab} component of the repulsive force is related directly to the pressure and can be written,

$$R_{ab} = \begin{cases} 0.01 \left(\frac{P_a}{\rho_a^2} + \frac{P_b}{\rho_b^2} \right) ; & \text{if } P_a > 0 \text{ and } P_b > 0 \\ R_a + R_b ; & \text{otherwise} \end{cases} \tag{3.91}$$

where R_a and R_b are evaluated in a similar manner,

$$R_a = \begin{cases} \epsilon \left(\frac{P_a}{\rho_a^2} \right) ; & \text{if } P_a < 0 \\ 0 ; & \text{otherwise} \end{cases} \tag{3.92}$$

The value of R_b is obtained from (3.92) by replacing the pressure and density of particle a with that of particle b. A typical value chosen for ϵ is 0.2, but this may vary depending on the type of problem to be modelled (see Section 4.2). Equation (3.91) contains an expression for R_{ab} for use when both particles have a positive

pressure and is designed to prevent the development of linear particle groupings. The coefficient ϵ is in this case reduced to 0.01.

To complete the repulsive force, a second component directly related to the kernel, f_{ab} is introduced. This term is designed to increase as the separation between the two particles in the pair decreases and takes the form,

$$f_{ab} = \frac{W_{ab}}{W(r_0)} \tag{3.93}$$

where r_0 is the initial particle spacing in the region surrounding particle a. Monaghan (2000) suggests that for fluid dynamics simulations, f_{ab} be raised to the power k (3.90) forcing the term to decrease rapidly as the separation between the particle pair increases. In the present work k has been set to 4 as recommended by Monaghan (2000).

3.3.3   Reintialisation of the density field

Evolving the density field through the discrete SPH form of the continuity equation (3.54) does not exactly enforce consistency between the particle mass, volume and density (Colagrossi and Landrini, 2003). In regions where the compact support of the standard kernel is not entirely filled with particles – near solid boundaries or a free surface – the direct density approach (3.47) produces a density that is smaller than its value at the previous step in time. By calculating a reduced density value, the pressure at the same particle would be lower than expected and ultimately the entire velocity field would become corrupt.

The moving least squares approach described by Belytschko et al. (1998) and Dilts (1999) was implemented by Colagrossi and Landrini (2003) in a procedure designed to restore the consistency between particle mass, density and volume by periodically reinitialising the density field. Equation (3.47) was modified to include the MLS kernel described in Section 3.1.3,

$$\rho_a = \sum_{b=1}^{N_b} m_b W_{ab}^{MLS} \tag{3.94}$$

Colagrossi and Landrini (2003) applied the density reinitialisation procedure every 20 time steps to a free-surface dam break test problem (see Section 4.4) with only a slight increase in computation time reported. Results showed an improved, more regular pressure distribution and improved energy conservation when used in conjunction with the artificial viscosity (see Section 4.1).

3.3.4 Particle motion

The uncorrected SPH method does not include any limiting factors on the space occupied by a given particle which can give rise to the possibility of two or more particles occupying the same space. Penetration of neighbouring particles is a problem, particularly with high Mach number flows, and can quickly corrupt the density, pressure and velocity fields.

Monaghan (1989, 1994) proposed a solution, known as the XSPH variant, to the penetration problem by adding a correcting factor $\Delta \mathbf{u}_a$ to the rate of change of position (3.95). To maintain consistency, the new corrected velocity is carried though to the continuity equation.

$$\frac{d\mathbf{r}_a}{dt} = \mathbf{u}_a + \Delta \mathbf{u}_a \tag{3.95}$$

where

$$\Delta \mathbf{u}_a = \varepsilon_X \sum_{b=1}^{N_b} m_b \frac{(\mathbf{u}_b - \mathbf{u}_a)}{\bar{\rho}_{ab}} W_{ab} \tag{3.96}$$

It can be seen in (3.96) that the XSPH variant is summed over all neighbouring particles within the compact support of the kernel W_{ab} using the mean density of the particle pair $\bar{\rho}_{ab}$. Typically the constant ε_X is chosen to be 0.5, which is strong enough to encourage particles in the local area to move with a similar velocity. Monaghan (1994) states that the correction is not necessarily important for placid flows such as the free-surface dam-break (see Section 4.4) but does become critical for complex flows such as the formation of jets.

3.4 Time stepping

Like many other computational fluid dynamics techniques, the discrete SPH equations can be solved using a variety of different methods. As the equations of motion in SPH reduce to a set of ordinary differential equations, simple time stepping schemes such as the first order Euler method can be used for the solution.

While efficient in memory use, the first order Euler method can be quite unstable so Monaghan (1989) described an improved predictor-corrector Euler method which has been implemented in this thesis for its simplicity and improved accuracy. Other SPH authors (Colagrossi, 2004 and Pakozdi, 2008) have employed higher order Runge-Kutta schemes which allow for larger time steps at the expense of computational efficiency in the evaluation of the forces on individual particles.

The predictor-corrector scheme moves the particle positions through the full time step Δt based on the instantaneous particle velocity and acceleration,

$$\mathbf{r}_c = \mathbf{r}_t + \mathbf{u}_t \Delta t + \frac{1}{2}\frac{d\mathbf{u}_t}{dt}(\Delta t)^2 \tag{3.97}$$

The particle velocity is first predicted using the standard Euler approach,

$$\mathbf{u}_p = \mathbf{u}_t + \frac{d\mathbf{u}_t}{dt}\Delta t \tag{3.98}$$

Likewise the predicted density is evaluated from the time derivative of the density ρ_t at the current time step,

$$\rho_p = \rho_t + \frac{d\rho_t}{dt}\Delta t \tag{3.99}$$

Using the predicted quantities, the change in density and velocity with time is evaluated for a second time. The final corrected velocity is then obtained using the average of the initial and predicted acceleration,

$$\mathbf{u}_c = \mathbf{u}_t + \frac{1}{2}\left(\frac{d\mathbf{u}_p}{dt} + \frac{d\mathbf{u}_t}{dt}\right)\Delta t \tag{3.100}$$

Likewise the final corrected density is,

$$\rho_c = \rho_t + \frac{1}{2}\left(\frac{d\rho_p}{dt} + \frac{d\rho_t}{dt}\right)\Delta t \tag{3.101}$$

Rearranging (3.98) and (3.99), and replacing the initial values of the density and velocity in (3.100) and (3.101) with expressions containing the predicted values gives the final equations for the corrected velocity and density,

$$\mathbf{u}_c = \mathbf{u}_p + \frac{1}{2}\left(\frac{d\mathbf{u}_p}{dt} - \frac{d\mathbf{u}_t}{dt}\right)\Delta t \tag{3.102}$$

$$\rho_c = \rho_p + \frac{1}{2}\left(\frac{d\rho_p}{dt} - \frac{d\rho_t}{dt}\right)\Delta t \tag{3.103}$$

Following Monaghan (1999), the time step Δt is governed by the Courant-Fredreichs-Lewy stability condition which is based on the smoothing length h, the speed of sound in the fluid c_s and a viscosity condition,

$$\Delta t = \beta_t \min_a \left(\frac{h}{c_s + \sigma_a}\right) \tag{3.104}$$

where σ_a is similar to μ_{ab} in equation (3.89) and provides the maximum viscosity component expected through the duration of the simulation,

$$\sigma_a = \max_b \left(h\frac{(\mathbf{u}_b - \mathbf{u}_a) \cdot (\mathbf{r}_b - \mathbf{r}_a)}{|(\mathbf{r}_b - \mathbf{r}_a)|^2}\right) \tag{3.105}$$

The value of β_t in equation (3.104) is dependent upon the type of time stepping scheme. Colagrossi (2004) set β_t to 2.5 when employing a fourth-order Runge-Kutta scheme for modelling two phase flows, while Monaghan (1999) recommends 0.3 for the predictor-corrector improved Euler approach. Following Feldman (2006), the value of β_t in this thesis has been set at 0.1, with the aim of enhancing the accuracy of the algorithm.

3.5   Nearest neighbour particle search method

Kernel functions in the SPH method - as described previously in Section 3.1 - have a compact support in which only a finite number of particles are able to interact with the particle of interest. Due to the Lagrangian nature of the method, particles can move in and out of another particle's compact support freely. Consequently a suitable nearest neighbour searching strategy is required in order to locate those particles lying within the compact support of a given particle of interest. A number of approaches have been reported in the literature including the simple all-pair search, the linked list algorithm and the tree search.

Without doubt the simplest, albeit naive method for creating a list of nearest neighbours is the all-pair search. Often criticised for its computational inefficiency, this method was used in this thesis as part of the early validation models due to its simplicity. For any given particle of interest, the distance to every particle within the computational domain is calculated. If this separation is less than or equal to the radius of the compact support, and the smoothing length of each particle is equal, the two particles are recorded as an interacting particle pair. By searching over N particles for each particle of interest, the time taken is of order N^2 and becomes particularly time consuming as the number of particles in the domain increases.

To improve the computational efficiency of the SPH solver, the all-pair search was replaced with a linked list algorithm. This is implemented by laying a grid over the computational domain and assigning fluid particles to a cell. Each cell is of equal height and width that as a rule must be greater than or equal to the compact support radius of the kernel. The grid search process then steps across each cell from left to right and along every row from bottom to top, building a list of the particles located within the cell and linking it to a list of particles in the eight neighbouring cells (see Figure 3.4a). A periodic search similar to the all-pair search is then actioned on the listed particles.

With a constant smoothing length in use each pair interaction will be symmetric, which reduces the number of cells required to be searched. Figure 3.4b demonstrates that particles in the red cell need only search for neighbours in the cells immediately

north-west, north, north-east and east. Particles in the other immediate cells labelled *x* have previously searched the red cell for nearest neighbours. This reduces the number of cells searched from eight to four, further increasing the computational efficiency (see Figure 3.4b).

Employing the linked list algorithm reduces the time taken towards order N if the size of each cell is sufficiently small. In practice however, the cells are set with sides approximately 25% larger than the radius of the kernel to allow a number of time steps to be completed between linked list allocations. This is also true for the subsequent nearest neighbour search as it is much more efficient in terms of time, with only a slight increase in memory use.

For more complex SPH simulations involving variable smoothing lengths and/or variable particle sizes, using the linked list algorithm can be problematic. Some authors have implemented a tree search algorithm which has a complexity of order $Nlog_{10}N$ and is hence considerably more efficient than the simple all pair approach. By repeatedly splitting the problem domain into quadrants (Figure 3.5b), the tree algorithm moves through multiple levels until a cell is occupied by only a single particle.

(a)   (b)
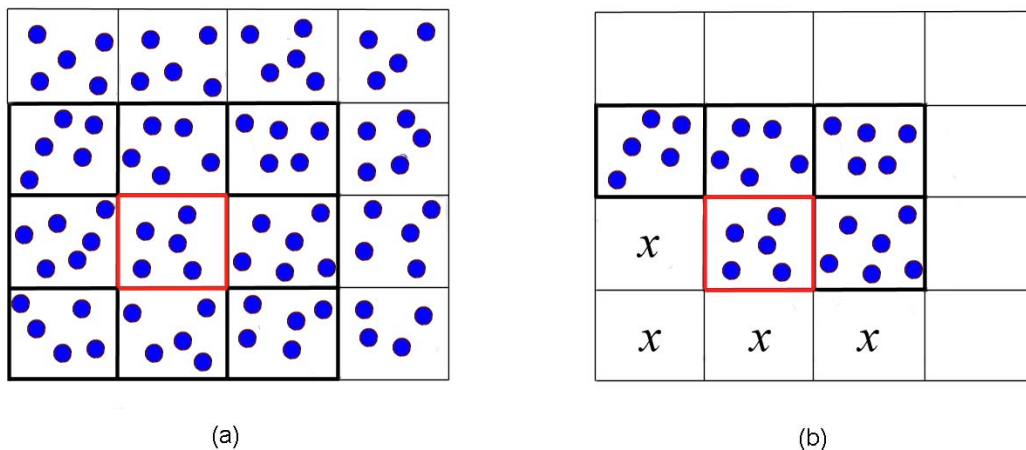
Figure 3.4 – The linked list search algorithm describing (a) the initial grid overlay with neighbouring cells and (b) the simplified approach for a constant smoothing length. The cells labelled *x* have already searched the red cell of interest for neighbouring particles.
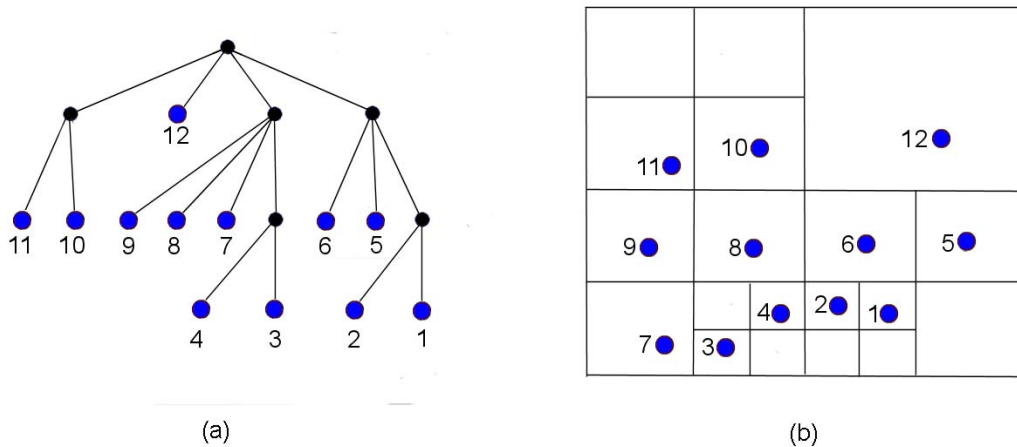
Figure 3.5 – The structure produced using the tree search algorithm (a)
for a given particle distribution (b).

The nearest neighbour search is completed by stepping down each level of the tree through individual branches. At each level a check is made to see if the compact support of the particle of interest overlaps the given quadrant. If there is an overlap, the descent continues until the quadrant represents a single particle. Without an overlap, the descent stops and moves on to the next branch of the tree (Figure 3.5a). Alimi et al. (2003) used this method to search for nearest neighbours and determine the gravitational forces on particles in the formation of a star.

All problems modelled in this thesis have used a uniform particle size and smoothing length throughout the fluid domain. Therefore the tree search algorithm is not required, but instead the simpler linked list process has been implemented because of its efficiency.

3.6 Treatment of boundaries

In this thesis two major boundary conditions have been enforced, the free surface and the solid boundary. Other typical CFD boundary conditions such as the periodic boundary were not required and so will not be discussed here.

3.6.1 Free surface

Described as the most complex boundary condition by White (1999), the free surface (or liquid-gas interface) has its position in two dimensions described by,

$$y_{fs} = \eta(x,t) \tag{3.106}$$

The transition from liquid to gas is instantaneous and so the vertical velocity of both fluids must be equal across the interface,

$$\mathbf{v}_{liq} = \mathbf{v}_{gas} = \frac{d\eta}{dt} = \frac{\partial \eta}{\partial t} + \mathbf{u}_{fs}\frac{\partial \eta}{\partial x} \tag{3.107}$$

Equation (3.107) is referred to as the *kinematic free surface condition*. For single phase flows in SPH, this condition is satisfied implicitly as liquid particles on the free surface stay on the free surface. Mechanical equilibrium is also be enforced across the free surface, but because the present SPH model is inviscid all viscous stresses can be ignored. Pressure on the other hand cannot be ignored and must be an equal and continuous function. Known as the *dynamic free surface condition*, it is defined by,

$$P_{liq} = P_{gas} \tag{3.108}$$

$$\frac{\partial P}{\partial y_{fs}} = 0 \tag{3.109}$$

The dynamic condition is easily enforced in single phase SPH. Initial conditions are set such that the pressure of any free surface particle is zero in order to match the atmospheric pressure outside the liquid (3.85). Applying the direct form of the discrete density approximation (3.47) would result in negative pressures at the free surface as the compact support cannot be filled by particles. In order to avoid this clear violation of the dynamic condition, the discrete form of the continuity equation (3.54) is used (Colagrossi et. al, 2007). The divergence of the velocity field and the time derivative of the density at this location are both zero for regularly spaced particles. In practice, variations in particle spacing will result in a non-zero divergence of the velocity field. However, in comparison with the failings of the direct density approach, these small variations are negligible. For regularly spaced particles in a uniform velocity field the dynamic condition is implicitly satisfied.

3.6.2   Solid boundaries

Boundary particle method

A number of different solid boundary treatments have been developed for use in SPH. One of the earliest methods utilised by Monaghan (1994) involved boundary particles. Fixed along the boundary's edge at approximately half the spacing of the fluid particles (see Figure 3.6), the boundary particles do not contribute to the density and momentum equations, but simply exert a repulsive force on the fluid inspired by the known forces between molecules.

The force per unit mass $\boldsymbol{f}$ on a fluid particle separated by a distance r from the boundary particle takes the Lennard-Jones form,

$$\boldsymbol{f} = D_B \left[\left(\frac{r_0}{r}\right)^{p_1} - \left(\frac{r_0}{r}\right)^{p_2} \right] \frac{\mathbf{n}}{r^2} \tag{3.110}$$

where $\mathbf{n}$ is the vector normal to the boundary. This force is purely repulsive and is zero if the initial particle separation r_0 is greater than the separation of the fluid particle and the boundary. Monaghan (1994) suggests that the values of p_1 and p_2 be set to 4 and 2 respectively, however reasonable results have been obtained with other values provided p_1 is greater than p_2. The coefficient D has units $\mathrm{m}^2/\mathrm{s}^2$, is problem-dependent and is usually related to the depth of the fluid for problems involving dams and tanks.
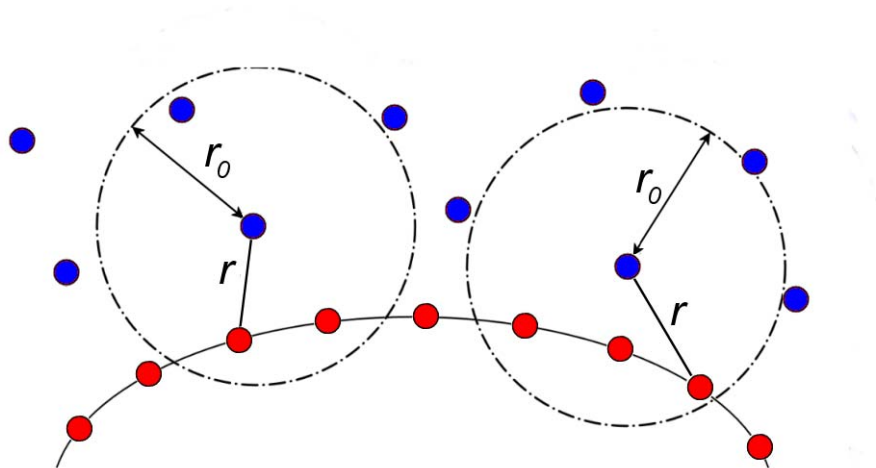
Figure 3.6 – The Lennard-Jones method for determining the boundary forces on fluid particles (blue) due to the neighbouring boundary particles (red).

A more advanced repulsive force using a function similar to the kernel was described by Monaghan (2005). Here, the force per unit mass f is given by,

$$\boldsymbol{f} = \Gamma(y)\chi(x)\mathbf{n} \tag{3.111}$$

The function $\chi(x)$ ensures that a fluid particle moving parallel to a boundary (fixed along the x axis) always experiences the same force, independent of where it lies between boundary particles,

$$\chi(x) = \begin{cases} \left(1 - \dfrac{x}{\Delta p}\right) & if\ 0 < x < \Delta p \\ 0; & \text{otherwise} \end{cases} \tag{3.112}$$

where Δp is the boundary particle separation and x is the tangential distance along the boundary surface between the fluid and boundary particles. Assuming the cubic spline kernel is in use, $\Gamma(y)$ takes a form similar to the gradient of the cubic spline,

$$\Gamma(y) = B_B \begin{cases} \frac{2}{3}; & \text{if}\ 0 < q < \frac{2}{3} \\ \left(2q - \frac{3}{2}q^2\right); & \text{if}\ \frac{2}{3} < q < 1 \\ \frac{1}{2}(2 - q)^2; & \text{if}\ 1 < q < 2 \\ 0; & \text{otherwise} \end{cases} \tag{3.113}$$

where $q = y/h$ and B_B is $0.02c_s^2/y$. Introducing the coefficient B_B ensures that particles will not penetrate the boundary as the value of $\Gamma(y)$ increases as y approaches zero.

The boundary particle method described by Monaghan (1994, 2005) has been utilised in many free surface models, however these particles do not contribute to the density of the fluid. In addition the particle number density near a boundary falls as the compact support stretches in to areas not occupied by any fluid particles. Without a regular reinitialisation of the density field, the solution would progressively become corrupt.

Feldman and Bonet (2007) proposed an improved boundary force method – known as the Contact Force – using a Lagrangian that also prevents a reduction in the fluid particle density due to the presence of the boundary. If the compact support near a boundary is not filled (e.g. equation (3.18) is not satisfied) then the fluid particle density is renormalised using a method similar to the Shepard filter (3.23). The same

scale factor is then included in the calculation of the internal force on a given fluid particle (3.67) in order to force it away from the solid boundary. A more detailed description of boundary treatment using the Contact Force method can be found in Feldman and Bonet (2007).

Filled boundary method

Morris et al. (1997) developed a method that filled non-fluid regions of the problem domain with particles to avoid an unfilled compact support (Figure 3.7). These boundary particles are effectively fluid particles fixed on a Cartesian lattice that allow their density and pressure to evolve with time via the standard SPH equations of motion. In order to correctly evolve the density of a fluid particle *a* by the continuity equation, the fixed boundary particles require a velocity. For the case of a no-slip stationary boundary, the boundary particles are assigned an artificial velocity based on the normal distance d_b to each boundary particle and the velocity of the fluid particle extrapolated across the boundary,

$$\mathbf{u}_b = -\frac{d_b}{d_a}\mathbf{u}_a$$

(3.114)

Filled boundary regions can easily cope with complex geometries just like the Monaghan repulsive force method. Curved boundaries are treated slightly differently by using a local tangent line to extrapolate the fluid velocity across the boundary (Morris et al., 1997). A global boundary velocity can also be applied by replacing $\mathbf{u}_a$ with the fluid velocity relative to the boundary surface.
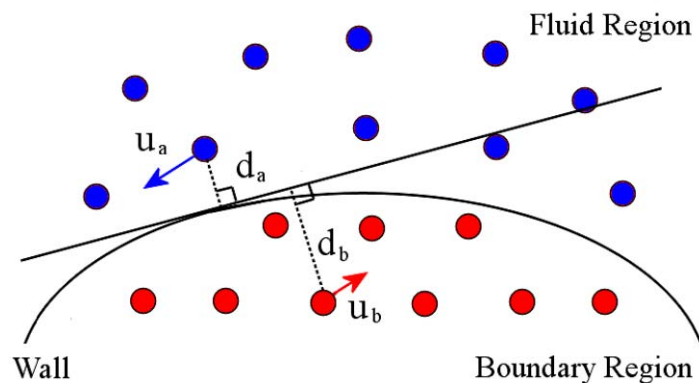
Figure 3.7 – The filled boundary method. Fluid particles (blue) can be randomly distributed unlike the boundary particles (red) that are fixed on a regularly spaced lattice.

Ghost particle method

The ghost particle method is inspired by the treatment of sources, sinks, vortices and other flow patterns near a boundary in potential flow. The image method in potential flow replaces the physical wall boundary with a mirror image of the local fluid. The fluid then behaves as if a solid wall boundary existed at the line of symmetry. In SPH, creating ghost particles that mirror the fluid particles about the solid boundary has the same advantage as the image method in potential flow.

Like the filled boundary region, the ghost particle approach is designed to encourage smoother behaviour amongst fluid particles within close proximity of a solid boundary. Despite the similarities between the two methods there is one major difference which sets them apart. Filled boundary particles are positioned on a regular lattice and are fixed inside the reference frame of the boundary region (Figure 3.7), whereas the positions, velocities, pressures and densities of ghost or image particles are directly related to the properties of the neighbouring fluid particles.

For the simple case of a single straight wall section fixed in space and time, every fluid particle within a kernel's radius κh of the wall creates an artificial ghost particle directly opposite the boundary with the same density and pressure (Figure 3.8). In order to enforce the free slip condition, the ghost velocity component parallel to the wall is set to match that of the corresponding fluid particle. To prevent any fluid particles from penetrating the boundary, the velocity component along the normal directly opposes that of the fluid particle.

In practice not every wall boundary is treated as simply as the stationary vertical wall in Figure 3.8. If the boundary is moving with a velocity along the normal $\mathbf{u}_w$, then the normal $\mathbf{u}_{nb}$ and tangential $\mathbf{u}_{tb}$ velocity components of the ghost particle are,

$$\mathbf{u}_{nb} = 2\mathbf{u}_w - \mathbf{u}_{na} \qquad (3.115)$$

$$\mathbf{u}_{tb} = \mathbf{u}_{ta} \qquad (3.116)$$

where $\mathbf{u}_{ta}$ and $\mathbf{u}_{na}$ are the tangential and normal components of the fluid particle velocity.
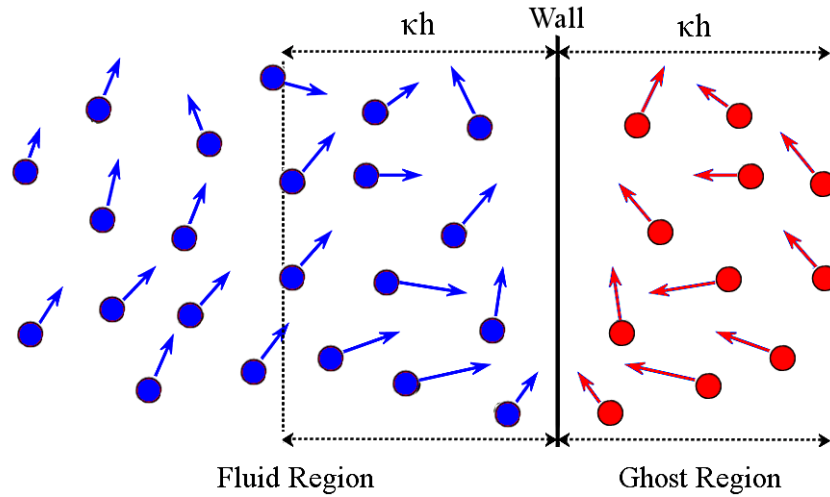
Figure 3.8 – Ghost particles (red) created about a stationary vertical boundary due to the presence of neighbouring fluid particles (blue).

Allocation of ghost velocities is more complicated if the boundary velocity is not along the normal. In this case the ghost velocity is found by transforming the reference frame from the global fluid domain to one in which the wall boundary is stationary. Velocities of the ghost particles are calculated in the new stationary wall reference frame before transforming back to the global fluid domain.

The pressure and density of a ghost particle mirrored about a vertical boundary is typically kept the same as the corresponding fluid particle. Ghost particles at horizontal boundaries, or any boundary not lying in the vertical plane, require further manipulation. For problems involving a gravitational acceleration, any relative difference in vertical separation between the ghost and fluid particles must contribute to the ghost particle pressure. To maintain a constant hydrostatic pressure gradient across a solid wall boundary, the pressure of any ghost particle b due to its corresponding fluid particle a is,

$$P_b = P_a + \rho_0 g (y_a - y_b) \qquad (3.117)$$

Occasionally the ghost method does not prevent particles from penetrating a wall boundary. Typically this occurs in areas where the total number of fluid and ghost particles is not sufficient to entirely fill the compact support. Any particle that moves

to within half of its radius of the wall is forced into a simple bounce back algorithm. The velocity of the fluid particle normal to the boundary is reversed to force it away from the wall preventing it from leaving the problem domain whilst conserving the energy of the system.

Unfortunately the ghost particle method does suffer from a lack of flexibility. As the geometry increases in complexity, so does the method for creating ghost particles. One of the simpler cases is that of fluid contained between two walls meeting at right angles. Left alone, the compact support of a fluid particle located within a kernel's radius κh of the intersection will not be entirely filled. As such the pressure gradient forcing the particle away from the walls will be reduced, potentially allowing particles to leak through the intersection point.

Figure 3.9 describes the method for ensuring the compact support of any particle near a right angle intersection remains filled. Any fluid particle located close to an intersection is reflected about both walls as described previously. However, if the particle lies within a kernels' radius of the intersection a ghost is created directly opposite (see Figure 3.9b). This ghost follows the hydrostatic pressure rule (3.117) and has a velocity equal in magnitude but opposite in direction to the fluid particle.
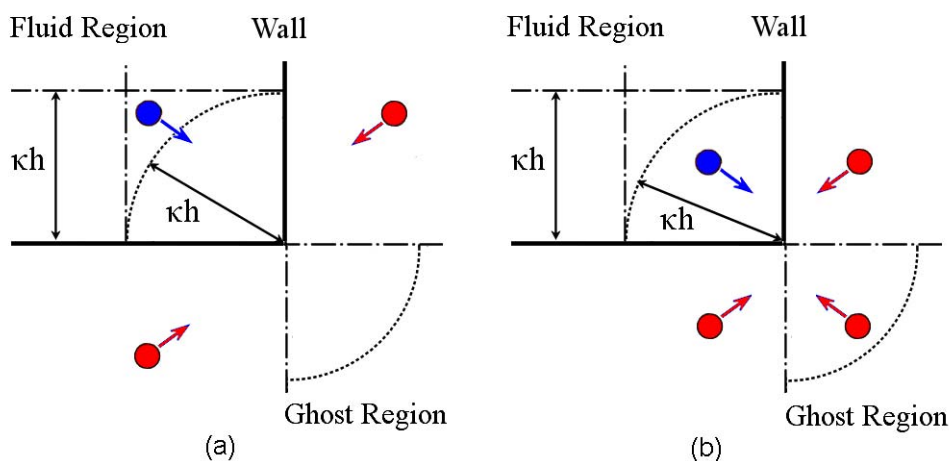
Figure 3.9 – Ghost Particles formed at internal right angle corners if the fluid particle is (a) located outside a kernel's radius κh of the intersection point and (b) inside κh of the intersection.

64

The other extreme is the opposite of Figure 3.9, where the ghost particles are located inside an obtuse intersection angle (see Figure 3.10). Fluid particles within a kernel's radius of each wall create a ghost particle in the same manner as in equations (3.115) to (3.117). To maintain a smooth approximation of the fluid properties near the intersection between the wall boundaries, fluid particles located directly adjacent to the intersection also create ghosts.

Unfortunately at this type of intersection the particle number density in the ghost region can be up to three times that of the fluid (see Figure 3.10). This can cause an artificial local increase in fluid pressure and ultimately degrade the model if left untreated. The solution for right angle intersections presented by Colagrossi et al. (2007) and generalised here, scales the kernel function for each ghost-fluid particle pair depending on the location of the fluid particle.

Ghost particles are created by both wall boundaries and the intersection point, overlapping in the region opposite the intersection from 2 in Figure 3.11. The calculated kernel for any ghost particle and fluid particle pair (if the ghost particle lies within the overlapping region) is multiplied by a scale factor S_i, where i is the boundary or intersection point for which the ghost was created.
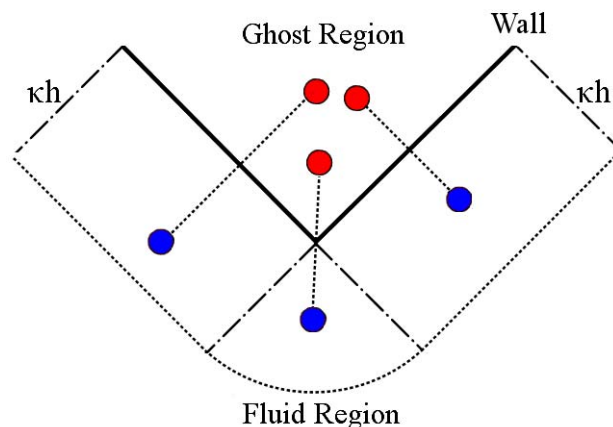
Figure 3.10 – Ghost particles located inside the obtuse angle between wall boundaries at an intersection point. A visible increase in ghost particle number density is identified.
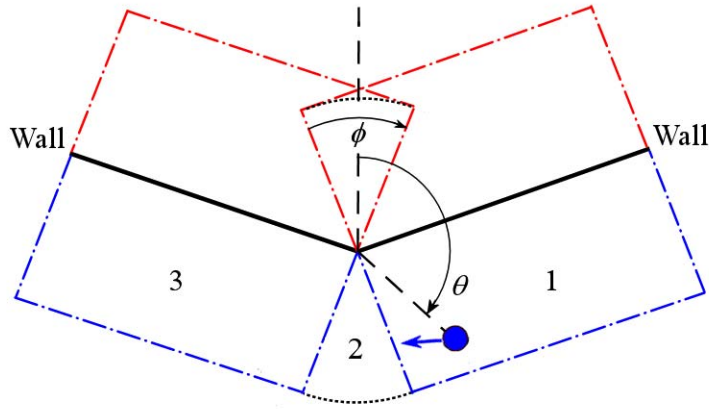
Figure 3.11 – Scaling of ghost particle interactions at obtuse intersections. Ghost regions overlap in the region opposite 2 spanned by the angle ϕ, forcing the kernel's strength associated with a ghost particle and fluid particle pair to be scaled.

Equations (3.118) through to (3.120) describe the scaling functions,

$$
S_1 = \begin{cases} 1 & ; \theta < (\pi - \emptyset) \\ \dfrac{1}{2}\cos\left(\dfrac{\pi}{\emptyset}(\theta + \phi - \pi)\right) + \dfrac{1}{2} & ; (\pi - \emptyset) \leq \theta \leq \pi \\ 0 & ; \theta > \pi \end{cases} \tag{3.118}
$$

$$
S_2 = \begin{cases} 0 & ; \theta < (\pi - \emptyset) \\ -\dfrac{1}{2}\cos\left(\dfrac{\pi}{\emptyset}(\theta + \phi - \pi)\right) + \dfrac{1}{2} & ; (\pi - \emptyset) \leq \theta \leq (\pi + \emptyset) \\ 0 & ; \theta > (\pi + \emptyset) \end{cases} \tag{3.119}
$$

$$
S_2 = \begin{cases} 0 & ; \theta < \pi \\ \dfrac{1}{2}\cos\left(\dfrac{\pi}{\emptyset}(\theta + \phi - \pi)\right) + \dfrac{1}{2} & ; \pi \leq \theta \leq (\pi + \emptyset) \\ 0 & ; \theta > (\pi + \emptyset) \end{cases} \tag{3.120}
$$

Here ϕ is the angle swept out by the overlapping region and θ is the bearing from the line bisecting the intersection point to the fluid particle. Therefore if the fluid particle

were to move from right to left in Figure 3.11, the influence of ghost particles created due to fluid particles in region 1 would be gradually reduced and the influence of ghost particles created due to the intersection would become more prominent. Figure 3.12 describes the scaling functions as a function of the bearing for two wall boundaries intersecting at 30° and 90°.

Curved solid wall boundaries are approximated by using a series of short straight line segments and the intersection scaling routine. The only restriction placed on the length of the straight sections is that they be longer than three times the smoothing length. This restriction was imposed to avoid an increase in computation time from having to perform a large number of kernel scaling routines every time step. Each section of curved solid wall modelled in this thesis was defined by a set of arbitrarily spaced nodes, no less than $3h$ apart.

Despite the more computationally demanding corrections and scaling functions, the ghost particle approach has been chosen over all the other wall boundary methods for use in this thesis. This choice is primarily due to the far smoother behaviour exhibited by fluid particles near a boundary treated by ghost particles.
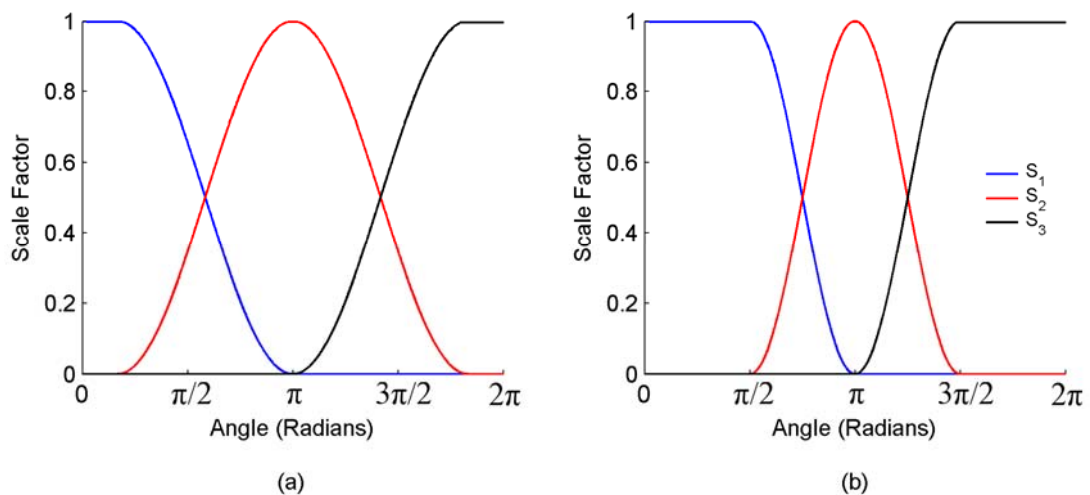
Figure 3.12 – Scaling functions for two solid wall boundaries
intersecting at (a) 30° and (b) 90°.

3.6.3 Dynamic response of solid boundaries

Most general fluid problems that involve the solid boundaries of a stationary or moving structure require a calculation of the local fluid pressure. Oger et. al. (2005) developed a projection method for evaluating the forces on a solid object due to neighbouring SPH fluid particles.

The method presented here is a simplification of that published by Oger et. al (2005) as the wall boundaries modelled in this thesis are typically a combination of linear segments. Each wall is divided into a series of small pressure sensors, approximately a smoothing length in width, and the pressure of each fluid particle located within a distance d (typically between $3h$ and $6h$) of the boundary is referenced. The mean pressure is calculated through a summation of the fluid particle pressures, with more weight given to those particles closer to the wall. The total force per unit width on the wall at the pressure sensor i over N_j fluid particles is given by,

$$\boldsymbol{F_i} = h\frac{\sum_{j=1}^{N_j} P_j}{N_j} \tag{3.121}$$

Arranging these small pressure cells along the surface of any object enables it to respond to the local fluid pressure. The response is calculated via a simple vector summation of the pressure sensors.
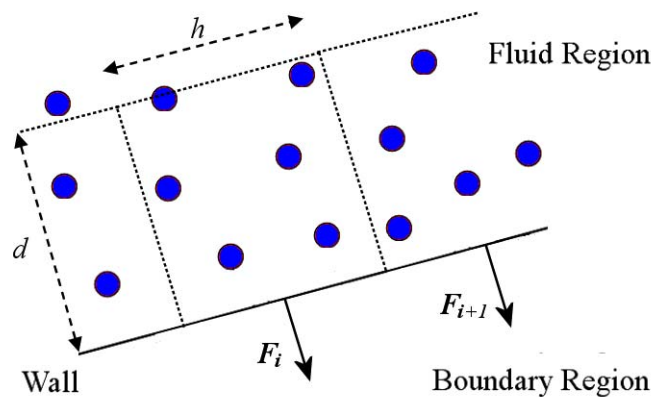
Figure 3.13 – Pressure sensors along a linear wall boundary.

3.7 Implementation of the algorithm

The SPH method and its corrections stated in the previous subchapters have been implemented in an algorithm constructed using the commercial software Matlab and C++. All simulations are begun by first describing the model geometry and initial fluid conditions in Matlab before setting the time step according to the CFL condition (see Section 3.4). Dependent on the particle resolution, maximum fluid velocities and the time step size, the following routine is run every 10 to 50 time steps,

- For problems involving solid wall boundaries, ghost particles are assigned with the properties described in 3.6.2.
- A fixed grid is positioned over the computational domain and all particles are assigned to cells. The linked list nearest neighbour search is performed and the particle pairs stored in an array (see Section 3.5).

Following this, the data is exported to C++ via a "mex" function and the density reinitialisation routine (see Section 3.3.3) is performed over all fluid particles to restore consistency. A number of time steps are then completed in parallel on a dual core desktop PC,

- Moving wall boundary positions are updated based on the fluid pressures calculated in the previous time step (see Section 3.6.3).
- The Gaussian cut-off kernel (3.41) is calculated for each particle pair and scaled for those pairs including a ghost particle at a wall boundary intersection point.
- Fluid particle pressures are calculated based on the density at the previous time step and the new change in density calculated via the continuity equation (3.54).
- The acceleration of every fluid particle is determined by way of the momentum equation (3.90), including the artificial viscosity and tensile stability control.

- The particle positions, velocities and densities are updated using the motion equations for the half time step in the predictor-corrector method (see Section 3.4).

- This list is then repeated using the predicted particle properties and the corrected values calculated for the full time step.

Finally, the calculated fluid properties, boundary positions and boundary forces are returned to Matlab and periodically saved. This SPH algorithm has been validated in the following chapter and applied to a number of fluid dynamic problems in Chapters 5 and 6.

Chapter 4

Validation of the Numerical Model

The present SPH method has been validated for a variety of free surface problems through analytical and experimental comparisons. Four benchmark validation test cases were examined:

- The evolution of an initially circular drop of fluid,
- The evolution of a rotating square fluid patch,
- The tank of hydrostatic fluid, and
- The breaking dam.

Colagrossi et al. (2007) describes the first two benchmark validation test cases as the most suitable for validating a newly developed SPH model. The circular drop and rotating patch – modelled in a void in the absence of external forces – were designed to determine if the kinematic and dynamic free surface boundary conditions were met. Both cases were also used to investigate the algorithm's sensitivity to the artificial viscosity, XSPH and density reinitialisation corrections. The ability of the modified SPH algorithm to manage a tensile instability has also been evaluated through the rotating square fluid patch.

External forces were included in the next two benchmark validation test cases. The contained tank of fluid and the classic two-dimensional dam break were simulated in order to examine the influence of solid boundaries using the ghost particle technique. Experimental data obtained by Martin and Moyce (1952) and Zhou et. al (1999) has been compared to the SPH dam break model with particular attention paid to the fluid pressures along the wall and the depth of the advancing fluid.

4.1 Evolution of an initially circular fluid patch

The first validation test case consists of a freely deforming initially circular drop of fluid that is completely surrounded by a void (Figure 4.1). The drop of fluid is inviscid and initially subjected to a prescribed velocity field illustrated in Figure 4.1 and given by,

$$\mathbf{u}_0(x, y) = u_0\mathbf{i} + v_0\mathbf{j} \tag{4.1}$$

where

$$\begin{aligned} u_0(x, y) &= -A_0x \\ v_0(x, y) &= A_0y \end{aligned} \tag{4.2}$$

The incompressible, irrotational fluid drop of radius R satisfies the Bernoulli equation,

$$P_0 + \frac{1}{2}\rho(u_0^2 + v_0^2) = \text{const} \tag{4.3}$$
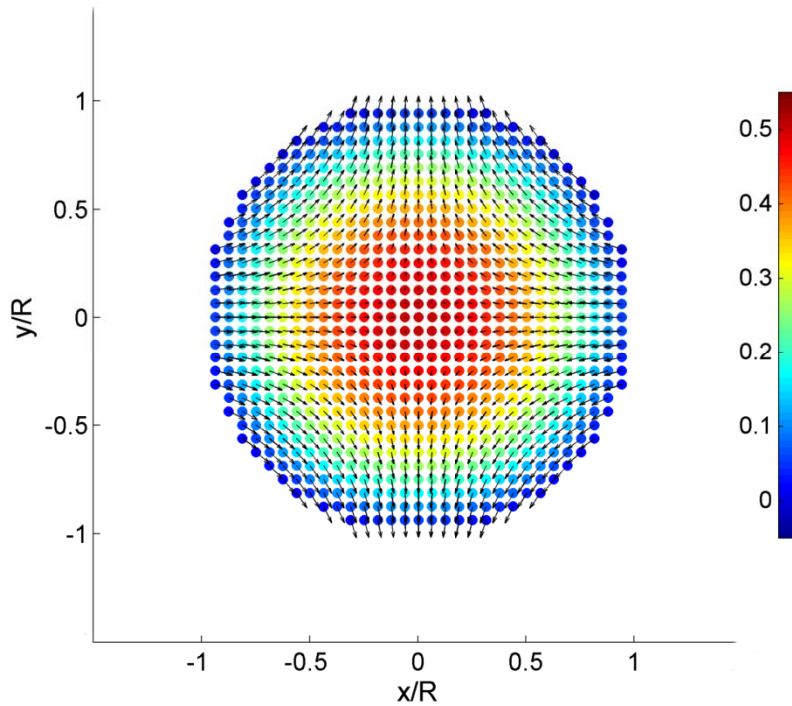
Figure 4.1 – Initial positions $\mathbf{r}/R$, velocity vectors and pressure $P/(\rho_0 A_0^2 R^2)$ of the SPH particles for the initially circular fluid drop.

At the free surface the fluid pressure is zero (due to the surrounding void) and the fluid velocity is a maximum ($|\mathbf{u}_0(R)| = A_0^2 R^2$). Therefore the constant on the right hand side of (4.3) is a function of the density and velocity. The Bernoulli equation can then be written,

$$P_0 + \frac{1}{2}\rho_0 A_0^2 (x^2 + y^2) = \frac{1}{2}\rho_0 A_0^2 R^2 \tag{4.4}$$

Rearranging (4.4) leads to an expression for the pressure at any point within the fluid,

$$P_0 = \frac{1}{2}\rho A_0^2 [R^2 - (x^2 + y^2)] \tag{4.5}$$

The irrotational drop problem is a particularly attractive validation case as an analytical solution for an incompressible fluid is easily attainable. Despite the fact that the applied SPH algorithm is most suited to compressible fluids, an approximation of an incompressible fluid can easily be made. This is achieved by setting the speed of sound to be at least an order of magnitude more than the maximum flow velocity. With a Mach number less than 0.1, the approximated fluid is termed weakly compressible as compression effects are negligible.

4.1.1 Analytical solution

The initial velocity field described by (4.2) suggests the fluid will form an ellipse over time. Assuming the fluid drop does maintain an elliptical form and the velocity field remains irrotational throughout the entire simulation, the position of a particle at any time t is given by,

$$\mathbf{r}(t) = \begin{cases} x(t) = \dfrac{a(t)}{R} x_0 \\ y(t) = \dfrac{b(t)}{R} y_0 \end{cases} \tag{4.6}$$

where $a(t)$ and $b(t)$ respectively denote the instantaneous semi-minor and semi-major axes of the elliptical fluid domain, and x_0 and y_0 are the components of the initial position of a generic SPH particle. Time differentiating (4.6) gives the initial

velocity field,

$$\mathbf{u}(t) = \begin{cases} u(x,t) = \dfrac{da}{dt}\dfrac{x(t)}{a(t)} \\ v(y,t) = \dfrac{db}{dt}\dfrac{y(t)}{b(t)} \end{cases} \tag{4.7}$$

In order to conserve mass, the product of the semi-major and semi-minor axes must be constant. The derivative of the product of the two axes is therefore,

$$\frac{d}{dt}\big(a(t)b(t)\big) = 0 \tag{4.8}$$

Applying the product rule and rewriting (4.8) gives,

$$\frac{da}{dt}b(t) + \frac{db}{dt}a(t) = 0$$
$$-\frac{da}{dt}\frac{1}{a(t)} = \frac{db}{dt}\frac{1}{b(t)} \tag{4.9}$$

The expression for the velocity field (4.7) can be simplified by replacing (4.9) with the function $A(t)$ such that,

$$A(t) = -\frac{da}{dt}\frac{1}{a(t)} = \frac{db}{dt}\frac{1}{b(t)} \tag{4.10}$$

So the velocity field at any time t becomes,

$$\mathbf{u}(t) = \begin{cases} u(x,t) = -A(t)x(t) \\ v(y,t) = A(t)y(t) \end{cases} \tag{4.11}$$

Initially at the point $(x,y) = (R,0)$ the fluid velocity in the x direction is $-A_0 R$ (4.2). Therefore (4.11) has the initial condition $A(0) = A_0$ (Colagrossi, 2004).

An analytical solution for the pressure of the incompressible fluid at any time can be found by including the velocity field (4.11) in the Euler equation. The governing

incompressible Euler equation is given by,

$$\frac{d\mathbf{u}}{dt} = -\frac{1}{\rho}\nabla P \tag{4.12}$$

The Euler equation can also be expressed as,

$$-\frac{1}{\rho}\nabla P = \frac{\partial \mathbf{u}}{\partial t} + (\mathbf{u}\cdot\nabla)\mathbf{u} \tag{4.13}$$

Partially differentiating in the x direction yields an expression for the pressure gradient,

$$-\frac{1}{\rho}\frac{\partial P}{\partial x} = \frac{\partial u(x,t)}{\partial t} + u(x,t)\frac{\partial u(x,t)}{\partial x} + v(y,t)\frac{\partial u(x,t)}{\partial y}$$

$$\frac{\partial P}{\partial x} = \rho\left[\frac{dA}{dt}x(t) - A(t)^2 x(t)\right] \tag{4.14}$$

Likewise the pressure gradient in the y direction is given by,

$$\frac{\partial P}{\partial y} = -\rho\left[\frac{dA}{dt}y(t) + A(t)^2 y(t)\right] \tag{4.15}$$

Integrating both components of the pressure gradient gives two expressions for the pressure field,

$$P = \rho\left(\frac{dA}{dt} - A(t)^2\right)\frac{x(t)^2}{2} + f_1(y,t) \tag{4.16}$$

$$P = -\rho\left(\frac{dA}{dt} + A(t)^2\right)\frac{y(t)^2}{2} + f_2(x,t) \tag{4.17}$$

Both (4.16) and (4.17) must be true for all time, therefore the pressure field is given by,

$$P = \frac{\rho}{2}\left[\left(\frac{dA}{dt} - A(t)^2\right)x(t)^2 - \left(\frac{dA}{dt} + A(t)^2\right)y(t)^2\right] + c(t) \tag{4.18}$$

The function $c(t)$ can be determined for any value of t by including the initial pressure at $(a(t), 0)$. Here the pressure is zero as this point lies on the free surface,

therefore (4.18) reduces to,

$$P = \frac{\rho}{2}\left[\left(\frac{dA}{dt} - A(t)^2\right)(x(t)^2 - a(t)^2) - \left(\frac{dA}{dt} + A(t)^2\right)y(t)^2\right] \quad (4.19)$$

Equation (4.19) allows the pressure at any location within the incompressible fluid to be determined at any time. However, the values of $a(t)$, $b(t)$, the function $A(t)$ and its derivative with respect to time are still unknown. So, by noting that the fluid pressure at $(0, b(t))$ must always be zero, the expression inside the square parentheses can be written,

$$\left(\frac{dA}{dt} - A(t)^2\right)a(t)^2 = -b(t)^2\left(\frac{dA}{dt} + A(t)^2\right) \quad (4.20)$$

Differentiating both sides of (4.19) by the product rule leads to,

$$\frac{d^2A}{dt^2} - 4A(t)\frac{dA}{dt} + 2A(t)^3 = -\frac{b(t)^2}{a(t)^2}\left(\frac{d^2A}{dt^2} + 4A(t)\frac{dA}{dt} + 2A(t)^3\right) \quad (4.21)$$

Replacing the $a(t)$ and $b(t)$ terms with $A(t)$ and its derivatives (4.10) gives the following differential equation,

$$\frac{d^2A}{dt^2}A(t) - 4\left(\frac{dA}{dt}\right)^2 + 2A(t)^4 = 0 \quad (4.22)$$

The analytical solution of (4.22) was established numerically by way of a predictor-corrector algorithm with the initial conditions $A(0) = A_0$ and $dA/dt = 0$ following Colagrossi (2004). After solving for $A(t)$ the values of $a(t)$ and $a = b(t)$ are found via,

$$a(t) = Re^{-\int_0^t A(t)dt} \quad (4.23)$$

$$b(t) = Re^{\int_0^t A(t)dt} \quad (4.24)$$

By implementing this analytical approach it is possible to solve for the position of the free surface or any given particle, the pressure field and the velocity field at any time.

4.1.2   SPH simulation

The SPH algorithm outlined in Section 3.7 was used to model the evolution of the initially circular fluid patch at a number of particle resolutions. Equations (4.2) and (4.3) describe the initial velocity and pressure fields, where A_0 is set to 100 s^{-1}, the radius R is 1 m and the density of the fluid is 1025 kg m^{-3}. Four models of varying particle resolution $(R/r_0 = 50, 100, 150 \text{ and } 250)$ were simulated using a smoothing length of $h = 1.33r_0$ for a period of 0.02 s (which equates to a dimensionless time of $tA_0 = 2.0$). The analytical solution of (4.22) predicts the free surface will accelerate to a maximum velocity of $1.4RA_0$ along the semi-major axis. This speed is not exceeded anywhere within the fluid domain, so to keep the maximum Mach number less than 0.1, the sound speed in the fluid was set to $14RA_0 = 1400 \text{ m/s}$ (Colagrossi 2004).

Every numerical correction described in Section 3.3 was put into practice when modelling the evolution of the ellipse. In this test case the artificial viscosity coefficient α was set to 0.03 and the density reinitialisation routine was applied every 20 time steps so as to preserve smooth density and pressure fields. The tensile stability correction has also been applied with ϵ set to 0.2, however in this test case the fluid particle pressure rarely drops below zero so the correction has very little effect on the simulation.

Figure 4.2 describes the position of the free surface and the fluid pressure at a number of dimensionless time instants. All of the SPH fluid particles are contained within the line predicted by the analytical solution to be the location of the free surface. Furthermore the fluid pressure at the free surface was initially defined to be zero and has maintained this throughout the simulation. Therefore the model satisfies the free surface dynamic boundary condition as the pressure at the free surface remains constant.

The fluid particles were initially arranged on a Cartesian lattice similar to that described in Figure 4.1. Beginning the simulation with this initial condition can produce poor results as the velocity field forces the particle separation in the x direction to decrease while simultaneously increasing in the y direction (see Figure

4.3 a and b). Long widely spaced strings of particles form, causing a slight artificial increase in the local fluid pressure. At $tA_0 = 1.0$ the free surface fluid particles begin to redistribute in a more random pattern, but by this point in time the free surface particles lie outside the analytical free surface position (see Figure 4.3). This is not a violation of the kinematic free surface condition, but the predicted free surface position is no longer accurate.
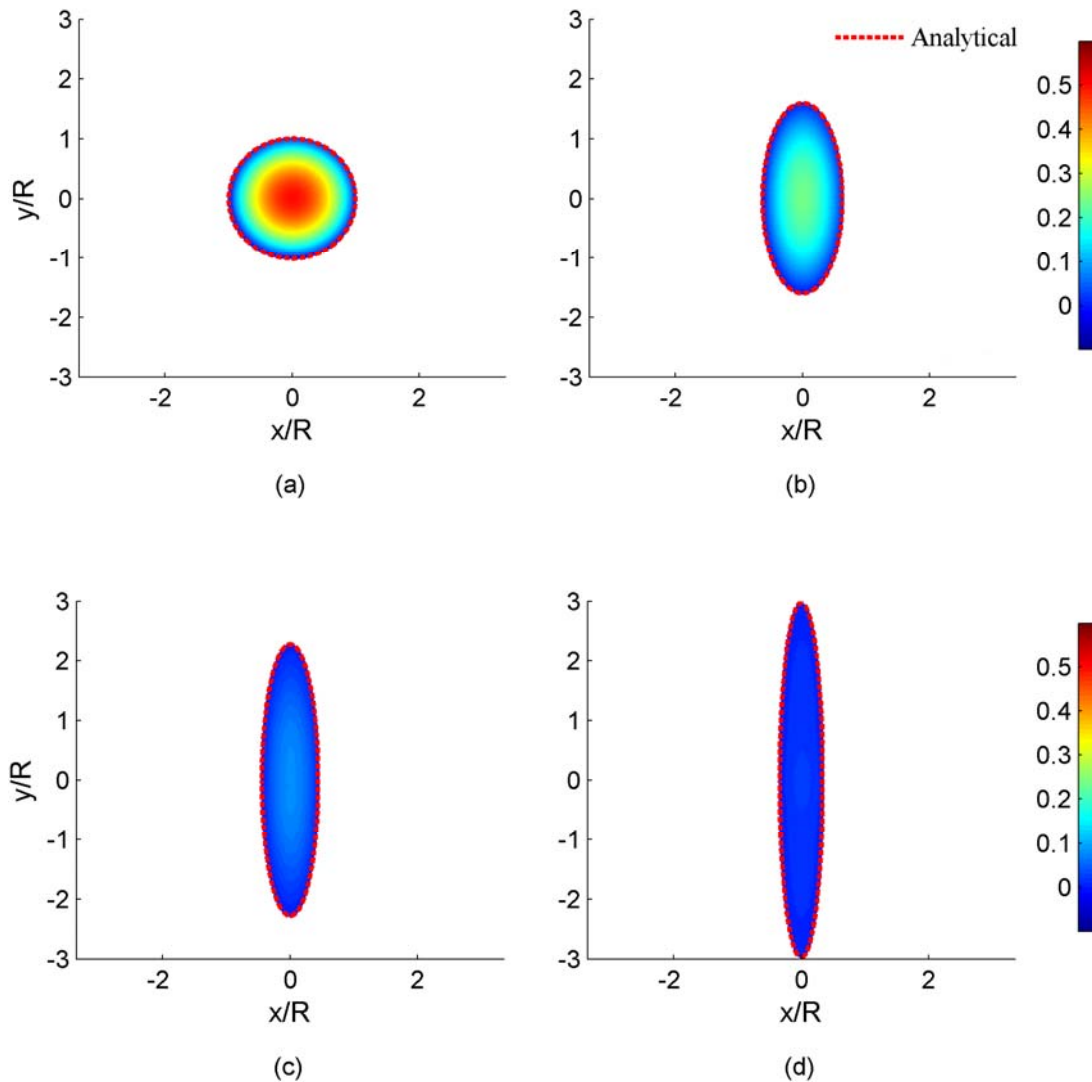
Figure 4.2 – Dimensionless positions and pressure, $P/(\rho_0 A_0^2 R^2)$, of 70681 SPH particles ($R/r_0 = 150$) at time instants (a) $tA_0 = 0$, (b) $tA_0 = 0.5$, (c) $tA_0 = 1.0$ and (d) $tA_0 = 1.5$. The red dashed line indicates the analytical free surface position.
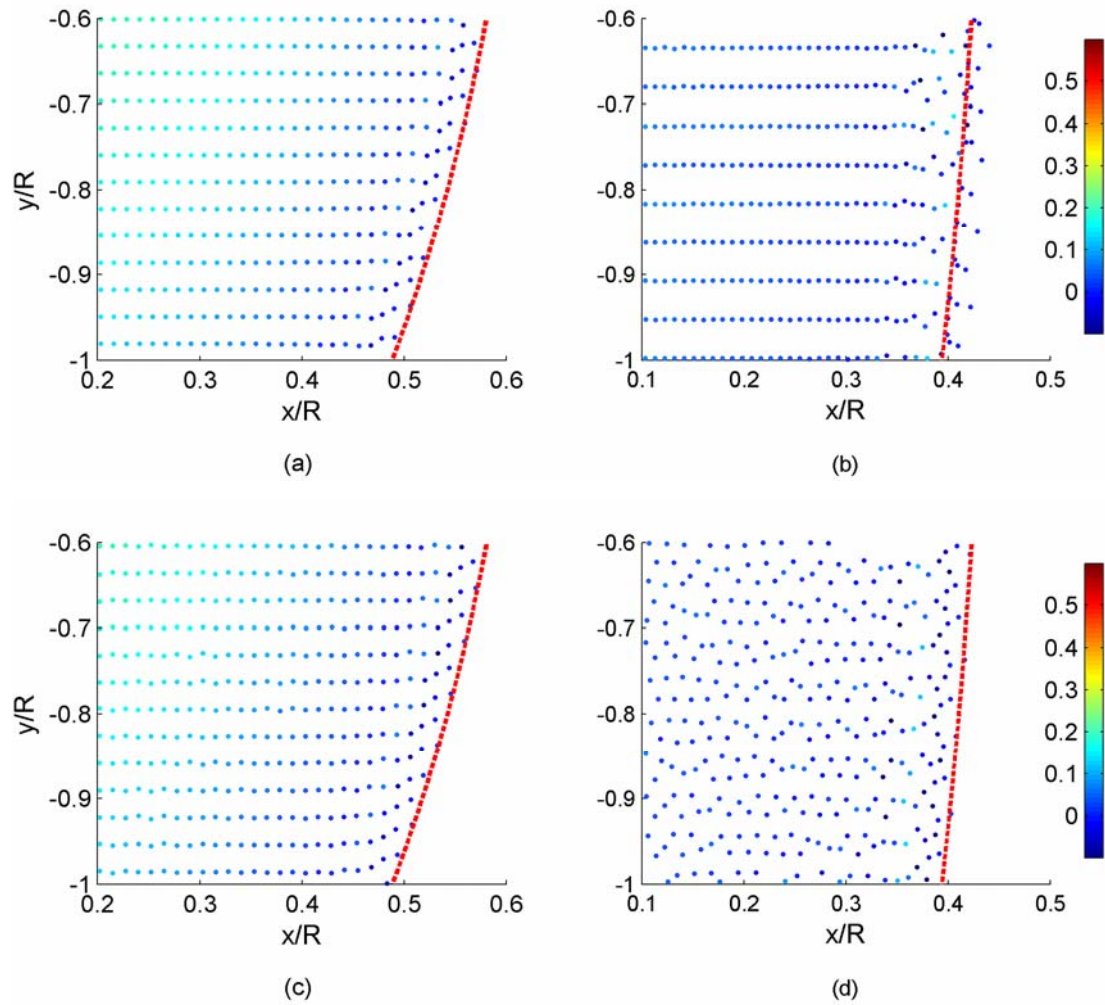
Figure 4.3 – Magnified particle positions of the 7845 particle model $(R/r_0 = 50)$ without (top) and with (bottom) noise applied to the initial positions. The red dash line indicates the analytical position of the free surface at two time instants, $tA_0 = 0.5$ (left) and $tA_0 = 1.0$ (right).

To alleviate this problem, each particle's initial position was adjusted by introducing a small random variation – typically a maximum of 2% of the initial semi-major axis – in order to encourage the particles to redistribute easily. In Figure 4.3c, the particles at $tA_0 = 0.5$ still appear to be well ordered on a Cartesian lattice with a few exceptions, but by $tA_0 = 1.5$ (Figure 4.3d) the particles have scattered into a much more evenly spaced system. The prediction of the free surface at $tA_0 = 1.5$ now

agrees well with the analytical solution. Furthermore, the fluid particles located on the free surface at $tA_0 = 0$ have remained on the free surface for the duration of the simulation, hence satisfying the kinematic free surface boundary condition.

The particle number density at the free surface is still slightly higher than in the remainder of the computational domain because the pressure of individual particles is near, or at times less than, zero. In this case the force on an individual particle can be attractive resulting in an artificial clustering of particles. This is particularly evident if the tensile stability correction is not included as the higher number density causes a significant distortion of the free surface.

The analytical approach also provides a solution for the pressure at any point in the fluid through equation (4.19). A numerical gauge was placed at the centre of the drop (0,0) and the pressure was determined by smoothing over all particles located within $3h$ of the gauge using the Gaussian cut-off kernel. At the lowest resolution, $R/r_0 = 50$, the SPH pressure signal oscillates about the analytical solution, for the most part without a discernable frequency (see Figure 4.4). As the particle resolution increases, the oscillations in the pressure signal become more regular with larger amplitude. The frequency of oscillation of the $R/r_0 = 250$ model containing 196 321 fluid particles varied from $6.3A_0$ near $tA_0 = 0.5$ up to $12.7A_0$ at $A_0 = 2.0$. Colagrossi (2004) notes that the resonant acoustic frequency has a dominant mode with a wavelength of $\lambda = 4a(t)$, and so the expected frequency at any time throughout the simulation can be found from,

$$f = \frac{c_s}{\lambda} = \frac{14RA_0}{4a(t)} \tag{4.25}$$

Evaluating (4.25) at $tA_0 = 2.0$ yields an expectant resonant frequency of $12.9A_0$, which compares well with the simulated value. These natural modes of vibration are evident in most SPH simulations and will be investigated further in Section 4.3.

The clearly defined pressure signals observed in Figure 4.4 would not be possible if not for the smoothing nature of the density reinitialisation correction. Figure 4.5 illustrates the noise that progressively destroys the pressure field when the

reinitialisation is not implemented. Early in the simulation, the pressure field is very similar to that illustrated in Figure 4.2, albeit with some random noise, particularly near the free surface. This is primarily due to the, at best, half-full compact support of the free surface particles slightly disturbing the calculated density. These small disturbances can also be caused by particles not necessarily located on, but within a compact support of the free surface as they too have a compact support which in part is not occupied by fluid particles. Over time the noise propagates through the solution, spoiling the otherwise smooth pressure and density fields.
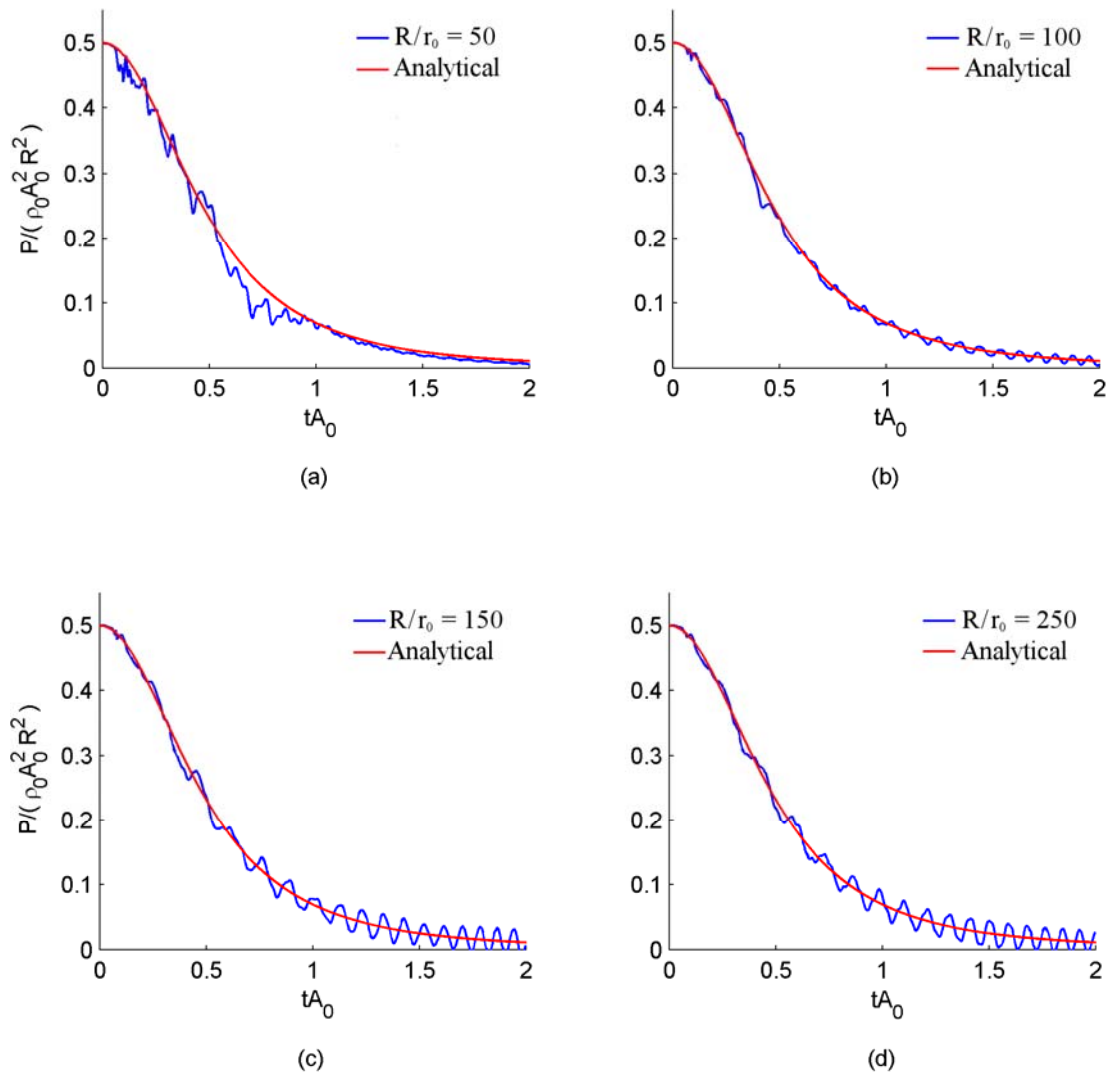
Figure 4.4 – Dimensionless pressure of the elliptical drop at point $(0,0)$ with dimensionless time tA_0 for a particle resolution of (a) $R/r_0 = 50$, (b) $R/r_0 = 100$, (c) $R/r_0 = 150$ and (d) $R/r_0 = 250$.
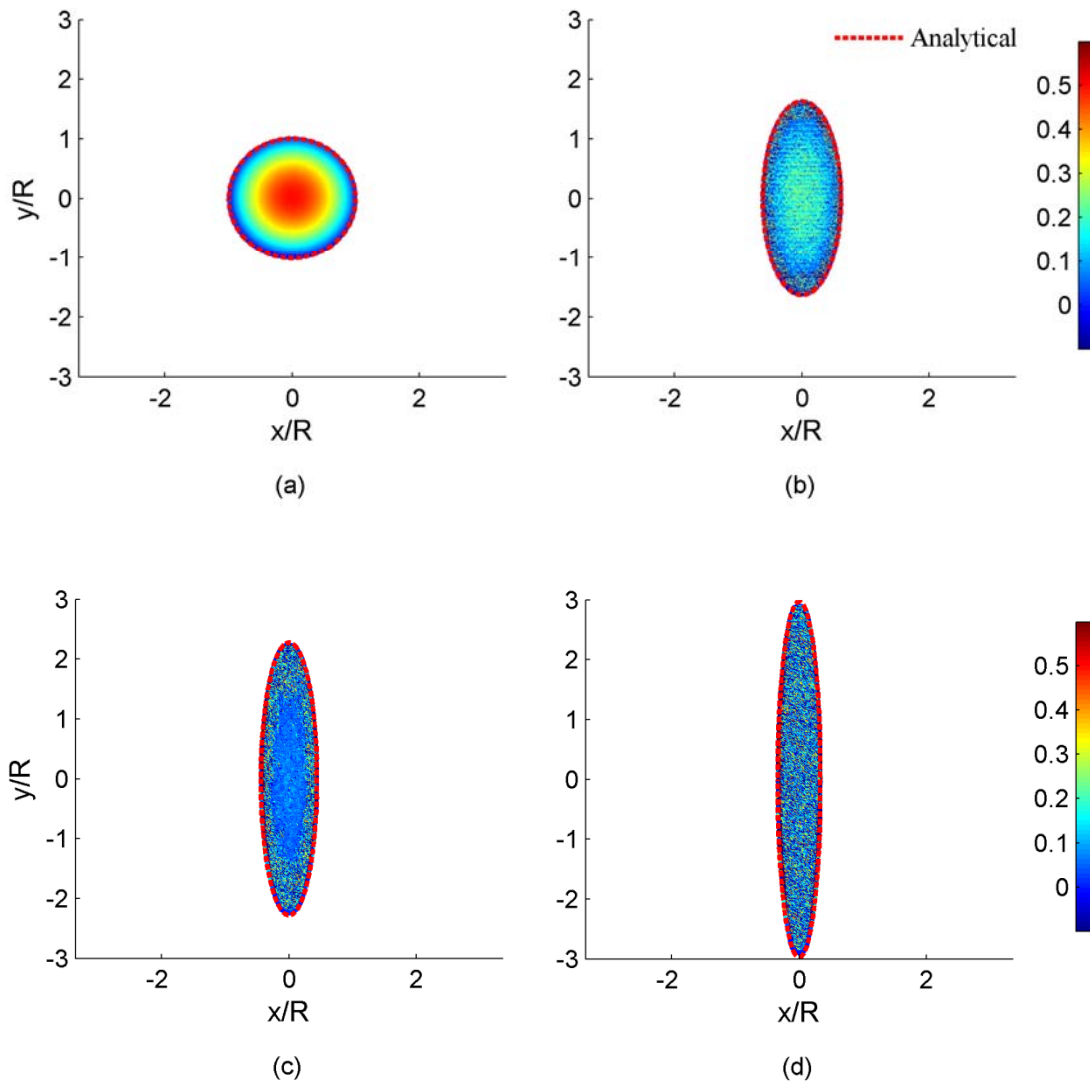
Figure 4.5 – Dimensionless positions and pressure, $P/(\rho_0 A_0^2 R^2)$, of 70681 SPH particles ($R/r_0 = 150$) without density reinitialisation at (a) $tA_0 = 0$, (b) $tA_0 = 0.5$, (c) $tA_0 = 1.0$ and (d) $tA_0 = 1.5$.

Another two gauge points were placed at (0.5R, 0) and (0, 0.5R) in order to record the fluid velocity as the drop evolved. Figure 4.6 describes the fluid velocity at both gauge points for varying particle resolution and compares the weakly compressible SPH model to the calculated velocities of the analytical incompressible solution. To determine the SPH fluid velocity at the gauge, the Gaussian cut-off kernel was used to perform a summation of the velocities of the individual fluid particles located within a compact support radius.
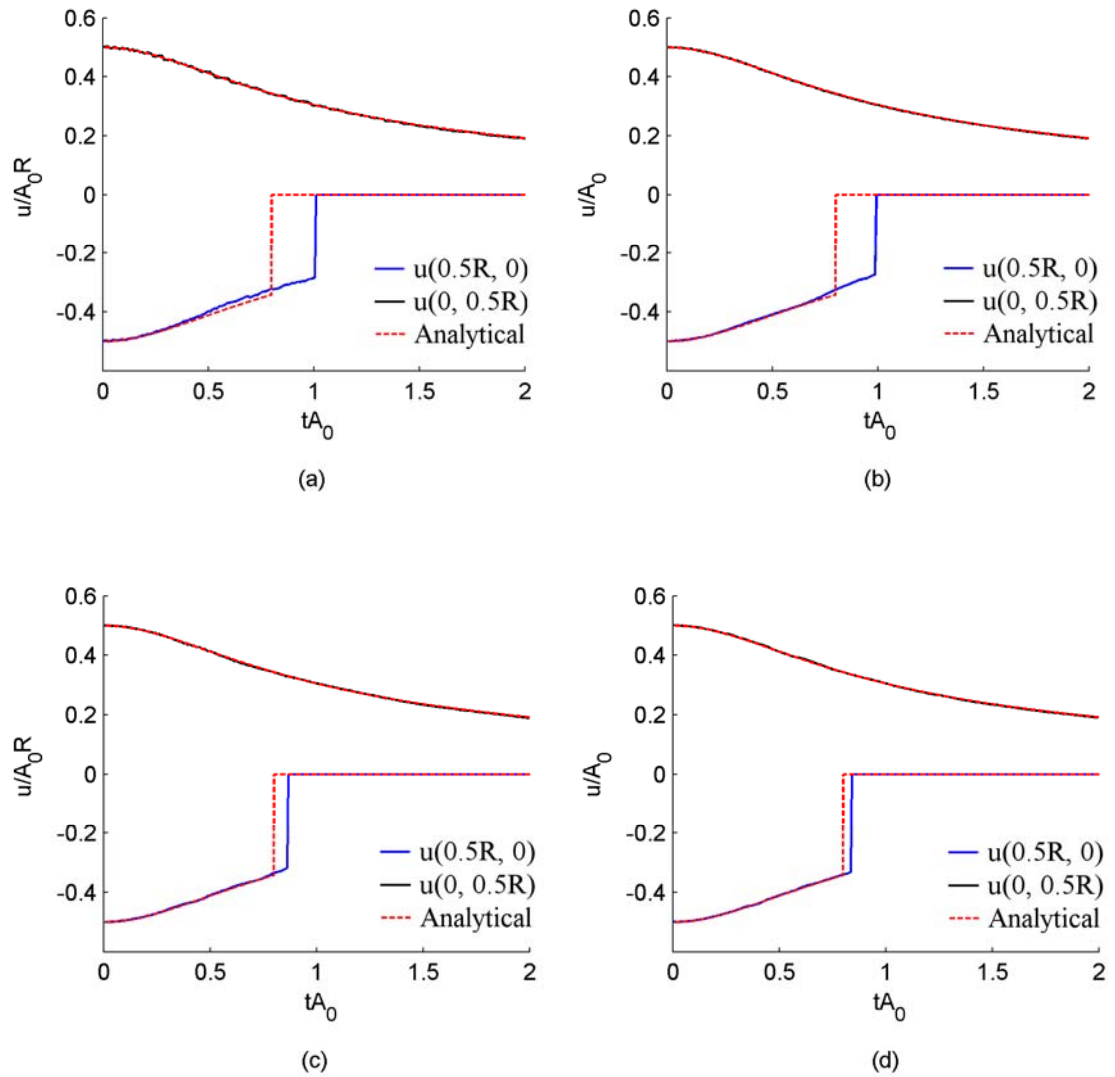
Figure 4.6 – Dimensionless velocity of the elliptical drop at points (0.5R, 0) and (0, 0.5R) with dimensionless time for particle spacing of (a) $R/r_0 = 50$, (b) $R/r_0 = 100$, (c) $R/r_0 = 150$ and (d) $R/r_0 = 250$.

At (0, 0.5R), all four SPH models agree well with the analytical fluid velocity for the entire simulation while at (0.5R, 0) the solutions are in agreement up until $tA_0 = 0.8$. The sharp change in the analytical fluid velocity coincides with the passage of the free surface. After the free surface had passed the sensor location the velocity of the fluid was undefined, but in order to illustrate the difference at each resolution (see Figure 4.6) the fluid velocity after this point in time was set to zero. At low resolution, the SPH free surface passes this point $tA_0 = 0.2$ after the analytical.

However the SPH model appears to converge towards the incompressible solution as the resolution is increased, to the point where the free surface of the $R/r_0 = 150$ model crosses (0.5R, 0) just $tA_0 = 0.04$ after the analytical. Increasing the resolution decreases the size of the fluid particles, resulting in a more accurate estimation of the moment the free surface crosses the gauge point.

Energy in the SPH method is not entirely conserved, particularly at low particle resolution. Figure 4.7 illustrates the ratio of the total kinetic energy at any given point in time to that of the initial system of particles. At low resolution the energy drops to 95% of its initial value by $tA_0 = 2$, which can be attributed to the influence of the artificial viscosity term. Colagrossi (2004) notes that as the resolution increases the energy conservation improves due to the smaller size of the compact support radius. Unfortunately due to the inherent SPH instabilities requiring correction via the artificial viscosity, some energy loss is unavoidable.
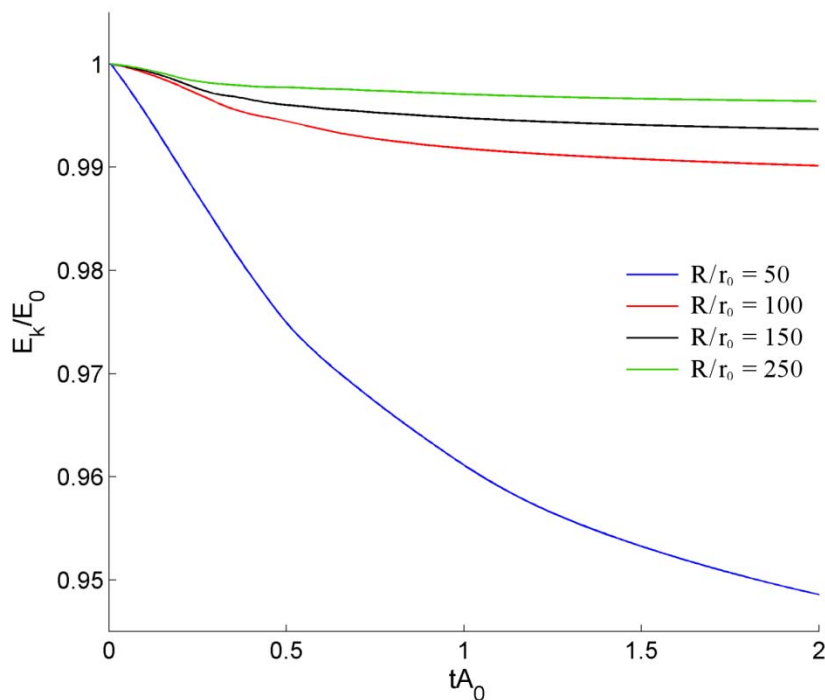
Figure 4.7 – Total kinetic energy ratio of the elliptical fluid drop at
a number of particle resolutions.

4.2 Evolution of a rotating square fluid patch

The second free surface problem considered as part of the validation process was the rotating square fluid patch. Modelled in a void of zero pressure, this test case is designed to test the response of the SPH algorithm to large negative fluid pressure and large vorticity. Like the elliptical drop problem, the fluid is inviscid and is governed by the Euler equation. Following Colagrossi (2004), the initial positions, pressures and velocity vectors of the SPH particles are described in Figure 4.8.

The square fluid patch with sides of length L was subjected to solid body rotation about (0,0) with constant angular velocity ω_0. The initial velocity field was given by,

$$\mathbf{u}_0(x,y) = \omega_0 \mathbf{r}$$

$$\mathbf{u}_0(x,y) = \begin{cases} u_0(x,y) = -\omega_0 y \\ v_0(x,y) = \omega_0 x \end{cases} \tag{4.26}$$
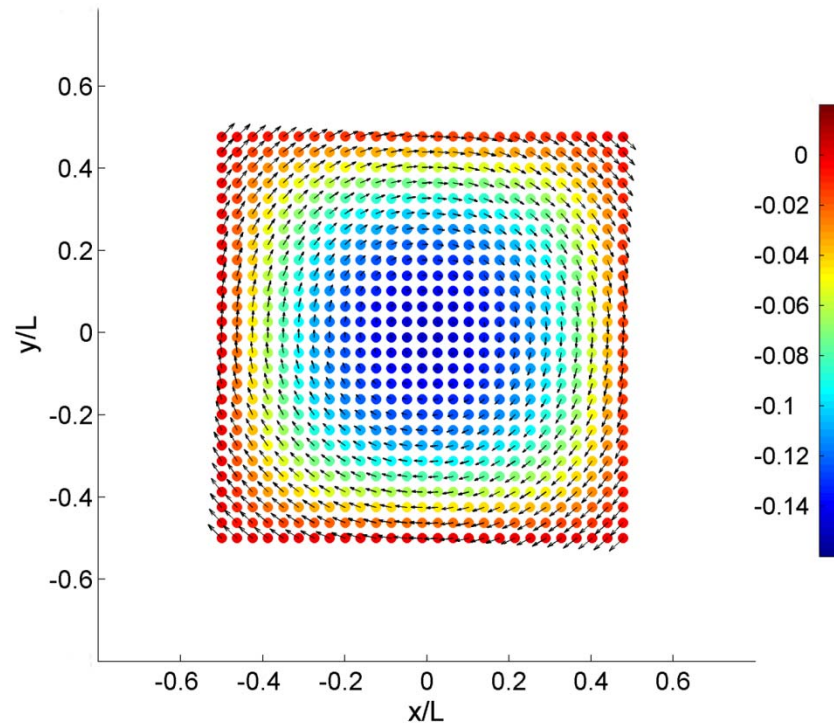
Figure 4.8 – Initial positions and velocity vectors of SPH particles coloured by dimensionless pressure, $P/(\rho_0 \omega_0^2 L^2)$, for the rotating square fluid patch.

It is convenient to write the initial velocity field in tensor form as,

$$\nabla \mathbf{u}_0(x, y) = \begin{bmatrix} 0 & \omega_0 \\ -\omega_0 & 0 \end{bmatrix} \tag{4.27}$$

Evaluating the curl of the velocity tensor yields an expression for the vorticity ζ of the incompressible fluid,

$$\zeta = \nabla \times \mathbf{u}_0(x, y) = 2\omega_0 \tag{4.28}$$

By Kelvin's theorem for inviscid, barotropic flow, the circulation around a closed loop - without crossing any boundaries - must be constant in time (White, 1999). So, the vorticity of the rotating fluid patch remains unchanged in space and time.

4.2.1 Analytical solution

A full analytical solution for the rotating square patch is yet to be found, however by considering the dynamic and kinematic conditions for free surface flow it is possible to predict the motion of some of the fluid particles. For an inviscid, incompressible fluid, the vorticity is conserved by Kelvin's theorem and, following the dynamic condition, the pressure at the free surface must be zero. This implies that the particles initially placed on a vertex remain on a vertex, and that each vertex particle maintains the velocity defined by the initial condition.

The initial pressure field must satisfy the pressure Posisson equation defined by Colagrossi (2004),

$$\frac{1}{\rho}\nabla^2 P = (\nabla \times \mathbf{u}) - \nabla \mathbf{u} : \nabla \mathbf{u} \tag{4.29}$$

Including the vorticity (4.28) and the inner product of the initial velocity tensor yields,

$$\frac{1}{\rho}\nabla^2 P_0 = 2\omega_0^2 \tag{4.30}$$

The solution to (4.30) was obtained by expanding P_0 in a series of sine functions to

give (Colagrossi, 2004),

$$P_0(x, y) = -\rho \sum_{i}^{\infty} \sum_{j}^{\infty} \frac{32\omega_0^2}{ij\pi^2 \left(\left(\frac{j\pi}{L}\right)^2 + \left(\frac{i\pi}{L}\right)^2 \right)} \varphi \qquad (4.31)$$

where,

$$\varphi = \sin\left(\frac{i\pi x}{L} + \frac{i\pi}{2}\right) \sin\left(\frac{jy}{L} + \frac{j\pi}{2}\right) \qquad (4.32)$$

The initial pressure field is found by summing over the odd integers i and j, where L is the length of one side of the patch. Equations (4.31) and (4.32) converge to a solution after just a few iterations.

4.2.2 SPH simulation

A similar method to that employed to simulate the evolution of the initially circular fluid drop was used to model the evolution of the square fluid patch. The initial angular velocity was set to $\omega_0 = 100 \text{ rad/s}^{-1}$ for a square with sides of length 1 m. Particles located on the vertices move with a maximum velocity of $0.7LA_0$, which requires a sound speed of at least $7LA_0 = 700$ m/s to avoid compressibility effects. However in order to be consistent with the initially circular drop test case, the sound speed in the rotating patch was set to $14LA_0 = 1400$ m/s (Colagrossi 2004). Four models of varying particle resolution ($L/r_0 = 50, 100, 150$ and 200) were modelled over a period of 0.02 s ($t\omega_0 = 2.0$) using a smoothing length of $h = 1.33r_0$.

The dimensionless positions and pressures of the SPH particles at multiple time instants are illustrated in Figure 4.9. In order to compare against the analytical solution, the initial position of the free surface of the patch is depicted by the black dashed line. The blue dots and dashed lines are the theoretical positions and trajectories of the vertex particles respectively. Early in the simulation, particularly at the first two time instants, the particles initially located on the free surface do follow the expected trajectory. However as the patch evolves further in time the vertex particles depart from their expected path. When the strength of the artificial viscosity

is increased by increasing the coefficient α in equation (3.88) the vertex particles depart further from the expected path (see Figure 4.10). Removing the artificial viscosity altogether allows the particles to maintain a trajectory very near that expected, but does add significant noise to the pressure field particularly near the free surface.
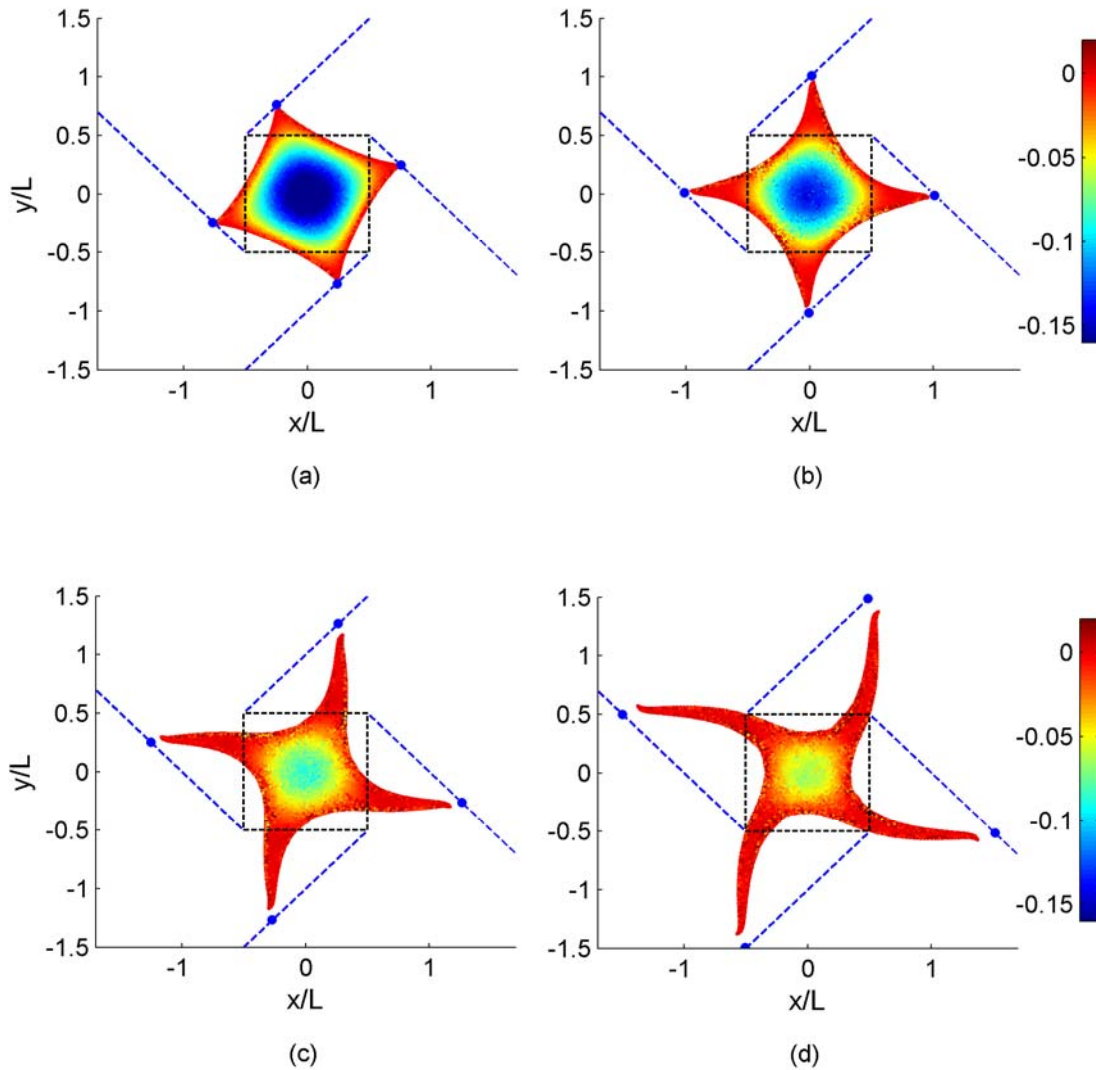
Figure 4.9 – Positions of SPH fluid particles at a resolution of $L/r_0 = 150$ coloured by dimensionless pressure $P/(\rho_0 \omega_0^2 L^2)$ at four time instants (a) $t\omega_0 = 0.5$ (b) $t\omega_0 = 1.0$ (c) $t\omega_0 = 1.5$ and (d) $t\omega_0 = 2.0$. The blue dashed lines are the expected trajectories of the vertices and the black dashed line describes the initial free surface position.
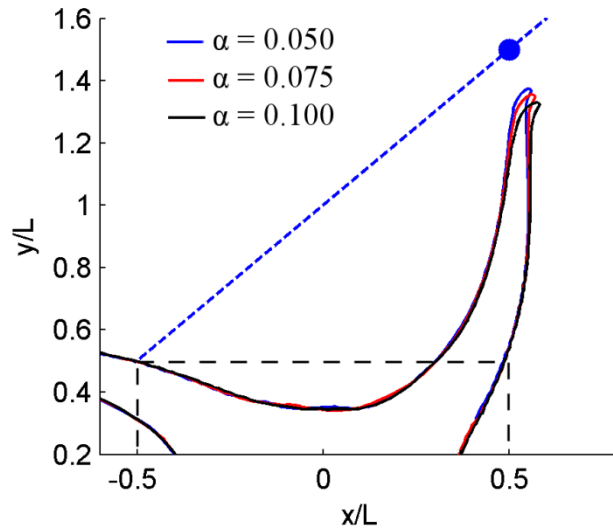
Figure 4.10 – Free surface position for three values of α ($L/r_0 = 150$) at $t\omega_0 = 2.0$. The blue dot indicates the theoretical position of the vertex.

At the centre of the patch, the pressure gradually increases towards zero with time. It is not possible to predict the pressure at any point in the fluid domain, so Colagrossi (2004) implemented a Boundary Element Method (BEM) algorithm based on that used by Greco (2001) in order to compare the pressures of the SPH particles against a reference solution. The BEM is one of the more accurate solvers when modelling free surface flows but it does require the free surface to be unbroken and free of any fragmentation throughout the course of the simulation. The rotating square patch maintains an unbroken free surface and so the very efficient BEM is well suited to solving the problem and providing a reference solution.

A numerical pressure gauge was placed at the centre of the patch $(0,0)$ in a similar fashion to the initially circular drop. Figure 4.11 describes the pressure at $(0,0)$ with time for a number of simulations with varying particle resolution. The BEM solution for the pressure (Colagrossi, 2004) follows an upward trend similar to that of a weak exponential decay function. Each SPH solution follows a similar trend, oscillating about a mean value slightly lower than that predicted by the BEM model. The acoustic resonant frequency of the $L/r_0 = 100$ model starts at $9.7\omega_0$ and increases to $12.0\omega_0$ as the patch evolves through time. Increasing the particle resolution from $L/r_0 = 50$ through to $L/r_0 = 200$ yields a pressure signal of smaller amplitude that more closely approximates the reference BEM solution.
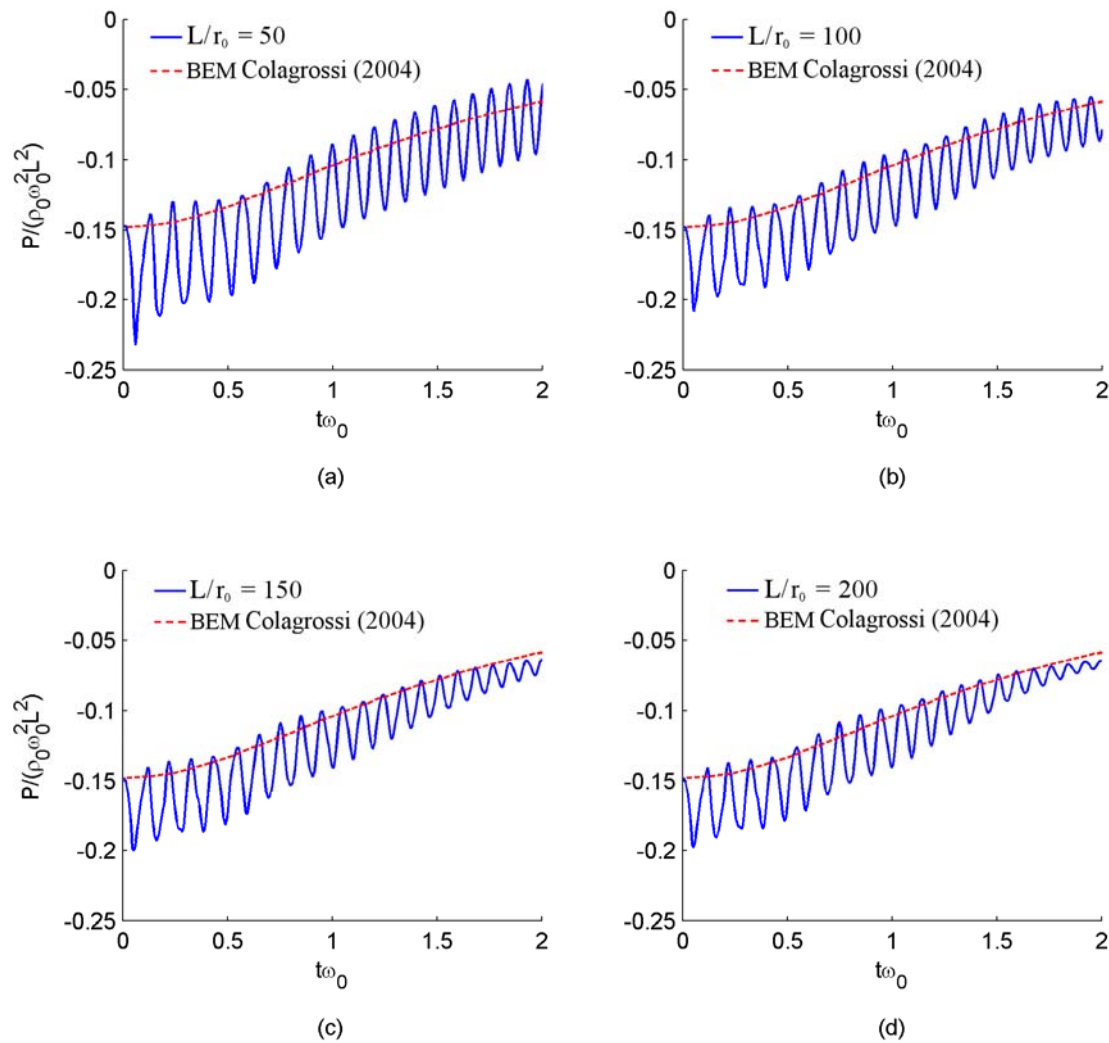
Figure 4.11 – Pressure at the centre of the square fluid patch compared
with the BEM solution of Colagrossi (2004) at varying particle resolution
(a) $L/r_0 = 50$, (b) $L/r_0 = 100$, (c) $L/r_0 = 150$ and (d) $L/r_0 = 200$.

The smooth pressure field and regular particle spacing illustrated in Figure 4.9 is achieved only by including the density reinitialisation routine and the correction for tensile stability. Removing both of these corrections has a detrimental effect that can be seen in Figure 4.12. The negative pressure at the centre of the patch encourages the fluid particles - via the momentum equation (3.66) - to cluster together in a high particle number density that is not reflected in the fluid density. The tensile stability correction prevents this artificial clustering from occurring by including a repulsive term in the momentum equation (see Section 3.3.2). Removing the density
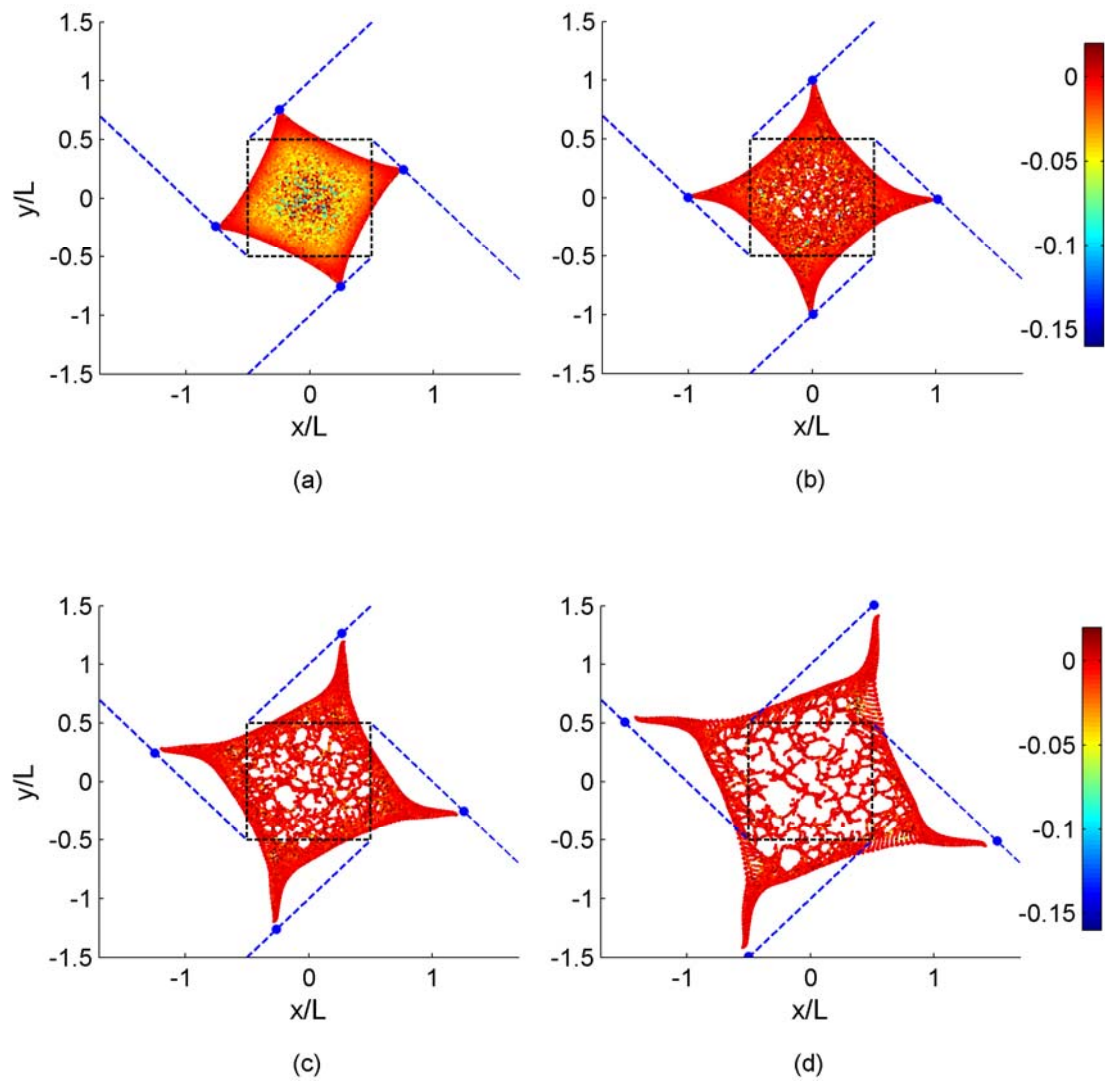
Figure 4.12 – Positions of SPH fluid particles at a resolution of $L/r_0 = 150$ without density reinitialisation and the correction for tensile stability. Particles are coloured by dimensionless $P/(\rho_0 \omega_0^2 L^2)$ pressure at (a) $t\omega_0 = 0.5$ (b) $t\omega_0 = 1.0$ (c) $t\omega_0 = 1.5$ and (d) $t\omega_0 = 2.0$.

reinitialisation routine gradually degrades the pressure field when the particles are ordered, but as the particles begin to cluster in the absence of the tensile stability control the pressure of the entire field quickly approaches zero. Figure 4.13a outlines the pressure at the centre of the patch for two cases, with tensile stability ($\epsilon = 0.2$) and without ($\epsilon = 0.0$). The pressure initially has a similar trend to the BEM solution, but without the tensile stability correction the pressure at the gauge quickly rises to

zero. At this point small voids have begun to form in the fluid, leaving some particles without a filled compact support. This in turn forces the local pressure, and over time the global pressure, to tend towards zero.

The SPH system kinetic energy shown in Figure 4.13b does not maintain a constant value as expected for an inviscid simulation. The models studied in this thesis with all corrections implemented lost between 2 and 5 percent of their initial energy over $t\omega_0 = 2.0$ in a similar trend, but there is a noticeable difference between the models with and without the tensile stability control. The total energy of the SPH model without tensile stability control drops sharply as soon as voids begin to appear at $t\omega_0 = 0.3$. From this point on, the particles at the centre of the patch lose angular momentum as the clusters develop. So to prevent any corruption of the pressure field and artificial clustering of fluid particles, the tensile stability correction (with $\epsilon = 0.2$) and the density reinitialisation procedure have been included in all models described throughout the remainder of this thesis.
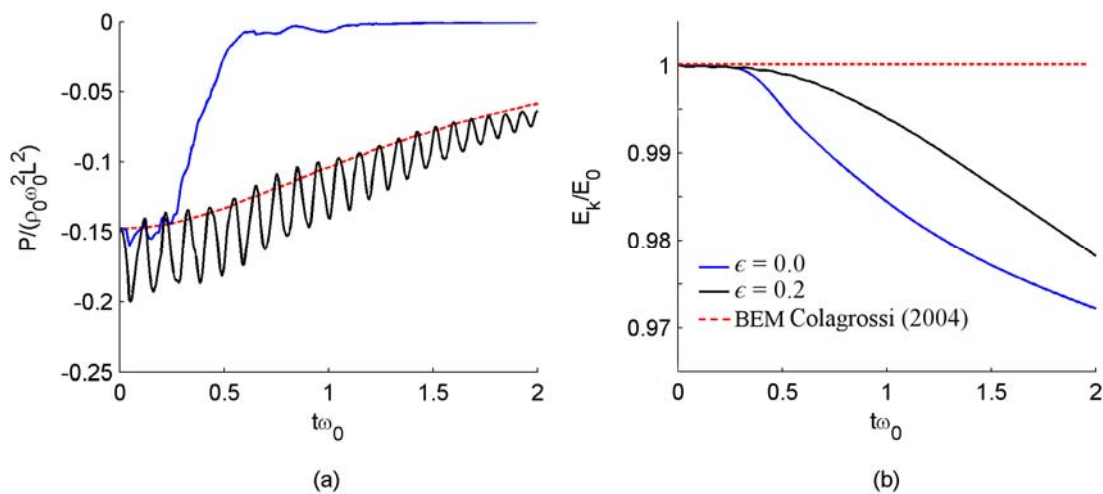
Figure 4.13 – The dimensionless pressure (a) and system kinetic energy ratio (b) for two SPH models with ($\epsilon = 0.2$) and without ($\epsilon = 0.0$) tensile stability at a particle resolution of $L/r_0 = 150$.

4.3   Contained hydrostatic fluid

The analysis of fluid-structure interaction is also of major importance in SPH simulations and so it is vital that the boundary methods be investigated thoroughly before modelling complex geometries. One of the simplest cases suited for testing the boundary methods outlined in Section 3.6.2 is an open-topped stationary rectangular tank filled with water (Pakozdi, 2008). In this test case the rigid wall boundary condition is enforced by applying the ghost particle method.

As for the elliptical drop and the rotating patch, the motion of the fluid in the tank is also governed by the Euler equation (3.55), but in this test case the gravitational force component has now been included. The gravitational force is also responsible for the initial hydrostatic pressure field (see Figure 4.14) given by,

$$P(x, y) = \rho_0 g (H - y) \tag{4.33}$$

where H is the depth of the fluid and ρ_0 is the density of the fluid at standard temperature and pressure.
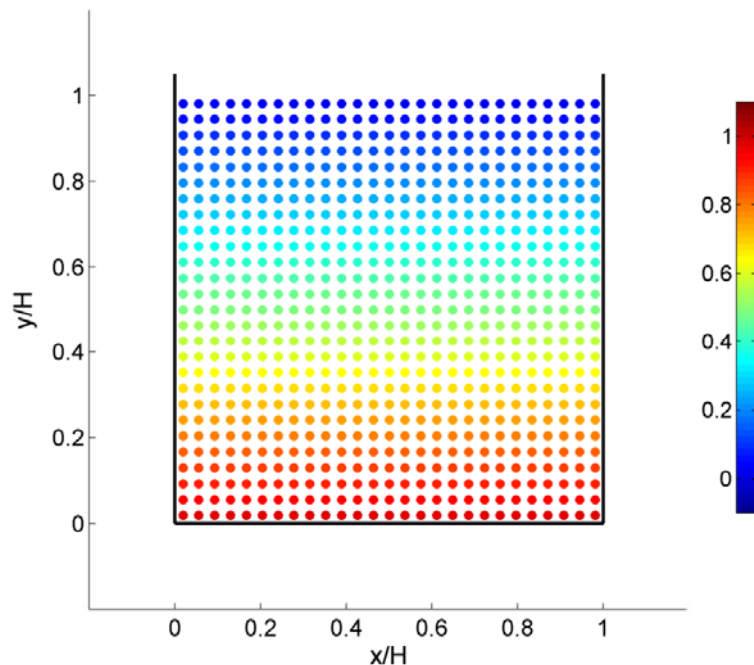
Figure 4.14 – Initial SPH particle positions and pressure for the contained tank problem. Particle positions and pressures are quoted as dimensionless variables x/H and $P/(\rho_0 g H)$ respectively.

Studying the behaviour of an incompressible fluid using the weakly compressible SPH method can be problematic. For instance, if the weakly compressible fluid is made too compressible, the fluid can compress under its own weight (Pakozdi, 2008). This becomes obvious, particularly near the solid wall at the bottom of the tank, as the fluid particles located near the boundary are forced closer. The separation between the fluid and ghost particles near the horizontal boundary reduces, so in turn the local fluid pressure rises. Finally the fluid particles are pushed away from the boundary due to the increase in pressure. This can be detrimental to the simulation or can simply manifest itself as periodic oscillations in the potential energy of the fluid. Pakozdi (2008) defines the set of natural frequencies of oscillation for the static tank as,

$$f = \frac{c_s}{2} \sqrt{\left(\frac{2m_v}{L}\right)^2 + \left(\frac{2n_v + 1}{2H}\right)^2} \tag{4.34}$$

where m_v and n_v describe the mode of vibration in the horizontal and vertical planes respectively and L is the width of the tank.

4.3.1 SPH simulation

In order to model the fluid in the tank, the SPH algorithm used to simulate the elliptical drop and the rotating patch was extended to include ghost particles. Four models of varying particle resolution ($H/r_0 = 50, 100, 150$ and 200) were modelled for a depth of $H = 1$ m over a period of 4.0 s using a smoothing length of $h = 1.33r_0$ (following Pakozdi, 2008). If one of the side walls was removed and the fluid allowed to flow out along a horizontal surface, the maximum speed of the surge front would be $\sqrt{2gH}$. So in order to prevent any compression effects, the fluid sound speed was set to $c_s = 11\sqrt{2gH}$ (Pakozdi, 2008).

At a sound speed of 48.7 m/s, the potential energy of the system was calculated and compared against the initial value (see Figure 4.15). Every model studied follows a similar trend over time; the potential energy drops from its initial value (by less than 0.02%) and then in all cases but the lowest resolution, the system energy gradually

begins to climb. The small oscillations in the potential energy ratio (less than 0.01%) are due to the slight compression experienced at the base of the tank as a result of the weakly compressible approximation. A fast Fourier transform of the energy ratio at $H/r_0 = 200$ found a dominant frequency at $3.90\sqrt{g/H}$ and a secondary peak at $11.70\sqrt{g/H}$ (see Figure 4.17). These compare well with the expected resonant frequency, $3.88\sqrt{g/H}$, and the first harmonic, $11.66\sqrt{g/H}$, calculated from equation (4.34).
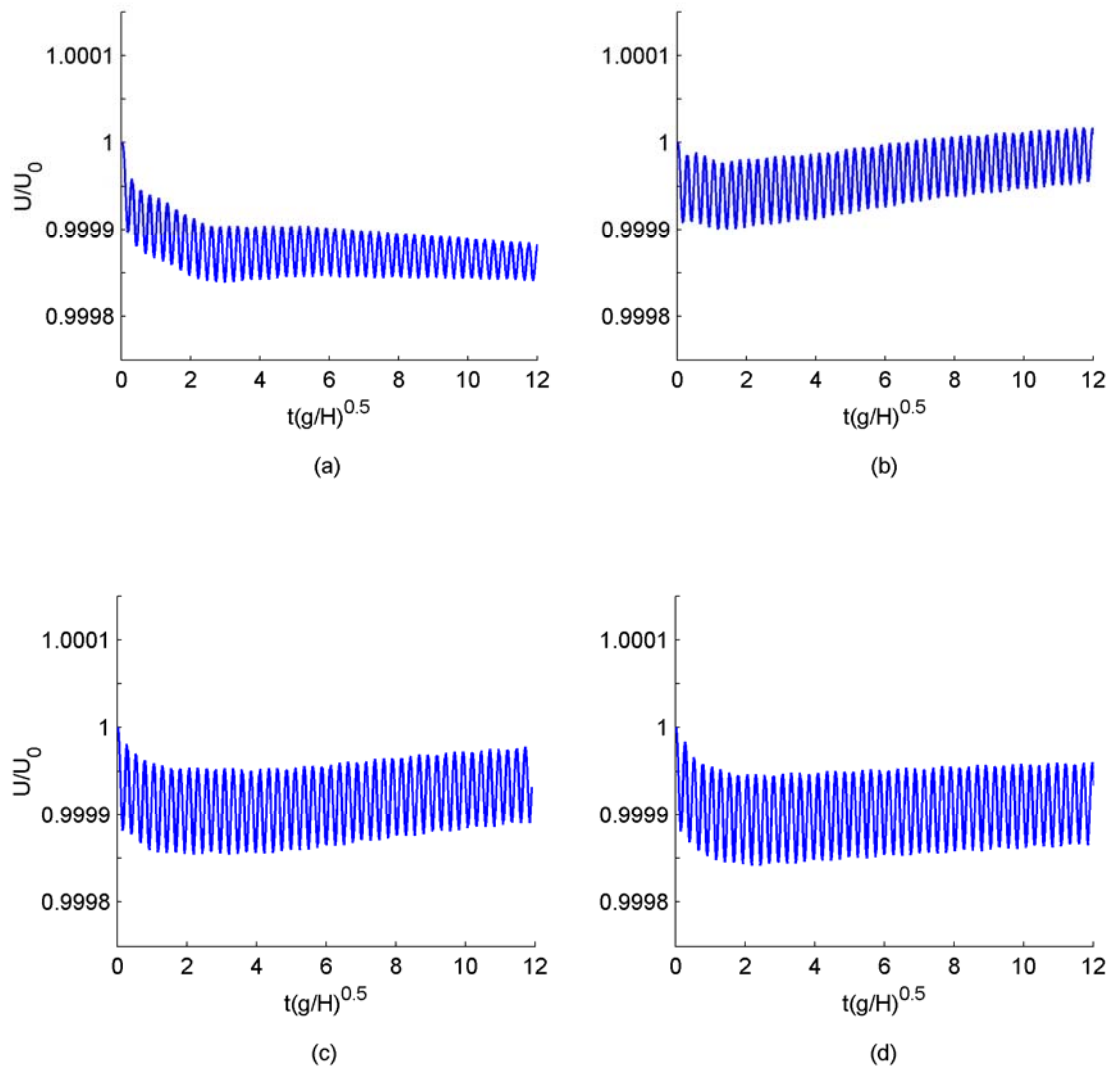
Figure 4.15 – Potential energy of the fluid at four different particle resolutions (a) $H/r_0 = 50$, (b) $H/r_0 = 100$, (c) $H/r_0 = 150$ and (d) $H/r_0 = 200$.

Numerical pressure sensors (similar to that used in Section 4.1) were placed down the centreline of the tank at depths of $0.33H$ and $0.66H$ in order to measure the fluid pressure. Figure 4.16 illustrates the pressure as a function of time measured at each of the sensor locations with a particle resolution of $H/r_0 = 200$. At each sensor the pressure oscillated about a mean value close to that expected with a maximum amplitude of approximately 2-3%. Like the potential energy, the noise in the pressure signal is due primarily to compressibility effects as the frequency of oscillation has been related directly to the prescribed speed of sound. The first two peaks in the fast Fourier transform of the pressure signal are at the same frequencies as those calculated from the potential energy, however the fast Fourier transform of the pressure signal at the centre of the tank clearly indicates that there is indeed another harmonic at $19.50\sqrt{g/H}$. The simulated third harmonic agrees well with the expected result for $m_v = 0$ and $n_v = 2$ in equation (4.34), $19.44\sqrt{g/H}$.

Although the potential energy and pressure traces oscillate about their mean and expected values, the approximation of an incompressible fluid with a weakly compressible one is valid as these variations are very small. Therefore, for the case of fluid contained in a static tank, compressibility effects when using a sound speed at least one order of magnitude greater than the maximum fluid velocity are negligible.
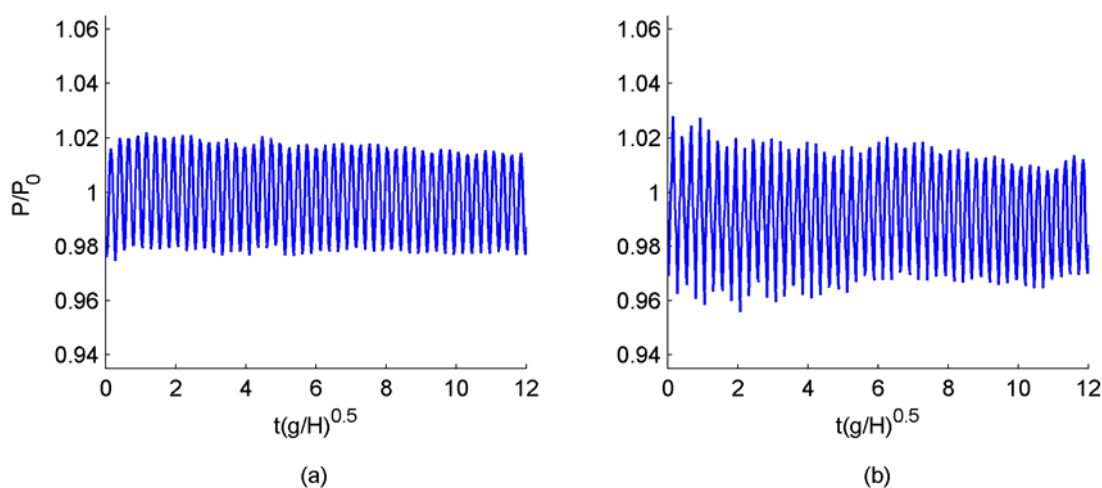
Figure 4.16 – Pressure variation at two points in the tank (a) (0.5L, 0.33H) and (b) (0.5L, 0.66H) at a particle resolution of $H/r_0 = 200$.
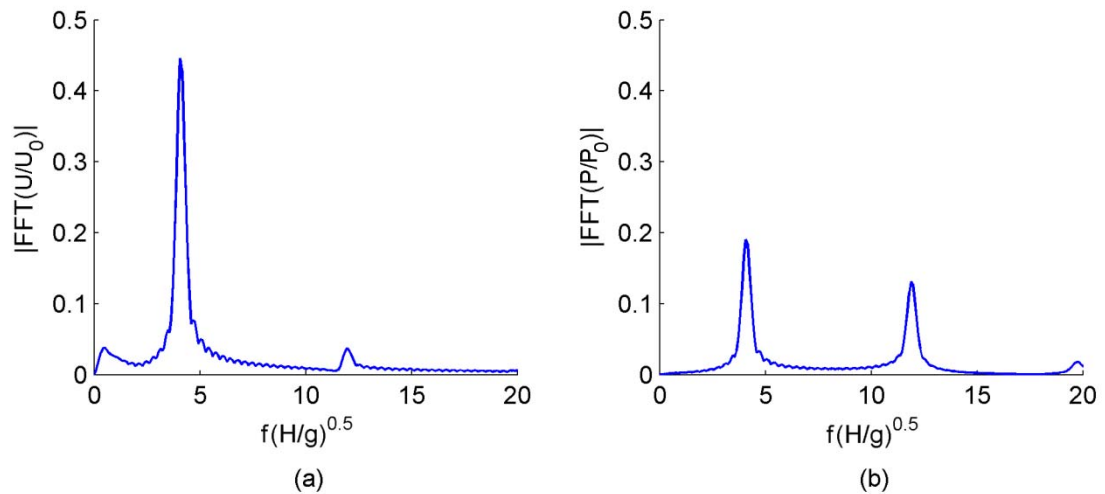
Figure 4.17 – FFT of (a) the system energy and (b) the pressure variation
at 0.33H at a particle resolution of $H/r_0 = 200$.

4.4 The breaking dam

One of the most widely used SPH validation test cases is the breaking dam. Many SPH authors have used this example as a primary model for validating their numerical algorithm due to its simplicity and the availability of experimental data. Martin and Moyce (1952) performed this experiment in a Perspex lined channel using a paper diaphragm to hold the reservoir (of equal length and depth) in place. When the diaphragm was released, the resultant fluid flow was photographed at 300 frames per second in order to determine the position of the surge front.

Zhou et al. (1999) extended the experiment of Martin and Moyce (1952) by measuring and simulating the height of the surge front using a number of water depth probes, two of which are located at points A and B, 1.03 m and 1.53 m respectively from the reservoir (see Figure 4.18). In this case the reservoir ($L = 1.2$ m wide and $H = 0.6$ m deep) was held in place by a plastic flap which was lifted rapidly in order to allow the water to flow into the flume and strike the far wall. To determine the loads on the far wall a number of pressure sensors were placed at different heights along the wall, where C (0.16 m above the channel floor) is the lowest gauge. Data from these three sensors have been used as a basis for the validation of the SPH algorithm.
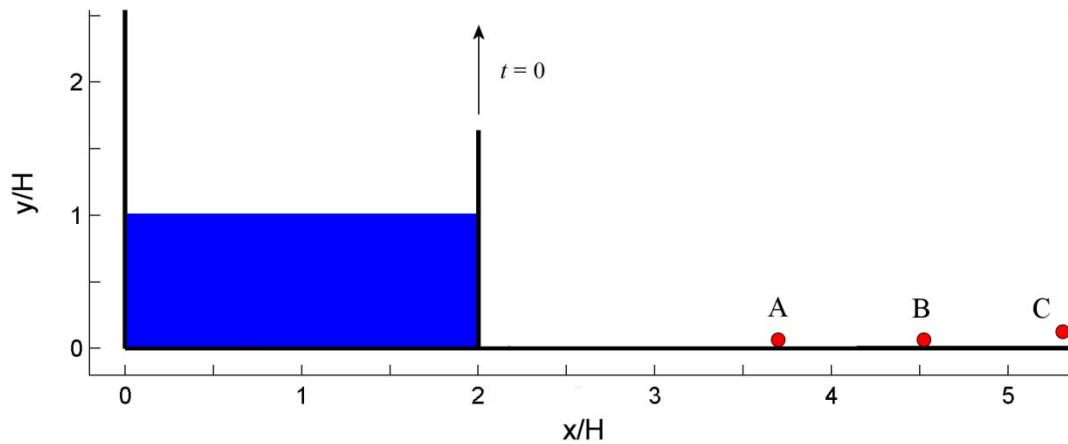
Figure 4.18 – Schematic diagram of the dam break experiment
conducted by Zhou et al. (1999).

4.4.1 SPH simulation

The experiment conducted by Martin and Moyce (1952) was replicated by setting the initial depth of the fluid H and the width of the reservoir L to 1.0 m. At time $t = 0$ the retaining wall was removed and the fluid allowed to flow into an infinitely long channel. Like the tank problem described in Section 4.3, the sound speed was set such that the maximum expected fluid velocity did not exceed $0.1c_s$ in an attempt to minimise compression effects. In a dam break situation, the surge front accelerates to a maximum velocity of $\sqrt{2gH}$ which yields a sound speed of $c_s = 11\sqrt{2gH}$. As recommended by Colagrossi and Landrini (2003), the artificial viscosity was included ($\alpha = 0.03$) and the density field was reinitialised every 20 time steps.

When held behind the reservoir wall the pressure field takes the same hydrostatic form as the initial condition for the fluid contained in a motionless tank. If the reservoir wall is removed after the SPH simulation has begun, the fluid pressure at the newly exposed free surface quickly drops to zero. This sudden drop in pressure on the side of the reservoir causes a large pressure wave to propagate through the fluid domain, reflecting off the solid walls and over time destroying the expected near-hydrostatic pressure field. To prevent this from occurring, the dam is initially set with the reservoir wall removed and a pressure field (see Figure 4.19) originally

developed by Pohle (1950) given by,

$$P(x,y) = \rho g y - \frac{8\rho g H}{\pi^2} S_P \tag{4.30}$$

where,

$$S_P = \sum_{n=0}^{\infty} \frac{1}{(2n+1)^2} e^{\frac{(2n+1)\pi\left(x-\left(L-\frac{B}{2}\right)\right)}{2H}} \cos\left(\frac{(2n+1)}{2H}\pi(y+H)\right) \tag{4.31}$$

Greco (2001) implemented this analytical solution for the pressure field as part of a BEM study of the two dimensional dam break. Pohle (1950) defines this pressure field for a reservoir of infinite length, however Greco has shown that (4.42) can be successfully applied if the reservoir length L is greater than or equal to $3H$. In this thesis the analytical solution has been applied to dam breaks with a length less than $3H$ by including the ghost particles opposite the left wall in the initial pressure field. This approximation serves well to preserve a smooth, near hydrostatic pressure field throughout the simulation.
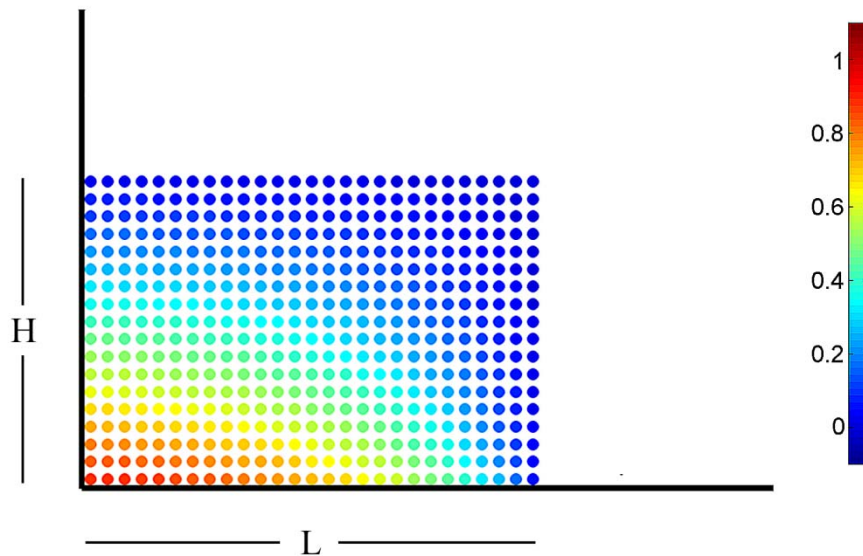
Figure 4.19 – Initial positions and dimensionless pressure $(P/(\rho_0 g H))$ of SPH particles for a dam break.

40000 SPH particles ($H/r_0 = 200$) initially placed on a Cartesian lattice in a dam of aspect ratio 1 were released at time $t = 0$ and allowed to flow into the adjacent channel. The position of the leading particle was plotted over time and compared against the SPH results of Colagrossi (2004) and the experimental findings of Martin and Moyce (1952). Colagrossi's SPH algorithm is very similar to the method used here and this is reflected in the plot of the surge front position with time (see Figure 4.20). One reasonable explanation for the considerable over-estimation of the experimental surge front position by both SPH models is the lack of viscosity. No other plausible explanation has been found.

Martin and Moyce (1952) only provided information on the surge front position, not its form nor the pressure that the surge exerts on the channel floor. The experimental results of Zhou et al. (1999) provide an indication of the shape of the surge by measuring its height above the channel at points A and B (see Figure 4.18). Figure 4.21 describes the height of the surge at the two sensors and compares the SPH simulation with the experimental and BEM study performed by Greco (2001) for a reservoir with an initial aspect ratio of 2.
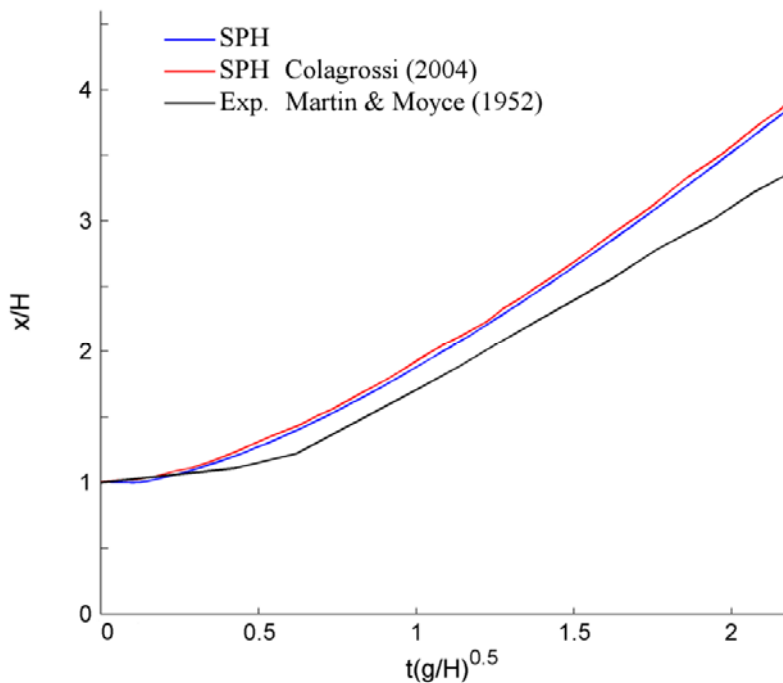
Figure 4.20 – Surge front position with time of the $L = 1$ and $H = 1$ dam break compared against the SPH results of Colagrossi (2004) and the experimental data of Martin and Moyce (1950).
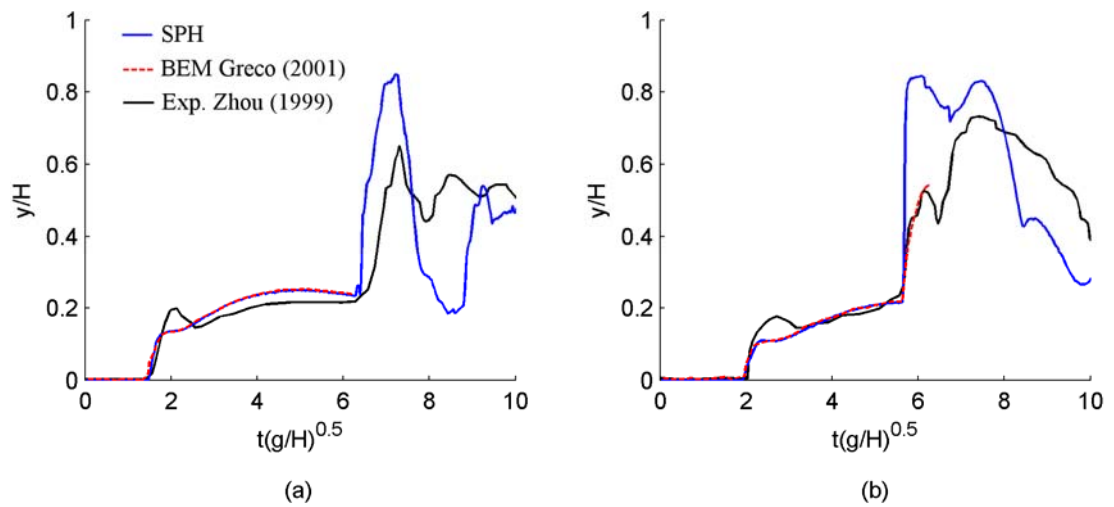
Figure 4.21 – Water depth at points A and B with reference to Zhou et al. (1999) and the BEM simulation of Greco (2001) for 80000 fluid particles at a resolution of ($H/r_0 = 200$), where $H = 1$ m and $L = 2$ m.

The initial rise in water height at both sensors coincides with the passage of the toe of the surge front. The toe height measured by the experiment is slightly greater than that predicted by both numerical methods, suggesting that the advancing surge measured by Zhou et al. (1999) was breaking rather than flowing smoothly. It is worth noting that the boundary element method requires the free surface of the fluid to be smooth and unbroken in order to resolve the properties of the fluid. So, when the free surface fragments after striking the far wall, running up it and overturning as a breaking wave (see Figure 4.22) the BEM solution ends. Until this point, $t(g/H)^{0.5} = 6.0$ (dimensionless time instant), the SPH simulation almost exactly matches the BEM data at both height sensors with the exception of a slight disagreement after $t(g/H)^{0.5} = 5.6$ at sensor B.

The heights measured by Zhou et al. (1999) differ slightly from the BEM and SPH simulations as the toe passes each sensor. Beyond this point, until the fluid overturns and breaks at $t(g/H)^{0.5} = 6.0$, the surge heights are quite similar. After the water overturns there is considerable difference in the fluid depth as the SPH model is single phase and therefore neglects any influence air may have on the shape of the free surface.

(a)

(b)
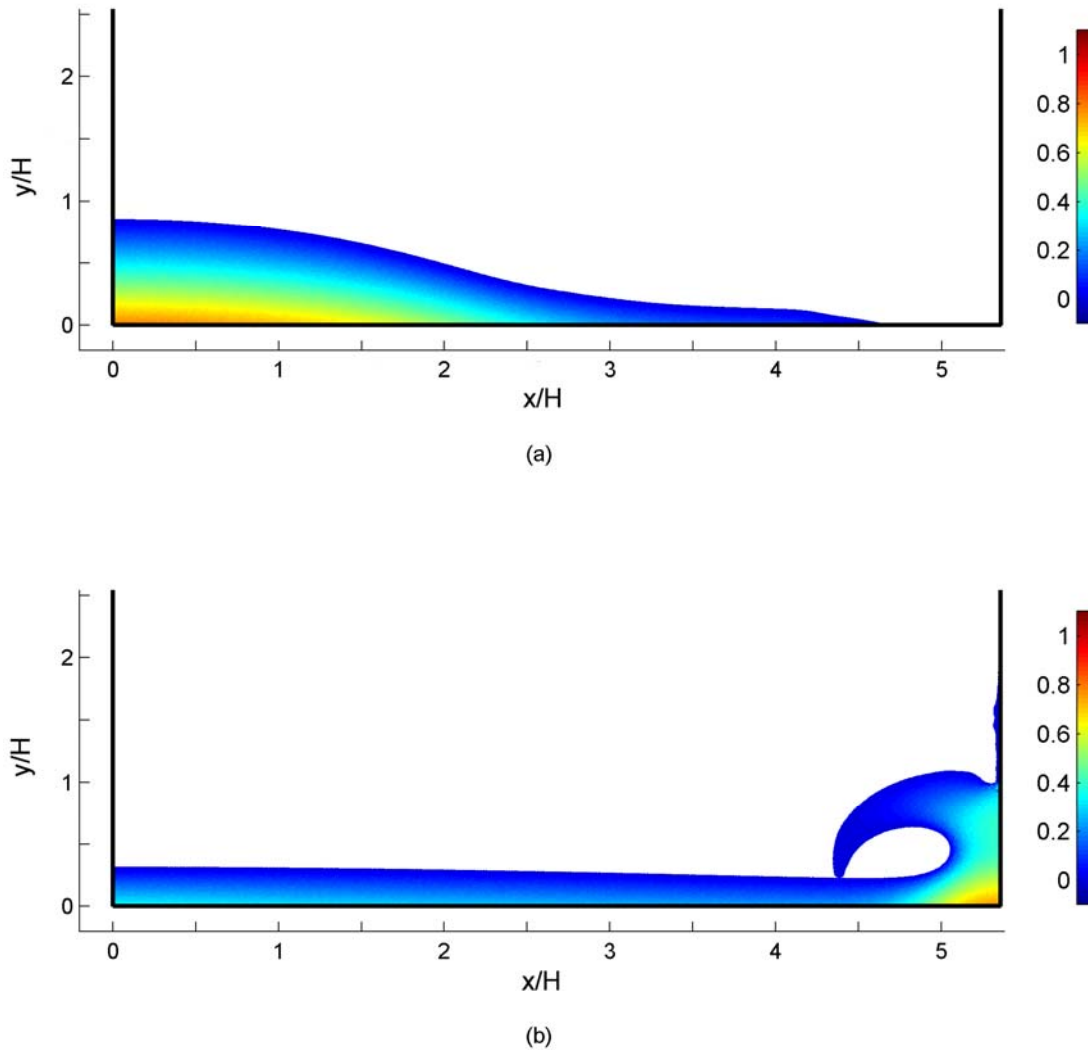
Figure 4.22 – The Zhou et al. (1996) dam break simulation at two dimensionless time instants (a) $t\sqrt{g/H} = 2$ and (b) $t\sqrt{g/H} = 6$. Each of the 80000 fluid particles is coloured by dimensionless pressure, $P/\rho_0 gH$.

The pressure field $t\sqrt{g/H} = 2$ after the retaining wall was released (see Figure 4.22a) has a smooth, almost hydrostatic, form. This is carried through to $t\sqrt{g/H} = 6$, with the exception of the high pressure region located around the bottom right corner of the channel. Figure 4.23 compares the pressure measured by Zhou et al. (1999) at point C, 0.16 m above the channel floor (see Figure 4.18), with the pressure simulated by both the BEM and SPH methods. The numerical pressure sensors used a simple averaging technique to determine the local fluid pressure. Each sensor had a

diameter of $4h$ (26.6 mm) and sampled any particles located within $5h$ (33.3 mm) of the solid wall. To reduce the numerical noise outliers were removed and the final pressure was calculated by determining the mean pressure of the particles remaining inside the sensor.

All three pressure traces begin to measure fluid pressure above atmospheric a short moment after the toe meets the wall ($t\sqrt{g/H} = 2.5$) and climb with similar gradient. While the BEM slightly under-predicts the initial pressure peak, the SPH solution is comparable to the experimental value. From here on the SPH simulation slightly over predicts the pressure at point C until the fluid overturns and breaks. Without air in the problem domain, the SPH fluid pressure climbs artificially as the fluid collapses upon itself, generating a pressure peak approximately 20% greater than the experimental pressure.
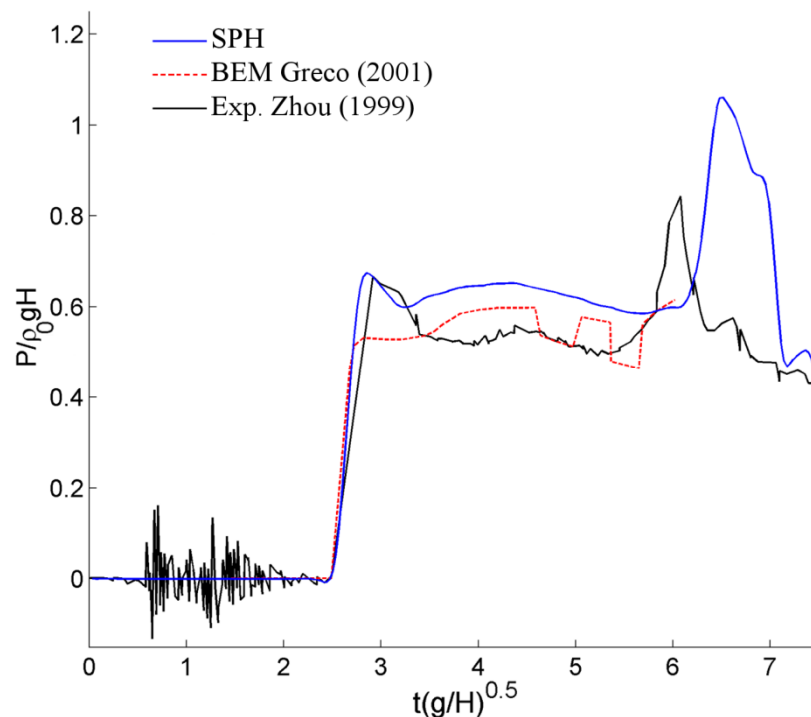
Figure 4.23 – Fluid pressure on the wall at point C with reference to the experiments of Zhou et al. (1999) and the BEM simulation of Greco (2001) for 80000 fluid particles at a resolution of $H/r_0 = 200$.
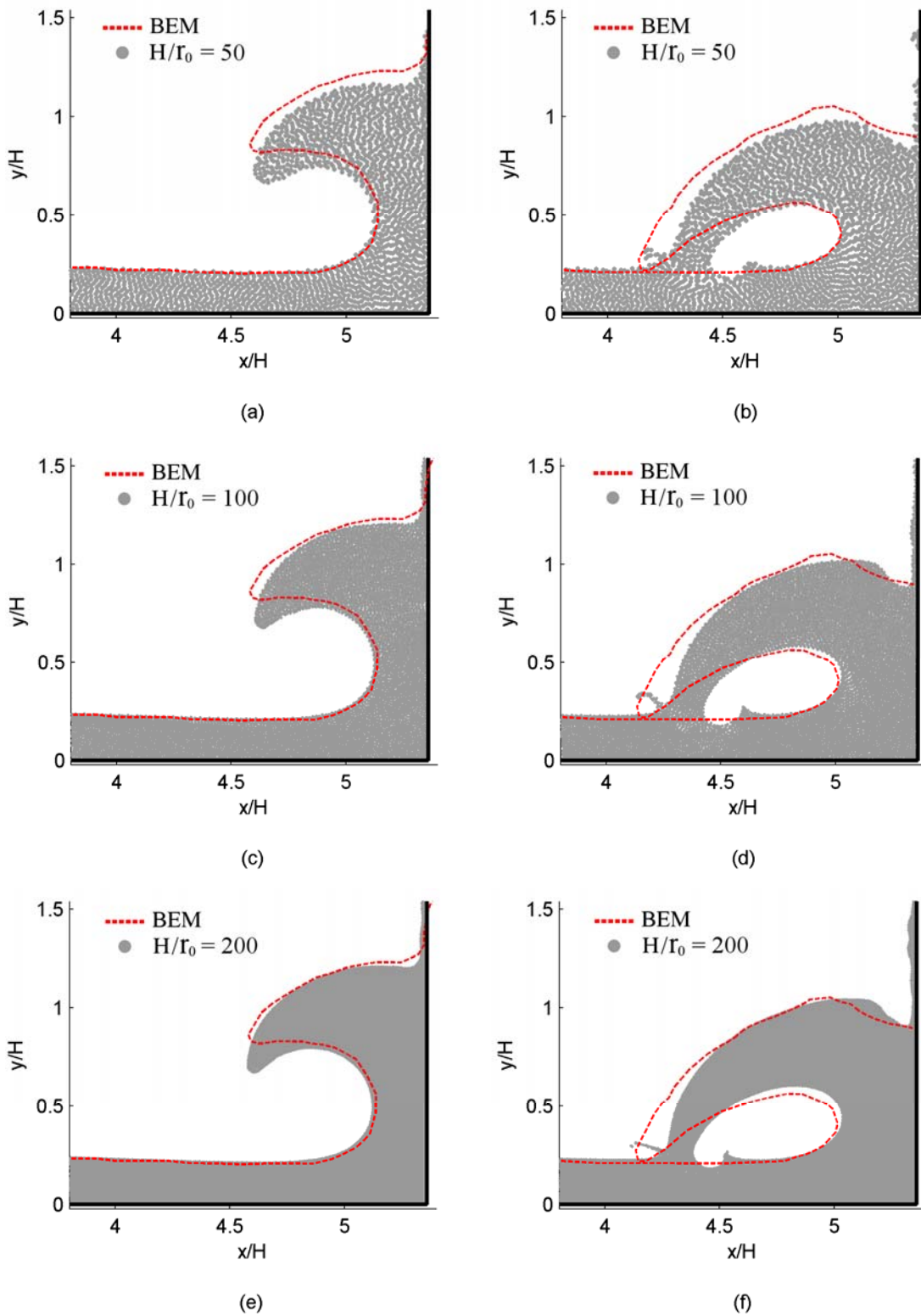
Figure 4.24 – Free surface comparison with the BEM study of Greco (2001) at $t\sqrt{g/H} = 5.6$ (left plots) and $t\sqrt{g/H} = 6.2$ (right plots) with varying particle resolution.

Like the three previous validation test cases, the dam break was modelled at varying particle resolution to study the convergence of the SPH method. Figure 4.24 examines the particle positions at two time instants, $t\sqrt{g/H} = 5.6$ and $t\sqrt{g/H} = 6.2$, after the fluid strikes the far wall. Increasing the particle resolution brings the free surface slightly closer to that predicted by the BEM, however the SPH simulation does appear to lead the BEM solution at each time instant. The definition of the free surface becomes clearer as the resolution is increased, particularly the early formation of the jet after impact. Although the differences between each particle resolution are subtle, greater variation between the coarse and fine resolution models can be seen in the system energy traces (see Figure 4.26).

Modelling the dam break using a single phase model predicts the motion of the fluid and the pressure at the far wall favourably, until the point where the overturning wave strikes the water surface. Beyond this moment the simulation suffers without air, particularly in the formation of the breaking wave. Typically air would become trapped in the void somewhat cushioning its collapse. Without air, the void collapses and generates large pressure shock waves as illustrated in Figure 4.25. Beyond $t\sqrt{g/H} = 8.4$ the pressure field loses its smooth appearance resulting in large variations in the pressure measured at the gauges. Further flow-on effects are seen in the height traces (Figure 4.21) which do not follow the experimental data after the fluid has overturned. The collapsing void changes the dynamics of the problem and the lack of viscosity encourages the jet to reach higher above the channel floor while leaving a lower than expected water level behind.

At each particle resolution the total system energy was also monitored. As in the previous validation cases, the SPH models containing a low number of particles tend to lose far more mechanical energy with time. Figure 4.26 shows that the SPH dam break system energy reduces sharply at three different moments in time, coinciding with major changes in the fluid flow. The first major shift at $t\sqrt{g/H} = 2.4$ occurs at the point when the surge front initially strikes the far right wall. More energy is lost at $t\sqrt{g/H} = 6.0$ when the overturning wave initially strikes the water surface and finally after $t\sqrt{g/H} = 8.4$ as the void formed by the overturning wave collapses. In

the experiment conducted by Zhou et al. (1999) some of the fluid energy would be lost to the environment, however in the SPH simulation the fluid changes both linear and angular momentum rapidly at each of these moments in time. Where the difference in velocity between two particles is greater, the artificial viscosity term in the momentum equation becomes more influential. This in turn has a detrimental effect on energy conservation, forcing a greater reduction in the system energy in the SPH simulation than would be seen in an experiment.

(a)

(b)
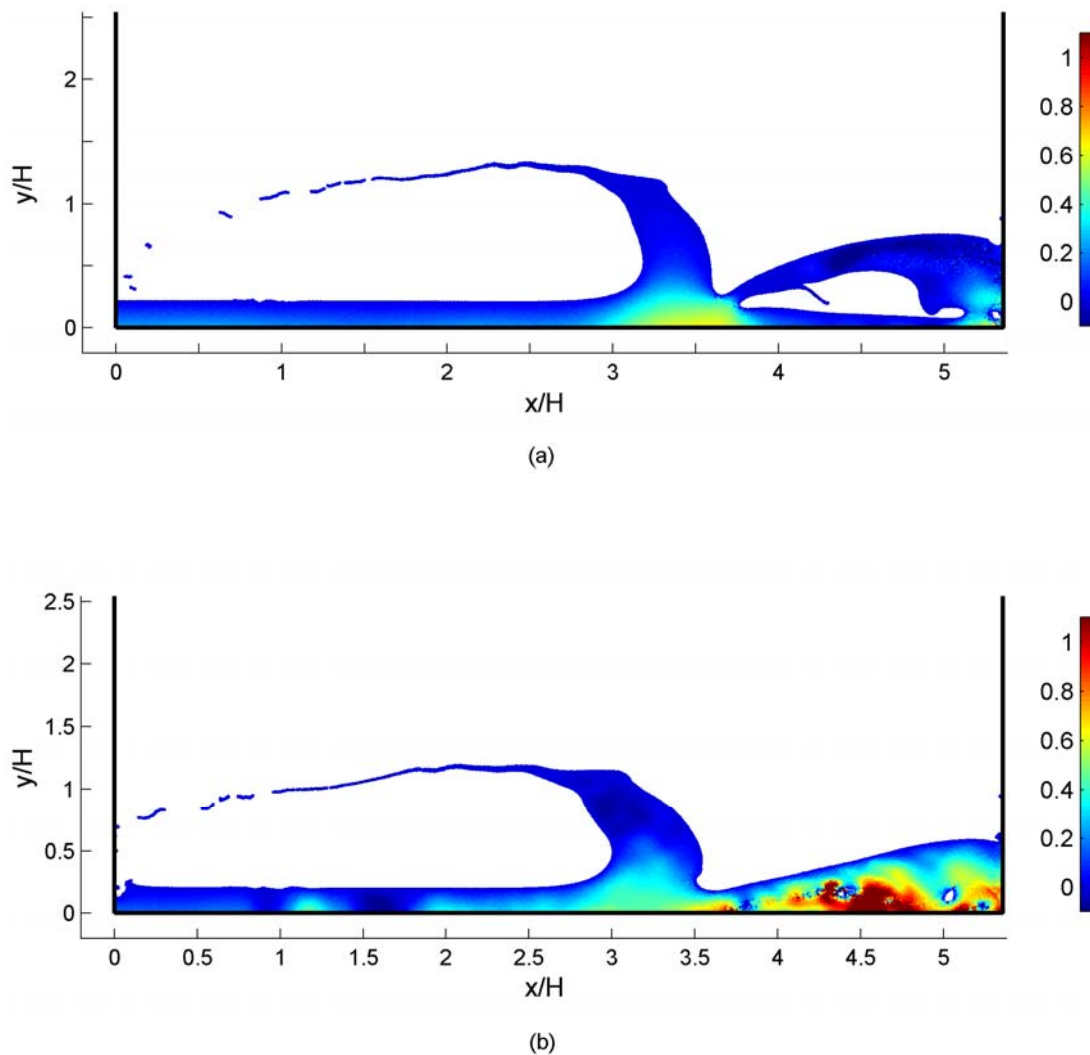
Figure 4.25 – Collapse of the void formed after the fluid overturns at the vertical wall. Depicted at two dimensionless time instants (a) $t\sqrt{g/H} = 8.0$ and (b) $t\sqrt{g/H} = 8.4$, the fluid consists of 80000 particles ($H/r_0 = 200$) coloured by dimensionless pressure, $P/\rho_0 gH$.
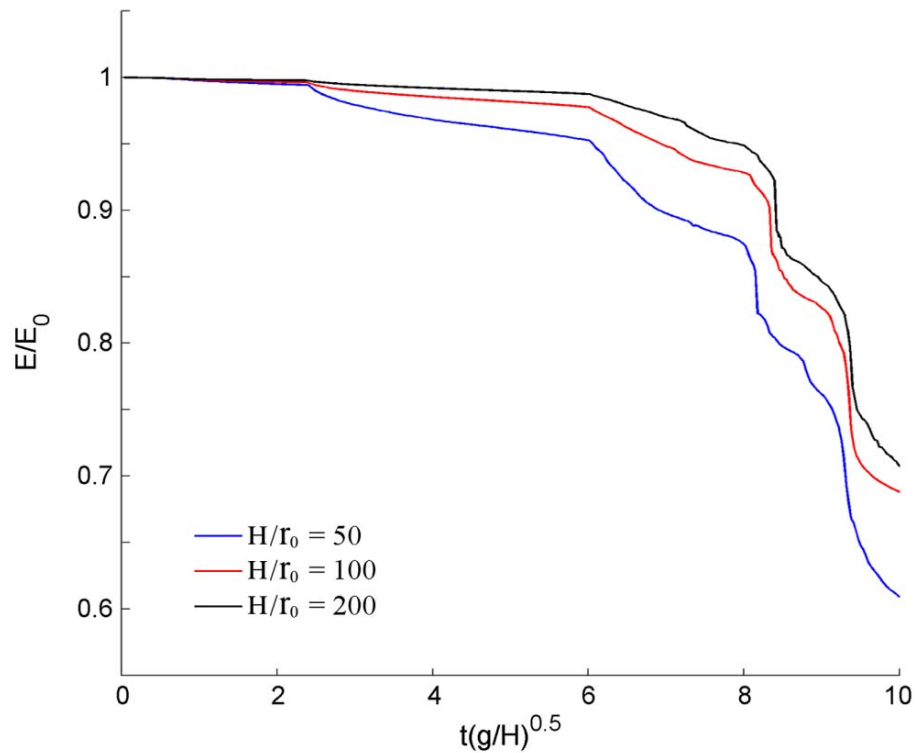
Figure 4.26 – SPH system energy ratio of the Zhou et al. (1999) dam break configuration at a number of particle resolutions.

4.5 Summary

In this chapter the SPH algorithm was validated for free surface flows by modelling four benchmark test cases. The first of these, the evolution of an initially circular patch of fluid, demonstrated that the present SPH algorithm met the kinematic and dynamic free surface conditions. The free surface definition improved with an increase in resolution and a smooth pressure field was maintained by introducing the density reinitialisation routine. Good agreement with the analytical solution for the pressure at the centre of the patch and the position of the free surface was found.

The effect of the tensile stability correction was studied by modelling the evolution of the initially square patch of fluid. Without this correction, the large negative pressure at the centre of the patch forces the fluid particles to attract, forming long tightly spaced strings and large voids. Implementing the correction forced the fluid

107

particles to maintain regular spacing and prevented the formation of voids. While there was no analytical solution available for comparison, the pressure at the centre of the patch compared well with the BEM solution of Colagrossi (2004). This good agreement would not have been possible were it not for the stabilising characteristics of each of the numerical corrections (see Section 3.3).

Solid boundaries, enforced by the ghost particle method, were introduced to the free surface flow validation process by modelling the fluid contained within a static tank. Small oscillations were noted in the total potential energy, suggesting that the particles periodically rise and fall over time. Despite this, a smooth hydrostatic pressure field was maintained throughout the simulation. This smooth pressure field was also noted during the dam break simulation prior to impact with the far wall. The height of the free surface above two points on the tank floor and the pressure recorded during impact at the far wall were found to agree with the experimental results of Zhou et al. (1999). After the water overturned and impacted upon itself a reduction in the system energy was noted, suggesting that the influence of air during the experiments was significant.

In conclusion, the validation process showed that the present SPH algorithm was capable of modelling broken free surface flows with reasonable accuracy.

Chapter 5

Water Entry of Wedge and Ship Bow Sections in Two Dimensions

5.1 Introduction

The water entry of a two-dimensional hull section is validated in this chapter. The impact of fluid against a stationary boundary was validated in Section 4.4, and this has been extended to the problem of a wedge entering still water vertically at constant speed. Experimental results reported by Breder (2005) were used as a benchmark for wedges of varying deadrise angle impacting a still water surface at a range of velocities. While constant velocity impacts are a good example for validation, they are rarely seen in real world applications. The motions of a full scale hull are partially influenced by a slam event; therefore the SPH algorithm was extended to allow the falling body to dynamically respond to the loads experienced. The drop tests of 15° and 25° deadrise wedges completed by Whelan (2004) were used as a point of reference. The water entry of a flat plate was not considered in the present SPH study due to the air cushion effect noted by Chuang (1966) (see Section 2.2.1), which cannot be accounted for in a single phase algorithm.

Wedge shaped sections are widely used for planing craft but not for displacement vessels. So the flared bow section studied by Aarsnes (1996) – consisting of a rounded keel and a constant deadrise segment towards the knuckle – was modelled using the SPH algorithm and the results compared with the BEM investigation completed by Sun (2007). This two-dimensional model provides a basic insight into the transient entry of a bow section, but does ignore three-dimensional effects such as forward speed and the shape of the water surface. Some three-dimensional effects are considered using a similar hull form in Chapter 6.

5.2 Constant velocity wedge impacts

The ability of the present SPH algorithm to resolve the fluid pressure directly adjacent to a stationary solid boundary was evaluated using the dam break validation case (Section 4.4). A ship hull form striking a still water surface requires the application of moving solid walls (see Section 3.6), so to assess the algorithm's ability to correctly resolve the local pressure field during an impact, the simple case of a two-dimensional triangular wedge has been simulated.

At full scale, the relative motion between a ship hull and the water surface in regular head seas follows a time varying, near sinusoidal pattern. Therefore the relative vertical velocity between the hull and the water surface will also change in time due to the pitch and heave motions of the ship, which in turn are affected by the loads experienced by the hull. For the simple case of a two-dimensional wedge dropped from a height into still water, the velocity profile is governed purely by the gravitational acceleration and the loads experienced during the entry process. The load on the wedge can be derived from the local pressure in the fluid, which is validated here for a moving boundary. To simplify the process further, a number of wedges of differing deadrise angle striking a still water surface at constant velocity have been simulated using the SPH algorithm.

5.2.1 Experimental study

Breder (2005) conducted a number of experiments of slamming pressures and loads on a carbon fibre, epoxy and balsa sandwich hull panel as part of a Master's thesis (see Section 2.2.1). The results of this experimental programme have been used as a validation benchmark for the constant velocity SPH simulations. The constant velocity impacts were conducted in a cylindrical tank of diameter 3.5 m and typical water depth 1.5 m. Each panel was attached to a hydraulic ram capable of maintaining a constant velocity within a 5% tolerance limit up to and including 5 m/s for a wedge with a dead rise angle of 10°. The panels stretched 0.605 m from keel to chine and were made of a carbon fibre composite with a mass of 75 kg (see Figure 5.1).

Three further panels were also fixed on the hydraulic ram to constrain the fluid flow. One panel, lying in the vertical plane, was attached to the keel of the test panel and acted as a plane of symmetry. This allows the experiment to be approximated by a two-dimensional wedge of the same deadrise angle as the flow is symmetrical. The other two panels, also lying in the vertical plane, were attached to the ends of the test panel to prevent the fluid from venting.

Breder (2005) drilled holes in each hull panel to accommodate a number of piezoelectric pressure sensors. Five sensors, the first 60 mm from the keel, were spaced 107.5 mm apart along the middle of the panel and labelled P_1 through to P_5 (see Figure 5.1). A load cell was mounted between the panel and the ram and an accelerometer was attached. This accelerometer fed back load information to the control system so a constant velocity could be maintained. No correction was made for hydroelasticity in the load calculations, but Beder (2005) did note that the measured pressures could be up to 12.3% higher for a completely rigid 10° deadrise panel at entry speeds above 6.0 m/s.
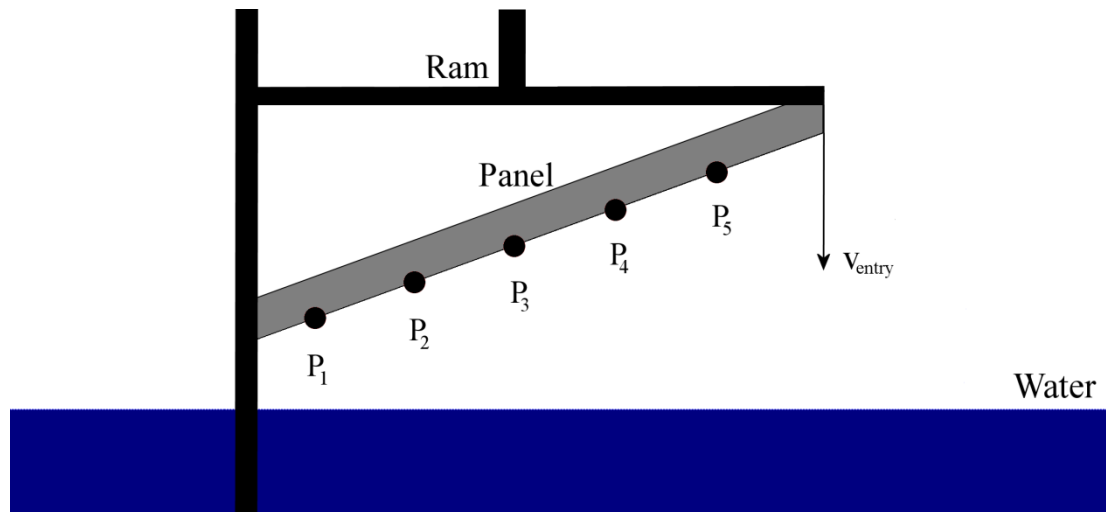
Figure 5.1 – Schematic diagram of the Breder (2005) experimental apparatus. The carbon fibre panel contains five equally spaced pressure sensors labelled P_1 through to P_5 and moves downwards with speed v_{entry}. The testing tank is not shown in this diagram.

5.2.2   SPH simulation

To simulate the constant velocity impacts of Breder (2005), a two-dimensional tank of width 3.5 m and water depth 1.5 m was filled with 210 000 SPH particles at a resolution of 200 particles per metre, the maximum resolution at which the dam break was modelled (see Section 4.4). The experimental test panel with the limiting vertical panel along the keel was replaced with a wedge of the same deadrise angle and beam (varying between 1.04 m and 1.18 m depending on the deadrise angle). The model simulations were started with the keel of the wedge one compact support radius ($3h$) above the water surface (see Table 5.1 for a summary of the models simulated). To determine a suitable sound speed, the 30° deadrise wedge was forced into the centre of the free surface at 5 m/s and the maximum fluid velocity measured was found to be 20 m/s. So to avoid compressibility effects, the sound speed for all models was set to 200 m/s (see Section 3.2.4). For consistency, the artificial viscosity, tensile stability and XSPH corrections used the same coefficients as the dam break (see Section 4.4).

Wedge	Impact Speed	Duration
	1.0 m/s	0.12 s
10° Deadrise	2.0 m/s	0.06 s
	3.0 m/s	0.06 s
	2.0 m/s	0.11 s
20° Deadrise	3.0 m/s	0.08 s
	4.0 m/s	0.06 s
	2.0 m/s	0.14 s
30° Deadrise	4.0 m/s	0.08 s
	5.0 m/s	0.05 s

Table 5.1 – Summary of the SPH simulations completed in the constant velocity wedge impact program.

The numerical pressure sensors used the same averaging technique as described in Section 4.4. All of the numerical pressure sensors sampled at 1.75 kHz, considerably lower than the experimental pressure sensors (20 kHz). Breder (2005) did not

indicate whether or not the experimental pressure traces were filtered, so the raw numerical pressure traces were used for the first comparison. However, considerable noise was found after the initial peak in the numerical pressure trace, so a low pass filter was applied. The cut-off frequency was varied in an attempt to remove the noise without altering the overall trend and 400 Hz was found to produce the best result.

A similar method to that used to measure the local fluid pressure was employed to calculate the total load on the wedge. At each time step, the surface of the wedge was divided into a series of pressure sensors two smoothing lengths wide and five deep (see Section 3.6.3). The mean pressure was calculated at each sensor and the total load found by summing across all pressure sensors. As this was performed at each time step (see Section 3.4), the load was sampled at 21 kHz, slightly higher than the experimental study. Breder (2005) smoothed the load traces using a 400 Hz low pass filter, so for consistency the same was applied to the load calculated using the SPH algorithm.

5.2.3 SPH results

Figure 5.2 depicts the local pressure field surrounding a 30° deadrise wedge impacting the initially still free surface at three time instants. At $t = 0.03$s the pressure immediately adjacent to the keel rises to approximately 10 kPa while a small region of much higher fluid pressure can be seen at the still water level. At each moment in time the pressure field is smooth near the keel, indicating that the scaling function designed to eliminate excess ghost mass (see Section 3.6.2) is functioning correctly. Furthermore, as the jet passes the knuckle of the wedge it continues on approximately the same trajectory, having not been affected by the local excess in ghost mass.

As the wedge sinks further into the tank, the small high pressure region seen at the initial still water level at $t = 0.03$s tracks along the surface of the wedge. This area of high pressure remains on the still water level until the knuckle drops below it. It is responsible for the large pressure peaks seen in both the experimental and numerical pressure traces as the sensor passes the still water level (see Figure 5.6).
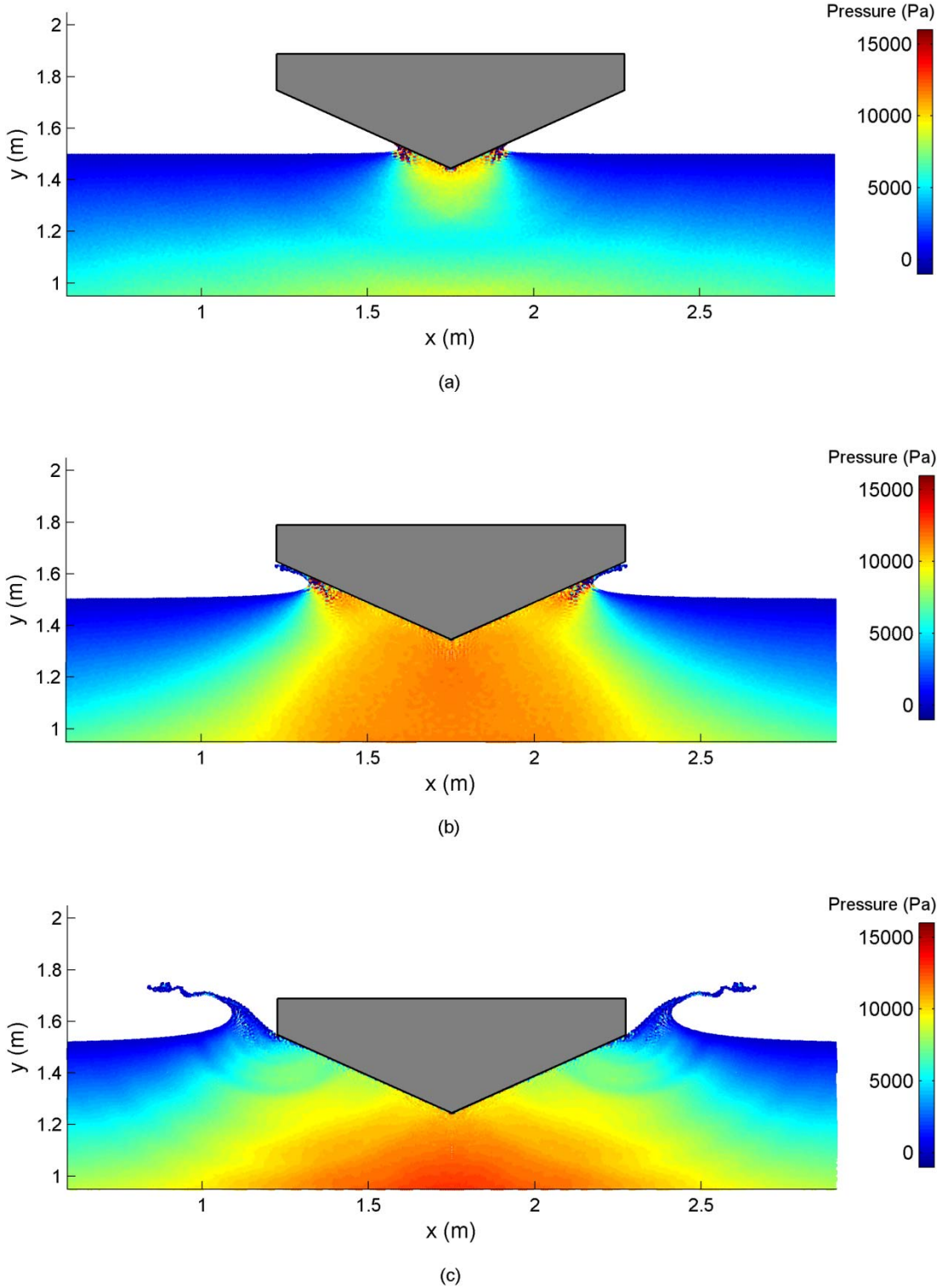
Figure 5.2 – SPH simulation of a 30° deadrise wedge impacting the free surface at a constant 2.0 m/s. The pressure field is illustrated at (a) 0.03s, (b) 0.08s and (c) 0.13s after initial impact with the free surface. The tank walls are located at $x = 0$ m and $x = 3.5$ m.

Since the high pressure region immediately adjacent to the surface is small in comparison to the size of the wedge, the number of particles within it is low. Consequently, some of the particles develop an abnormally high pressure compared to those in their immediate surrounds, and so the peak pressure recorded can vary from sensor to sensor (see Figure 5.6).

Figure 5.3 describes the fluid flow speed field of the same case: a 30° deadrise wedge impacting the free surface at a constant velocity of 2.0 m/s. The high pressure region immediately surrounding the wedge in Figure 5.2 causes a jet to form. A small number of particles are propelled along the surface of the wedge at a maximum speed of 10.0 m/s, while the majority of the fluid particles remain almost stationary for the entire simulation.

The load on a 10° deadrise wedge impacting the free surface at 2.0 m/s is described in Figure 5.4. At this shallow deadrise angle, the wedge is similar in geometry to a flat plate. In an experiment, the wedge will experience some air cushioning immediately before it strikes the water surface. The SPH simulation does not include air compressibility effects, so the force calculated is approximately twice that of the measured value. The air cushion effect is also reflected in the pressure traces as the SPH pressure is approximately twice as large as the experimental after the initial peak. Furthermore, Breder (2005) noted that the panels used in the experiment were able to flex slightly on impact. Fully rigid panels (such as the SPH models) could experience pressures up to 16% larger than those measured in the experiment.

Increasing the deadrise angle to 20° (Figure 5.5) reduces the air cushion effect. Here the load calculated by the SPH simulation agrees well with that measured in the experiment. The maximum load experienced has dropped significantly to 12.0 kN (SPH) and 10.5 kN (Breder, 2005) when compared with the peak load of 30 kN on the 10° wedge. The SPH peak pressures measured at each sensor are still slightly higher than those measured experimentally, however this could be due to the flexibility of the experimental panel. Better agreement between the SPH model and the experiment is found when the deadrise is increased to 30° (see Figure 5.6). A plausible explanation for this is a reduction in the flex in the experimental panel due to the decrease in the measured load with increasing deadrise angle (Breder, 2005).
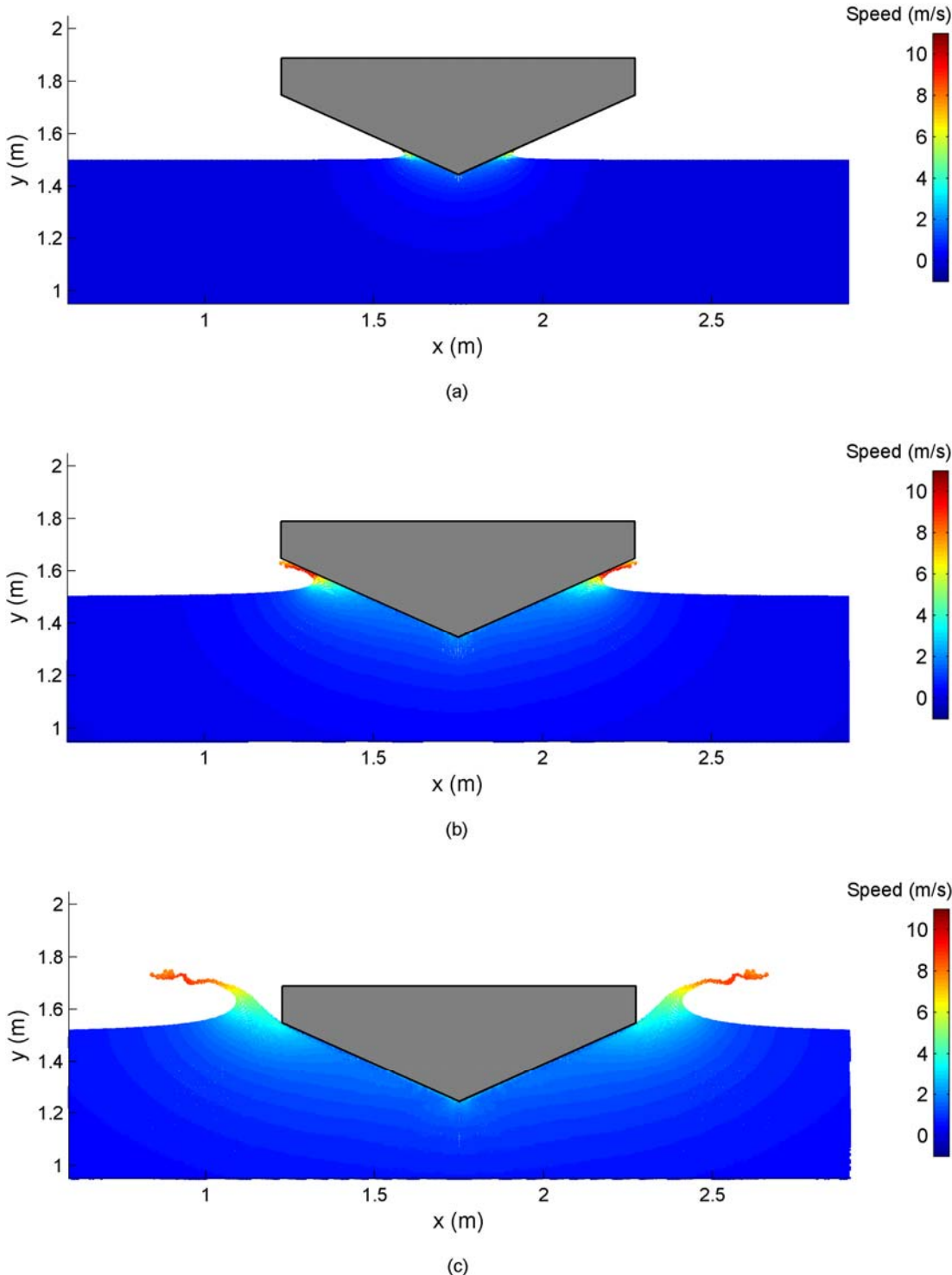
Figure 5.3 – SPH simulation of a 30° deadrise wedge impacting the free surface at a constant 2.0 m/s. The flow speed is illustrated at (a) 0.03s, (b) 0.08s and (c) 0.13s after initial impact with the free surface. The tank walls are located at $x = 0$ m and $x = 3.5$ m.
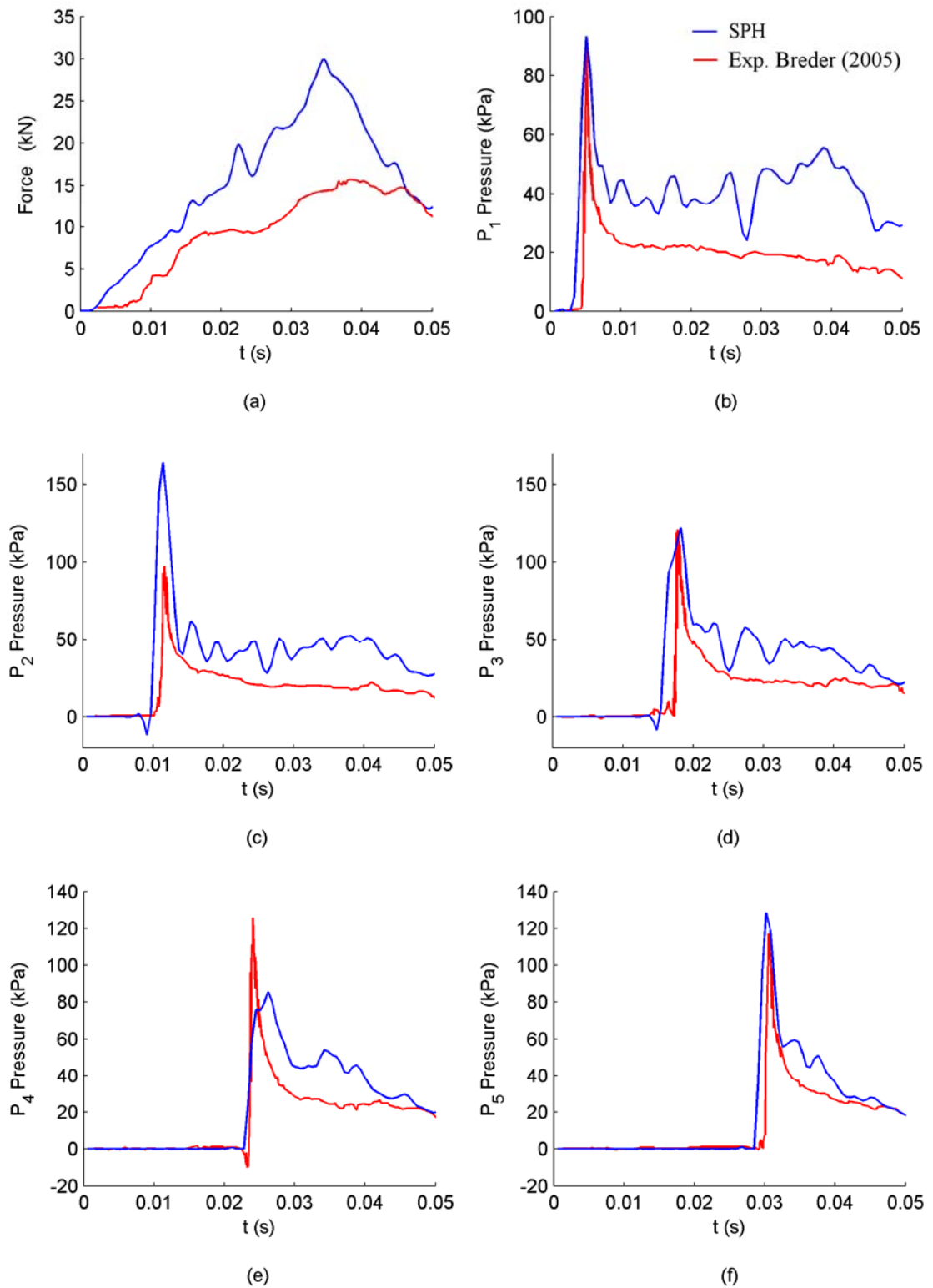
Figure 5.4 – Vertical force and pressure sensor traces of a 10° deadrise wedge impacting the still water surface at 2.0 m/s.
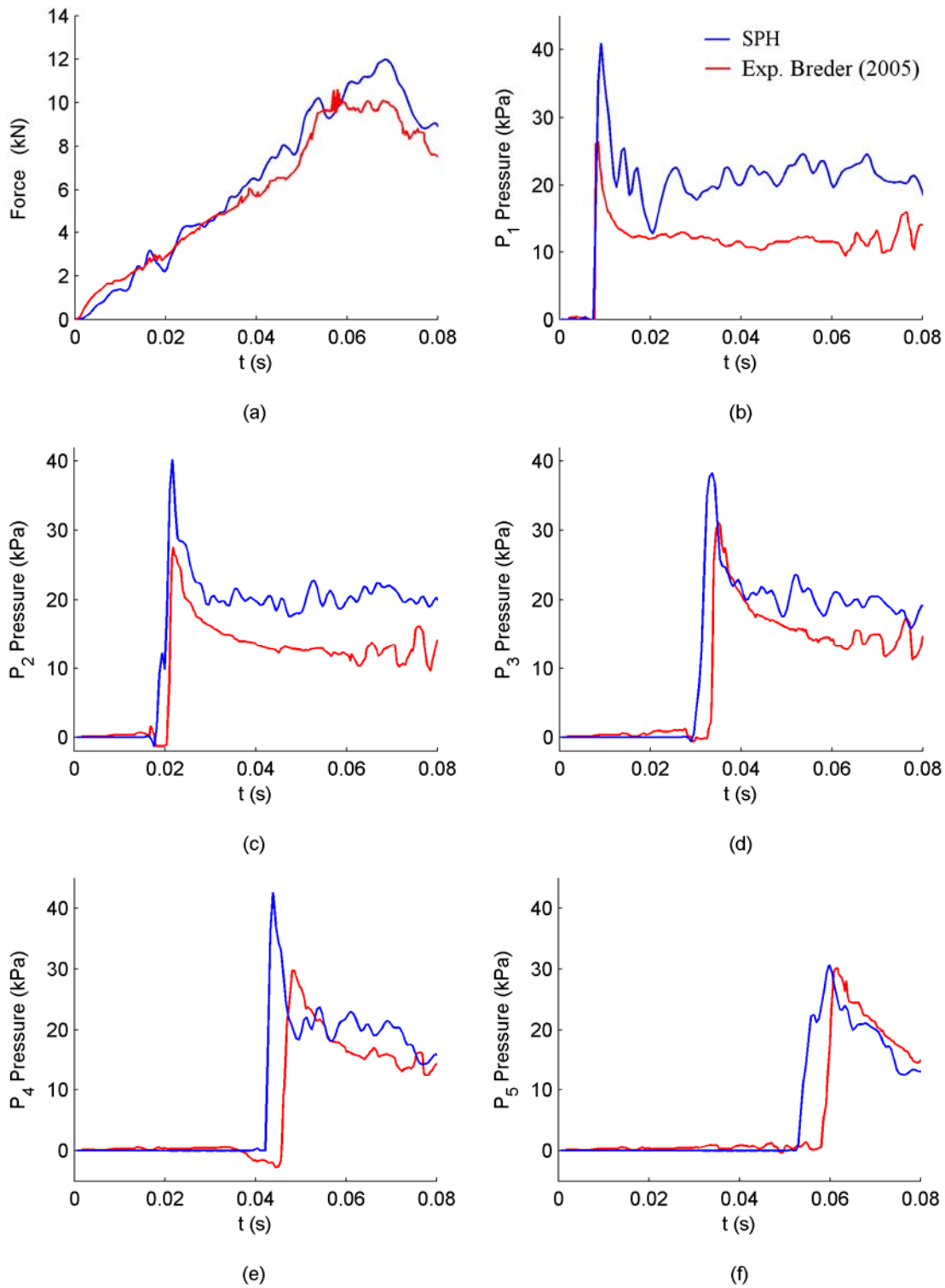
Figure 5.5 – Vertical force and pressure sensor traces of a 20° deadrise
wedge impacting the still water surface at 2.0 m/s.
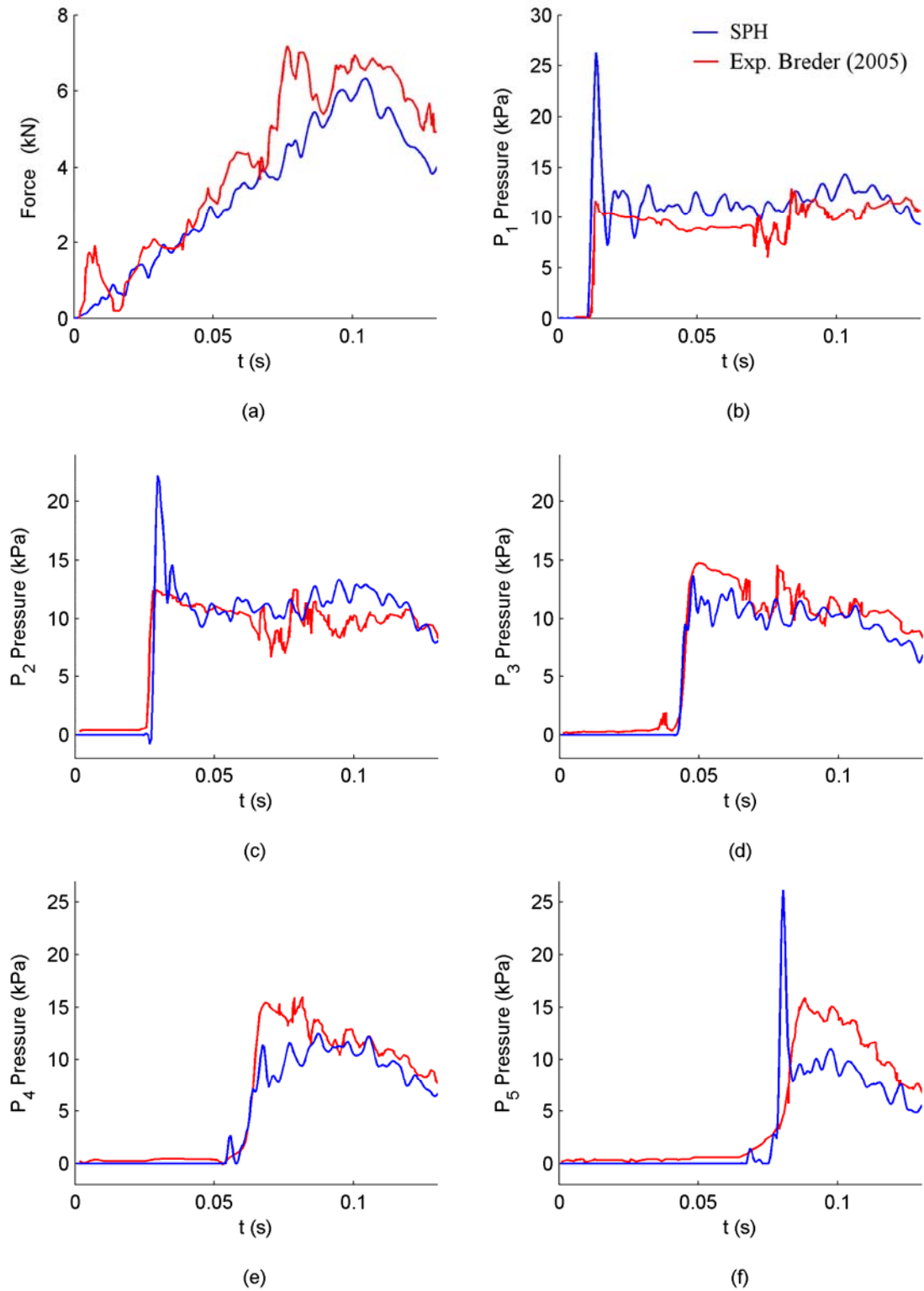
Figure 5.6 – Vertical force and pressure sensor traces of a 30° deadrise
wedge impacting the still water surface at 2.0 m/s.
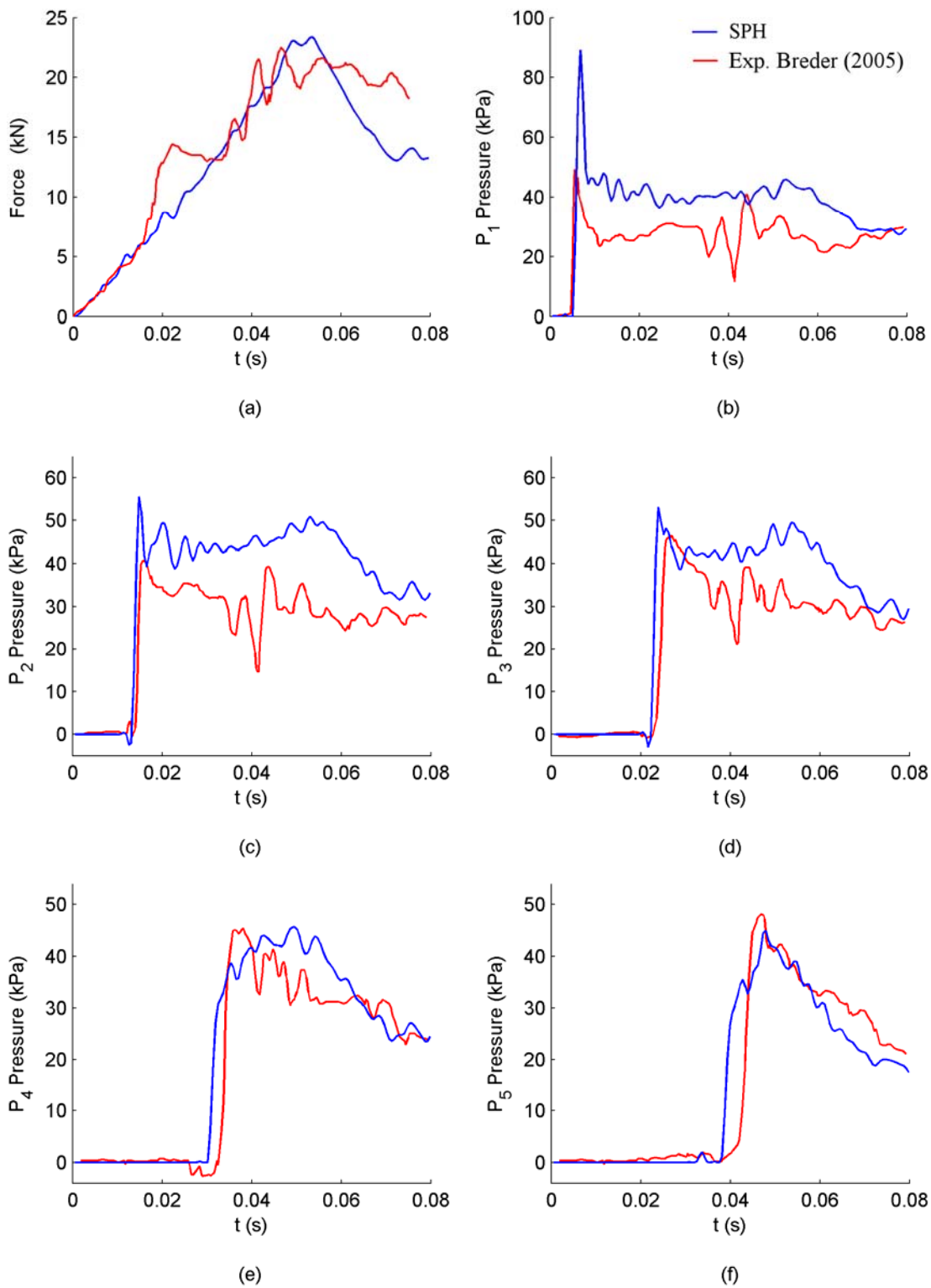
Figure 5.7 – Vertical force and pressure sensor traces of a 30° deadrise
wedge impacting the still water surface at 4.0 m/s.

120
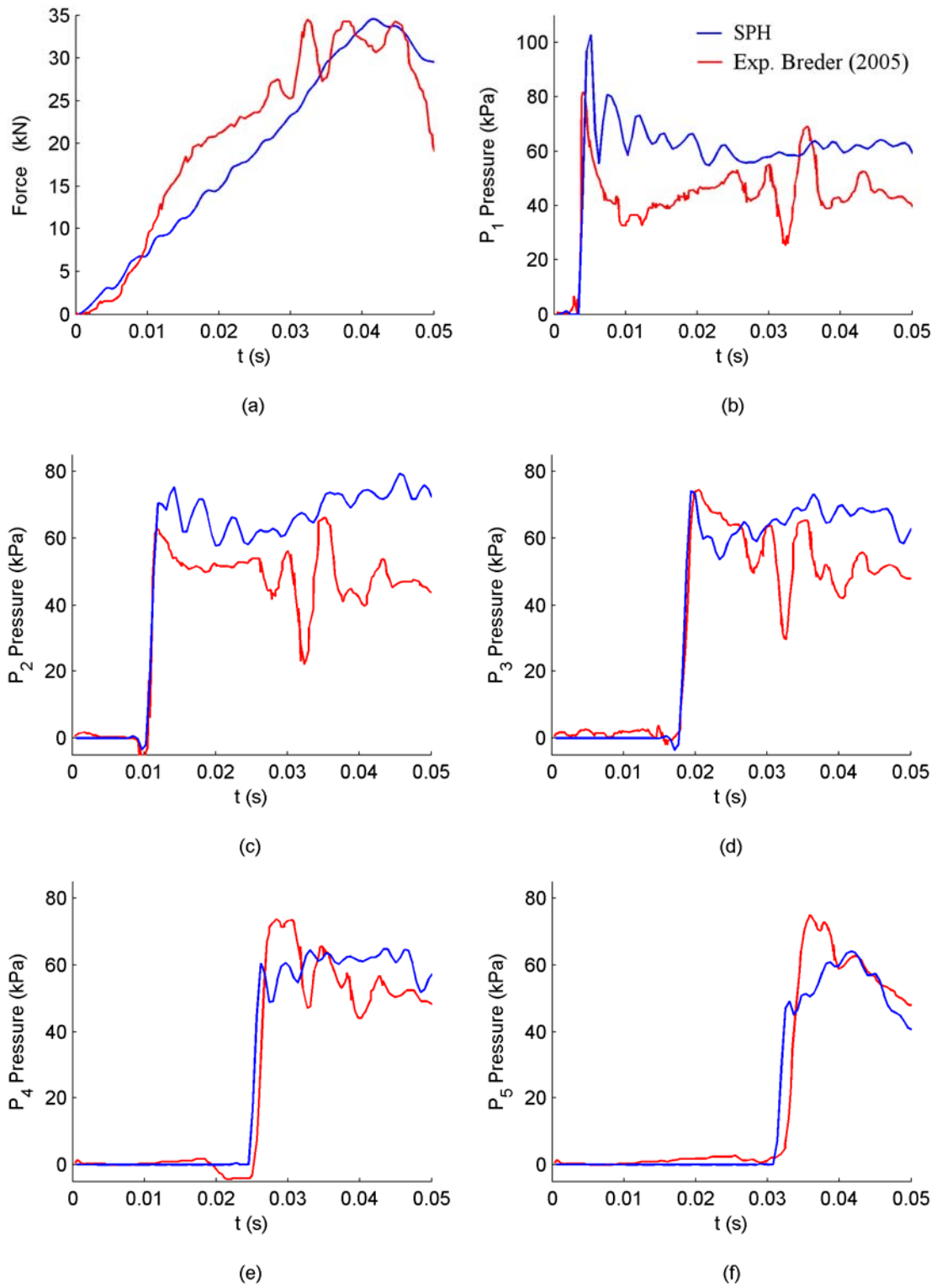
Figure 5.8 – Vertical force and pressure sensor traces of a 30° deadrise wedge impacting the still water surface at 5.0 m/s.

Figures 5.6 to 5.8 demonstrate the effect entry speed has on the load and pressures experienced by a 30° deadrise wedge. The simulated peak load on the wedge increases from 6.3 kN at 2.0 m/s through to 34.5 kN at 5.0 m/s. Likewise, the maximum pressures measured at each pressure sensor occur sooner, from 0.10 s at 2.0 m/s through to 0.04 s at 4.0 m/s. However, it is worth noting that with the low sample rate used in the SPH simulation, the peak size may not be captured perfectly.

The peak SPH pressure recorded over all the sensors is compared with the theoretical values determined by Wagner's (1932) added mass method (see Section 2.2.1) and those measured experimentally by Breder (2005) in Figure 5.9. For both the 20° and 30° deadrise wedges, the Wagner prediction over-estimates the measured peak pressure. At 20° deadrise the SPH values lie close to the Wagner curve, however at 30° the SPH peaks over-estimate both the theoretical and experimental pressure. Due to the low sample rate and the 400 Hz low pass filtering, the actual SPH peaks could easily be much larger than displayed in Figure 5.9, but there is a general agreement between all three techniques. Furthermore the low number of particles contained within the sensor can also contribute to the variation in peak pressure if any one particle has a considerably lower or higher pressure than the others.
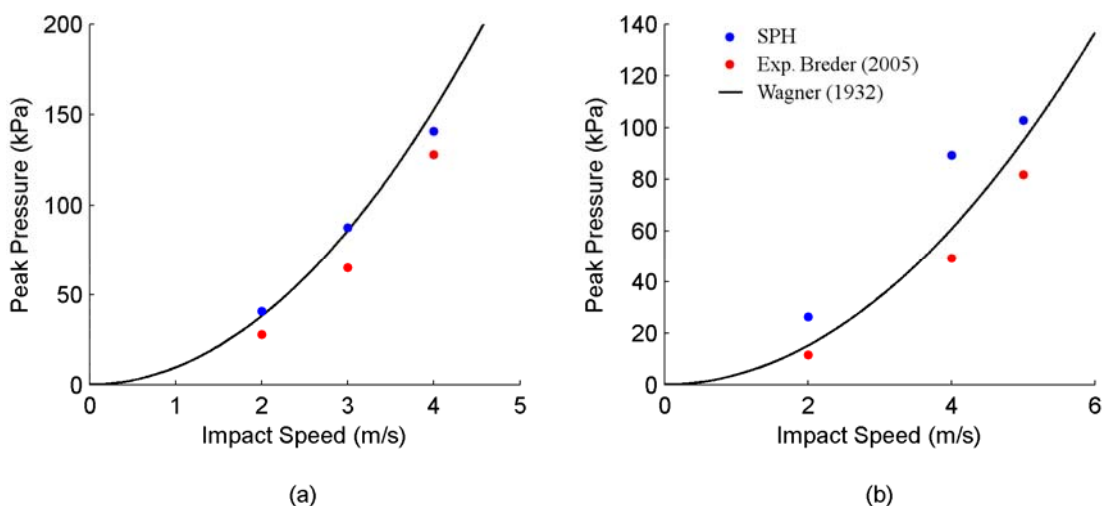
Figure 5.9 – The peak SPH pressure compared against the theoretical added mass method of Wagner (1932) and the experimental results of Breder (2005). Results are shown for the (a) 20° deadrise wedge and the (b) 30° deadrise wedge.

Similarities were noted in the behaviour of the pressure traces for all models. Small amplitude oscillations can be seen in the pressure traces, particularly at low deadrise angles. These oscillations are caused by the pressure waves, generated at the moment the keel strikes the water surface, reflecting off the base and sides of the tank. It is also noted that the experimental pressure peaks lag behind that predicted by the SPH algorithm, particularly at sensors P_4 and P_5. While the experiment attempted to maintain a constant velocity, the wedge decelerated by up to 5% due to the load on the panel, forcing the fluid to reach each sensor at a later time (Breder, 2005).

In summary, the SPH simulations agree well with the loads and pressures measured by Breder (2005) for both the 20° and 30° deadrise wedges over a range of entry velocities. The peak pressures measured experimentally and simulated using SPH also agree well with Wagner's (1932) theoretical added mass method (see Section 2.2.1). At lower deadrise angles the SPH algorithm grossly over-predicts the loads and pressures measured in the experiment, possibly because the effect of air on the model is ignored.

5.3   Variable velocity wedge impacts

The ability of the SPH algorithm to resolve the local pressure field near a moving solid boundary was evaluated in the previous Section. However during most hull section drop tests the model does not move at a constant velocity, so the local SPH pressure field must be fed back in to the algorithm in order to determine the motions of the model. The experimental study of Whelan (2004) was used as a basis for the validation of the now dynamically responsive solid wall boundaries.

5.3.1   Experimental study

Whelan (2004) included two wedge shaped cross-sections of 15° and 25° deadrise in a study of wet-deck slamming on catamaran hull cross-sections (see Figure 5.10). The two wedges were dropped and allowed to fall freely from a range of heights into a tank of still water measuring 0.3 m wide, 1.2 m deep and 2.4 m long. The tank was filled to a depth of 1.0 m and the model was attached to the base of a centre post that had been restrained in all degrees of freedom except the vertical. The mass of the entire falling rig was 74.0 kg.
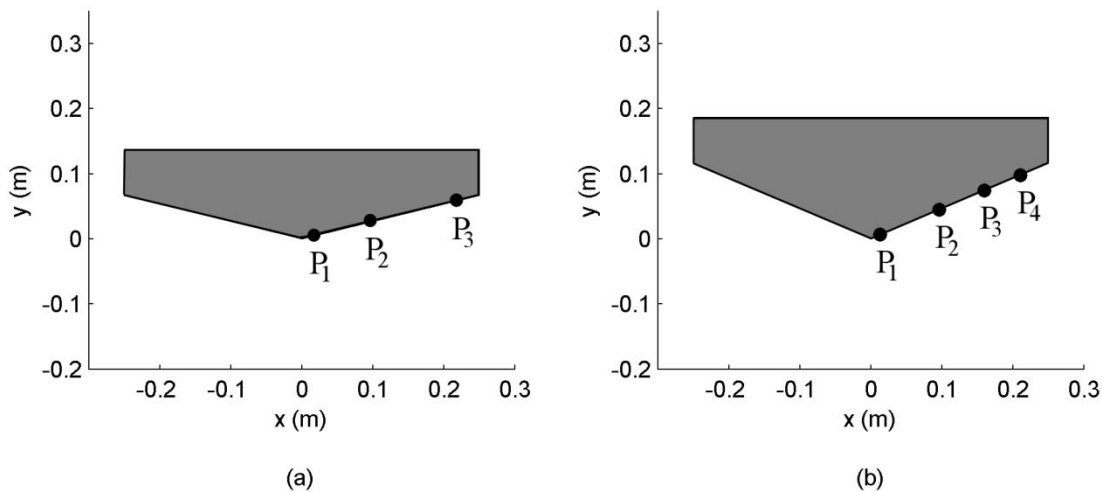
Figure 5.10 – The model geometry of the (a) 15° and (b) 25° deadrise wedges. Pressure sensors are located at each of the black dots.

Both wedge models were moulded from a single sheet of 5 mm thick aluminium plate. The width of each model was approximately 0.02 m less than the width of the tank to allow for some venting of air and water at the ends of the wedge, without compromising the two dimensional approximation along the centre. A number of holes were drilled along the middle of the wedge stretching from the keel to the chine in order to accommodate up to four piezoelectric pressure sensors. Each sensor had a face diameter of 3.8 mm and was capable of measuring up to 3.4 MPa (see Figure 5.10). An accelerometer ($\pm30g$) was fixed to the centre post to measure the load on the model and determine the velocity and position of the wedge with time.

Full scale ship slamming occurs at a wide range of relative velocities (between the ship bow and the water surface) so Whelan (2004) dropped the wedge models from a range of heights to gain an understanding of the loads expected at varying impact velocities. With the intention of replicating a full-scale slam at model scale, the drop heights were normalised by the beam to achieve a comparable relative impact velocity. Equivalent to an effective Froude number, the normalised drop height H^* is,

$$H_H^* = \sqrt{\frac{2H_H}{B_H}} \qquad (5.1)$$

where H_H is the initial vertical distance from the still water surface to the keel and B_H is the beam of the wedge. The vertical velocity expected from the drop height at the moment the wedge strikes the water surface was never achieved due to friction between the centre post and its guide. So to compensate for the reduced velocity, all SPH simulations were initialised using the impact velocity measured in the experiment.

5.3.2   SPH simulation

In an attempt to simulate Whelan's investigation, the SPH study was carried out in a tank measuring 1.2 m deep and 2.4 m long using wedges with a beam of 0.5 m. The wedges used in the constant velocity impacts (Section 5.2) varied in beam from 1.04 m through to 1.18 m; more than twice that of the wedges used in the present study. Therefore to keep a comparable particle resolution, the tank was filled with 384 000 SPH particles at a resolution of 400 particles per metre. To determine a suitable sound speed the 25° deadrise wedge was dropped from a normalised drop height of 1.01 and the maximum fluid speed was measured. The fluid speed was found to not exceed 10 m/s so the sound speed for all of the models simulated was set to 100 m/s. For consistency, the artificial viscosity, tensile stability and XSPH corrections used the same coefficients as the constant velocity wedge and the dam break (see Sections 4.4 and 5.2).

Wedge	Normalised Drop Height H_H^*	Initial Impact Speed
15° Deadrise	0.62	1.32 m/s
	0.73	1.57 m/s
	0.93	1.96 m/s
25° Deadrise	0.47	0.93 m/s
	0.61	1.26 m/s
	0.84	1.74 m/s
	1.01	2.11 m/s

Table 5.2 – Summary of the SPH simulations completed in the variable velocity wedge impact program.

Table 5.2 outlines the wedge models simulated using the SPH algorithm. All of the simulations were conducted with a fixed wedge mass, although Whelan (2004) did perform a number of further drop tests with differing mass.

5.3.3 SPH results

Figure 5.11 illustrates the pressure field at a number of time instants during the impact of a 25° deadrise wedge dropped from a normalised height of $H_H^* = 0.61$. At $t = 0.03$ s after impact (Figure 5.11a), a high pressure region can be seen directly adjacent to the surface of the wedge at the initial still water level. This high pressure region tracks along the surface of the wedge and is responsible for the large peaks seen at each pressure sensor in Figure 5.14. By $t = 0.06$ s, the pressure field immediately surrounding the wedge has reduced in value, a jet has formed and the underside of the wedge is completely wetted. At this moment in time the vertical acceleration experienced by the wedge has reached a maximum, a trend that was noticed in all of the drop tests by Whelan (2004). At $t = 0.09$ s, the knuckles of the wedge have passed the initial still water level and the acceleration has reduced to a near constant value just above zero. By this time the pressure field has also begun to return to a near hydrostatic state.

The flow speed field for the same time instants is illustrated in Figure 5.12. The high pressure region immediately adjacent to the wedge at the still water level forces the fluid to form a jet travelling parallel to the wedge at high velocity. The jet reaches a maximum speed of 6.5 m/s, which is approximately five times that of the maximum wedge speed. The speed of the jet decreases as the deadrise angle of the wedge is increased, but increases with drop height.

The acceleration, velocity and pressure traces for a wedge with a deadrise angle of 15° (Figure 5.13) were compared with those of a 25° deadrise wedge (Figure 5.14). The distance from the knuckle to the water surface was the same for both wedges. However because the depth of each wedge model was different, the normalised drop height was 0.73 for the 15° deadrise wedge and 0.61 for the 25° deadrise wedge. To remove any numerical noise, the acceleration and pressure traces calculated using the SPH algorithm were smoothed using a 500 Hz low pass filter.

(a)

(b)

(c)
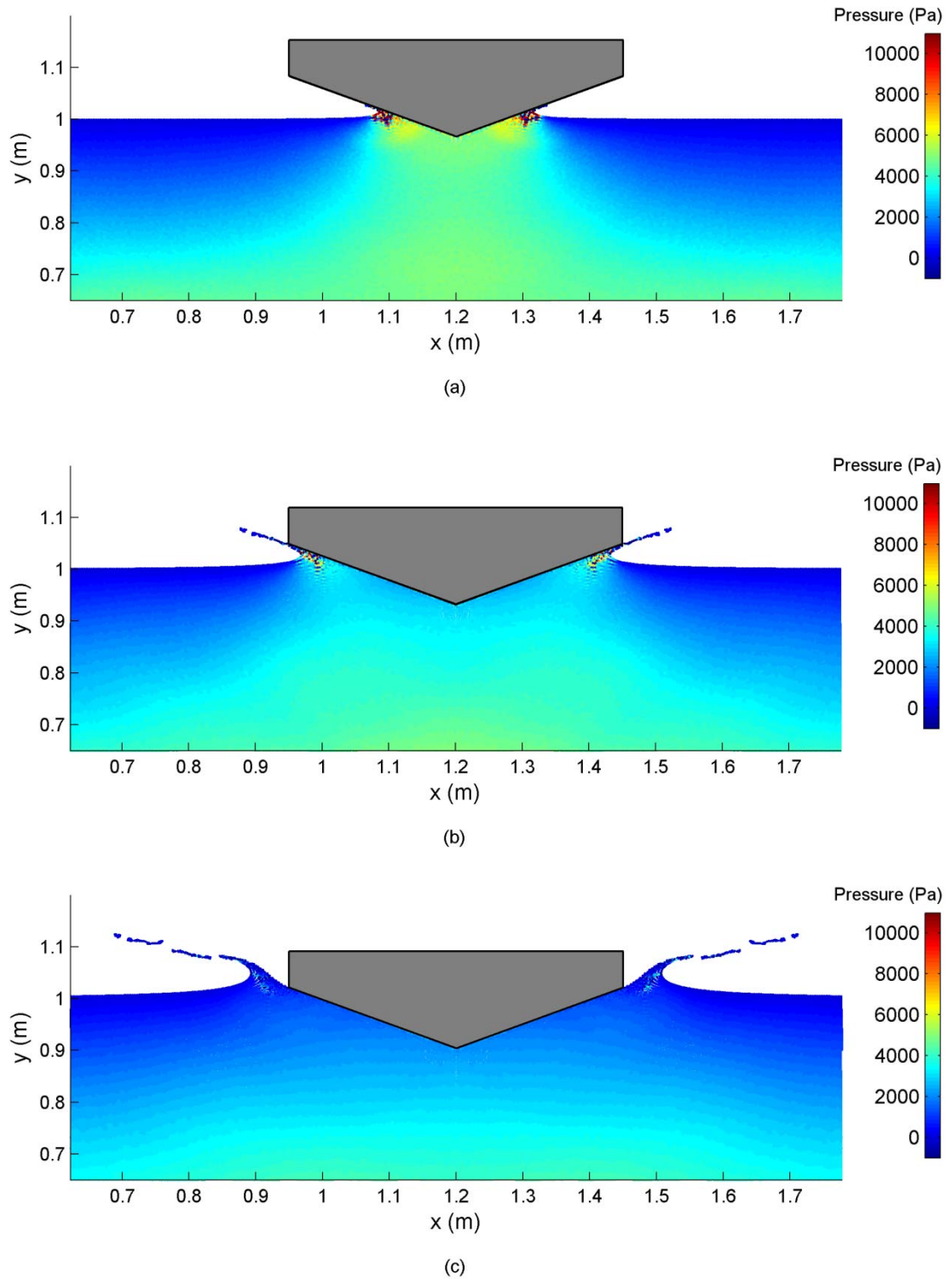
Figure 5.11 – SPH particles coloured by pressure during the impact of a

25° deadrise wedge dropped from a normalised height of $H_H^* = 0.61$.

Images are taken (a) 0.03 s, (b) 0.06 s and (c) 0.09 s after

initial impact with the free surface.
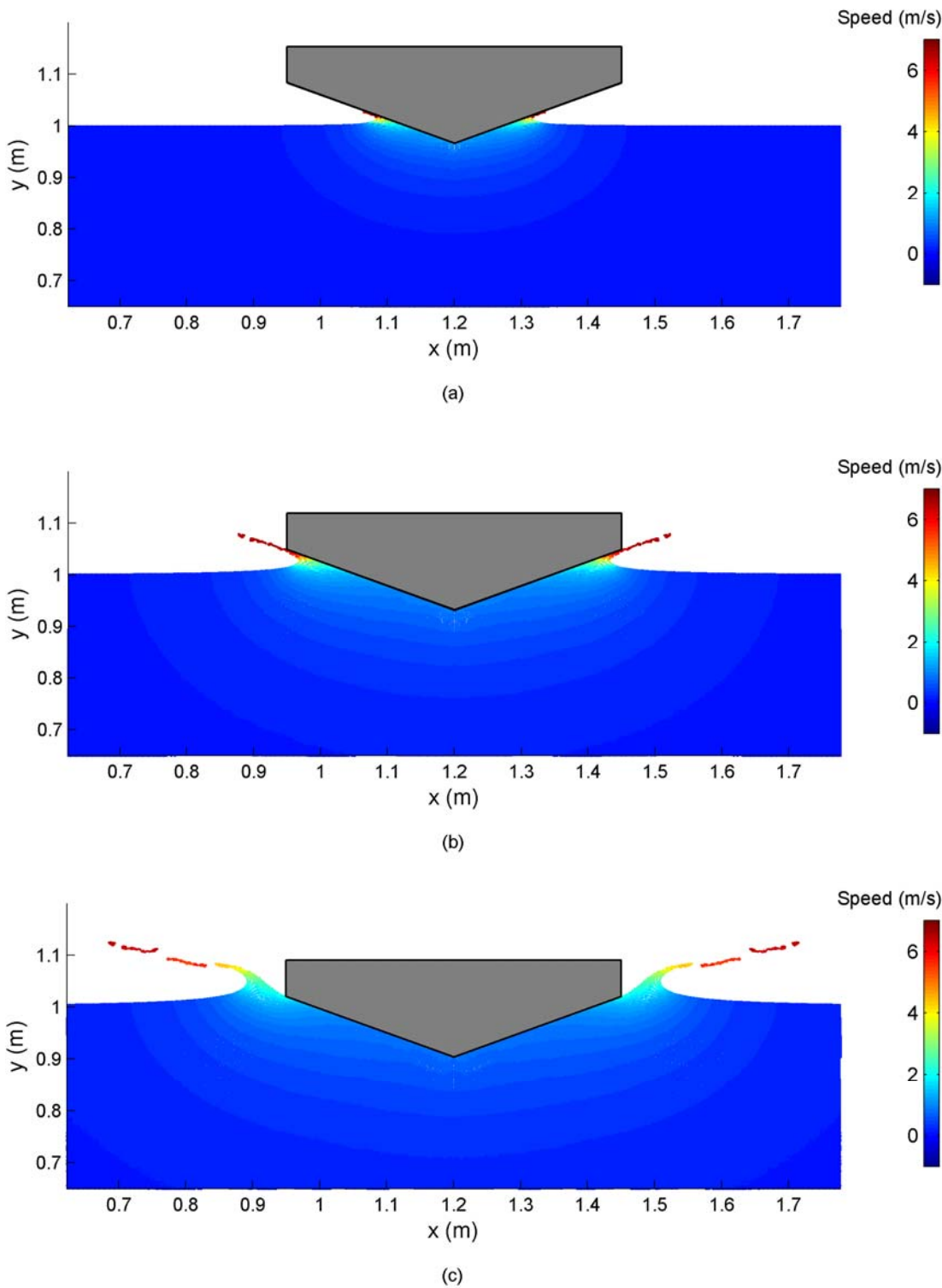
Figure 5.12 – SPH particles coloured by flow speed during the impact of a
25° deadrise wedge dropped from a normalised height of $H_H^* = 0.61$.
Images are taken (a) 0.03 s, (b) 0.06 s and (c) 0.09 s
after initial impact with the free surface.
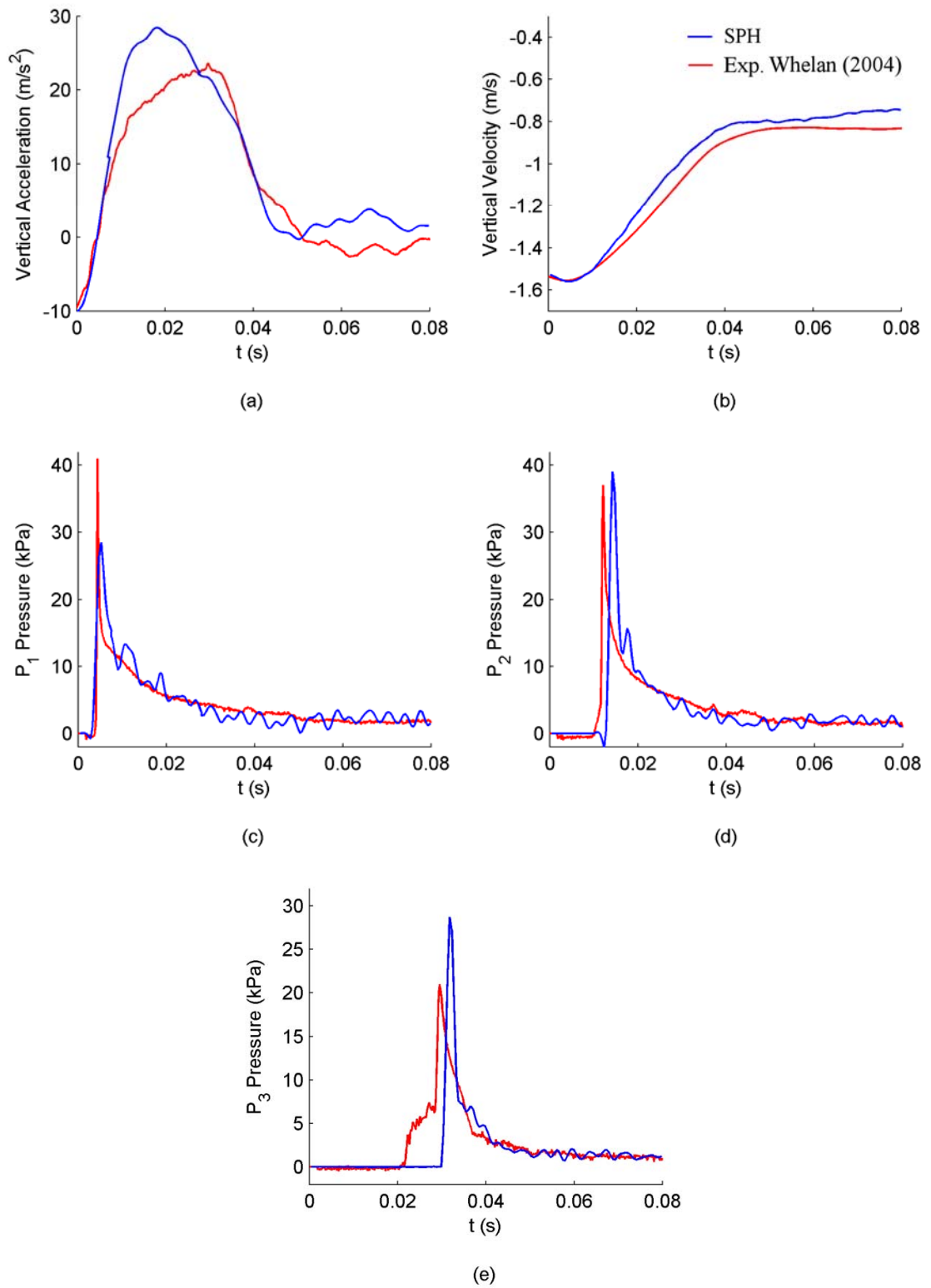
Figure 5.13 – The vertical acceleration, vertical velocity and pressure at three pressure sensors of a 15° deadrise wedge dropped from $H_H^* = 0.73$.
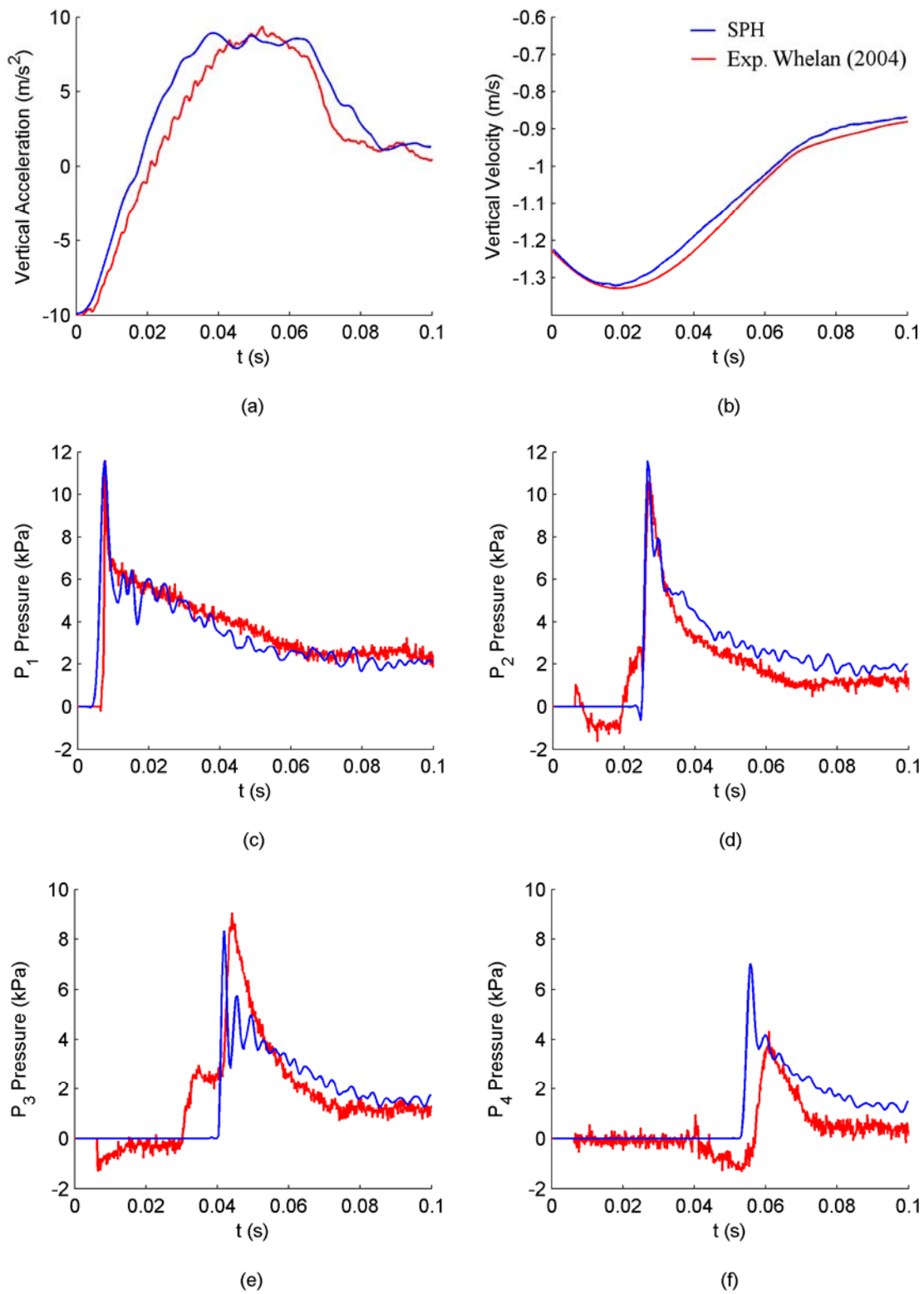
Figure 5.14 – The vertical acceleration, vertical velocity and pressure at four pressure sensors of a 25° deadrise wedge dropped from $H_H^* = 0.61$.
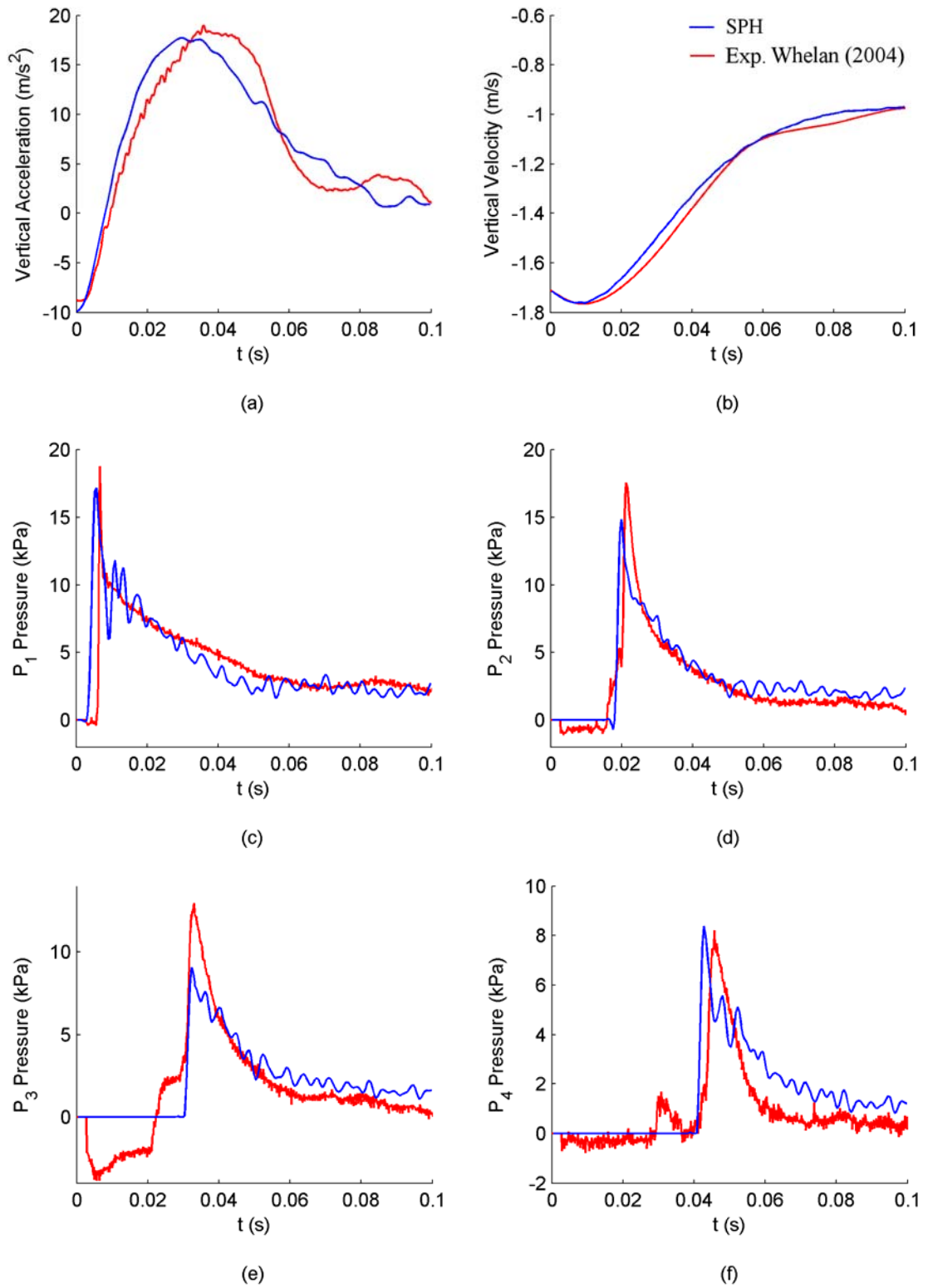
Figure 5.15 – The vertical acceleration, vertical velocity and pressure at four pressure sensors of a 25° deadrise wedge dropped from $H_H^* = 0.84$.
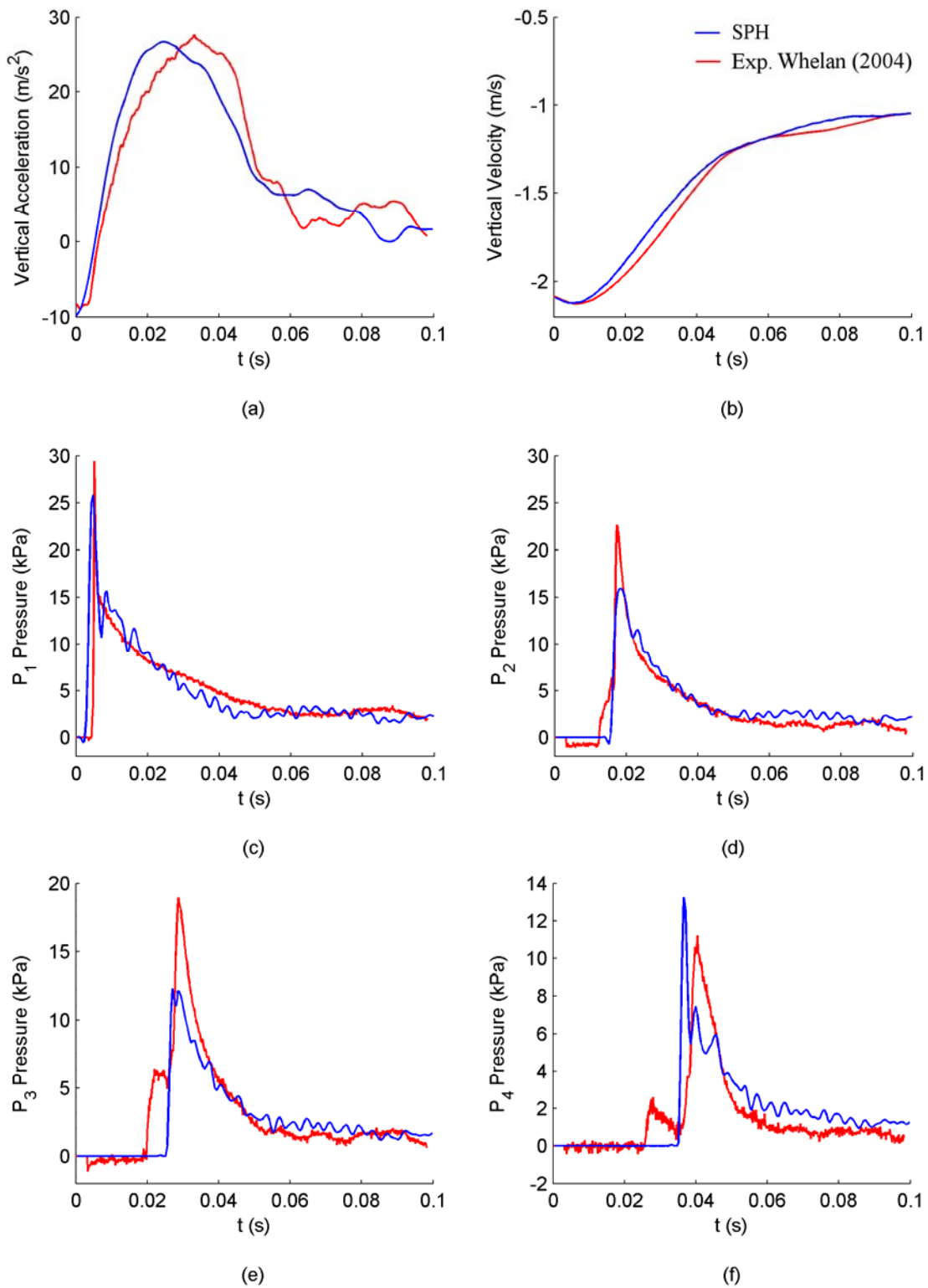
Figure 5.16 – The vertical acceleration, vertical velocity and pressure at four pressure sensors of a 25° deadrise wedge dropped from $H_H^* = 1.01$.

The acceleration trace of the simulated 15° deadrise wedge initially matches the experimental trace, but continues to climb higher after 0.01 s. The predicted acceleration peak occurs sooner and has a higher value than the experimental. The most probable cause of this is the lack of air cushioning in the SPH model as the wedge initially breaks through the free surface. At 25° deadrise angle, the acceleration traces are in good agreement as air cushion effects become negligible (Chuang, 1967). The velocity of the 15° deadrise wedge is also in agreement initially, but as the velocity of the body is directly integrated from the acceleration, the vertical speed predicted by the SPH model is slightly less than that measured experimentally. Furthermore the slower entry speed shifts the pressure peaks measured at each sensor to a slightly later time[1].

Generally the experimental and numerical pressure traces of the 15° deadrise wedge agree well, with the exception of the peak pressures at P_1 and P_3. Whelan (2004) sampled the pressure at approximately 7.0kHz, while the SPH pressure has only been sampled at 2.1kHz. Therefore it is possible that the SPH peak at P_1 has occurred between two sample points, resulting in the slight under prediction of the peak pressure. Conversely at P_3 the SPH pressure peak is slightly over-estimated, possibly due to numerical error in the evaluation of the pressure of the fluid particles.

The drop height affects the impact velocity, and hence the acceleration and fluid pressure experienced during impact. Figures 5.13 through to 5.15 illustrate the acceleration, velocity and the pressure experienced by the 25° deadrise wedge at $H_H^* = 0.47$, 0.61 and 1.06 respectively. All three SPH acceleration traces agree well with those of Whelan (2004). The peak acceleration occurs sooner as the drop height is increased, with some air cushion effect visible at $H_H^* = 1.01$ (see Figure 5.16a). The pressure peaks follow a similar pattern due to the increased entry velocity.

The pressure peaks of the 15° deadrise wedge were found to be considerably larger than those of the 25° deadrise wedge (see Figure 5.17). An increase in deadrise angle of just 10° has dropped the maximum pressure peak measured from 21.0 kPa

---

[1] A comparison between variable and constant velocity water entries of a 15° deadrise wedge can be found in Appendix B.
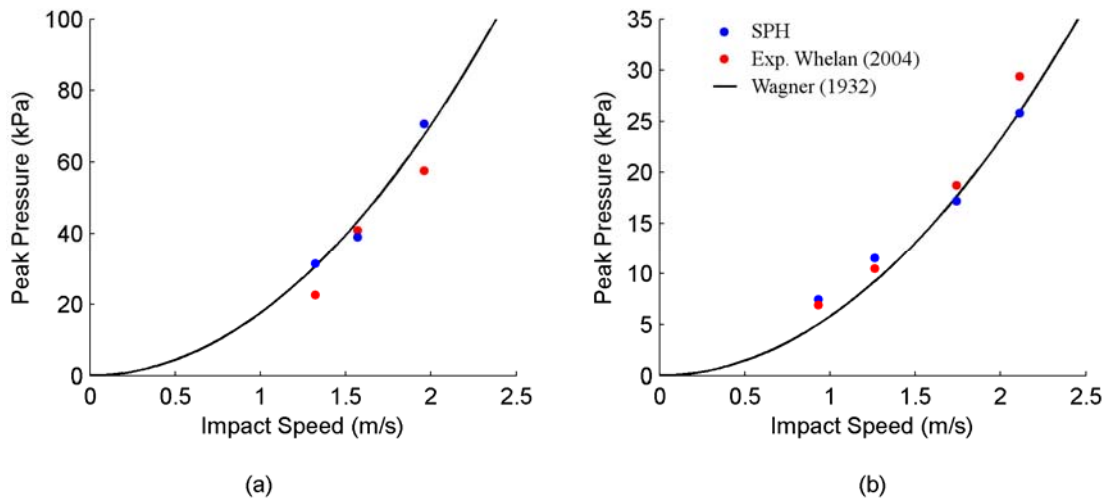
Figure 5.17 – The peak SPH pressure recorded at a number of entry speeds compared against the theoretical added mass method of Wagner (1932) and the experimental results of Whelan (2004). Results are shown for the 15° deadrise wedge (a) and the 25° deadrise wedge (b).

(experiment) and 28.5 kPa (SPH) to 11.6 kPa (experiment and SPH). The measured peak pressures increase as the drop height and subsequent impact velocity increase, following the theoretical trend described by Wagner (1932). The SPH peaks do not consistently over or under estimate the theoretical or experimental values. This scatter is possibly due to the low SPH pressure sample rate causing the actual peak to be missed. However by examining Figure 5.17, it can be concluded that both the SPH and theoretical peak pressures agree well with the maximum pressures recorded in the experiment.

In summary, the SPH simulations agree well with the experimental acceleration, velocity and pressure sensor data for both the 15° and 25° deadrise wedges over a range of entry velocities. The peak pressures predicted by Wagner (1932) also agree well with the maximum pressure recorded over all the SPH pressure sensors.). However, the present SPH algorithm is limited to modelling large deadrise angles as air is not present in the model and any compression effects are therefore ignored.

5.4 Variable velocity mono-hull impacts

Sections 5.2 and 5.3 focused on validating the moving boundary method for both constant velocity and dynamically responsive wedge impacts. The wedge shapes approximate the hull of a planing craft, however most large ships have a more complex hull form, particularly near the bow. A typical flared bow section has been modelled using the SPH algorithm and the results compared with previous experimental and numerical studies.

5.4.1 Experimental study

Aarsnes (1996) performed a series of drop tests using a 30° deadrise wedge and a sample ship bow section. The ship bow section measured 1.0 m in length and consisted of a 0.1 m measurement section with two 0.45 m dummy sections attached at either end. The beam of the measurement section was 0.32 m and the mass of the total falling rig was 261 kg. Four pressure sensors were placed in a line stretching from the keel to the hard chine at the middle of the hull section (see Figure 5.18) and two force transducers were positioned between the model section and the falling rig in order to determine the total load during impact.
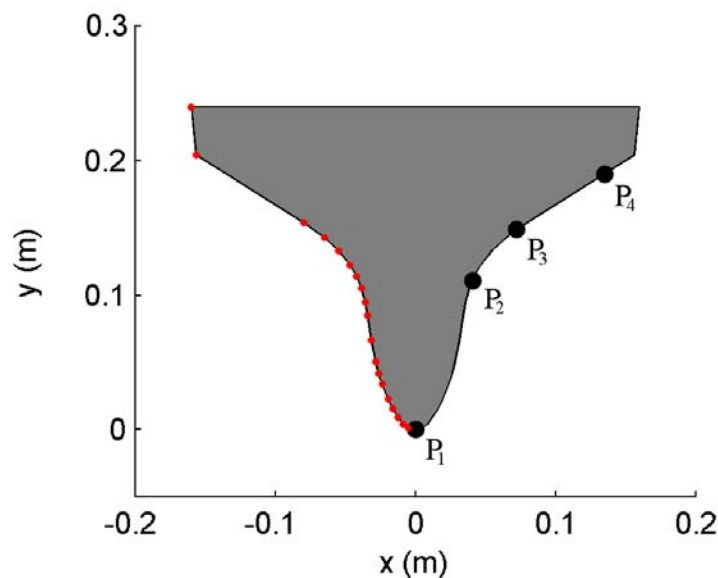
Figure 5.18 – The ship bow section studied by Aarsnes (1996). The red dots indicate the intersections between straight line segments that approximate the curvature of the hull and the black dots show the locations of the pressure sensors.

Sun (2007) performed a BEM analysis of the same drop tests and the results have been used here as a reference numerical solution. The initial stage of Sun's numerical hull impact was modelled using von Karman's (1929) theory. After the keel had passed the still water level (0.0008s to 0.003s into the simulation) and the maximum pressure was calculated, the BEM simulation was started.

5.4.2   SPH simulation

The Aarsnes (1996) hull form was approximated by a series of small straight line segments with a length no shorter than $3h$ (see Figure 5.18 for the locations of the short line segment intersection points and Section 3.6.2). Four drop tests were simulated using the SPH algorithm from a range of normalised drop heights (see Table 5.3). To be consistent with the wedge drop tests analysed in Section 5.3, the normalised height was calculated from the beam and the vertical distance between the keel and the still water surface by equation (5.1).

The size of the tank in which the experimental drop tests occurred was unknown, so the same tank used to simulate the Whelan (2004) experiments was also used here. Although the beam of the Aarsnes (1996) hull section is 36% less than the Whelan wedges, the same particle resolution (400 particles per metre) was used here for computational efficiency. It is worth noting that the wetted perimeters of the 25° wedge and the hull section are the same (0.55 m).

Section	Normalised Drop Height H_H^*	Initial Impact Speed
	0.34	0.58 m/s
	0.35	0.61 m/s
Aarsnes (1996)	0.86	1.48 m/s
	1.41	2.43 m/s

Table 5.3 – Outline of the variable velocity mono-hull impacts
modelled using the SPH algorithm.

5.4.3   SPH results

Figures 5.19 and 5.20 illustrate the pressure and velocity fields at three moments in time after the hull section, dropped from a normalised height of $H_H^* = 0.35$, strikes the initially still water surface. As the surface of the hull is steep near the keel, the pressure field immediately surrounding the hull at 0.1 s increases only slightly from its initial hydrostatic value. The fluid velocity at this point reaches a maximum of 1.5 m/s as a small jet – caused by the increase in local fluid pressure – begins to form. In the next time instant (0.13 s after impact), the flared section of the bow strikes the water surface and the local fluid pressure increases. A small region of high pressure fluid tracks along the surface of the hull, encouraging the formation of the jet. By the third time instant, the jet has separated from the surface of the hull section and propagates away with a maximum velocity of 5 m/s. At greater drop heights, the maximum velocity in the jet increases up to 9.5 m/s (at $H_H^* = 1.41$). A sustained high pressure region in the concave section of the hull drives the fluid particles away from the hull surface, an element not seen in any of the wedge impacts studied in the Sections 5.2 and 5.3.

The same method described in Section 5.1.2 for determining the load and the pressure at each sensor was also used for Aarsnes' (1996) hull section (see Figure 5.18). All experimental measurements were smoothed using a low pass filter of 300 Hz, so a filter with the same cut-off frequency was used in the SPH calculation. The experimental vertical force still shows obvious oscillations with a frequency of approximately 100 Hz at a normalised drop height of 1.16, believed to be due to vibrations in the drop rig (see Figures 5.21 to 5.23).

The SPH vertical force traces at all drop heights agree well with the experimental and BEM results. In each case the BEM peak is approximately 10-15% higher than that calculated using SPH. The experimental peak is matched by the SPH algorithm at a normalised drop height of 0.35 (Figure 5.21), however the SPH peak is considerably less than the experimental peak at 0.86 (Figure 5.22). This variation in the experimental results could be due to the excitation of the drop rig affecting the measured load (Sun, 2007). The BEM and SPH peaks also agree well in

time, but the experimental peak load lags slightly behind. This lag is primarily due to friction between the drop rig and its guide (Sun, 2007), which is accounted for by initialising the simulation with the impact velocity measured in the experiment.

Pressure sensors P_2 and P_3 display similar behaviour at each drop height. As each sensor becomes wetted, the pressure increases quickly to a rounded peak before easing slightly as the chine passes the still water level (see Figure 5.19c and Figure 5.21). However P_1 – in all models except $H^* = 0.35$ – recorded a very short peak the moment the keel struck the water surface, which was typically the maximum pressure recorded anywhere in the fluid during the simulation (see Figures 5.21 to 5.23). Generally the SPH solution for the pressure is in good agreement with the BEM solution. Conversely the SPH pressure appears to overestimate the experimental pressure by 10-15% for all time except for the initial pressure peak at P_1. The low sample frequency (2.1 kHz) is a possible cause for this low pressure calculation as the actual peak could have occurred between samples (the peak was typically no more than three data points wide).

The impact of the hull section with the water surface does generate pressure waves that propagate throughout the tank in the SPH simulation. These waves reflect off the side walls and the base, resulting in the observation of some noise in the pressure signals. The frequencies of oscillation are consistent with the natural modes of vibration of the tank (see chapter 4.3) and are a predominant feature of the weakly-compressible SPH method. Pressure waves are also present in the real case but have much smaller amplitude and are not noticeable.

Both numerical methods successfully predicted the acceleration and pressures experienced by the Aarsnes (1996) hull section during water entry. However the pressure field resolved by the weakly-compressible SPH method is characterised by large amplitude pressure waves. The BEM does not suffer from this problem, but unlike SPH the BEM cannot simulate fracturing of the free surface. While both methods have negative aspects, they are both capable of simulating the water entry of two-dimensional bodies.
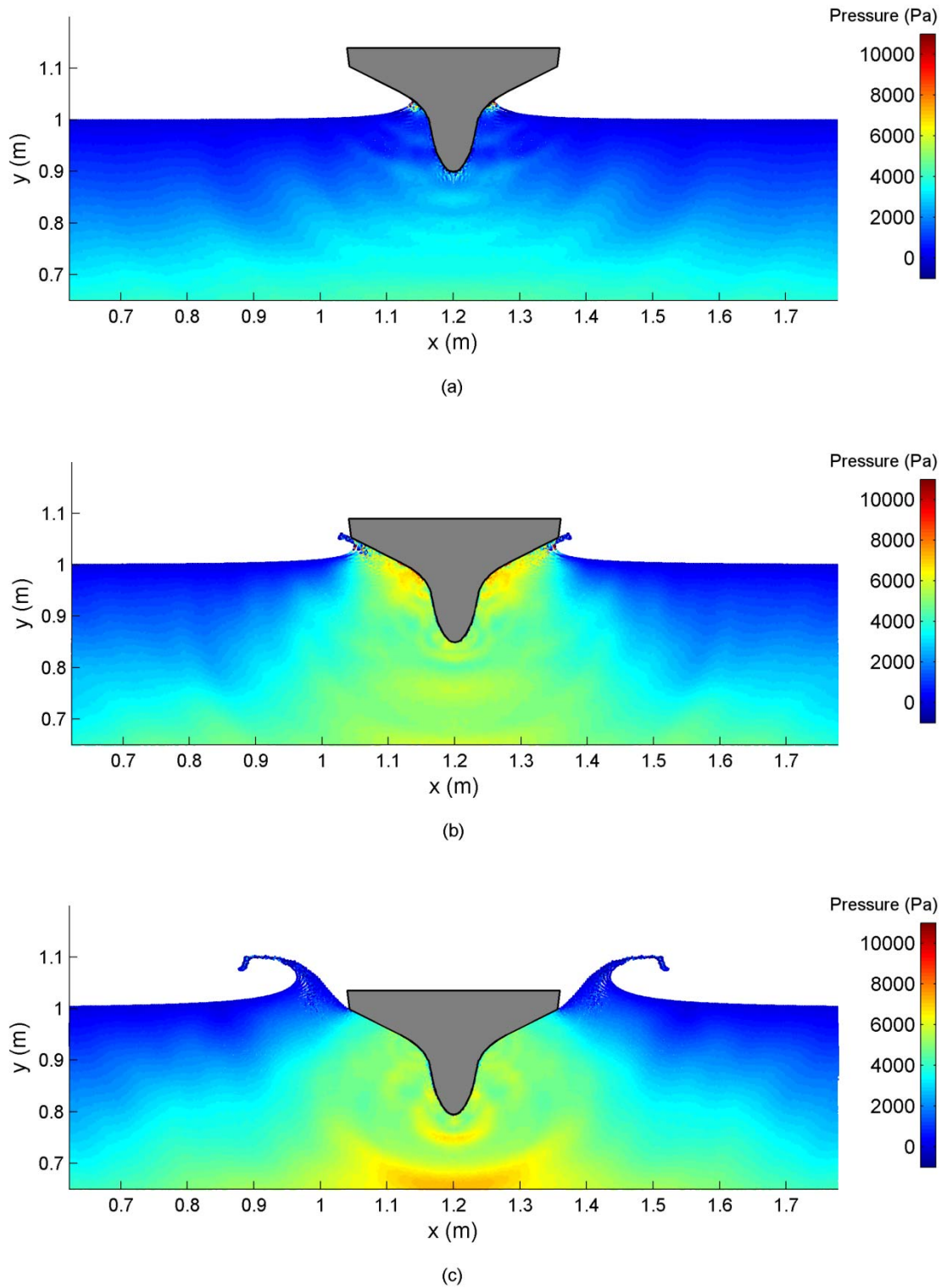
Figure 5.19 – SPH particles coloured by pressure after the impact of the Aarsnes (1996) hull cross-section dropped from $H_H^* = 0.35$. Images are shown at (a) 0.10 s, (b) 0.13 s and (c) 0.16 s after impact.
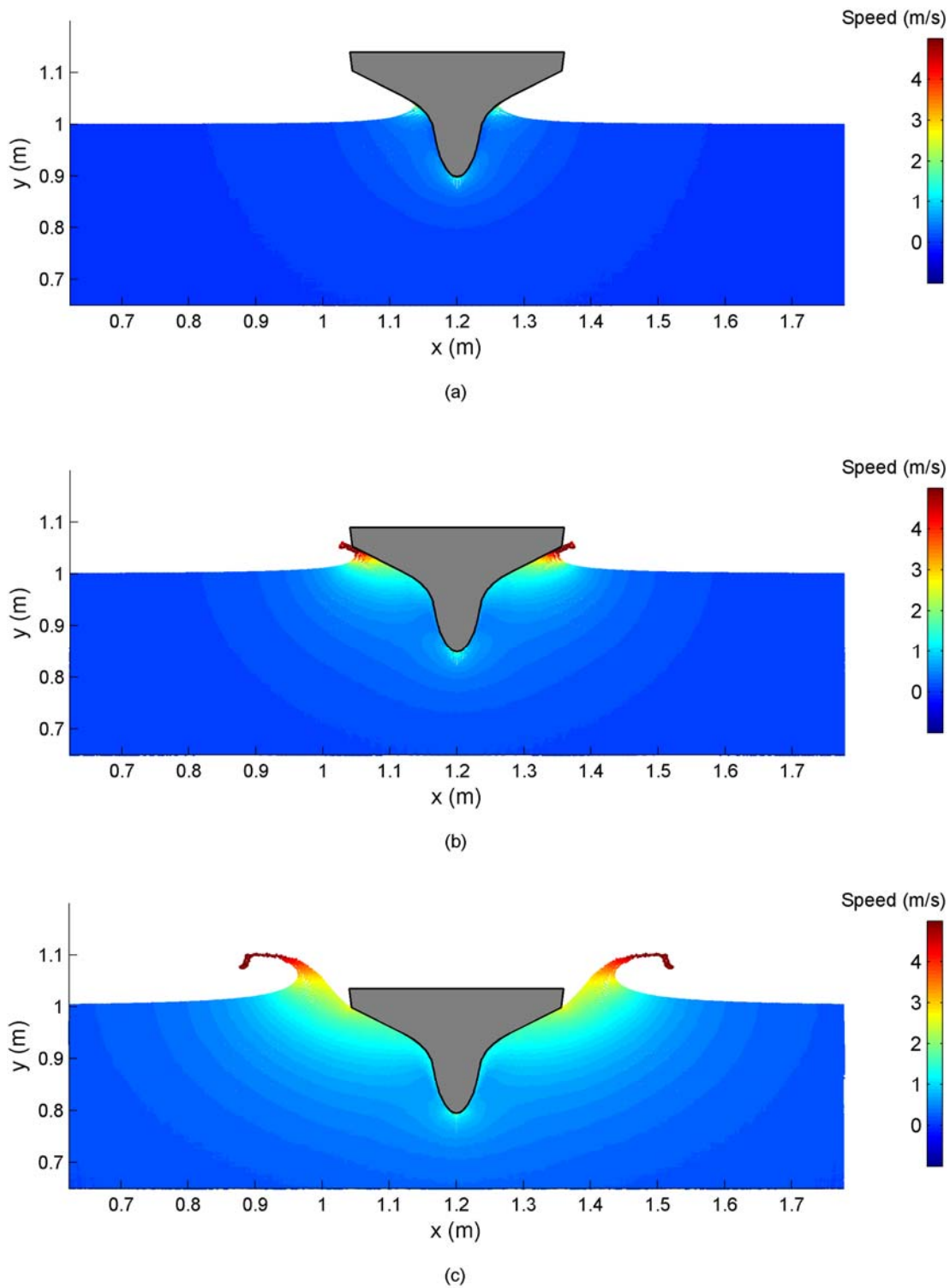
Figure 5.20 – SPH particles coloured by flow speed after the impact of the Aarsnes (1996) hull cross-section dropped from $H_H^* = 0.35$. Images are shown at (a) 0.10 s, (b) 0.13 s and (c) 0.16 s after impact.
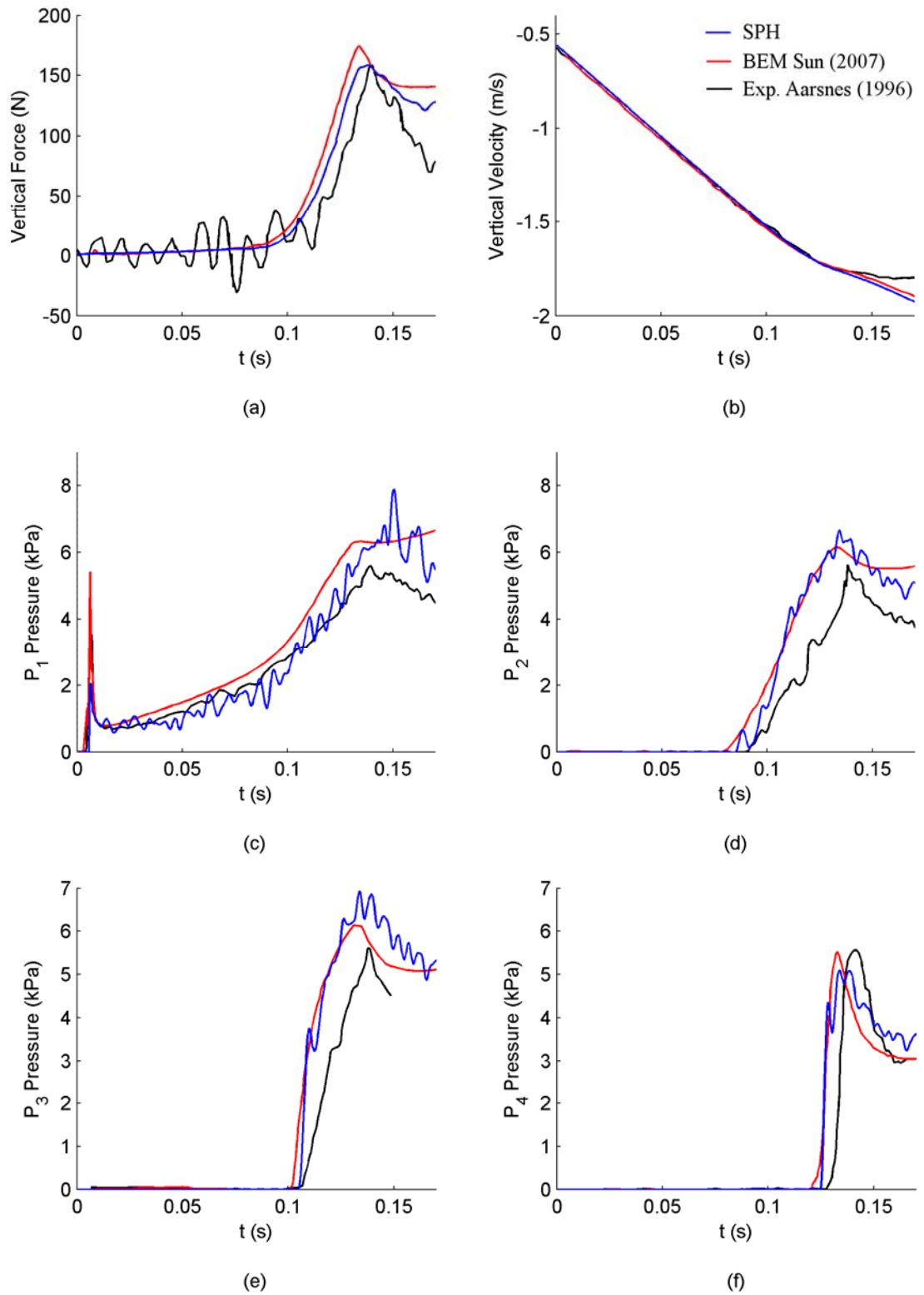
Figure 5.21 – Vertical force, hull velocity and pressure sensor traces of the Aarsnes (1996) ship bow section at $H_H^* = 0.35$.
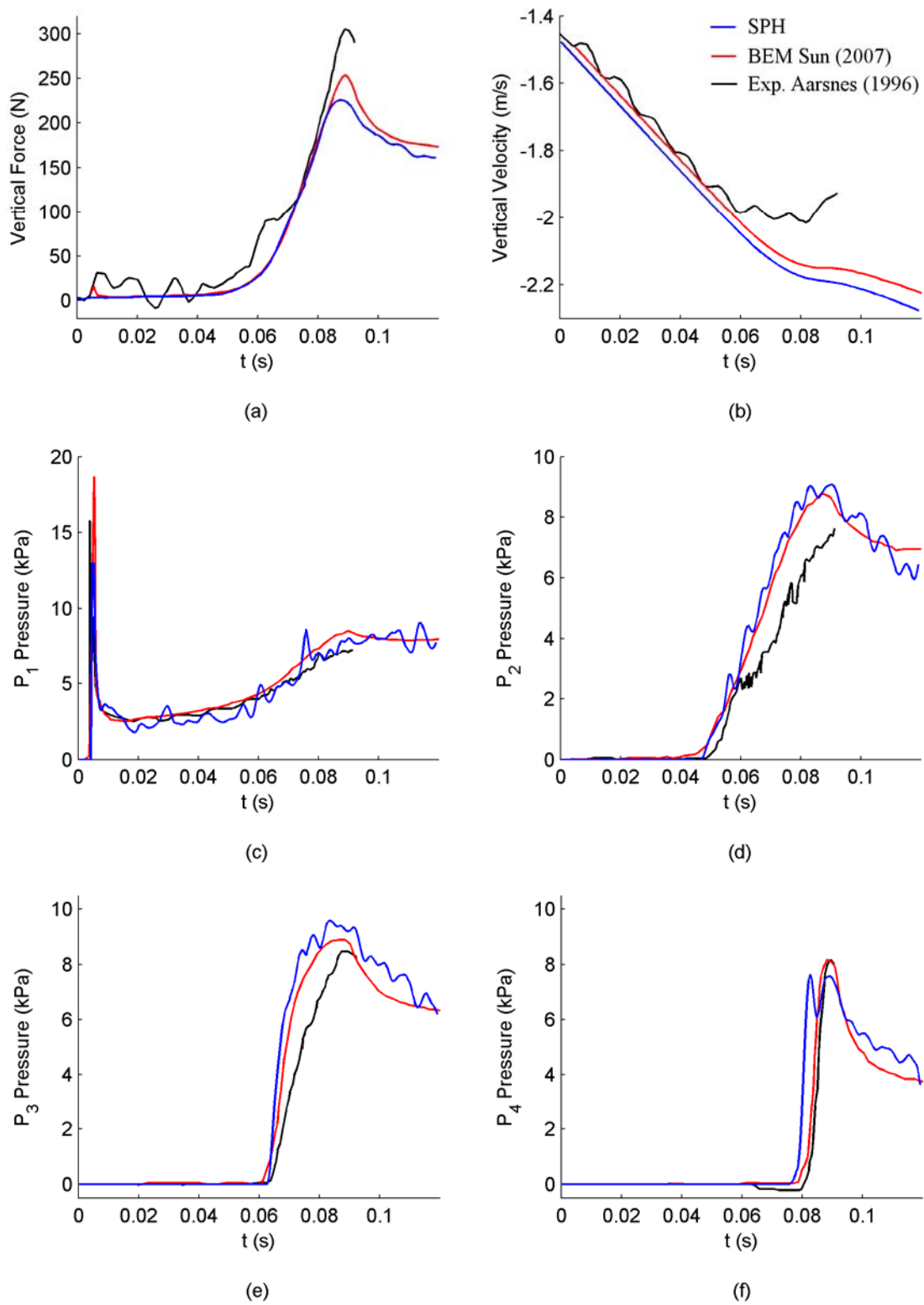
Figure 5.22 – Vertical force, hull velocity and pressure sensor traces of the Aarsnes (1996) ship bow section at $H_H^* = 0.86$.
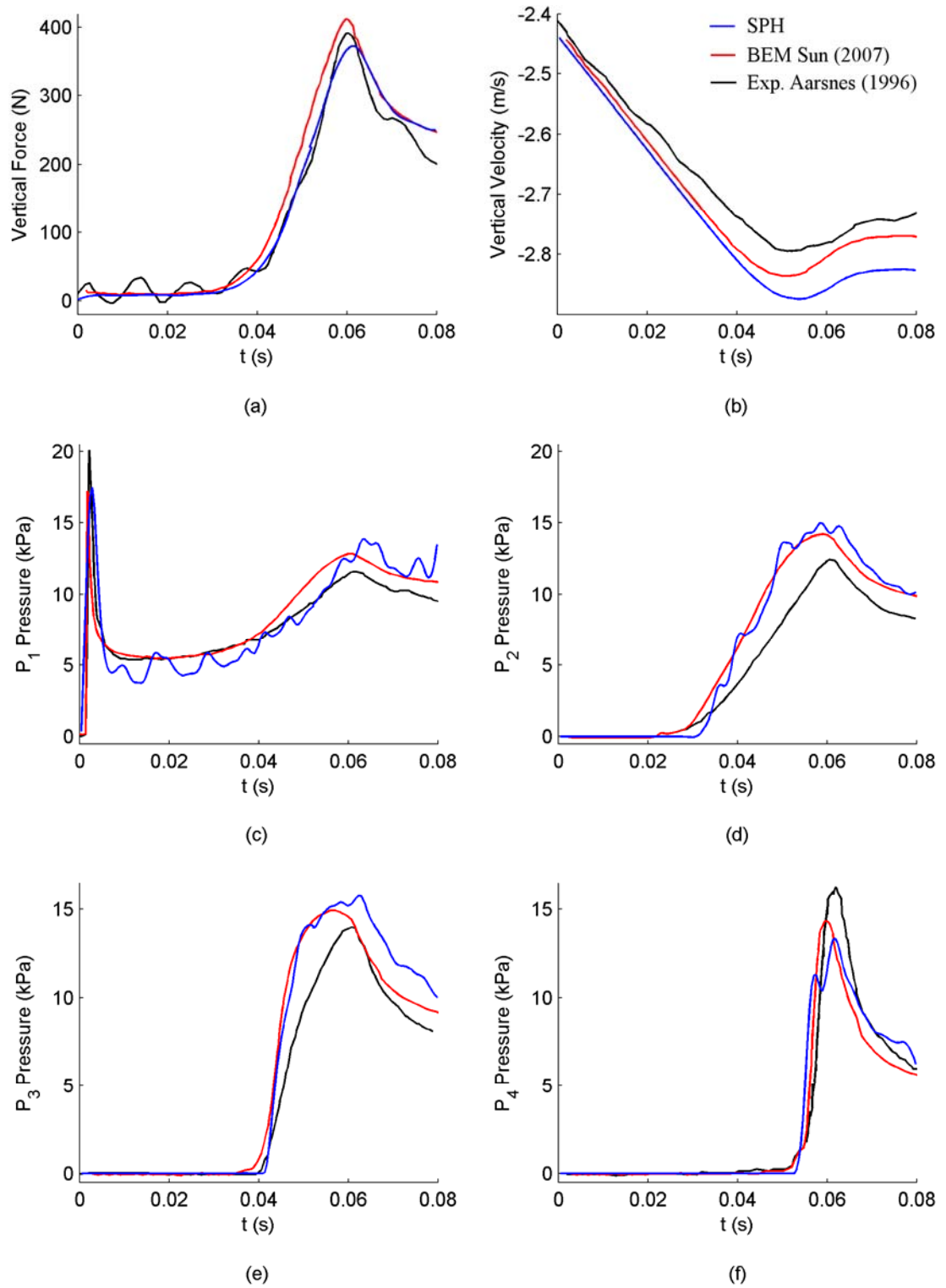
Figure 5.23 – Vertical force, hull velocity and pressure sensor traces of the Aarsnes (1996) ship bow section at $H_H^* = 1.41$.

5.5   Summary

The water entries of arbitrary two-dimensional bodies were modelled using the present SPH algorithm in this chapter. Wedges moving at constant vertical speed were forced into initially still water to simulate the experiments of Breder (2005). Good agreement between the SPH and experimental results was found for the 20° and 30° deadrise angle wedges, however the SPH algorithm considerably overestimated the load on the 10° deadrise wedge. This discrepancy is due to air compressibility and entrainment effects that influence the load on the experimental wedge, so a two fluid algorithm should be developed to accurately simulate the water entry of a low deadrise angle wedge.

Whelan (2004) dropped 15° and 25° deadrise wedges that were free to move in the vertical direction from a range of heights. The results of these drop tests were used as a benchmark for comparison with the dynamically responding SPH wedges. The SPH load and pressure sensor measurements corresponded with the results of Whelan (2004), but small air compression effects were noted during drop tests of the 15° deadrise wedge. The SPH wedge water entry simulations were also found to agree well with the theoretical peak pressures of Wagner (1932).

The results achieved for both the variable and constant velocity wedges allowed the complexity of the falling body's geometry to be increased. An SPH model of the Aarsnes (1996) flared bow section was created and the total load and the fluid pressure at a number of sensors was recorded. The experimental (Aarsnes, 1996) and BEM results of Sun (2007) were compared against the data recorded during the SPH simulation and all were found to be in agreement.

The simulations performed in this chapter, be it variable or constant velocity, supported the ability of the SPH algorithm to resolve the water entry of two-dimensional bodies.

Chapter 6

Slamming of a Slender Ship in Regular Waves

6.1 Introduction

The global motion of a large slender ship in regular waves is only slightly affected by slamming at the bow, with the exception of extremely violent slam events. The relative motion between the bow and the water surface follows a near sinusoidal pattern during impact, which is evident in the model scale experiments of Hermundstad and Moan (2005) and Sebastiani et al. (2001). The two-dimensional SPH slamming study completed in Chapter 5 focused on simulating the water entry of hull sections at both constant and variable (governed by the local fluid pressure) velocity. The loads and peak pressures measured in SPH simulations of both types of water entry are very different (see Appendix B) and neither follows the near sinusoidal profile noted in the ocean wave basin experiments of Hermundstad and Moan (2005). So in order to accurately simulate the three-dimensional bow slamming experiments, the hull section should follow a vertical speed profile determined from the relative motion between the bow and the water surface.

In this chapter the relative vertical velocity profile measured by Hermundstad and Moan (2005) at a single cross-section on a bulbous bow has been imposed on a two-dimensional SPH model. The purpose of this was to test the ability of the SPH algorithm to resolve the local fluid pressure surrounding a hull section under the influence of a prescribed vertical velocity profile. Completion of this validation allowed for the introduction of a more complex 2D + t approach to simulate bow slamming.

Divided into two parts, the 2D + t method calculates the motions of the hull – caused by the ship moving through regular waves – using the commercial seakeeping (strip theory) software package SEAWAY (Journée and Adegeest 2003) and then determines the relative vertical velocity between the hull and the water surface. Secondly, the relative vertical velocity profiles are then imposed on two-dimensional hull cross-sections in order to simulate the water entry process using SPH.

The tow tank experiments conducted on a slender V-form hull by Ochi (1958) were used to test the validity of this 2D + t approach. While the data available for comparison was limited, the result of this study is a method that can be used to visualise a slam on a three-dimensional ship using a combination of strip theory and two-dimensional SPH. The maximum slamming pressure and load at any location along a slender ship's hull can also be determined using the 2D + t method.

6.2   Slamming with relative vertical velocity

SPH simulations of the water entry of a two dimensional hull section were validated against experimental drop test data in Section 5.4. The drop tests of Aarsnes (1996) allowed the hull section to respond to the local fluid pressure, causing the entry speed to vary over time. An example of the relative vertical velocity measured by Aarsnes (1996) throughout a drop test is illustrated in Figure 6.1a. During ocean wave basin
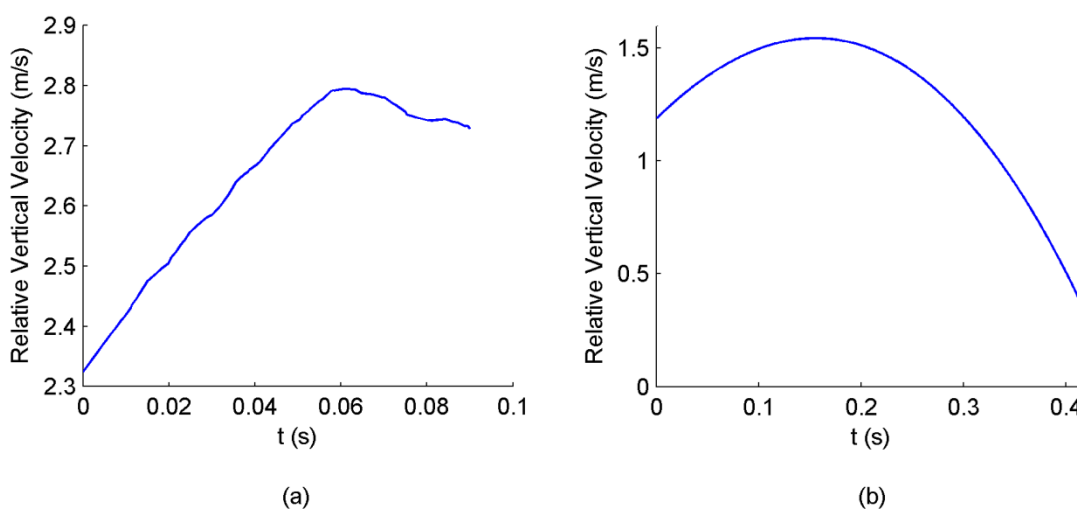
Figure 6.1 – Relative vertical velocity between the hull and the water surface during (a) the drop test of a bow section (Aarsnes, 1996) and (b) the ocean wave basin experiments of Hermundstad and Moan (2005).

experiments on a slender ship model (Hermundstad and Moan, 2005), the relative motion was found to follow a near sinusoidal pattern (Figure 6.1b). Construction of a 2D + t method for simulating bow slamming requires each hull section to follow a velocity profile based on this sinusoidal motion. So the water entry of a hull under the influence of a prescribed velocity profile is validated in this Section.

6.2.1   Experimental study

Hermundstad and Moan (2005) studied the motions of a 1:21.6 scale model of the 120 m car carrier *Autoprestige* in the 80 m by 50 m ocean wave basin at MARINTEK, Norway. The model was self-propelled at 2.2 m/s through regular waves of height 0.1 m and period 1.9 s; conditions that produced regular bow flare slamming. To measure the slamming-induced loads on the bow the authors placed two identical slam panels (large area pressure gauges) near the top of the flared bow section, $0.05L_{pp}$ aft of the forward perpendicular (see Figure 6.2). Each panel was mounted to a force transducer with a natural period that was not known, but was assumed to be at least an order of magnitude less than the rise time from zero to maximum slamming pressure. The ship motions were measured using an optical system that sampled the relative elevation between the flared bow section and the water surface at 500 Hz. By differentiating the relative elevation time series, the relative vertical velocity was obtained.
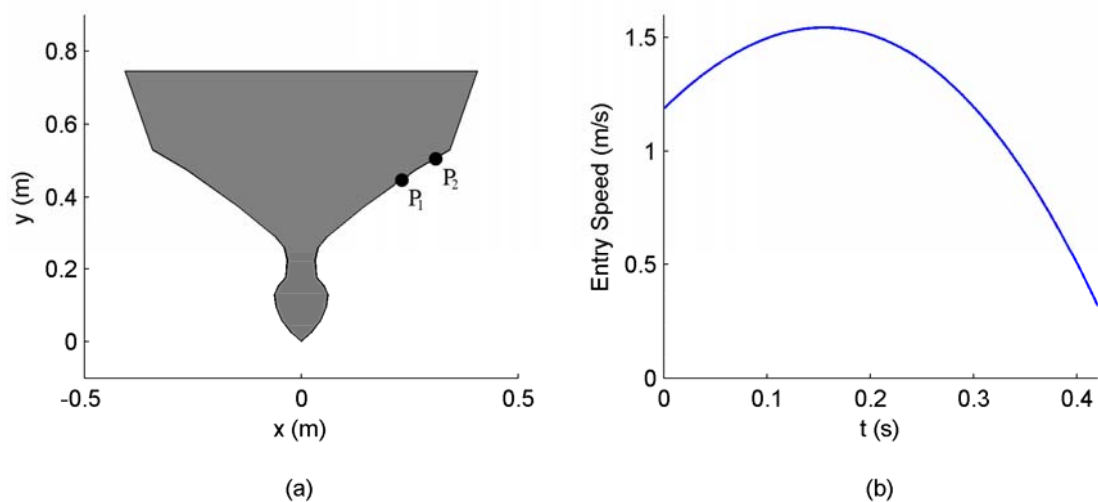
Figure 6.2 – The Hermundstad and Moan (2005) hull geometry (a) $0.05L_{pp}$ aft of the forward perpendicular and (b) the measured relative vertical velocity profile between the hull and the water surface.

The overall ship motions were also calculated by Hermundstad and Moan (2005) using a nonlinear rigid-ship strip theory model. In head seas the combination of just the calculated heave and pitch motions of the *Autoprestige* enabled the absolute vertical motion of the hull to be determined. Including the surge of the model ship and the incident wave elevation allowed for the calculation of the relative vertical velocity between any given hull cross-section and the water surface. The longitudinally flat keel of the *Autoprestige* allows this relative vertical velocity profile to be used for two-dimensional slamming pressure calculations.

The time series of the relative vertical velocity was used to calculate the slamming pressure at each patch via the simplified two-dimensional potential flow theory of Zhao et al. (1996). The method included ship generated waves – which were found to have minimal effect – and assumed the hull motion was not affected by the onset of whipping immediately after the slam event occurred. The calculated maximum slamming pressure agreed with that measured in the experiment, however the calculated peak lagged approximately 0.1 s behind the experimental.

Hermundstad and Moan (2005) demonstrated that a potential flow method could be used to accurately calculate the slamming pressure from a relative vertical velocity time series. In spite of this the method cannot accurately simulate extreme free surface fragmentation and deformation. To enable the free surface problem to be visualised, the hull section of the $0.05L_{pp}$ aft of the *Autoprestige's* forward perpendicular has been modelled using the SPH algorithm.

6.2.2 SPH simulation

The hull section of the *Autoprestige* $0.05L_{pp}$ aft of the forward perpendicular was digitised at model scale (see Figure 6.2) from the hull body plan published by Hermundstad and Moan (2005). The curved segments of the hull section were approximated by a series of small straight line wall boundaries in a method similar to that described in Section 5.4. The beam of the model measured 0.82 m, so the hull section was forced into a tank of water 3.5 m wide and 1.5 m deep in order to be consistent with Breder's (2005) 1.1 m wide constant velocity wedge water entries (see Section 5.2). Each constant velocity wedge water entry in Section 5.2 was

modelled at a particle resolution of 200 particles per unit length. The beam of the wedges modelled in Section 5.2 varied, but were approximately 1.3 times larger than the model *Autoprestige* hull section. Consequently the particle resolution for the *Autoprestige* model was increased to 260 particles per unit length to maintain a similar number of particles across the beam as in Section 5.2.

The model was initially placed a distance of $3h$ above the still water level and then subjected to the velocity profile illustrated in Figure 6.2b. Preliminary investigations found that the water speed in the jet rarely exceeded 4.0 m/s, so the sound speed could be set as low as 40 m/s without incurring compressibility effects. However the sound speed was set to 100 m/s, in order to be consistent with the dynamically responsive drop tests conducted in Chapter 5.

Figure 6.3 and Figure 6.4 describe the pressure and velocity fields at a number of time instants during the water entry process. As the bulb breaks through the free surface the neighbouring pressure field does not rise far above hydrostatic pressure due to the steep local deadrise angle; although the slight increase in pressure does generate low amplitude pressure waves that propagate throughout the fluid domain. The bottom of the hull section directs the fluid away from the model boundary at approximately 1.0 m/s causing a void to be formed immediately above the bulb. Approximately 0.12 s later, the fluid displaced during the initial impact strikes the lower part of the flare and the void collapses in on itself at 3.5 m/s. Water then impacts the vertical section above the bulb causing an increase in pressure (see Figure 6.3b) and as a result pressure waves propagate through the tank with an amplitude significantly larger than those caused by the impact of the bulb. Finally, as the flared section becomes fully wetted (see Figure 6.3c) a jet forms in a similar fashion to that seen during the wedge water entry simulations (see Chapter 5). By this time the vertical speed of the hull section has reduced to 0.8 m/s, resulting in a much lower local pressure than that recorded during the wedge simulations.

The pressure at each slamming panel was calculated using a similar method to that described in Section 5.2.2. In this case the width of the SPH pressure sensor was increased to 0.067 m, matching the size of the Hermundstad and Moan (2005)
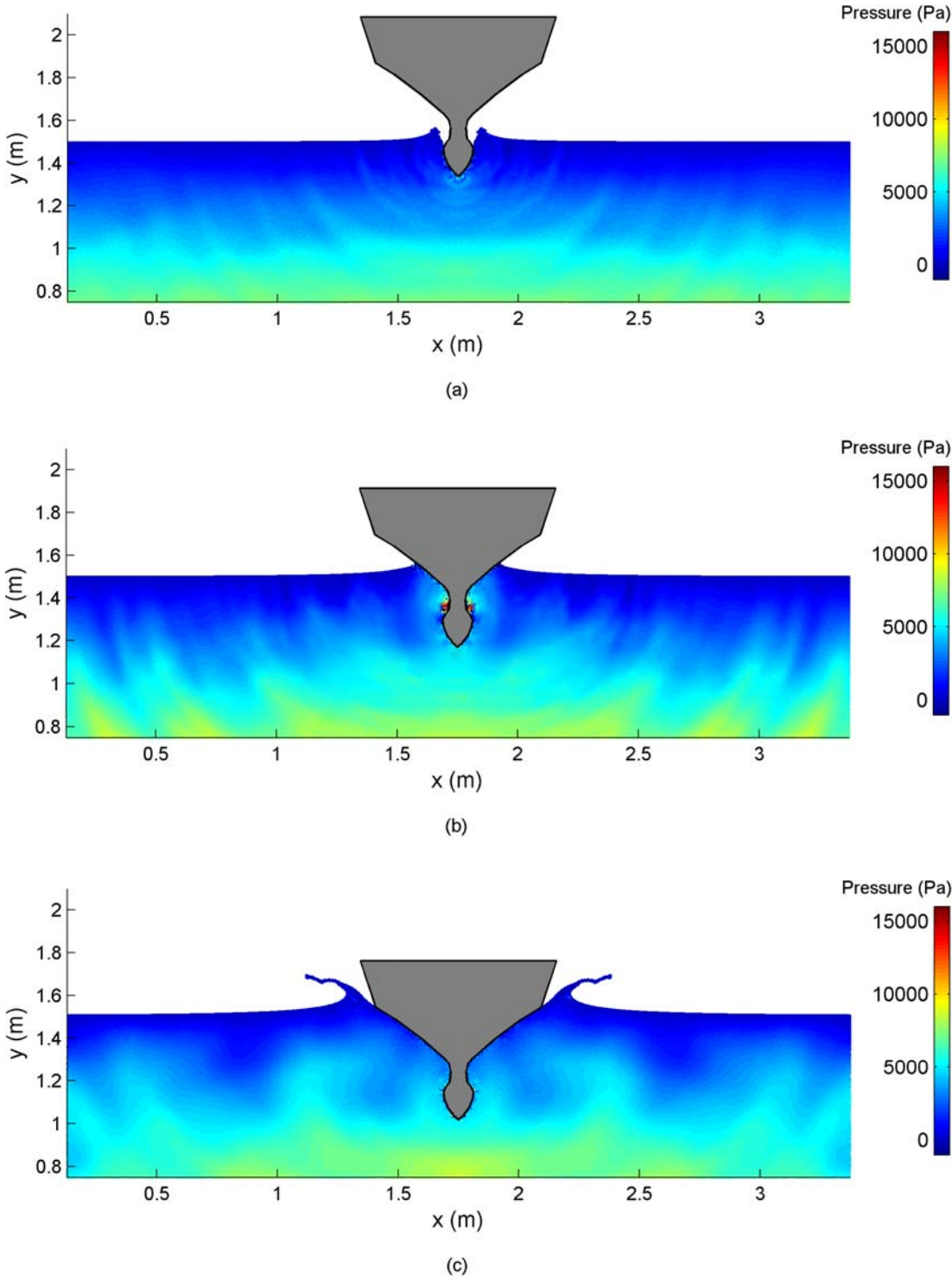
Figure 6.3 – The SPH pressure field during the water entry of the *Autoprestige* hull section. The field is illustrated at three time instants; (a) 0.12 s, (b) 0.24 s and (c) 0.36 s after the initial impact.
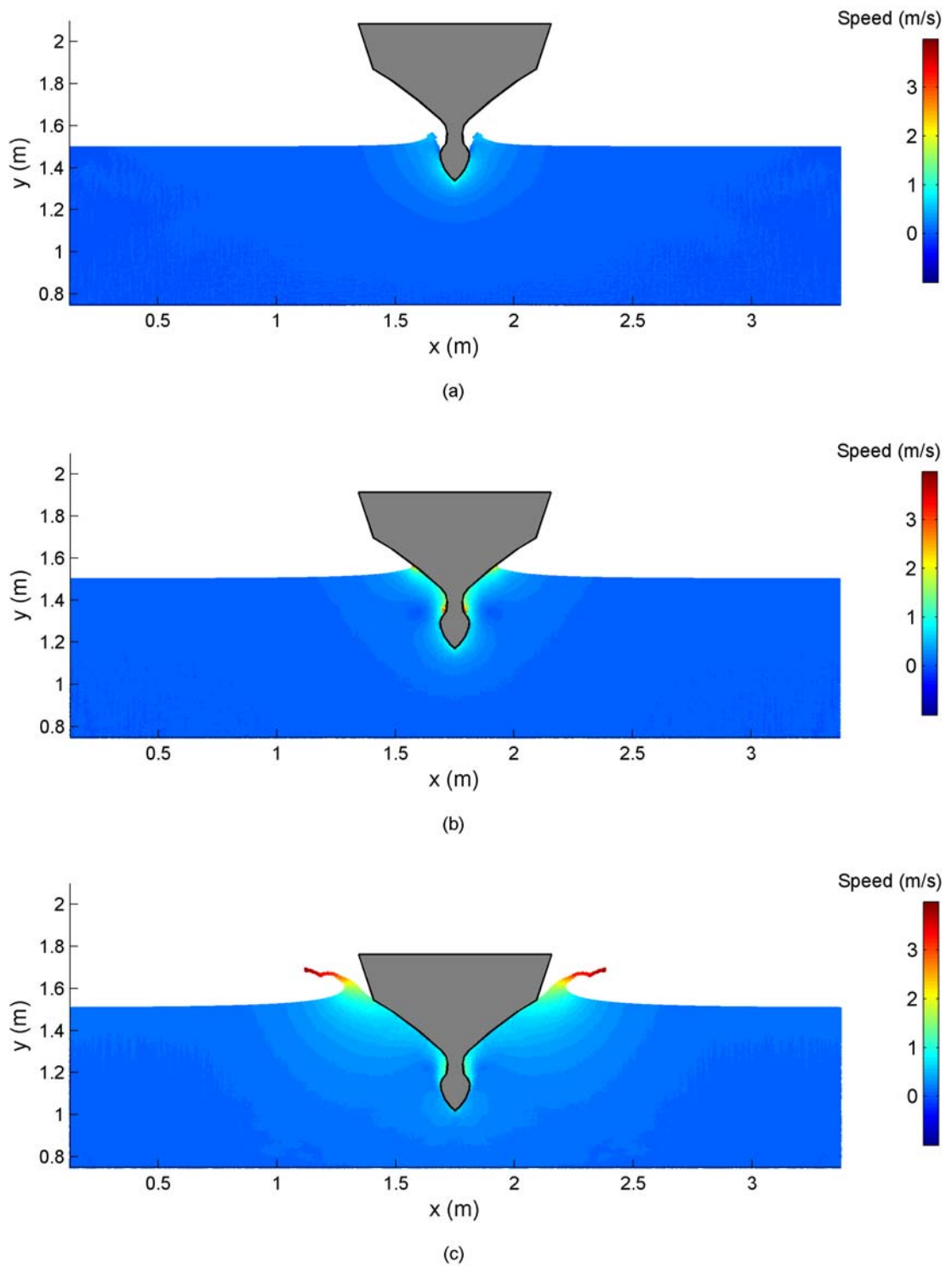
Figure 6.4 – The SPH flow speed field during the water entry of the *Autoprestige* hull section. The field is illustrated at three time instants; (a) 0.12 s, (b) 0.24 s and (c) 0.36 s after the initial impact.
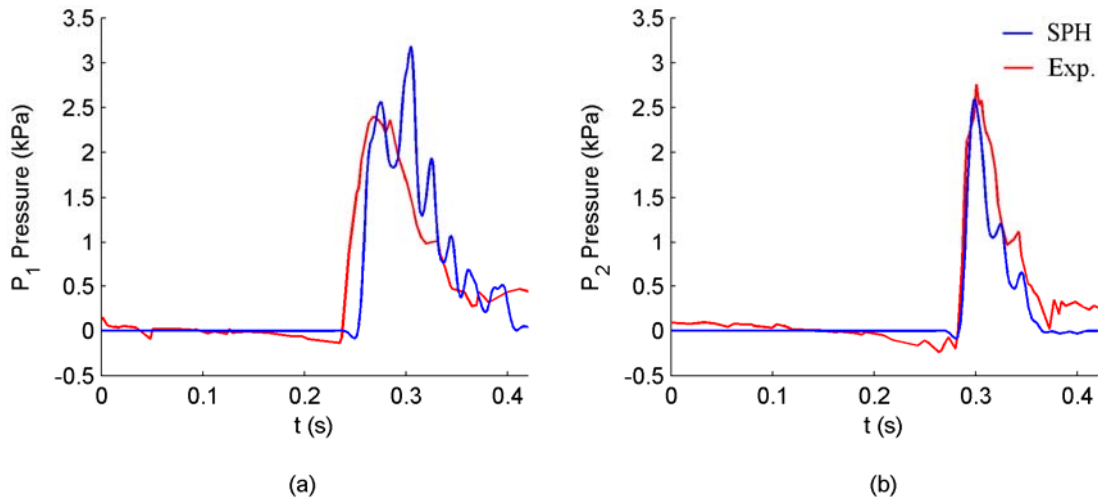
Figure 6.5 – The SPH and experimental pressure signals (Hermundstad and Moan, 2005) recorded at slamming panels (a) P_1 and (b) P_2.

slamming panels. The slamming pressure measurements in the experiment were sampled at 2.50 kHz but the authors gave no indication of the filtering, if any, that was applied to the pressure signals. Each SPH pressure signal was sampled at a lower frequency (1.11 kHz) producing a very noisy trace caused by the small differences in pressure between individual particles at each time step. As the peak pressure recorded on the *Autoprestige* model is approximately an order of magnitude less than those measured in Chapter 5, this noise appears to be much more significant. In order to remove the noise the signals were smoothed using a 100 Hz low pass filter.

The slamming pressure recorded at both panels over time is illustrated in Figure 6.5. Despite the application of the low pass filter, the pressure signals still show considerable oscillations during impact, particularly at P_1. Both SPH pressure signals agree well with the impact pressure measured during the experiment, however the SPH does lag behind the experimental by 0.02 s at P_1. The flared section of the bow is similar in shape to a wedge of deadrise angle 37° so it is possible to compare against the Wagner (1932) approximation for maximum pressure. The flared section of the bow initially strikes the free surface 0.21 s after the keel at a speed of 1.4 m/s, resulting in a maximum expected fluid pressure of 4.2 kPa via equation (2.1). This is much greater than the 3.2 kPa predicted by SPH and the 2.4 kPa recorded during the tow tank experiment, possibly because the local fluid is already in motion and follows a smooth path on to the flared section, rather than a sudden impact.

In conclusion, the present SPH algorithm has been successfully applied to the water entry of a two-dimensional flared bow section under the influence of an imposed velocity profile. The SPH pressure at each slamming panel agreed with the experimental measurements despite the presence of large pressure waves caused by the fluid impacting the vertical structure immediately above the bulb. The reasonable agreement between the SPH model and the experimental data allows for the development of a 2D + t method that can predict slamming loads via two-dimensional SPH cross-sections and commercial seakeeping software.

6.3   Slamming with motions predicted by strip theory

The two-dimensional hull model in the previous Section was forced into initially still water with a prescribed velocity profile determined from the experiments of Hermundstad and Moan (2005). Only one section of the hull was studied by Hermundstad and Moan (2005), limiting the amount of data available for comparison. Ochi (1958) instrumented a model V-form hull with pressure sensors at a number of locations and tested its susceptibility to slamming in regular head seas, but no indication of the hull motions was provided. With the aim of modelling slamming of this V-form hull using SPH, the ship motions were calculated using the commercial software package SEAWAY. The relative velocity between the hull and the water surface was then easily determined, enabling the impact to be modelled using a 2D + t method (see Section 1.1.3).

6.3.1   Model experiments

Two 6 m brass model hulls were self-propelled through regular waves in the 200 m Mejiro experimental tow tank in Tokyo, Japan by Ochi (1958). Both model hulls, a U-form and a V-form, were identical aft of midships but differed slightly in the bow. The U-form model was a 1:22 scale model of the MS *Mizukawa-Maru* (132 m) and had a rounded bow section, while the V-form (see Figure 6.6) was built to represent a number of typical merchant ships and was more wedge shaped at each bow cross-section. Each ship model was riveted together with all of the usual structural elements such as the centreline girder, frames and beams, but did not contain the transverse bulkheads as they were assumed to have no direct influence on the longitudinal strength of the hull.

153
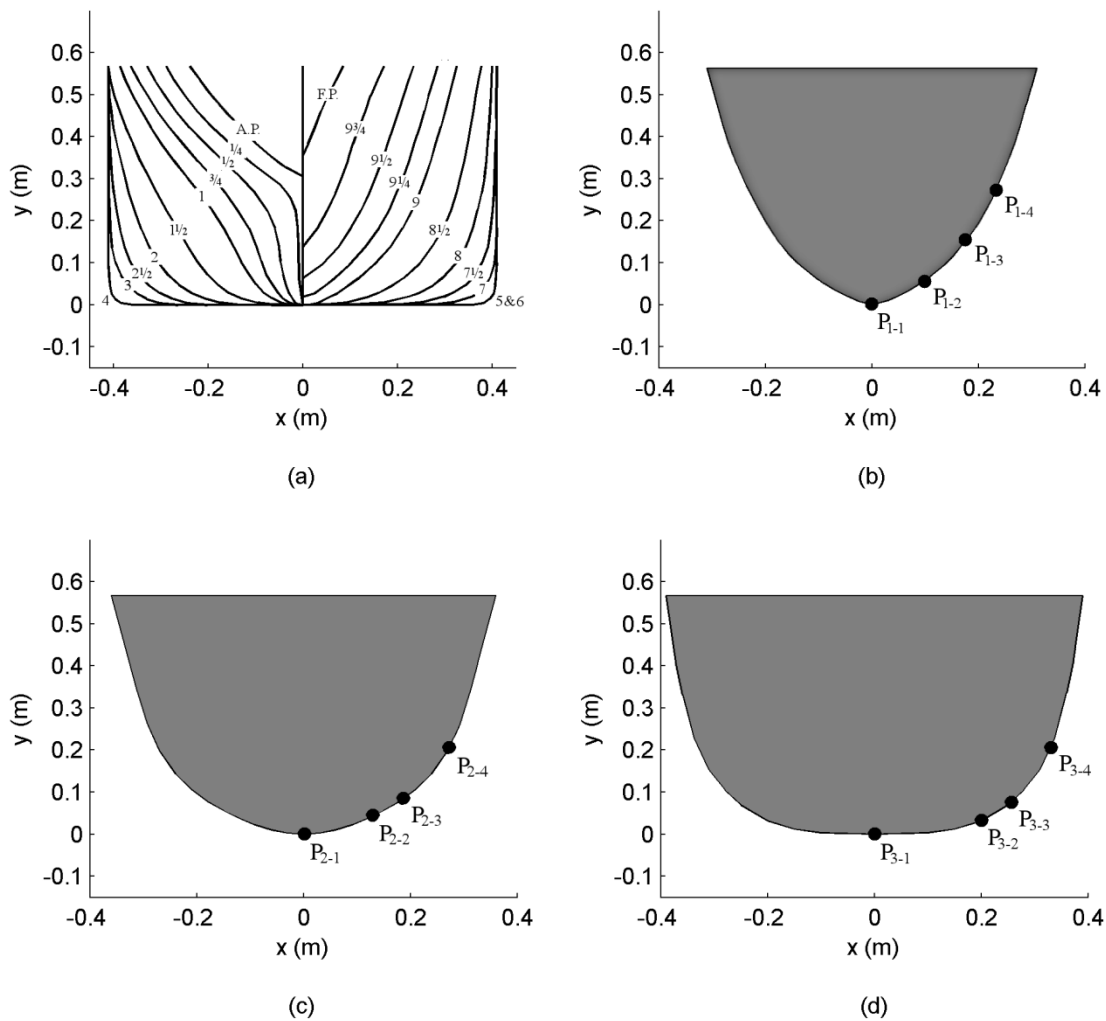
Figure 6.6 – Hull plan of the 6.0 m V-form merchant vessel model (a) and the two-dimensional cross-sections at (b) P_1 $0.093L_{pp}$, (c) P_2 $0.133L_{pp}$, and (d) P_3 $0.174L_{pp}$. The black dots indicate the position of the pressure sensors installed by Ochi (1958).

The towed models were allowed to pitch, heave and surge in regular waves with the intention of determining the influence of wave height, wave length and ship draft on slamming. Ochi (1958) placed a total of 19 pressure sensors, each 0.02 m in diameter, around the hull with the majority concentrated near the bow. In particular, four cross-sections located $0.093L_{pp}$, $0.133L_{pp}$, $0.174L_{pp}$ and $0.227L_{pp}$ aft of the forward perpendicular were each instrumented with four pressure sensors. The data recorded by each sensor was used to determine the position and magnitude of the maximum slamming pressure over a range of forward speeds (see Figure 6.6).

Ochi's (1958) study of the effect of forward speed on the slamming characteristics of the V-form model has been used as the benchmark for comparing the results of the 2D + t SPH simulations. The model hull – set with a draft of 0.2 m and trimmed down 0.08 m by the stern – was self-propelled through 0.2 m high regular waves with a wavelength equal to the hull's length (6 m). Ochi (1958) recorded the maximum pressure measured by the sensors at each forward speed but did not give any indication of the relative motion between the hull and the water surface.

6.3.2 Ship motion calculations

Simulating bow slamming of a three-dimensional hull with a predominantly flat keel using the two-dimensional SPH algorithm requires the relative vertical motion between the hull and the water surface to be known. To model the Ochi (1958) experiments, the relative motion was calculated using the commercial seakeeping software SEAWAY (see Section 1.1.3). The hull plan in Ochi (1958) was digitised, imported into SEAWAY and then interpolated, creating 100 evenly spaced cross-sections along the ship's length for use in the strip theory model. The properties of the hull (see Table 6.1) were calculated in SEAWAY after the interpolation and found to be within 2.5% of those measured by Ochi (1958).

Characteristics	Model (Ochi, 1958)	Model (SEAWAY)
Length (L_{pp})	6.0 m	6.0 m
Beam (B_H)	0.83 m	0.82 m
Draft (max)	0.36 m	0.36 m
Displacement	1334 kg	1331 kg
Block Coefficient	0.74	0.74
Prismatic Coefficient	0.75	0.75
Midship Coefficient	0.99	0.99
Water-plane Coefficient	0.83	0.84
Pitch Period (Max Draft)	1.36 s (measured)	1.39 s
Heave Period (Max Draft)	1.47 s (measured)	1.50 s

Table 6.1 – Comparison between the properties of
the experimental and numerical hulls.

The heave and pitch motions of the hull were then calculated by SEAWAY at 9 forward speeds - ranging from 1.2 m/s through to 2.8 m/s (model scale) - in regular head seas of height 0.2 m and period 2.0 s. Combining the heave and pitch motions enabled the relative velocity between any given hull cross-section and the water surface to be determined. The absolute elevation of the keel, $y_H(z, t^*)$ at any point z along the ship's length and any time t^* from an arbitrary fixed reference point was calculated by the following equation,

$$y_H(z, t^*) = A_H cos(\omega t^* + \phi_H) - z A_P cos(\omega t^* + \phi_P) \qquad (6.1)$$

where A_H, ϕ_H, A_P and ϕ_P are the amplitude and phase of the heave and pitch motions respectively and ω is the wave encounter frequency. The keel amidships was placed on the origin and the relative vertical velocity between the hull and the water surface v_{entry} was then determined via the following equation,

$$v_{entry} = \frac{d}{dt^*} [y_H(z, t^*) - \eta(z, t^*)] \qquad (6.2)$$

where $\eta(z, t^*)$ is the free surface position at any time t^* along the ship's hull. Examples of the velocity profiles experienced by cross-sections P_1, P_2 and P_3 at forward speeds of 1.6 m/s and 2.0 m/s can be seen in Figure 6.7, where t represents the time after initial impact with the still water surface.
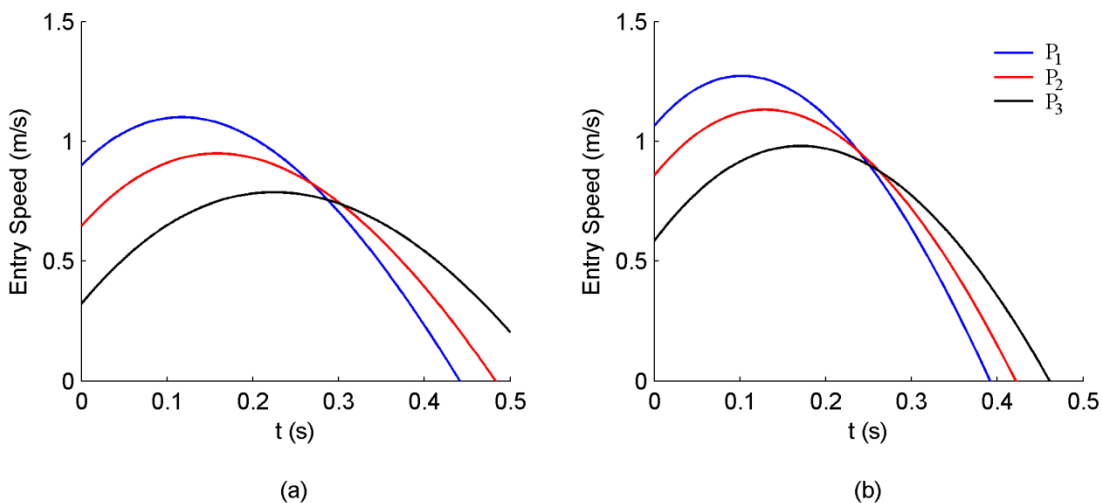
Figure 6.7 – Relative velocity profiles for each hull cross-section after initial impact $(t = 0)$ calculated using the heave and pitch motions generated by SEAWAY at (a) 1.6 m/s and (b) 2.0 m/s forward speed.

6.3.3 SPH simulation

Three cross-sections of the V-form hull were studied in detail using the SPH algorithm (see Figure 6.6). A fourth cross-section $0.227L_{pp}$ aft of the forward perpendicular was not modelled using SPH as the keel was similar in shape to a flat plate, which can cause air compressibility effects that are unable to be resolved by the present algorithm.

The width and depth of the Mejiro tow tank was unknown, so the same tank used to simulate the Whelan (2004) wedge experiments was also used here. The beam of the V-form hull was 0.83 m – approximately 65% larger than the Whelan (2004) wedges – but at maximum draft (0.36 m) the width of the cross-sections at the water line did not exceed 0.65 m. The 2.4 m wide and 1.0 m deep tank was considered large enough as the significant elements of the fluid flow were not affected by the presence of the solid tank boundaries. For consistency, the sound speed imposed on the Hermundstad and Moan (2005) SPH hull model was also used for the V-form hull simulations (100 m/s), as the maximum expected flow speed (7 m/s during the most extreme water entry of P_3) did not exceed the mach number criterion. Furthermore the same coefficients applied to the artificial viscosity, XSPH and tensile instability corrections during the SPH dam break model were also implemented here.

Each cross-section was initially placed a distance $3h$ above the free water surface. The tank was filled with 384 000 fluid particles at a resolution of 400 particles per metre and the relative vertical velocity profiles generated by SEAWAY were then imposed on each two-dimensional hull section. At nine forward speeds ranging from 1.2 m/s through to 2.8 m/s, all three cross-sections were modelled and then combined to simulate the V-form hull slamming.

Figures 6.8 and 6.9 show the bow striking the water surface (indicated by the solid blue line) at forward speeds of 1.6 m/s and 2.0 m/s respectively. At 1.6 m/s the third cross-section P_3 strikes the trough of the wave 0.05 s before P_2 and 0.10 s before P_1. Figure 6.8b illustrates the initial formation of the jet 0.13 s after P_3 strikes the free surface, which due to the difference in impact time is more evolved at P_3 than P_1.
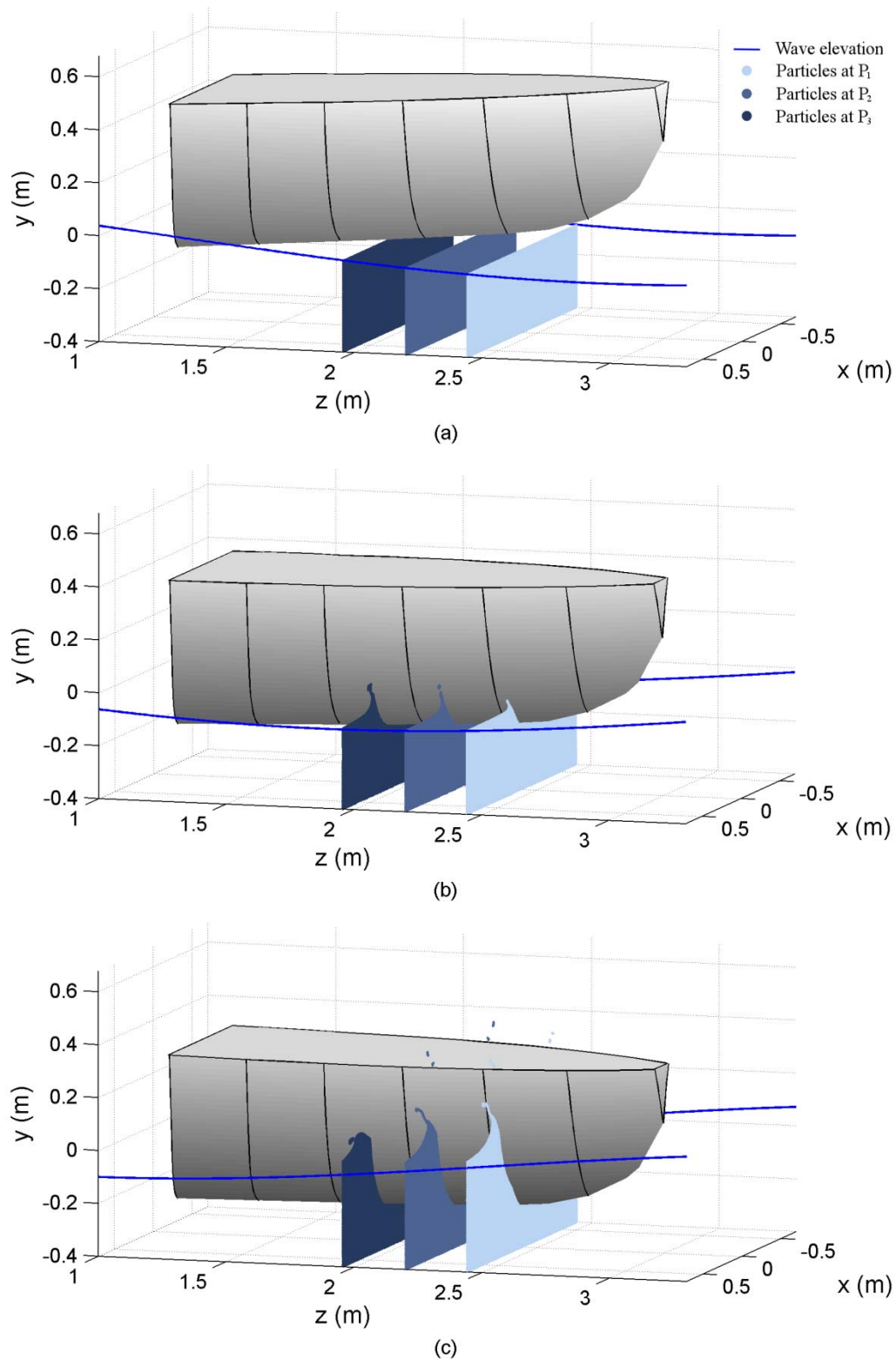
Figure 6.8 – SPH particle positions at 1.6 m/s forward speed (a) 0.07 s, (b) 0.13 s and (c) 0.33 s after initial impact with the free surface. The blue line indicates the undisturbed instantaneous free surface elevation.
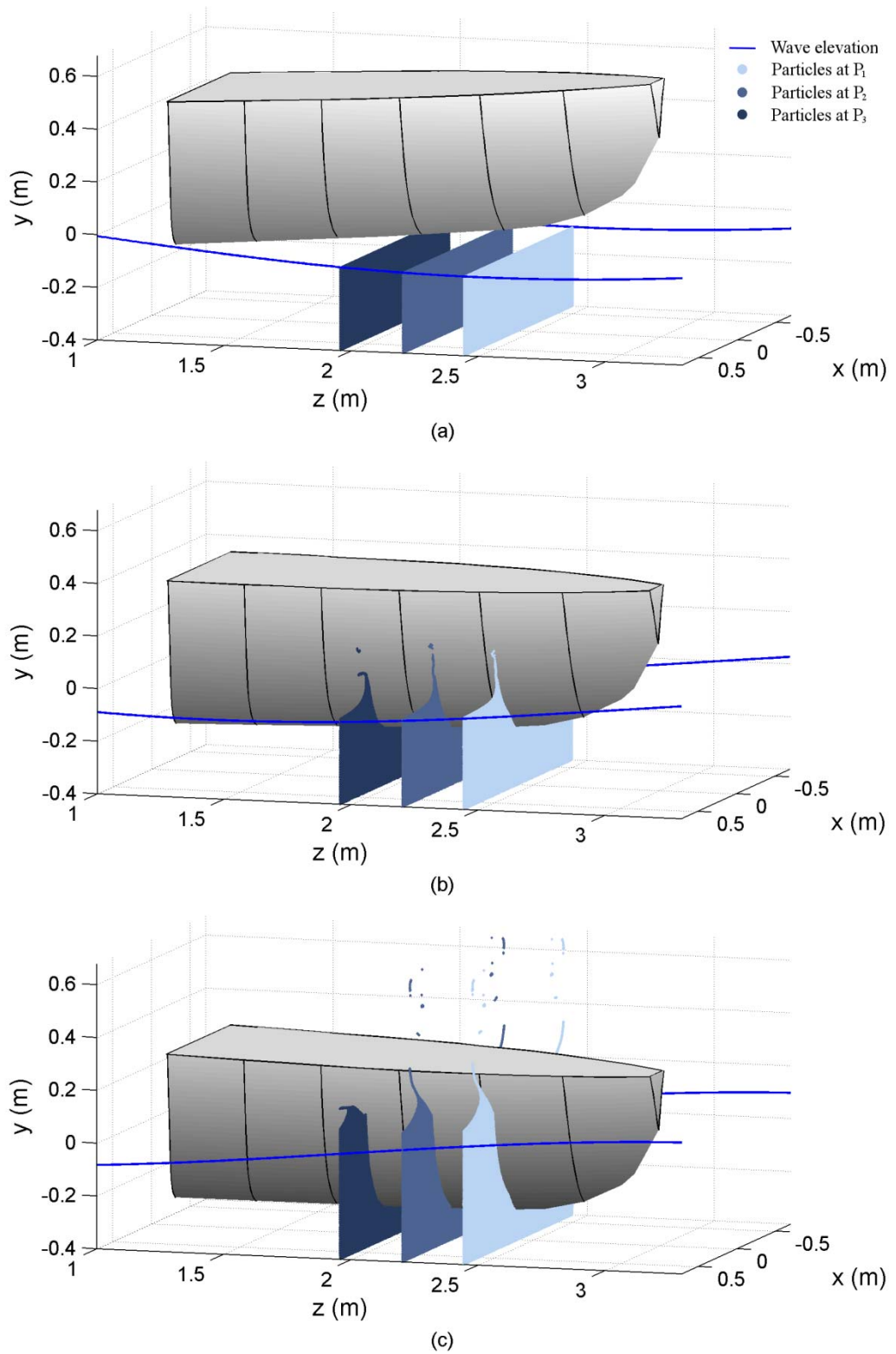
Figure 6.9 – SPH particle positions at 2.0 m/s forward speed (a) 0.07 s, (b) 0.13 s and (c) 0.33 s after initial impact with the free surface. The blue line indicates the undisturbed instantaneous free surface elevation.

A further 0.2 s later the jet at P_3 has slowed and begun to fall back towards the free surface while the jets at the other two cross-sections have peaked in height above the initial still water level and begun to fragment. At a forward speed of 2.0 m/s, the cross-sections strike the water surface just 0.01 s apart as the incident wave begins to climb away from the trough. Pressure sensor P_{1-1} experiences a maximum pressure at this speed (see Figure 6.12a) due to the particularly violent fluid motion. Despite their differences in shape, each cross-section causes the fluid jets to exhibit similar behaviour.

The pressure field immediately surrounding each hull cross-section 0.15 s after impacting the free surface at 2.0 m/s forward speed is illustrated in Figure 6.10. The relative motion between the hull and the water surface is much more pronounced at P_1 (1.06 m/s entry speed), yet the pressure field is less disturbed than that surrounding P_3 (0.58 m/s entry speed). Hull section P_3 has a much flatter keel causing a larger increase in fluid pressure during impact. The greater pressure then forces much larger amplitude pressure waves to propagate through the tank.

The water entry of hull section P_2 (forward speed 2.0 m/s) is studied in detail in Figure 6.11. At the first time instant, 0.1 s after initial impact, the pressure immediately adjacent to the keel has risen above hydrostatic to approximately 3.0 kPa. This higher pressure has forced pressure waves to propagate away from the surface, but 0.1 s later (Figure 6.11b) the waves have dissipated as the vertical speed has slowed significantly. By this point in time a jet has formed and began to fragment. Finally, 0.3 s after impact, the vertical speed of the hull section has reduced to 0 m/s and the pressure field has returned to a near hydrostatic profile.

Ochi (1958) measured the peak pressure at the keel of each hull cross-section using 0.02 m diameter brass resistance-type strain gauges (see Figure 6.12). The SPH pressures were measured using the same method described in Section 4.4 and smoothed using a 100 Hz low pass filter. The magnitude of the peak pressures predicted by the SPH algorithm at sections P_1 and P_2 were in fair agreement over the entire forward speed range, however it is worth noting that more information on the experimental motions would be required before concluding if the peak pressure differences are due to the calculated motions or the SPH simulation.

(a)

(b)

(c)
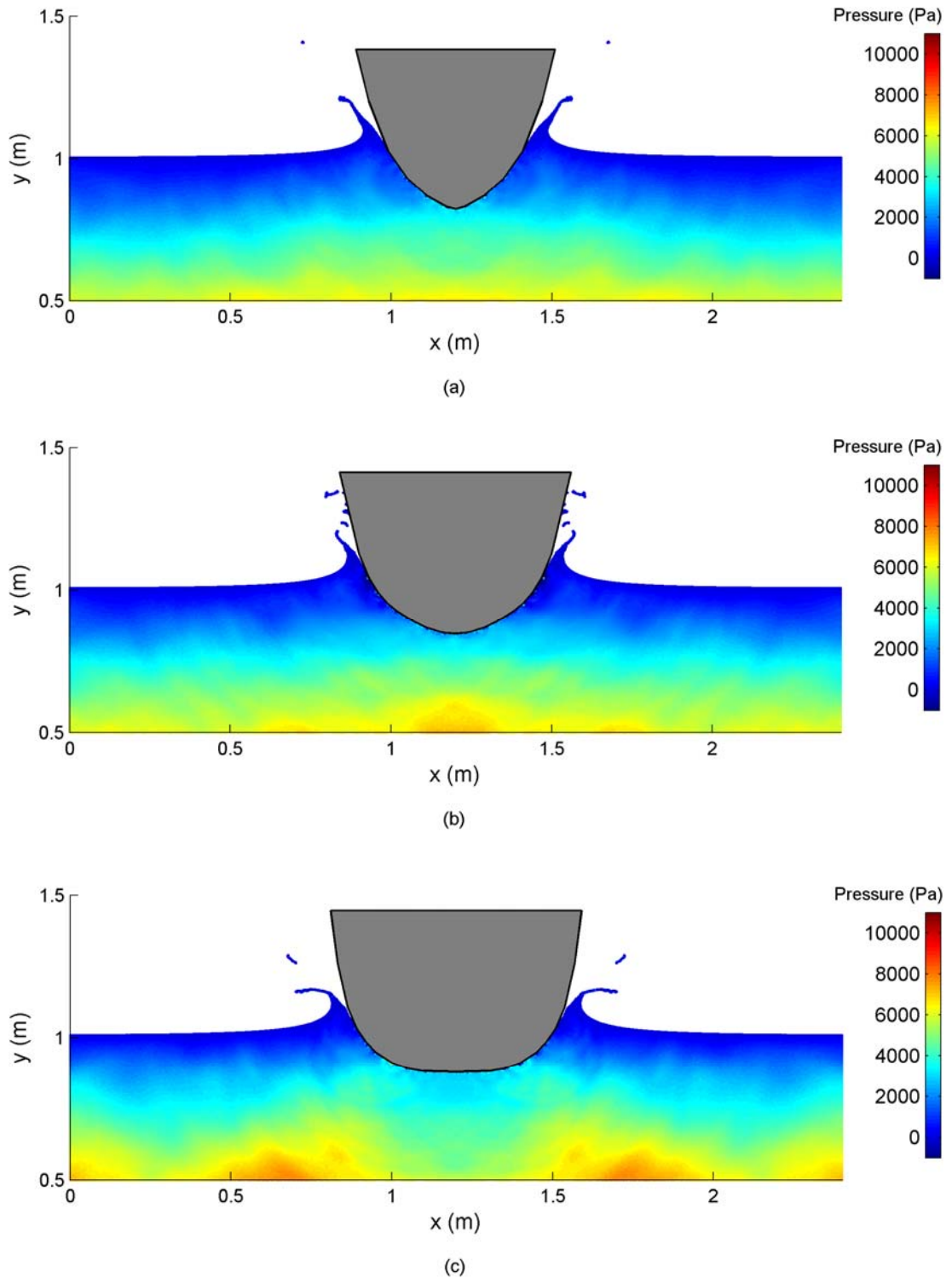
Figure 6.10 – Pressure field surrounding each section (a) P_1 $0.093L_{pp}$,
(b) P_2 $0.133L_{pp}$, and (c) P_3 $0.174L_{pp}$, 0.15 s after initially striking
the water surface at a forward speed of 2.0 m/s.
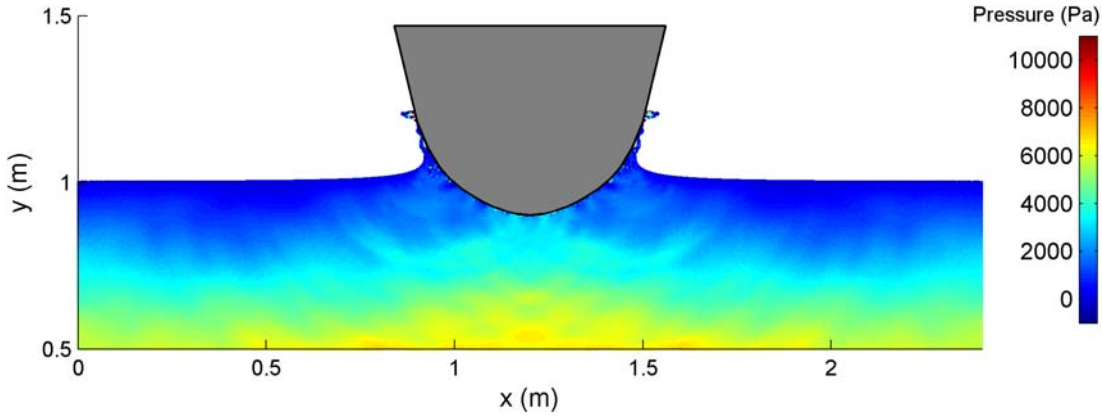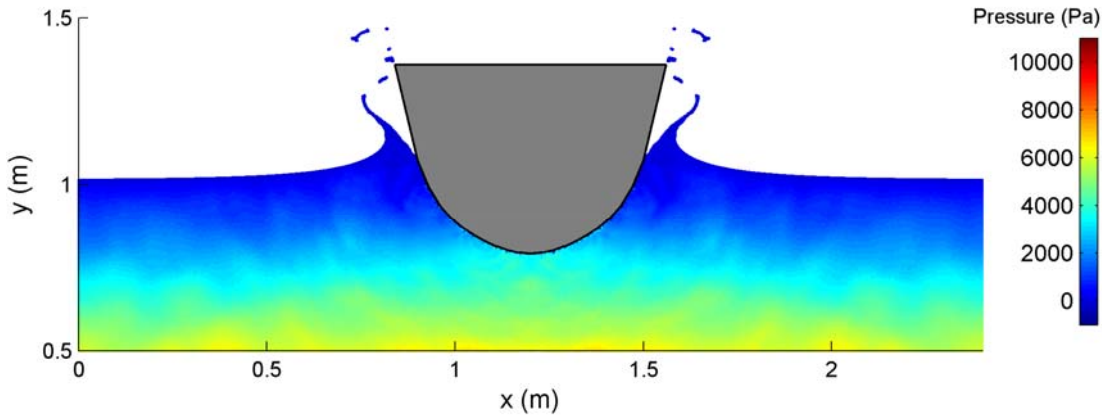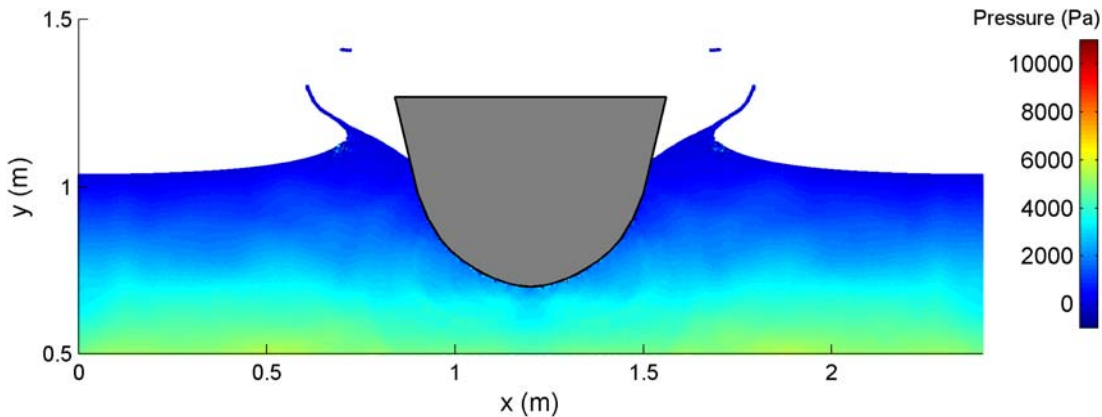
Figure 6.11 – Pressure field surrounding the second section P_2 (a) 0.1 s, (b) 0.2 s and (c) 0.3 s after initial impact with the water surface. The model had a forward speed of 2.0 m/s.
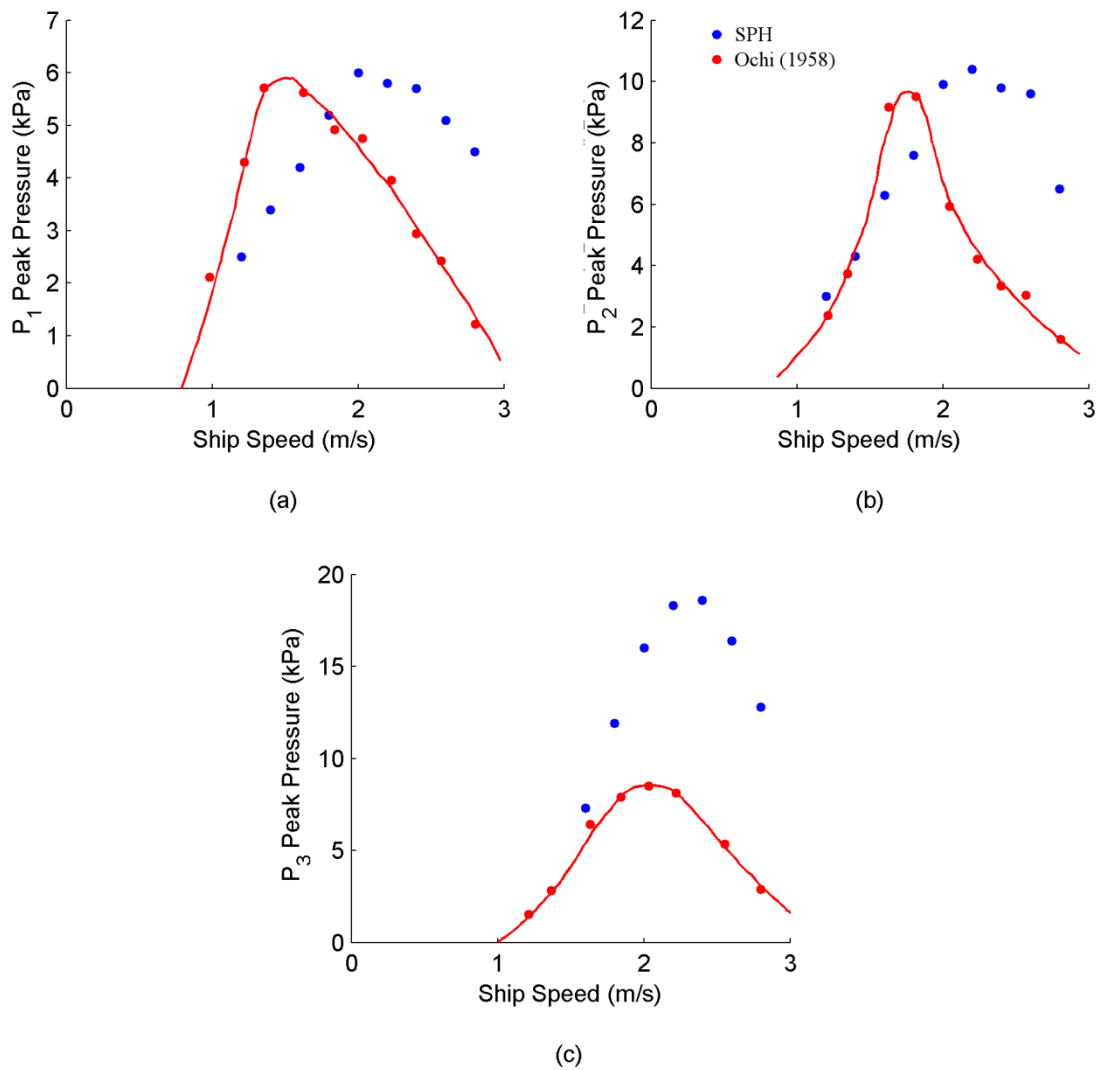
Figure 6.12 – Peak pressure measured by the sensors located on the keel of sections (a) P_1 $0.093L_{pp}$, (b) P_2 $0.133L_{pp}$, and (c) P_3 $0.174L_{pp}$.

The peak SPH pressures recorded at P_3 (see Figure 6.12c), are approximately twice as large as the experimental values. This is primarily due to the flat shape of the keel compressing air between the hull and the water surface in the experiment. The present SPH algorithm is not yet able to accurately model the interaction between the two fluids and the hull section.

Ochi (1958) also reported on the peak pressure measured at the other three pressure sensors at each cross-section, but only at a forward speed of 2.2 m/s. At this forward

speed the SPH peak pressure consistently overestimated the experimental peak pressure at all but one of the pressure sensors (see Figure 6.13). Three-dimensional effects (such as longitudinal water pile-up during the slam), incorrect calculation of the ship's motions and/or the use of a single fluid model that neglects the presence of air are probable causes of the over-estimation. The latter is likely for pressure sensor P_{3-1} as it lies on the flat bottom of the third hull cross-section. Nevertheless, at the foremost sections the decreasing trend in peak pressure between each sensor is similar for both the SPH 2D + t approach and the experimental study of Ochi (1958).
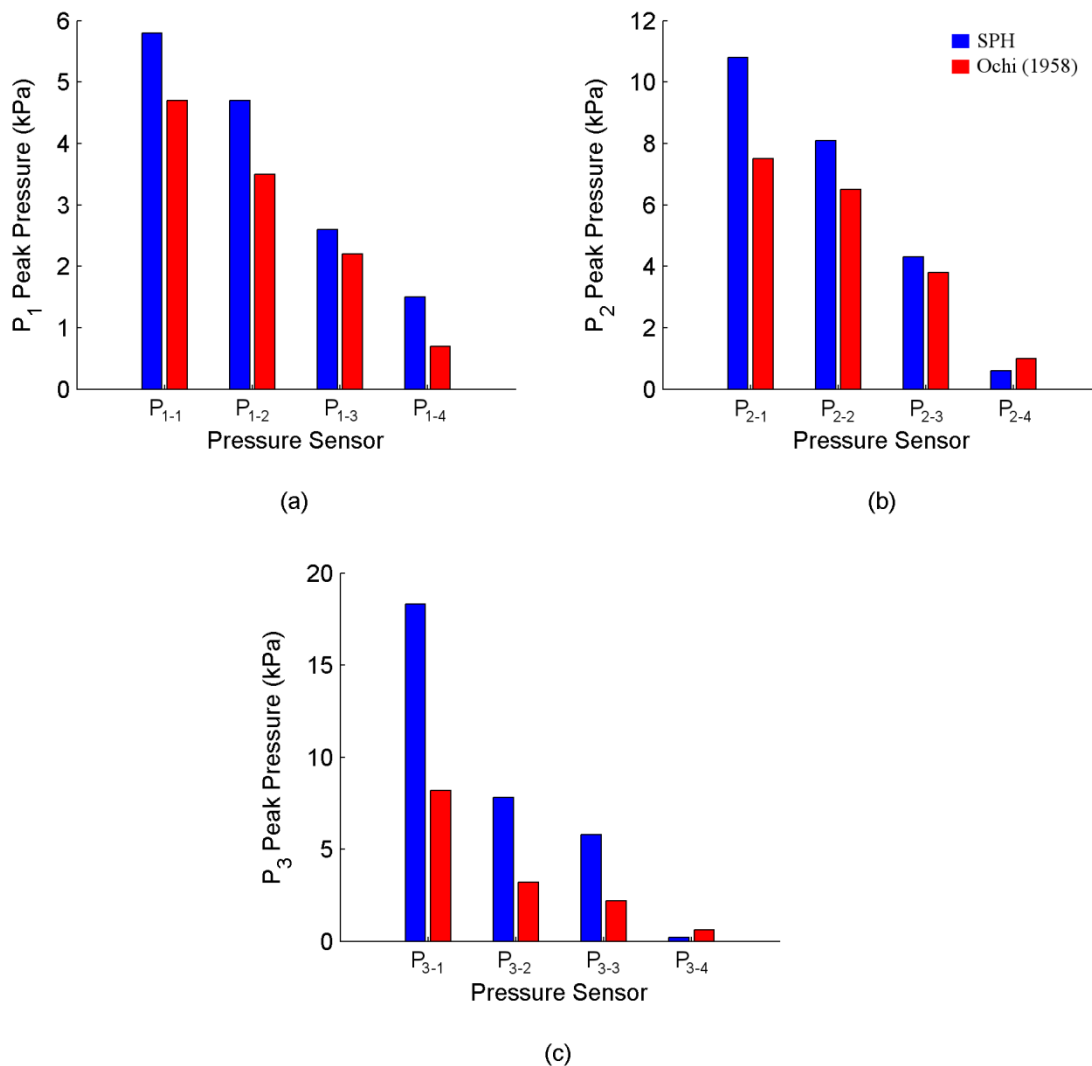
Figure 6.13 – Peak pressure measured by each sensor on cross-sections (a) P_1 $0.093L_{pp}$, (b) P_2 $0.133L_{pp}$, and (c) P_3 $0.174L_{pp}$. The pressures were recorded at a forward speed of 2.2 m/s.

6.4 Summary

In this chapter the SPH model was validated for use in the prediction of slamming loads for slender hulls in regular waves. The slamming data recorded on a model hull studied in an ocean wave basin by Hermundstad and Moan (2005) was used as a validation test case. During the experiments the relative vertical motion between the hull and the water surface was recorded and found to follow a near sinusoidal pattern, differing from the constant and variable velocity hull section water entries previously simulated in Chapter 5. Therefore to enable the SPH algorithm to simulate the Hermundstad and Moan (2005) hull section, the model was forced into still water with a prescribed velocity profile. The pressure recorded at two slamming panels during the experiment was found to agree with that sampled during the SPH simulation.

The good validation results led to the development of a 2D + t SPH method. The method enabled the water entry of a V-form bow to be visualised at a number of different forward speeds based on the heave and pitch moments predicted by the commercial seekeeping software SEAWAY. The peak pressures recorded along the keel were comparable to those measured by Ochi (1958) across all forward speeds, however as the experimental data provided did not include full pressure traces or detailed measurements of the hull's motions it is not possible to draw a conclusion on the viability of the model. The differences between the experimental and SPH pressure peaks are possibly due to the uncertainty introduced when using SEAWAY to predict the hull motions and because some three-dimensional effects are neglected. Furthermore the pressure of the fluid surrounding hull cross-sections with low deadrise angles during water entry is influenced by the presence of air during experimental studies, so the SPH model should be extended to include both air and water. Further validation work based on the recorded data of other model hull forms in tow tanks and ocean wave basins is recommended in order to fully understand the limitations of the 2D + t SPH model.

Chapter 7

Conclusions and Recommendations

7.1 Summary and conclusions

A hybrid Matlab/C++ two-dimensional smoothed particle hydrodynamics algorithm was developed with the aim of modelling bow slamming of ships in regular ocean waves. The discrete forms of the symmetric momentum equation and the continuity equation formed the basis of the algorithm and were governed by the Gaussian cut-off kernel. Applying the equations of motion to a set of disordered SPH particles leads to numerical drift and an inherent lack of stability, so a number of corrections were introduced to the algorithm in order to improve stability. The artificial viscosity, tensile stability correction, XSPH variant and density reinitialisation routine all contributed to the development of a stable SPH algorithm with little numerical drift.

The SPH algorithm was successfully validated against two benchmark test cases that were free from the influence of external forces. The evolution of the initially circular drop of fluid with a prescribed initial velocity field confirmed that the algorithm satisfied the kinematic and dynamic free surface boundary conditions. The free surface definition improved with an increase in resolution and a smooth pressure field was maintained by introducing the density reinitialisation routine. The evolution of the initially square patch of fluid tested the influence of the tensile stability control by imposing a large negative pressure. Implementing the correction forced the fluid particles to maintain regular spacing and prevented the formation of voids. Both test cases were found to be in good agreement with their respective analytical solutions for the pressure field and free surface position. These results would not have been possible without the stabilising properties of the corrections.

Solid boundaries were introduced following the validation of the aforementioned free surface problems and were modelled using the ghost particle method. The effectiveness of the ghost particle method was evaluated by simulating fluid contained in a static tank and the two-dimensional dam break. A smooth hydrostatic pressure field was maintained in the tank despite small amplitude oscillations in the particle positions. The SPH dam break was found to agree with the height and pressure sensor results of Zhou et al. (1999) up until the void formed by the overturning fluid collapsed upon itself. A significant reduction in the system energy was noted after this point because the SPH algorithm was single phase and unable to include the effect of air on the model.

The dam break and subsequent wall impact was an ideal preparation test case for simulating the impact of a falling body on an initially still water surface. The wedges and hull sections modelled consisted of a number of straight line solid boundaries which met at a series of sharp corners. Applying the standard ghost particle technique resulted in an increase in the particle number density at each intersection point. The introduction of a scaling function which acted on the kernel reduced the particle number density imbalance and prevented the formation of large amplitude pressure waves.

The water entry of a wedge moving at a constant vertical speed was then modelled and the total load and neighbouring pressure field was found to be in agreement with the experimental results of Breder (2005). The wedges were then allowed to dynamically respond to the local pressure field and the simulated acceleration, velocity and pressure at a number of sensors on 15° and 25° deadrise wedges was recorded. The peak SPH pressures were found to be in agreement with the analytical approach proposed by Wagner (1932) and a comparison with the experimental data measured by Whelan (2004) also showed good agreement, which made it possible for the algorithm to be extended to free drop tests of hull sections with a more complex geometry. Aarsnes (1996) measured the load and pressure at a number of sensors on a typical flared bow section. An SPH model of the bow section was simulated and the total load and pressure at each sensor was found to agree with the experimental study. Each of the drop test simulations secured confidence in the ability of the SPH algorithm to resolve hull impact problems.

The complexity of the SPH slamming problem was increased by simulating the water entry of a given bow cross-section at forward speed. The ocean wave basin experiments of Hermundstad and Moan (2005) measured the relative vertical motion between a slender hull with a flared bow and the water surface. The slamming pressure at two panels on a model hull in regular waves was also recorded. Slamming was found to have negligible impact on the relative motions during the experiment, so the SPH model was forced into still water with the measured (Hermundstad and Moan, 2005) relative vertical velocity profile. The agreement found between the SPH and experimental pressure traces at each panel confirmed that the relative vertical velocity profile could be used to determine the slamming loads on a slender hull with a longitudinally flat keel in the bow section.

Finally, a 2D + t method was implemented using a combination of the commercial seakeeping software SEAWAY and the SPH algorithm. SEAWAY was employed to calculate the motions of a slender hull in regular waves and the SPH algorithm then imposed these ship motions on model cross-sections to determine the slamming loads. Comparisons with the peak pressures measured on a V-form hull with a longitudinally flat keel (Ochi, 1958) showed that the 2D + t method can be used to predict slamming loads on a slender hull. Nevertheless the introduction of SEAWAY (Ochi (1958) did not publish the ship motion data) does introduce an uncertainty in the ship motion predictions that can carry through to the slamming load calculations. The 2D + t method also suffers from a lack of ability to resolve three-dimensional effects such as the longitudinal fluid velocity for non-flat keels.

In conclusion the developed single fluid SPH algorithm has been shown to be suitable for the simulation of free surface flows with impact throughout the validation process. The application to three-dimensional bow slamming via a 2D + t method was satisfactory but carries with it several limitations, particularly when considering three-dimensional effects and the effect of air compressibility on low deadrise hull sections. Future work, as discussed in the next section, has the potential to resolve these limitations in forthcoming versions of the SPH algorithm.

7.2   Recommendations for future work

The work presented in this thesis has the potential to be expanded in a number of different directions, the first of which is the development of a two-fluid SPH algorithm that is able to account for the effect of air during water impacts. Whelan (2004) drop tested a number of multi-hulled cross-sections as well as the two-dimensional wedges described in Section 5.3. The presence of entrained air was noted after the arches of catamaran cross-sections fell below the still water level. The current SPH algorithm is unable to model air entrainment and cushion effects; which was evident in the simulation of a 25° deadrise wedge with side panels (see Figure 7.1).
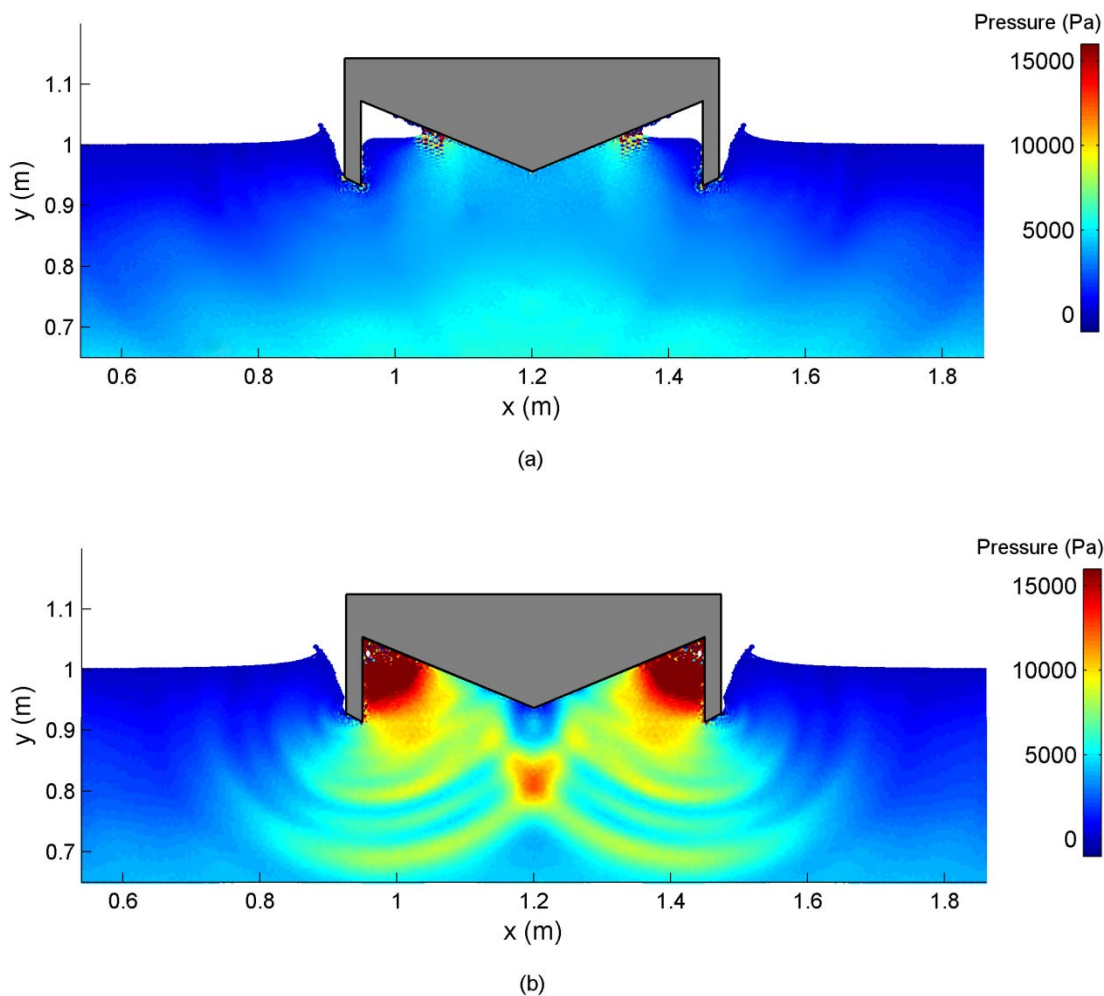
Figure 7.1 – SPH particles coloured by pressure after a 25° deadrise wedge with side panels was dropped from a height of 0.06 m. Images are shown at (a) 0.06 s and (b) 0.08 s after initial impact with the surface.

The initial water entry of the 25° deadrise wedge with side panels is smooth and approximates the motion measured by Whelan (2004), however as the simulation progresses in time the arches fill rapidly and the local fluid pressure exceeds 20 kPa. This spike in pressure is much higher than the 10 kPa recorded in the experiments and causes large pressure waves to propagate through the tank. Including air in the model will enable the air compression and entrainment to be simulated and will have the potential to produce pressure and acceleration traces that more closely resemble those measured by Whelan (2004).

Most of the catamaran hull sections examined by Whelan (2004) were not simple wedges with side panels attached. Some sections closely represented the curved catamaran hulls produced by Incat in Tasmania, Australia, but these are difficult to simulate using the ghost particle technique in SPH. The current method for applying ghost particles to curved sections is not well advanced and will need to be if mono and multi hulled cross-sections of considerable curvature are modelled. Other boundary methods such as the repulsive force method are already able to model curved sections but cannot maintain a relatively smooth pressure field like the ghost particle method. Development of a technique – possibly using conformal mapping – to apply ghost particles on a curved surface will improve the approximation of the fluid-structure interaction.

Currently the SPH code applied in this thesis is limited to run on dual and quad core computers and has only been able to model approximately 400 000 particles within a reasonable time frame. The introduction of variable particle sizes and smoothing lengths would enable the same total number of particles to be modelled, but would concentrate smaller particles in areas of the greatest interest. The far field would then be approximated by larger particles. This will increase the number of particles located at each pressure sensor, improving the accuracy of the approximation.

The current 2D + t algorithm was shown to be able to predict slamming loads on slender mono hulled ships, but it does miss three-dimensional effects. The model could be extended to include the horizontal component of the slam or the relative velocity along the normal of the keel in order to include these three-dimensional effects. Finally the capabilities of the SPH algorithm could be broadened so three-

dimensional slamming of a slender mono hulled ship can be simulated. However, performing full three-dimensional studies requires a significantly larger number of particles, which will not be possible on standard dual and quad core computers. Therefore the algorithm must be divided into a parallel form that can run on high performance computing systems and/or graphical processing units.

A parallelised version of a three-dimensional SPH algorithm could be used in conjunction with commercial seakeeping software such as SEAWAY to predict full three-dimensional bow slamming on a variety of ships. This approach would be ideal because SPH is most suited to modelling transient short time duration problems.

References

Aarsnes, J. V., 1996. Drop test with ship sections - effect of roll angle. Report N° 603834.00.01. *Norwegian Marine Technology Research Institute*, Trondheim, Norway.

Alimi, J.-M., Serna, A., Pastor, C. and Bernabeu, G., 2003. Smooth particle hydrodynamics: importance of correction terms in adaptive resolution algorithms. *Journal of Computational Physics* 192: 157-174.

Andrew, R. N., and Lloyd, A. R. J. M., 1981. Full-scale comparative measurements of the behaviour of two frigates in severe head seas. *The Naval Architect* 1: 1-31.

Anghileri, M., Castelletti, L. and Tirelli, M., 2005. Fluid-structure interaction of water filled tanks during impact with the ground. *International Journal of Impact Engineering* 31: 235-234.

Antoci, C., Gallati, M. and Sibilla, S., 2007. Numerical simulation of fluid-structure interaction by SPH. *Computers and Structures* 85: 879-890.

Arai, M. and Tasaki, R., 1987. A numerical study of water entrance of two-dimensional wedges. In *Proceedings of the 3rd International Symposium on Practical Design of Ships and Mobile Units*. Trondheim.

Arai, M., Cheng, L. Y. and Inoue, Y., 1994. A computing method for the analysis of water impact of arbitrary shaped bodies. *Journal of the Society of Naval Architects of Japan* 176: 233-240.

References

Arai, M., Cheng, L. Y. and Inoue, Y., 1995a. A computing method for the analysis of water impact of arbitrary shaped bodies (2nd report). *Journal of the Society of Naval Architects of Japan* 177: 91-99.

Arai, M., Cheng, L. Y., Inoue, Y., Miyauchi, T. and Ishikawa, M., 1995b. A study of slamming characteristics and optimization of bow forms of ships. In *Proceedings of the 6th International Symposium on Practical Design of Ships and Mobile Units*. Seoul.

Armand, J. L. and Cointe, R., 1987. Hydrodynamic impact analysis of a cylinder. *ASME Journal of Offshore Mechanics and Arctic Engineering* 109: 237-243.

Baker, W. E. and Westine, P. S., 1967. Model tests for structural response of Apollo command module to water impact. *Journal of Spacecraft and Rockets* 4 (2): 201-208.

Belytschko, T., Krongauz, Y., Dolbow, J. and Gerlach, C., 1998. On the completeness of meshfree particle methods. *International Journal of Numerical Methods in Engineering.* 43: 785-819.

Berczik, P., 1999. Chemo-dynamical smoothed particle hydrodynamic code for evolution of star forming disk galaxies. *Astronomy and Astrophysics* 348 (2): 371-380.

Bonet, J. and Lok, T. -S. L., 1999. Variational and momentum preservation aspects of Smooth Particle Hydrodynamic formulations. *Computer Methods in Applied Mechanics and Engineering* 180: 97-115.

Borg, S. F., 1957. Some contributions to the wedge-water entry problem. *Proceedings of the American Society of Civil Engineers, Journal of the Engineering Mechanics Division* Paper 1214.

Breder, J., 2005. Experimental testing of slamming pressure on a rigid marine panel. MEng Thesis, Royal Institute of Technology, Sweden, Stockholm.

Brown, K. C., Wraith, R. G. and Joubert, P. N., 1999. Local pressure on hull plating due to slamming. In *Proceedings of the 5th International Conference on Fast Sea Transportation*. Seattle.

Bisplinghoff, R. L. and Doherty, C. S., 1952. Some studies of the impact of vee wedges on a water surface. *Journal of the Franklin Institute* 253: 547-560.

Cartwright, B., Groenenboom, P. and McGuckin, P., 2004. Examples of ship motion and wash predictions by Smoothed Particle Hydrodynamics (SPH). In *Proceeding of the 9th Symposium on Practical Design of Ships and Other Floating Structures*. Lübeck- Travemünde, Germany.

Cartwright, B., Xia, J., Cannon, S., McGuckin, D. and Groenenboom, P., 2006. Motion prediction of ships and yachts by smoothed particle hydrodynamics. In *Proceedings of 2nd High Performance Yacht Design Conference*. Auckland.

Chihua, L. and Yousheng, H., 1997. Ship hull slamming analysis with nonlinear boundary element method. *China Ocean Engineering* 11 (4): 411-418.

Chuang, S., 1966. Experiments on flat-bottom slamming. *Journal of Ship Research* 10 (1): 10-17.

Chuang, S., 1967. Experiments on slamming of wedge-shaped bodies. *Journal of Ship Research* 11 (3): 190-198.

Chuang, S., 1969. Theoretical investigations on slamming of cone-shaped bodies. *Journal of Ship Research* 13 (4): 276-283.

Clarke, J. D., 1982. Measurement of hull stresses in two frigates during a severe weather trial. *The Naval Architect* (2): 63-74.

Cleary, P. W., Ha, J., Prakash, M. and Nguyen, T., 2006. 3D SPH flow predictions for high pressure die casting of automotive components. *Applied Mathematical Modeling* 20 (11): 1406-1427.

Colagrossi, A., 2004. A meshless lagrangian method for free-surface and interface flows with fragmentation. PhD Thesis, Università di Roma, Rome.

Colagrossi, A. and Landrini, M., 2003. Numerical simulation of interfacial flows by smoothed particle hydrodynamics. *Journal of Computational Physics* 191: 448-475.

Colagrossi, A., Colicchio, G. and Le Touzé, D., 2007. Enforcing boundary conditions in SPH applications involving bodies with right angles. In *Proceedings of the 2nd International SPHERIC Workshop*. Madrid.

Colagrossi, A., Le Touzé, D. and Colicchio, G., 2007. An in-depth investigation of Smoothed Particle Hydrodynamics applied to free-surface problems. Submitted to *Journal of Computational Physics*.

Conolly, J. E., 1974. Standards of good seakeeping for destroyers and frigates in head seas. In *Proceedings of the International Symposium on the Dynamics of Marine Vehicles and Structures in Waves*. London.

Dalrymple, R. A. and Rogers, B. D., 2005. Numerical modeling of water waves with the SPH method. *Coastal Engineering* 53 (2-3): 141-147.

Davis, M. R. and Whelan, J. R., 2007. Computation of wet deck bow slam loads for catamaran arched cross sections. *Ocean Engineering* 34: 2265-2276.

Delorme, L., Colagrossi, A., Souto-Iglesias, A., Zamora-Rodriguez, R. and Botia-Vera, E., 2009. A set of canonical problems in sloshing. Part I: Pressure field in forced roll. Comparison between experimental results and SPH. *Ocean Engineering* 36 (2): 168-178.

Dessi, D. and Mariani, R., 2008. Analysis and prediction of slamming-induced loads of a high-speed mono hull in regular waves. *Journal of Ship Research* 52 (1): 71-86.

Dilts, G. A., 1999. Moving-least-squares-particle hydrodynamics – I. consistency and stability. *International Journal for Numerical Methods in Engineering* 44: 1115-1155.

Dobrovol'skaya, Z. N., 1969. On some problems of similarity flow of fluid with a free surface. *Journal of Fluid Mechanics* 36 (4): 805-825.

Faltinsen, O. M., 1990. *Sea loads on ships and offshore structures*. Cambridge University Press, Cambridge.

Faltinsen, O. M., 2002. Water entry of a wedge with finite dead-rise angle. *Journal of Ship Research* 46 (1): 39-51.

Faltinsen, O. M., 2005. *Hydrodynamics of high-speed marine vehicles*. Cambridge University Press, New York.

Feldman, J., 2006. Dynamic refinement and boundary contact force in Smoothed Particle Hydrodynamics with applications in fluid flow problems. PhD Thesis, School of Engineering, University of Wales, Swansea.

Feldman, J., Bonet, J., 2007. Dynamic refinement and boundary contact forces in SPH with applications in fluid flow problems. *International Journal for Numerical Methods in Engineering* 72: 295-324.

Garabedian, P. R., 1953. Oblique water entry of a wedge. *Communications on Pure and Applied Mathematics* 6: 157-165.

Gingold, R. A. and Monaghan, J. J., 1977. Smoothed Particle Hydrodynamics: Theory and application to non-spherical stars. *Monthly Notices of the Royal Astronomical Society* 181: 375-389.

Gingold, R. A. and Monaghan, J. J., 1982. Kernel estimates as a basis for general particle methods in hydrodynamics. *Journal of Computational Physics* 46: 429-453.

Gomez-Gesteira, M., Cerqueiro, D., Crespo, A. J. C. and Dalrymple, R. A., 2005. Green water overtopping analyzed with a SPH model. *Ocean Engineering* 32: 223-238.

Greenhow, M., 1987. Wedge entry into initially calm water. *Applied Ocean Research* 9 (4): 214-223.

Greco, M., 2001. A two-dimensional study of green-water loading. PhD Thesis, Faculty of Marine Technology, Norwegian University of Science and Technology, Trondheim, Norway.

Hay, B., Bourne, J., Engle, A. and Rubel, R., 1994. Characteristics of hydrodynamic loads data for a naval combatant. In *Proceedings of the International Conference on Hydroelasticity in Marine Technology*, edited by O. M. Faltinsen. Rotterdam.

Hermundstad, O. A. and Moan, T., 2005. Numerical and experimental analysis of bow flare slamming on a Ro-Ro vessel in regular oblique waves. *Journal of Marine Science and Technology* 10: 105-122.

Iglesias, A. S., Rojas, L. P. and Rodríguez, R. Z., 2004. Simulation of anti-roll tanks and sloshing type problems with Smoothed Particle Hydrodynamics. *Ocean Engineering* 31: 1169-1192.

Journée, J. M. J. and Adegeest, L. J. M., 2003. *Theoretical Manual of Strip Theory Program "SEAWAY for Windows"*.

Kalis, J., 2007. Validation of Smoothed Particle Hydrodynamics for water entry phenomena, Master of Science Thesis, Faculty of Mechanical, Maritime and Materials Engineering, Delft University of Technology.

Korobkin, A. A., 1996. Water impact problems in ship hydrodynamics. In *Advances in Marine Hydrodynamics*, edited by M. Ohkusu, Boston.

Korobkin, A. A. and Pukhnachov, V. V., 1988. Initial stage of water impact. *Annual Review of Fluid Mechanics* 29: 159-185.

Korvin-Kroukovsky, B. V. and Jacobs, W. R., 1957. Pitching and heaving motions of a ship in regular waves. *Transactions of the Society of Naval Architects and Marine Engineers* 65: 590-632.

Landrini, M., Colagrossi, A. and Faltinsen, O. M., 2003. Sloshing in 2-D flows by the SPH method. In *Proceedings of the 8th International Conference on Numerical Ship Hydrodynamics*. Busan, Korea.

Liu, M. B., Liu, G. R., Lam, K. Y. and Zong, Z., 2003. Smoothed particle hydrodynamics for numerical simulation of underwater explosion. *Computational Mechanics* 30: 106-118.

Lloyd, A. R. J. M., 1989. *Seakeeping: Ship Behaviour in Rough Weather*. Ellis Horwood Limited, Chichester.

Lu, C. H., He, Y. S. and Wu, G. X., 2000. Coupled analysis of nonlinear interaction between fluid and structure during impact. *Journal of Fluids and Structures* 14: 127-146.

Lucy, L. B., 1977. A numerical approach to testing the fission hypothesis. *The Astronomical Journal* 82 (12): 1013-1024.

Manganelli, P., Wagemakers, B. and Wilson, P. A., 2003. Investigation of slamming loads using slam patches on a scale model of an open 60' class yacht. *International Journal of Small Craft Technology* 145: 47-62.

Martin, J. C. and Moyce, W. J., 1952. An experimental study of the collapse of liquid columns on a rigid horizontal plane. *Philosophical Transactions of the Royal Society of London* 244 (882): 312-324.

Monaghan, J. J., 1989. On the problem of penetration in particle methods. *Journal of Computational Physics* 82: 1-15.

Monaghan, J. J., 1994. Simulating free surface flows with SPH. *Journal of Computational Physics* 110: 399-406.

Monaghan, J. J., 2000. SPH without a tensile instability. *Journal of Computational Physics* 159: 290-311.

Monaghan, J. J., 2005. Smoothed particle hydrodynamics. *Reports on Progress in Physics* 68: 1703-1759.

Monaghan, J. J. and Kos, A., 1999. Solitary waves on a cretan beach. *Journal of Waterway, Port, Coastal and Ocean Engineering* 125 (3): 145-154.

Monaghan, J. J. and Lattanzio, J. C., 1985. A refined particle method for astrophysical problems. *Astronomy and Astrophysics* 149: 133-143.

Morris, J. P., Fox, P. J. and Zhu, Y., 1997. Modeling low Reynolds number incompressible flows using SPH. *Journal of Computational Physics* 136: 214-226.

Ochi, K., 1958. Model experiments on ship strength and slamming in regular waves. *Transactions of the Society of Naval Architects and Marine Engineers* 66: 345-383.

Ochi, M. K., 1964. Prediction of the occurrence and severity of ship slamming at sea. In *Proceedings of the 5th O.N.R Symposium*. Bergen.

Oger, G., Doring, M., Alessandrini, B. and Ferran, P., 2005. Two-dimensional SPH simulations of wedge water entries. *Journal of Computational Physics* 213: 803-822.

Pakozdi, C., 2008. A Smoothed Particle Hydrodynamics study of two-dimensional nonlinear sloshing in rectangular tanks. PhD Thesis, Department of Marine Technology, Norwegian University of Science and Technology, Trondheim

Payne, P. R., 1981. The vertical impact of a wedge on a fluid. *Ocean Engineering* 8 (4): 421-436.

Pohle, F. V., 1950. The Lagrangian equations of hydrodynamics: solutions which are analytic functions of the time, PhD thesis, Graduate School of Arts and Science, New York University, New York.

Randles, P. W. and Libersky, L. D., 1996. Smoothed particle hydrodynamics: Some recent improvements and applications. *Computer Methods in Applied Mechanics and Engineering* 139: 375-408.

Roberts, T. J., Watson, N. L. and Davis, M. R., 1997. Evaluation of sea loads in high speed catamarans. In *Proceedings of the 5th International Conference on Fast Sea Transportation*, edited by N. Baird. Sydney, Australia.

Roubtsova, V. and Kahawita, R., 2005. The SPH technique applied to free surface flows. *Computers and Fluids* 35 (10): 1359-1371.

Sarpkaya, T., 1978. Wave impact loads on cylinders. In *Proceedings of the 10th Annual Offshore Technology Conference*. Houston.

Sebastiani, L., Valdenazzi, F., Grossi, L. and Kapsenberg, G. K., 2001. A theoretical/experimental investigation of the slamming pressures on fast monohull vessels. In *Proceedings of the 6th International Conference on Fast Sea Transportation*. Southampton, UK.

Shao, S., 2009. Incompressible SPH simulation of water entry of a free-falling object. *International Journal for Numerical Methods in Fluids* 59 (1): 91-115.

Shepard, D. 1968. A two-dimensional interpolation function for irregularly-spaced data. In *Proceedings of the 23rd ACM National Conference*. New York.

Steinmann, P., Fach, K., and Menon, B., 1999. Global and slamming sea loads acting on an 86m high speed catamaran ferry. In *Proceeding of the 5th International Conference on Fast Sea Transportation*. Seattle, USA.

Sun, H., 2007. A boundary element method applied to strongly nonlinear wave-body interaction problems. PhD Thesis, Department of Marine Technology, Norwegian University of Science and Technology, Trondheim.

Sun, H. and Faltinsen, O. M., 2008. Asymmetric water entry of a bow-flare ship section with roll angle. In *Proceedings of the IUTAM Symposium on Fluid-Structure Interaction in Ocean Engineering*, edited by E. Kreuzer. Hamburg, Germany.

Thomas, G. A., Davis, M. R., Holloway, D. S., Watson, N. L. and Roberts, T. J., 2003. Slamming response of a large high-speed wave-piercer catamaran. *Marine Technology* 40 (2): 126-140.

Tulin, M. P. and Landrini, M., 2001. Breaking waves in the ocean and around ships. In *Proceedings of the 23rd Symposium on Naval Hydrodynamics*. Val de Reuil, France.

Tveitnes, T., Fairlie-Clarke, A. C. and Varyani, K., 2008. An experimental investigation into the constant velocity water entry of wedge-shaped sections. *Ocean Engineering* 35: 1463-1478.

Vinje, T. and Brevig, P., 1980. Nonlinear two-dimensional ship motions. In *Proceedings of the 3rd International Conference on Numerical Ship Hydrodynamics*. Paris, France.

Viviani, M., Brizzolara, S. and Savio, L., 2009. Evaluation of slamming loads using smoothed particle hydrodynamics and Reynolds-averaged Navier-Stokes methods. *Proceedings of the Institution of Mechanical Engineers, Part M: Journal of Engineering for the Maritime Environment* 223 (1): 17-31.

von Karman, T., 1929. The impact of sea plane floats during landing. Technical Report No. 321, National Advisory Committee for Aeronautics, Washington, USA.

Vulovich, R., Hirayama, T., Toki, N. and Mizuno, H., 1989. Characteristics of hull stresses measured on a large containership in rough seas. *Transactions of the Society of Naval Architects and Marine Engineers* 97: 397-428.

Wagner, H., 1932. The phenomena of impacts and sliding on liquid surfaces. NACA translation 1366, National Advisory Committee for Aeronautics, Washington, USA.

Whelan, J. R., 2004. Wetdeck slamming of high-speed catamarans with a centre bow. PhD Thesis, School of Engineering, University of Tasmania, Hobart.

White, F.M., 1999. *Fluid Mechanics*, McGraw-Hill, Singapore.

Wraith, R., 1998. Pressure loads on ship hull plating caused by slamming. PhD Thesis, The University of Melbourne, Melbourne.

Yamamoto, Y., Iida, K., Fukusawa, T., Murakami, T., Arai, M. and Ando, A., 1985. Structural damage analysis of a fast ship due to bow flare slamming. *International Ship Building Progress* 32 (369): 124-136.

Zhao, R. and Faltinsen, O. M., 1993. Water entry of two-dimensional bodies. *Journal of Fluid Mechanics* 246: 593-612.

Zhao, R., Faltinsen, O. M. and Aarsnes, J., 1997. Water entry of arbitrary two-dimensional sections with and without flow separation. In *Proceedings of the 21st Symposium of Naval Hydrodynamics*. Trondheim.

Zhou, Z. Q., De Kat, J. O. and Buchner, B., 1999. A nonlinear 3-D approach to simulate green water dynamics on deck. In *Proceedings of the 7th International Conference on Numerical Ship Hydrodynamics*. Nantes, France.

Every reasonable effort has been made to acknowledge the owners of copyright material. I would be pleased to hear from any copyright owner who has been omitted or incorrectly acknowledged.

Appendix A

SPH Sound Speed and Compressibility

A.1 Introduction

Smoothed Particle Hydrodynamics simulations of low-speed problems involving water are often conducted by approximating the real fluid with one that is artificially more compressible. This approximation is applied by reducing the fluid sound speed (see Section 3.2.4) and is possible if the speed of sound is much greater than the maximum expected fluid flow velocity. The approximation is also necessary because the full sound speed requires a very small time step by the Courant–Friedrichs–Lewy condition (3.104), which in turn forces a long, inefficient computation time (see Table A.1). In this thesis the fluid sound speed was reduced to between 5% and 20% of its typical value in order to model efficiently the fluid contained within a static tank (see Section 4.3), the breaking of a dam (see Section 4.4) and the still water impact of a variety of two-dimensional objects (see Chapters 5 and 6).

To observe the effect the reduced sound speed had on the still water impact of a two-dimensional body, the experimental drop test of a 25° deadrise wedge conducted by Whelan (2004) was simulated at sound speeds of 100 m/s (reduced) and 1500 m/s (full). Both wedges were dropped from a normalised height of $H_H^* = 0.61$ and were modelled on a dual core, 2.40 GHz desktop PC, over an impact period of 0.15 s. The particle resolution was reduced from $R/H = 400$ (see Section 5.3) to $R/H = 150$ so that the actual sound speed simulation could be completed within a reasonable time. At this lower resolution, the wedge impact simulation with the full sound speed took approximately 15.5 times longer to complete than the reduced sound speed model (see Table A.1). Therefore using the full sound speed at a higher resolution is simply not feasible in terms of the required computation time.

Characteristics	$c_s = 100$ m/s	$c_s = 1500$ m/s
Particle Resolution	$R/H = 150$	$R/H = 150$
Number of Particles	54000	54000
Time Step Size	1.3×10^{-5} s	8.6×10^{-7} s
Total Time Elapsed	2 hrs 7 min	32 hrs 38 min

Table A.1 – Characteristics of the two SPH wedge impact simulations.

A.2 SPH results

The pressure fields surrounding the 25° deadrise wedge modelled using sound speeds of 100 m/s and 1500 m/s are illustrated in Figure A.1 and Figure A.2. Both simulations appear to be quite different in form, particularly when looking at the particle spacing. At the low sound speed the particles are easily displaced from their initial Cartesian lattice and form a coarse jet which is visible 0.12 s after the keel strikes the still water surface (see Figure A.2a). However, at the full sound speed the particles appear to maintain long strings that deform, but do not break and form a jet.

One possible explanation for the fluid particles maintaining these long structures is the artificial viscosity correction (see Section 3.3.1). The increase in sound speed is directly reflected in the strength of the artificial viscosity correction (3.88), therefore the particles are encouraged to maintain an even separation for the duration of the simulation. This also influences the local pressure field as the particles are compressed along the strings near where the wedge surface meets the initial still water level. The artificial viscosity has not allowed the particles to scatter and so the pressure further away from the wedge surface is greater than that seen at the lower sound speed.

Despite the differences noted in the particle positions and the local pressure field, the wedge acceleration, velocity and pressure traces are very similar. Figure A.3a compares the acceleration recorded in the experiment with both the low and high sound speed SPH simulations. The high sound speed acceleration peaks slightly earlier in time at approximately the same level as that recorded during the low sound

speed simulation, and this is reflected in a reduction of the vertical impact speed of the wedge. The strength of the artificial viscosity is again the main probable cause of this difference as the strings of fluid particles are compressed in the high sound speed simulation, causing the local fluid pressure immediately adjacent to the keel to rise slightly above that of the low sound speed model. This slows the wedge and causes the delay in peak pressures – relative to the experimental and low sound speed data – seen at each of the individual pressure sensors.
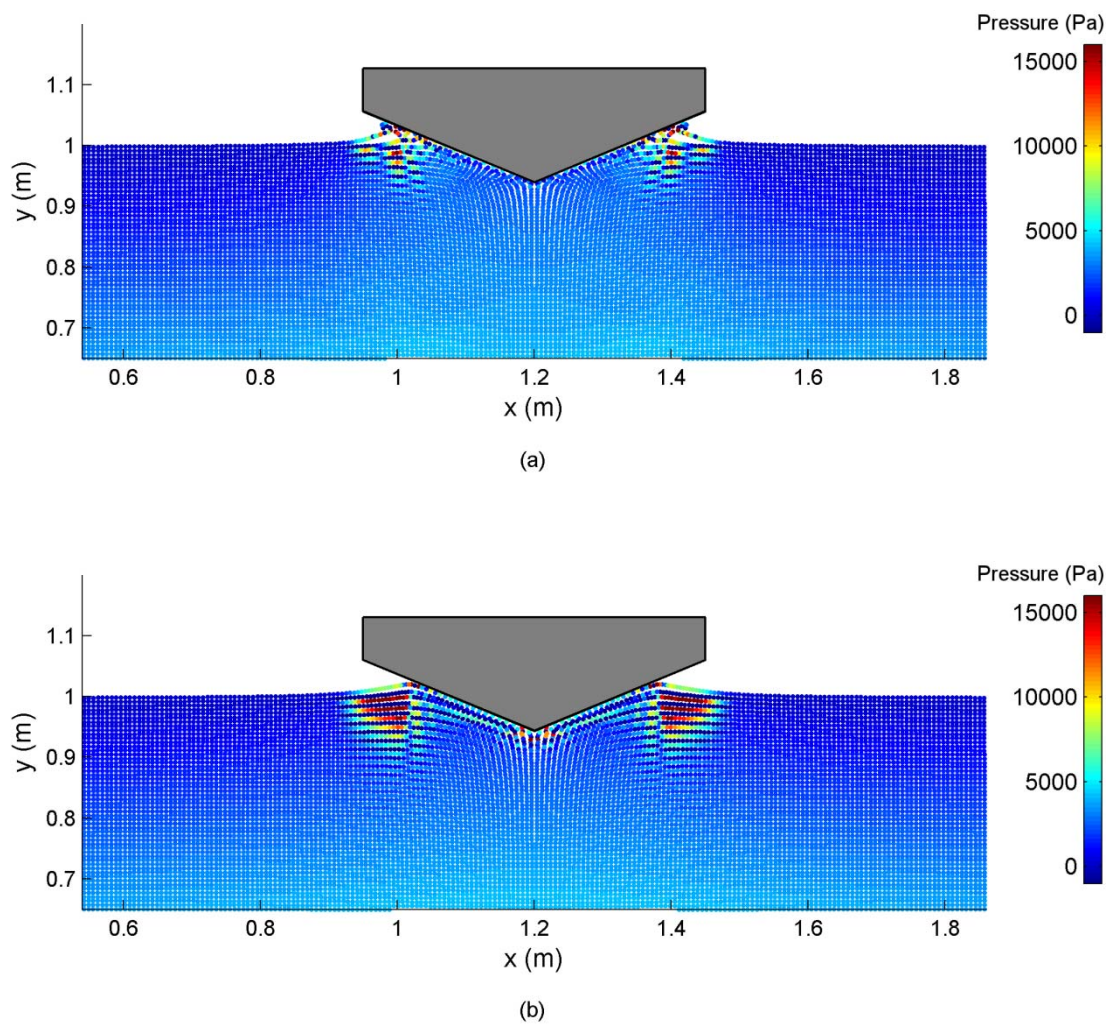

Figure A.1 – Pressure field surrounding the $25°$ deadrise wedge 0.06 s after initial impact with the free surface. The fluid sound speed was set at (a) $c_s = 100$ m/s and (b) $c_s = 1500$ m/s.

(a)

(b)

Figure A.2 – Pressure field surrounding the 25° deadrise wedge 0.12 s
after initial impact with the free surface. The fluid sound speed was
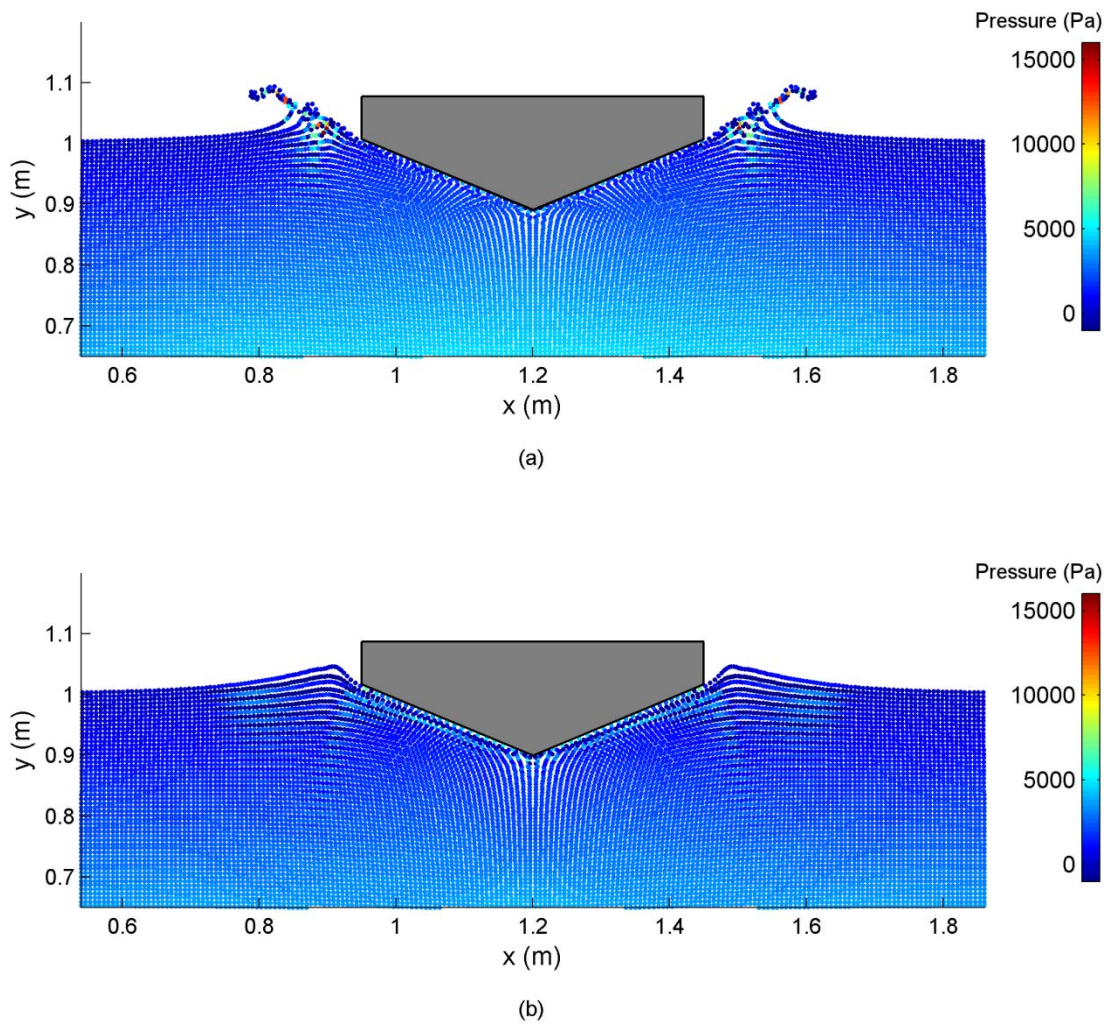set at (a) $c_s = 100$ m/s and (b) $c_s = 1500$ m/s.

Regardless of the lag, the peak pressures of the high sound speed model recorded at
all four pressure sensors (see Figure 5.10b for pressure sensor locations) are
comparable with the low sound speed and experimental peaks. However, after the
peak the pressure recorded at each sensor of the high sound speed model is slightly
higher than that recorded both in the experiment and the low sound speed model.
This elevated pressure is again due to the increase in absolute artificial viscosity
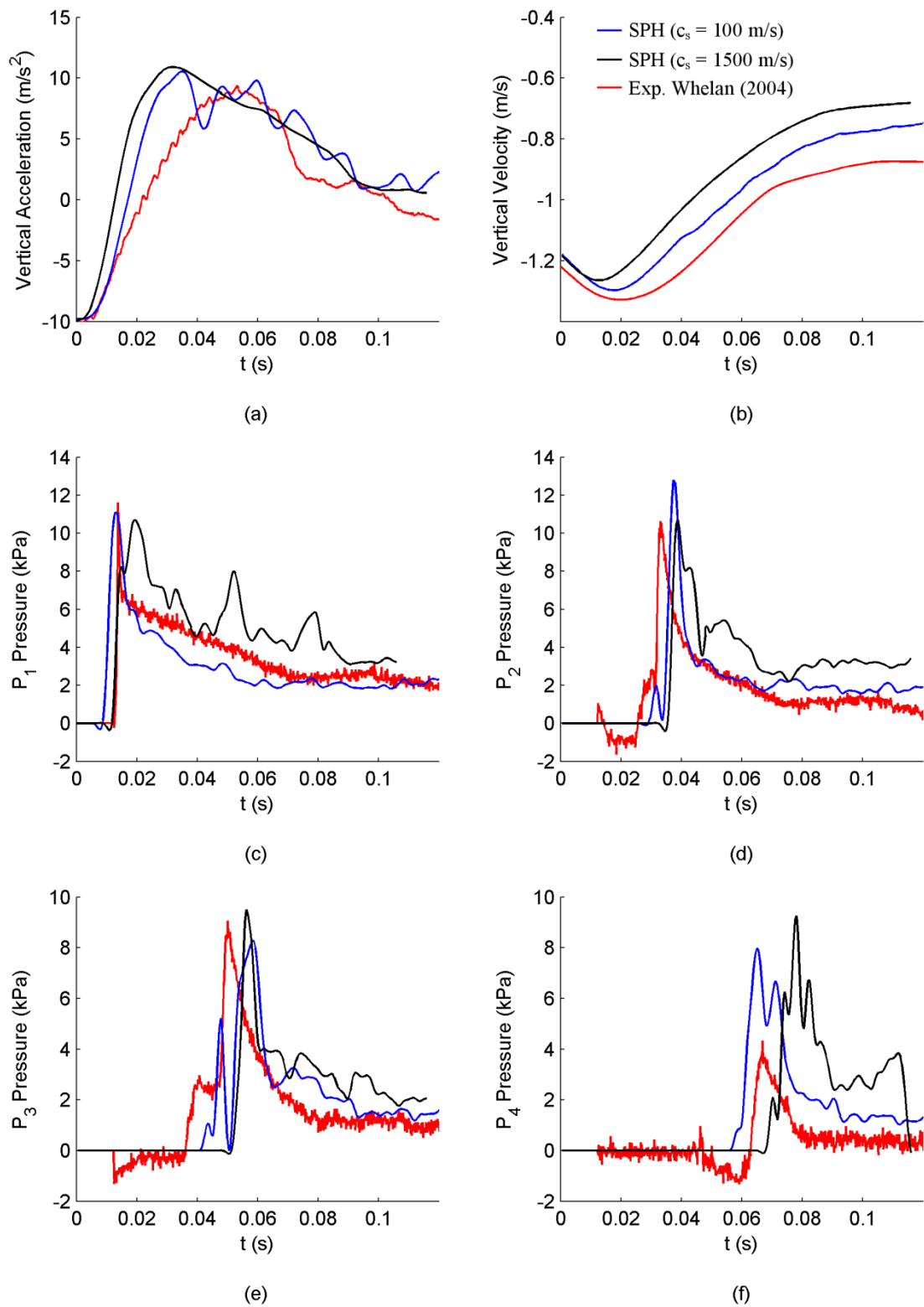causing an artificial increase in the local fluid pressure.

Figure A.3 – The vertical acceleration, vertical velocity and pressure at four pressure sensors of a 25° deadrise wedge dropped from $H_H^* = 0.61$.

An attempt was made to alleviate the influence of the artificial viscosity on the high sound speed simulation by reducing the value of the coefficient α in equation (3.88). Initial entry of the wedge was modelled successfully, but after 0.01 s the simulation deteriorated and the properties of the wedge and the fluid surrounding it could not be determined accurately. Numerical drift is one possible reason for this deterioration as the time step size was 150 times smaller than the low sound speed model. The weaker artificial viscosity was then no longer able to quell the influence of the very small numerical errors that can occur at each time step. Therefore with comparable artificial viscosity strength, the current version of the SPH code cannot resolve the water entry of a wedge using the full sound speed.

A.3 Summary

In conclusion the high sound speed and low sound speed SPH models were comparable in terms of the acceleration and peak pressures recorded during the still water impact of a two-dimensional wedge. However, some differences were noted in the particle positions, most probably due to an increase in the strength of the artificial viscosity correction. Reducing the artificial viscosity strength demonstrated that the full sound speed model suffered from numerical drift due to the very small time step. In spite of this, the comparison has shown that the SPH wedge water entry models conducted at the lower artificial sound speed do agree with those performed using the full sound speed, indicating that the weakly compressible approximation is valid.

Appendix B

Constant and Variable Velocity Water Entries of a 15° Wedge

The water entry of triangular wedges at both constant and variable entry speed was studied in Chapter 5 of this thesis. However the constant entry speed experiments of Breder (2005) and the variable entry speed drop tests of Whelan (2004) could not be compared directly because the wedges were not of a common deadrise angle. So in order to investigate the difference between the two types of water entries, the 15° deadrise wedge drop tested by Whelan (2004) was modelled at both variable and constant velocity using the SPH algorithm.

The 15° deadrise wedge dropped by Whelan (2004) from a normalised height of $H_H^* = 0.73$ (see Section 5.3.2) impacted the initially still water surface at 1.57 m/s. The constant velocity water entry modelled using the SPH algorithm was forced into the water at this speed, while the variable velocity water entry was allowed to respond to the loads caused by the increase in local fluid pressure, causing the vertical speed of the wedge to decrease over time (see Figure 5.13b).

The pressure recorded at three sensors located on the surface of the wedge (see Figure 5.10a) and the total vertical force is illustrated in Figure B.1. The vertical force measured during both SPH simulations rises at approximately the same rate as both wedges begin to break through the still water surface. After approximately 0.01s the variable velocity wedge begins to slow and the force peaks just below 3.0 kN. The force on the constant velocity wedge rises above 8.0 kN after 0.03 s (the point at which the wedge becomes fully wetted), which is considerably greater than the variable velocity water entries.
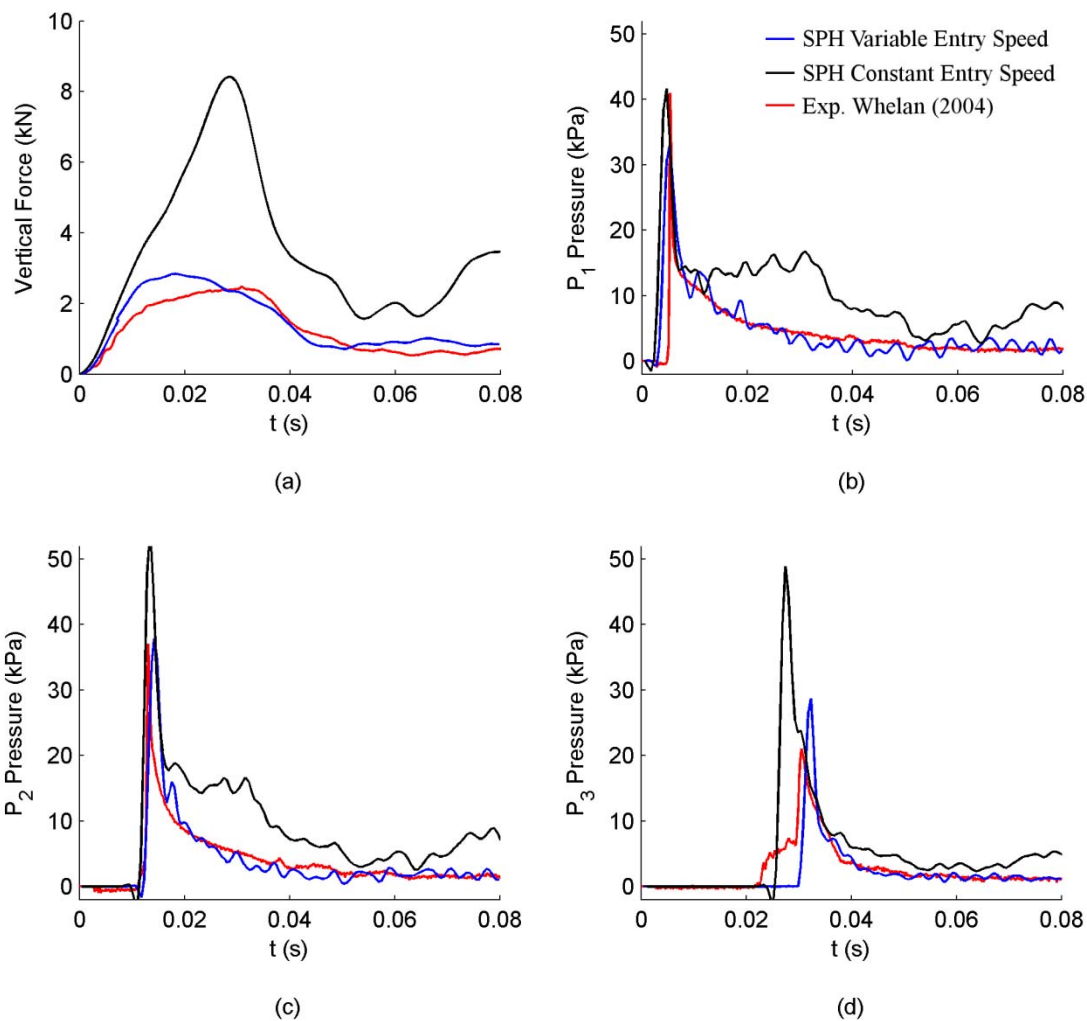
191

Figure B.1 – The vertical acceleration and fluid pressure at four

sensors of a 15° deadrise wedge dropped from $H_H^* = 0.73$.

An explanation for the greater force on the constant velocity wedge can be found by studying the pressure measured at each of the sensors. The pressure sensor P_1, located slightly above the keel, records peak pressures in both SPH models that are comparable to that measured by Whelan (2004) and in agreement with Wagner's (1932) approximation (see Figure 5.17). However at P_2 and P_3 the peak pressure recorded during the constant velocity water entry is approximately the same, while the peak pressures recorded during both the experimental and numerical variable velocity entries have decreased. This decrease in pressure is due to the small high pressure region – found on the surface of the wedge at the initial still water level (see

Figure 5.11) – decreasing in magnitude as the wedge slows, also causing a reduction in the measured and modelled vertical force.

In summary, the constant and variable velocity water entries display similar behaviour in terms of the pressure and vertical force traces early in the simulations. However, once the vertex entered the initially still water, the recorded pressure on the remainder of the wedge, and the resulting loads experienced, were much smaller for the variable entry speed case.
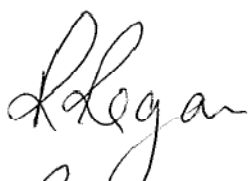
Appendix C

Copyright Permission

PERMISSION TO USE COPYRIGHT MATERIAL AS SPECIFIED BELOW:

Two photographs of a 56.8 m Armidale class patrol boat on page 2 of this thesis with the caption:

> Figure 1.1 – A 56.8 m Armidale class patrol boat is known to have excellent seakeeping qualities despite experiencing hull bottom slamming in rough seas (photographs courtesy of Austal, Australia, 2010).

I hereby give permission for Daniel Veen to include the above mentioned materials in his higher degree thesis for the Curtin University of Technology, and to communicate this material via the Australasian Digital Thesis Program. This permission is granted on a non-exclusive basis and for an indefinite period.

I confirm that I am the copyright owner of the specified material.

Signed: *[signature]*

Name: RICHARD REGAN

Position: MARKETING MANAGER

Date: 14/10/2010